AECL EACL

CA9700636

AECL-11494-2, COG-95-552-2

The Disposal of Canada's Nuclear Fuel Waste: A Study of Postclosure Safety of In-Room Emplacement of Used CANDU Fuel in Copper Containers in Permeable Plutonic Rock Volume 2: Vault Model

Le stockage permanent des déchets de combustible nucléaire du Canada : Étude de la sûreté post-fermeture de la mise en place en chambre du combustible CANDU irradié renfermé dans des conteneurs en cuivre enfouis dans la roche plutonique perméable Volume 2 : Modèle d'installation de stockage

L.H. Johnson, D.M. LeNeveu, F. King, D.W. Shoesmith, M. Kolar, D.W. Oscarson, S. Sunder, C. Onofrei, J.L. Crosthwaite

June 1996 juin

THE DISPOSAL OF CANADA'S NUCLEAR FUEL WASTE: A STUDY OF POSTCLOSURE SAFETY OF IN-ROOM EMPLACEMENT OF USED CANDU FUEL IN COPPER CONTAINERS IN PERMEABLE PLUTONIC ROCK VOLUME 2: VAULT MODEL

by

L.H. Johnson, D.M. LeNeveu, F. King, D.W. Shoesmith, M. Kolar,
D.W. Oscarson, S. Sunder, C. Onofrei and J.L. Crosthwaite

Atomic Energy of Canada Limited
Whiteshell Laboratories
Pinawa, Manitoba, Canada R0E 1L0
1996

AECL-11494-2
COG-95-552-2

THE DISPOSAL OF CANADA'S NUCLEAR FUEL WASTE: A STUDY OF POSTCLOSURE SAFETY OF IN-ROOM EMPLACEMENT OF USED CANDU FUEL IN COPPER CONTAINERS IN PERMEABLE PLUTONIC ROCK: VOLUME 2: VAULT MODEL

by

L.H. Johnson, D.M. LeNeveu, F. King, D.W. Shoesmith,
M. Kolar, D.W. Oscarson, S. Sunder, C. Onofrei and J.L. Crosthwaite

ABSTRACT

A study has been undertaken to evaluate the design and long-term performance of a nuclear fuel waste disposal vault based on a concept of in-room emplacement of copper containers at a depth of 500 m in plutonic rock in the Canadian Shield. The containers, each with 72 used CANDU® fuel bundles, would be surrounded by clay-based buffer and backfill materials in an array of parallel rooms, with the excavation boundary assumed to have an excavation-disturbed zone (EDZ) with a higher permeability than the surrounding rock. In the anoxic conditions of deep rock of the Canadian Shield, the copper containers are expected to survive for $>10^6$ a. Thus container manufacturing defects, which are assumed to affect approximately 1 in 5000 containers, would be the only potential source of radionuclide release in the vault.

The vault model is a computer code that simulates the release of radionuclides that would occur upon contact of the used fuel with groundwater, the diffusive transport of these radionuclides through the defect in the container shell and the surrounding buffer, and their dispersive and convective transport through the backfill and EDZ into the surrounding rock. The vault model uses a computationally efficient boundary integral model (BIM) that simulates radionuclide mass transport in the engineered barrier system as a point source (representing the defective container) that releases radionuclides into concentric cylinders, that represent the buffer, backfill and EDZ. A 3-dimensional finite-element model is used to verify the accuracy of the BIM.

The vault model uses distributed or probabilistic parameter values to account for both uncertainty and variability. In describing the model, particular emphasis is placed on the mechanistic understanding of the processes leading to radionuclide release, explaining the basis for the selection of parameter values used in the model, and justifying the exclusion of certain processes from the model.

The results obtained in the present study indicate the effectiveness of a design using in-room emplacement of long-lived copper containers in providing a safe disposal system even under permeable geosphere conditions.

Atomic Energy of Canada Limited
Whiteshell Laboratories
Pinawa, Manitoba, Canada R0E 1L0
1996

AECL-11494-2
COG-95-552-2

LE STOCKAGE PERMANENT DES DÉCHETS DE COMBUSTIBLE NUCLÉAIRE DU CANADA : ÉTUDE DE LA SÛRETÉ POST-FERMETURE DE LA MISE EN PLACE EN CHAMBRE DU COMBUSTIBLE CANDU IRRADIÉ RENFERMÉ DANS DES CONTENEURS EN CUIVRE ENFOUIS DANS LA ROCHE PLUTONIQUE PERMÉABLE VOLUME 2 : MODÈLE D'INSTALLATION DE STOCKAGE

par

L.H. Johnson, D.M. LeNeveu, F. King, D.W. Shoesmith, M. Kolar,
D.W. Oscarson, S. Sunder, C. Onofrei et J.L. Crosthwaite

RÉSUMÉ

On a réalisé une étude pour évaluer la conception et les performances à long terme d'une installation de stockage permanent des déchets de combustible nucléaire, fondée sur un concept de mise en place en chambres des déchets renfermés dans des conteneurs en cuivre, à une profondeur de 500 m dans la roche plutonique du Bouclier canadien. Les conteneurs, chacun ayant 72 grappes de combustible CANDU® irradié, seraient entourés par un matériau tampon à base d'argile et des matériaux de remblai, dans des chambres en parallèle; on a aussi supposé que la limite d'excavation aurait une zone perturbée par l'excavation d'une plus grande perméabilité que la roche environnante. En raison des conditions anoxiques qu'on trouve à grande profondeur dans le Bouclier canadien, les conteneurs en cuivre devraient résister pendant $>10^6$ a. Par conséquent, les défauts de fabrication des conteneurs, que l'on prévoit être d'environ 1 sur 5 000 conteneurs, constitueraient la seule source éventuelle de libération des radionucléides dans l'enceinte.

Le modèle d'installation de stockage est un code de calcul qui simule la libération de radionucléides qui se produirait au contact du combustible irradié avec les eaux souterraines, le processus de diffusion par lequel ces radionucléides quitteraient le conteneur (par suite du défaut du conteneur) et traverseraient le matériau tampon entourant le conteneur, de même que le processus de diffusion par dispersion et convection dans le remblai et la zone perturbée par l'excavation dans la roche environnante. Le modèle d'installation de stockage fait appel à un modèle des équations intégrales aux frontières efficace au point de vue du calcul, qui simule le transport de masse des radionucléides dans le système de barrières ouvragées comme étant une source ponctuelle (représentant le conteneur défectueux) de libération des radionucléides dans des cylindres concentriques représentant le matériau tampon, le remblai et la zone perturbée par l'excavation. On utilise un modèle par éléments finis tridimensionnel pour vérifier l'exactitude du modèle des équations intégrales aux frontières.

Le modèle d'installation souterraine utilise des valeurs paramétriques réparties ou probabilistes pour tenir compte de l'incertitude et de la variabilité. Pour la description du modèle, on a mis l'accent sur la compréhension mécaniste des processus menant à la libération des radionucléides, expliquant la raison du choix des valeurs paramétriques utilisées et justifiant l'exclusion de certains processus du modèle.

Les résultats obtenus dans le cadre de la présente étude démontrent l'efficacité de la mise en place en chambres des conteneurs en cuivre de longue durée de vie renfermant les déchets pour l'implantation d'un système de stockage permanent sûr, même dans des conditions de grande perméabilité de la géosphère.

Énergie Atomique du Canada Limitée
Laboratoires de Whiteshell
Pinawa (Manitoba) Canada R0E 1L0
1996

AECL-11494-2
COG-95-552-2

CONTENTS

PREFACE

The concept for disposal of Canada's nuclear fuel waste involves isolating the waste in corrosion-resistant containers emplaced and sealed within a vault at a depth of 500 to 1000 m in plutonic rock of the Canadian Shield. The technical feasibility and social aspects of the concept, and its impact on the environment and human health, are presented in an Environmental Impact Statement (EIS) (AECL 1994a), a summary of the EIS (AECL 1994b) and a set of nine primary references (Davis et al. 1993; Davison et al. 1994a,b; Goodwin et al. 1994; Greber et al. 1994; Grondin et al. 1994; Johnson et al. 1994a,b; Simmons and Baumgartner 1994).

The disposal concept permits a choice of methods, materials, site locations and designs (AECL 1994a,b; Johnson et al. 1994a; Simmons and Baumgartner 1994). This preface puts into perspective the following three studies which illustrate the long-term safety of different implementations of the concept:

- the postclosure assessment case study of a reference disposal system presented in the EIS (AECL 1994a,b; Goodwin et al. 1994);

- a study to illustrate how to identify a favourable vault location that would ensure long groundwater travel times from the vault to the accessible environment (Stevenson et al. 1995, 1996; Ophori et al. 1995, 1996); and

- the present study that illustrates (i) the flexibility for designing engineered barriers to accommodate a permeable host-rock condition in which advection is the rate-determining contaminant transport process (Baumgartner et al. 1996), and (ii) the flexibility of the modelling methodology to simulate the long-term performance of different design options and site characteristics (Goodwin et al. 1996a, Johnson et al. 1996, Stanchell et al. 1996, Wikjord et al. 1996, Zach et al. 1996).

THE POSTCLOSURE ASSESSMENT CASE STUDY PRESENTED IN THE EIS

The EIS (AECL 1994a,b) and four of the primary references (Davis et al. 1993, Davison et al. 1994b, Goodwin et al. 1994 and Johnson et al. 1994b) describe a case study of the long-term (i.e., postclosure) performance of a hypothetical implementation of the concept, referred to as the *reference disposal system.*

The reference system illustrates what a disposal system, including the vault, geosphere and biosphere, might be like. Although it is hypothetical, it is based on information derived from extensive laboratory, field and engineering investigations. Many of the assumptions made about the long-term performance of the reference system are conservative; that is, they would tend to overestimate adverse effects. The technology specified is either available or judged to be readily achievable. The reference disposal system includes one possible choice among the options for such things as the waste form, the disposal container, the buffer and backfill, the shaft seals and bulkheads, the location and depth of the vault, and the orientation and layout of the vault with respect to the geological features of the site. The components and designs chosen for the engineered barriers and the site conditions represented in the reference system are not being recommended, but rather, they illustrate a technically feasible way of implementing the disposal concept. In an actual implementation of the concept, the engineered system would be adapted to the lithostructural, hydrogeological, geochemical, geothermal, geomechanical, and geomicrobiological conditions of the host rock formation, and the expected evolution of those conditions over thousands of years.

The *reference vault* (Johnson et al. 1994b) of the EIS postclosure assessment case study includes used-fuel bundles from CANDU® reactors, encapsulated in thin-walled Grade-2 titanium alloy containers packed with particulate for mechanical support, emplaced in boreholes in the floor of rooms, and surrounded by a sand-bentonite mixture. The rooms are filled with a lower backfill of crushed granite and lake clay and an upper backfill of sand and bentonite, and the entrances are sealed with concrete bulkheads. The plan area and the design capacity of the vault were initially set at 4.0 km^2 and 10.1 million fuel bundles (191 000 Mg U) respectively. The fuel inventory is roughly equivalent to the waste that would accrue in 100 a at the current production rates in Canada. The plan area was subsequently reduced to 3.2 km^2 and the inventory to 8.5 million bundles (162 000 Mg U), as a result of design constraints to ensure a large margin of safety in the case study. The borehole-emplacement geometry was modelled as layered planar elements (slabs) representing the waste form, buffer, backfill and host rock.

The *reference geosphere* (Davison et al. 1994b) consists of the host rock formation, its groundwater flow system, the materials used to seal the shafts and exploration boreholes, and a water well. The geological characteristics of the reference geosphere are derived from data from AECL's Whiteshell Research Area (WRA), located near Lac du Bonnet, Manitoba. This area includes a substantive portion of the Lac du Bonnet Batholith, a large granitic rock body several kilometres deep with an exposed surface measuring over 60 km long and 20 km across at its widest part. The granitic body was intruded over 2.5 billion years ago into the rocks existing at the time. The batholith, the surrounding rocks, and the interfaces between them have been the subject of field investigations for more than 15 a. Most of the information about the rock mass, such as the location and orientation of fractures and fracture zones, is based on field studies of the WRA, including detailed investigations that were conducted to locate and construct an Underground Research Laboratory (URL) to a depth of 440 m. For geological structures outside the areas where detailed borehole information was available, inferences have been made on the basis of nearby boreholes; geological mapping; and satellite, airborne and ground-based geophysical surveys. The hypothetical vault for the reference system was located at a depth of 500 m within the rock mass investigated at the URL to ensure that the maximum amount of available subsurface data was used to construct the geosphere model.

In the postclosure assessment of the reference system, we assumed that a large, low-dipping, fracture zone — designated LD1 — was located close to the vault horizon. Although field evidence from the URL revealed that this fracture zone did not extend beyond a depth of about 400 m, we conservatively assumed that it continued to much greater depths and connected with other vertical fracture zones. In this situation, LD1 became a pathway for rapid groundwater flow from the depth of the hypothetical vault to the accessible environment. We constrained all waste disposal rooms to be located beneath LD1 (i.e., to the footwall side of the fracture) and imposed a waste exclusion distance of 50 m within the low-permeability, sparsely fractured rock domain between this fracture zone and the nearest waste disposal room of the vault. To accommodate the waste exclusion distance, we chose to restrict the waste capacity of the vault relative to the capacity specified in a conceptual engineering study (Simmons and Baumgartner 1994). These design constraints, together with the hydrogeological properties of the rock beneath LD1, ensured that (i) contaminants passed through the backfill, a large reservoir which reacts strongly with most of the contaminants, and (ii) diffusion was the dominant transport process from the waste disposal rooms through the lower rock domain to the fracture zone.

The *reference biosphere* (Davis et al. 1993) consists of the surface and near-surface environment, including the water, soil, air, people, and other organisms, as encountered on the Canadian Shield as a whole. However, the parts of the biosphere that interface with the geosphere are specific to the WRA. In all other respects, the biosphere is assumed to be typical of the Canadian Shield, consisting of rocky outcrops; bottom lands with pockets of soil, bogs, and lakes; and uplands with meadows, bush, and forests. No major changes in the topography of the region are likely to occur during the 10 000 a following closure of a disposal facility.

CANDU® is a registered trademark of Atomic Energy of Canada Limited (AECL)

Changes in climate, surface water flow patterns, soils, and vegetation types are expected to be within the range of variation currently observed across the Shield; such variations are included in the distributions of values of model parameters specified for the EIS case study.

The long-term safety analyses of this system of engineered and geological barriers indicated that the maximum estimated mean dose rate to an individual in the critical group during the first 10 000 a is about 100 million times smaller than dose rate from natural background radiation. The corresponding risk is about a million times smaller than the radiological risk criterion specified by the Atomic Energy Control Board in Regulatory Document R-104 (AECB 1987).

A STUDY TO IDENTIFY A FAVOURABLE VAULT LOCATION

In an actual implementation, it would be advantageous to locate the disposal vault in a hydraulically favourable setting within the large-scale groundwater flow system of a siting area. Recently, we completed a separate study to illustrate how such a location could be found within the WRA. The conceptual hydrogeological model of the WRA was revised using information from a program of regional geologic mapping, geophysical surveys and borehole drilling and testing (Stevenson et al. 1995, 1996). Large-scale groundwater flow modelling was then performed using a three-dimensional, finite-element hydrogeological code; and groundwater travel times, flow pathways and discharge locations were determined with a particle tracking code (Ophori et al. 1995, 1996).

This study has indicated that diffusion is the rate-determining transport process and diffusive transport times greater than 10^5 a could likely be achieved by selecting a vault location at 750 m depth about 5 km northeast of the URL. Advective travel times are about two orders of magnitude longer than the diffusive transport time. Since the groundwater flow and particle-tracking analyses indicated that such a favourable location would likely ensure a margin of safety even greater than that calculated for the EIS case study, a full systems analysis was not carried out. Instead, we directed our efforts to the present study in which we evaluate the long-term effects of a hypothetical geological setting with a permeable host-rock condition.

THE PRESENT STUDY

A wide range of design options is possible within the general definition of the disposal concept (AECL 1994a,b; Johnson et al. 1994a; Simmons and Baumgartner 1994). In the present study, we illustrate the potential of designing the engineered barriers and the vault to increase the robustness of the long-term safety case, or to compensate for hydrogeological conditions that could result in a less effective geosphere barrier than the one we specified for the EIS case study. In addition, we illustrate the flexibility of the modelling approach to integrate new features, processes and data representing different design options and site characteristics into a full systems assessment. To achieve these ends, we have undertaken an analysis of the feasibility and safety of emplacing long-lasting copper containers within vault rooms (as opposed to deposition in boreholes in the floor of rooms) in a hypothetical volume of permeable plutonic rock where advective travel times from the vault to the biosphere are very short relative to those in the EIS case study. Although we have not encountered such conditions at disposal-vault depths in our investigations at various research areas on the Shield, performance assessments done for the Swedish and Finnish nuclear waste disposal programs have considered these conditions in the crystalline rocks of the Fennoscandian Shield. We are not suggesting that such rock conditions might constitute favourable, desirable, or even acceptable conditions for an eventual disposal site on the Canadian Shield. Rather, the study is intended to illustrate the effectiveness of the in-room emplacement method and copper containers in inhibiting the release of contaminants from the vault.

The vault model for the present study simulates dissolution of used CANDU fuel in a geochemical environment, which evolves from an initial oxidative condition, caused by residual air and radiolysis, to an eventual steady-state anoxic condition. The model simulating the performance of copper containers is based on pinhole manufacturing defects and indefinite lifetime (i.e., no corrosion-induced failures). The in-room emplacement geometry is modelled as a line source representing the waste form, point sources representing pinholes in the defected containers randomly located in the vault, and concentric cylinders representing the buffer, backfill and excavation disturbed zone.

The geosphere model for the present study is more speculative than the one used for the EIS case study because it does not represent conditions we have encountered at any of our geologic research areas. We assume that the vault depth, the geometry of the geosphere model, and the arrangement of major fracture zones and rock mass domains surrounding the disposal vault are identical to those of the EIS case study. However, we assume much higher permeability and lower porosity conditions in the rock domain adjacent to the vault than the conditions observed at the URL and used in the EIS case study. As a result, the lower rock domain is not a diffusion-dominated barrier and the low-dipping fracture zone, LD1, is not the dominant advection pathway to the surface. The effects of geothermal gradient, vault heat and a water supply well on the groundwater flow field have been simulated and the implications on the long-term redox conditions in the vault have been assessed. The groundwater travel times from the disposal vault to the surface are up to 10 000 times shorter in this present geosphere model than in the model used for the EIS case study.

For this study, there is no advantage to constraining the location of the disposal rooms relative to LD1 as was done in the EIS case study. Thus the waste disposal rooms are located both below and above LD1 (i.e., on both the footwall and hangingwall sides of the fracture). The 50-m waste exclusion distance is retained but is relatively insignificant because advection is the dominant transport process in the permeable lower rock domain. Thermal restrictions and shielding requirements of the in-room emplacement option result in a reduction in the density of waste containers of roughly 50% relative to the borehole emplacement option of the EIS case study.

The biosphere model for the present study includes a number of changes, notably inclusion of additional radionuclides with shorter half-lives, inhalation pathways for animals, the most recent internal dose conversion factors of the International Commission on Radiological Protection (ICRP 1991a, b), geosphere dose limits for non-human biota, and updated values of model input parameters. Moreover, the part of the model representing the biosphere/geosphere interface was improved to account more fully for terrestrial discharge of radionuclides.

COMPARISON OF THE EIS CASE STUDY AND THE PRESENT STUDY

The key features of the EIS postclosure assessment case study and the present study are summarized as follows:

	EIS CASE STUDY	PRESENT STUDY
DESIGN CONSIDERATIONS		
Emplacement option	borehole	in-room
Vault area/depth	3.2 km^2/500 m	3.4 km^2/500 m
Fuel inventory: number of bundles	8.5 million	4.3 million
mass of uranium	162 000 Mg	82 000 Mg
Fuel Burnup	685 GJ/kg U	720 GJ/kg U
Fuel Cooling time	10 a	10 a
Number of bundles per container	72	72
Number of waste containers	118 700	60 100
Room locations	footwall of LD1	footwall and hangingwall of LD1

	EIS CASE STUDY	PRESENT STUDY
VAULT MODEL		
Vault model geometry	layered slabs	nested cylinders
Fuel dissolution model	thermodynamic	kinetic
Container shell material	Grade-2 Ti	high purity Cu
Container corrosion mechanisms	localized crevice and delayed hydride cracking	general corrosion and pitting
Fraction of containers failed instantly	10^{-3} to 10^{-4} (complete failure)	10^{-3} to 10^{-4} (pinhole failure)
Fraction of containers failed by 10^4 a	1.0	10^{-3} to 10^{-4}
Effective buffer thickness	0.25 m	1.48 m
Effective backfill thickness	1.4 m	0.76 m
Excavation disturbed zone	evaluated outside system model	evaluated explicitly within system model
GEOSPHERE MODEL		
Conceptual model of fracture zones and rock domains	URL area of WRA	URL area of WRA*
Permeability of rock domain surrounding vault	10^{-19} m^2	10^{-17} m^2
Effective transport porosity of rock domain surrounding vault	3×10^{-3}	10^{-3} to 10^{-5}
Minimum contaminant transport times from vault to biosphere	tens of thousands of years	tens of years
Rate-determining transport process	diffusion	advection
Maximum well depth	200 m	100 m
BIOSPHERE MODEL	BIOTRAC1 - typical of the Canadian Shield	BIOTRAC2 - modifications to improve the model and update the parameters
SYSTEMS ANALYSIS		
Computer Code	third generation code (SYVAC3-CC3-ML3)	prototype (PR4) of fourth generation code (SYVAC3-CC4)
Maximum estimated dose rate to a member of critical group up to 10^4 a	about 10^{-11} Sv/a	about 10^{-6} Sv/a
Time at which estimated dose rate reaches peak	> 10^5 a	about 10^4 a
Key radionuclides contributing to estimated dose rate up to 10^4 a	^{129}I ^{36}Cl ^{14}C	^{129}I, ^{36}Cl ^{14}C, ^{79}Se ^{90}Sr, ^{90}Y, ^{99}Tc
Principal safety feature	low permeability rock domain surrounding vault	long-lasting containers

* The conceptual model used for this present study does not represent a combination of conditions that we have encountered at any of our geologic research areas on the Shield. It has the same geometric arrangement of fracture zones and rock domains as was used in the EIS case study; however, the permeability of the rock domain surrounding the vault has been assumed to be 10^{-17} m^2. This permeability is 100 times greater than the value specified for the EIS case study, which was based on actual measurements within the lower rock zone at the URL.

The EIS case study, the study to identify a favourable vault location, and the present study illustrate the flexibility of AECL's disposal concept in taking advantage of the retention, delay, dispersion, dilution and radioactive decay of contaminants in a system of natural barriers provided by the geosphere and the hydrosphere and of engineered barriers such as the waste form, container, buffer and backfill. In an actual implementation, the engineered system would be designed for the geological conditions encountered at the host site.

HIERARCHY AND SCOPE OF DOCUMENTS FOR THE PRESENT STUDY

This study, presented in five main volumes and a number of supporting documents, is organized as follows:

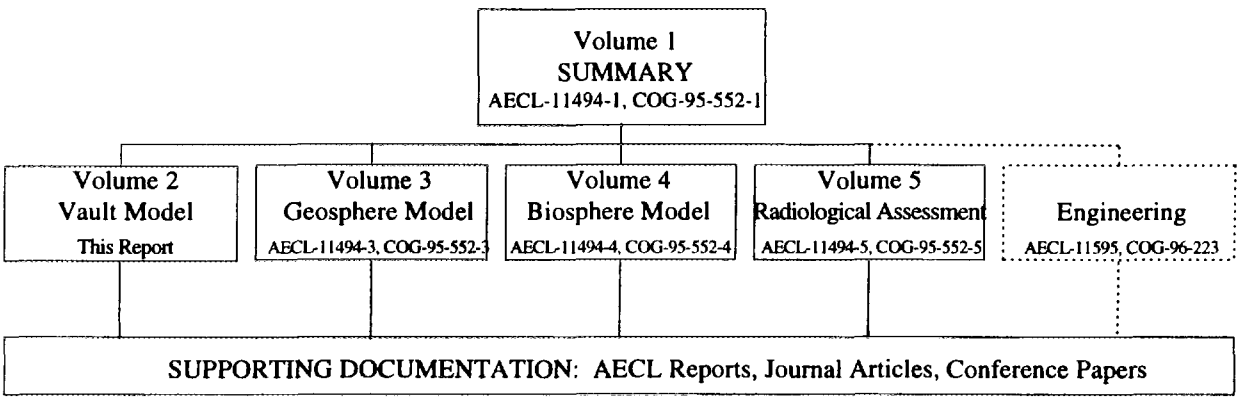

Volume 1, Summary (Wikjord et al. 1996), provides an overview of this study and summarizes the design considerations and safety of in-room emplacement of CANDU used-fuel in long-lasting copper containers in permeable plutonic rock.

Volume 2, Vault Model (this report), describes and justifies the assumptions, model and data used to analyze the long-term behaviour of the engineered system (the near-field), including the waste form (used CANDU fuel), container shell (deoxidized, low-phosphorous copper), buffer (precompacted bentonite clay and silica sand), backfill (glacial lake clay and crushed rock), and excavation disturbed zone.

Volume 3, Geosphere Model (Stanchell et al. 1996), describes and justifies the assumptions, model and data used to analyze the transport of contaminants through permeable plutonic rock of the Canadian Shield, including the effects of a pumping well. The geological characteristics assumed in this study are not based on an integrated data set for any particular field research area.

Volume 4, Biosphere Model (Zach et al. 1996), describes and justifies the assumptions, model and data used to analyze the movement of contaminants through the near-surface and surface environments and to estimate radiological impacts on humans and other biota.

Volume 5, Radiological Assessment (Goodwin et al. 1996), provides an estimate of long-term radiological effects of the hypothetical disposal system on human health and the natural environment, including an analysis of how uncertainties of the assumed site and design features affect system performance.

A separate engineering study (Baumgartner et al. 1996), shown by the dotted lines, is closely linked to this 5-volume series. It describes the conceptual design, technical feasibility, thermal and mechanical analyses, and project lifecycle for implementing an engineered system based on the in-room emplacement of copper containers. It is applicable to a broader range of geosphere conditions than assumed in the present study.

1. INTRODUCTION

In a previous study (Johnson et al.1994b), published as part of an Environmental Impact Statement (EIS) of a concept for disposal of Canada's nuclear fuel waste (AECL 1994), we described a model and long-term safety analysis for the disposal of used CANDU fuel in a hypothetical vault located in the Whiteshell Research Area in Manitoba. In the reference vault design, used fuel bundles were encapsulated in titanium containers, which were then emplaced in boreholes, surrounded by a bentonite-sand buffer material, in the floor of disposal rooms. The remaining excavations were proposed to be sealed with a backfill of crushed granite and clay.

It is recognized that a number of alternative design and material choices for the engineered barrier system are available (Johnson et al.1994a). In addition, a number of vault design alternatives had been examined (Simmons and Baumgartner 1994), and the in-room emplacement concept was identified as warranting detailed study. In particular, it was noted that it would be instructive to develop a vault and engineered barrier design that could compensate for a geosphere barrier that was less effective than the one adopted in the previous study.

The design developed for the present study is described in detail by Baumgartner et al.(1996), and is based on in-room emplacement of copper containers. We present here conceptual and mathematical models, completely revised relative to those of the previous study, that describe failure of containers, radionuclide release from the used fuel and mass transport through the sealing materials to the surrounding rock. In addition, data for all of the models were updated where important new information was available. The radiological dose estimates have been calculated with the SYVAC PR4 code. Because of the large number of model and data changes made, it is very difficult to make direct comparisons between the results obtained here and those of the previous case study. The reader is referred to Goodwin et al.(1996b) for the results of calculations that directly compare doses for in-room and borehole emplacement for a specific set of groundwater flow conditions.

2. DESCRIPTION OF THE VAULT SYSTEM

2.1 INTRODUCTION

The design of the vault system is described in detail by Baumgartner et al. (1996). For the present study, thermal restrictions and radiation shielding of the in-room emplacement option result in a reduction in the density of waste containers of roughly 50% relative to the borehole emplacement option described in the EIS (AECL 1994). A total of 81000 Mg of uranium in the form of 4.3 million used fuel bundles are assumed to be

emplaced in the vault. The used-fuel bundles are assumed to have been out of reactor for 10 a, and to have a burnup of 720 GJ·(kg U)$^{-1}$ (Floyd et al. 1992). Radionuclide inventories for the reference fuel are given in Appendix A.

2.2 GEOSPHERE SETTING

The geosphere model for the present study is hypothetical since it does not represent conditions we have encountered at any of our geologic research areas. The geometry of the geosphere model is identical to that used for the EIS case study and the disposal vault is located at a depth of 500 m. The rock surrounding the disposal vault is assumed to have the same arrangement of major fracture zones and rock mass domains as the EIS case study. However, the geosphere model for the present study assumes much higher permeability and lower porosity conditions in the rock domain surrounding the disposal vault than the conditions used in the EIS case study. As a result, the lower rock domain is not a dominant diffusion barrier and the low-dipping fracture zone, LD1, is not the dominant advection pathway to the surface. The groundwater travel times from the disposal vault to the surface are 1000 to 10,000 times shorter in this alternative geosphere model than in the model used for the EIS case study.

The geosphere model is described in detail by Stanchell et al. (1996).

2.3 DISPOSAL VAULT DESIGN

The disposal vault depth is assumed to be 500 m, the minimum depth considered in the design study by Baumgartner et al. (1996). The disposal containers are emplaced within rooms (Fig. 2.1), rather than within boreholes excavated into the floors of rooms. The general plan layout of the vault is described by Baumgartner et al. (1996).

A low-heat high-performance concrete is placed on the floor of the disposal rooms. Precompacted blocks of dense backfill (70% graded crushed granite, 25% glacial lake clay and 5% bentonite by dry mass) and buffer (a 1:1 mixture by dry mass of silica sand and bentonite) are placed above. The arrangement of blocks leaves horizontal cylindrical cavities for emplacement of containers. The upper backfill, which consists of a 1:1 mixture of granitic sand, i.e., crushed and graded granite, and bentonite, is pneumatically emplaced. The properties of the various sealing materials are discussed in Chapter 3.

2.4 DISPOSAL CONTAINER DESIGNS

Two container designs are considered for the present study, both with a 25.4-mm-thick copper shell. The packed-particulate design is based on the concept developed for the engineering study of Simmons and Baumgartner(1994), in which 72 used-fuel bundles are retained within a basket constructed of carbon-steel tubes, and the residual void in the container is filled with glass beads, compacted in place by vibration. In the design adopted for the present study the container aspect ratio is smaller, the bundles are placed

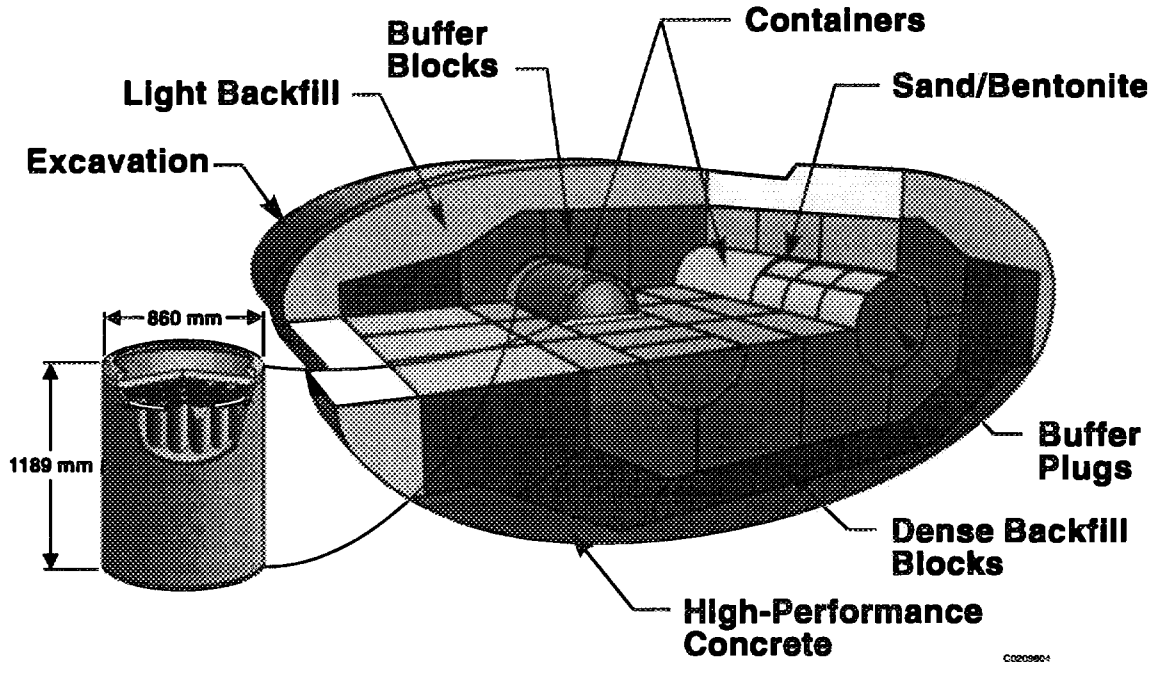

FIGURE 2.1: Layout of a Disposal Room

in a shorter basket, constructed of stainless steel tubes, and the void space is filled with either compacted glass beads or silica sand (Fig. 2.2).

The other container design concept being considered is a steel-shell-supported copper container, shown in Fig. 2.3. In this design, the basket (containing 72 used-fuel bundles) is placed within a 65-mm-thick carbon-steel shell. The steel shell is welded shut and placed within the copper shell, which is sealed by electron-beam welding. This container is designed to withstand the expected structural loads without additional internal support (i.e., particulate), although compacted glass beads or silica sand could also be used to fill the void space. The structural-performance assessment of the two designs is discussed in Chapter 4.

2.5 DESIGN MODIFICATIONS ARISING FROM PERFORMANCE ASSESSMENT CONSIDERATIONS

During the development of conceptual and mathematical models of the disposal vault, a number of issues arose regarding the post-closure performance of the design initially considered (Baumgartner et al. 1995) for the present case study. Based on preliminary modeling of the vault system, several design changes were made that were expected to

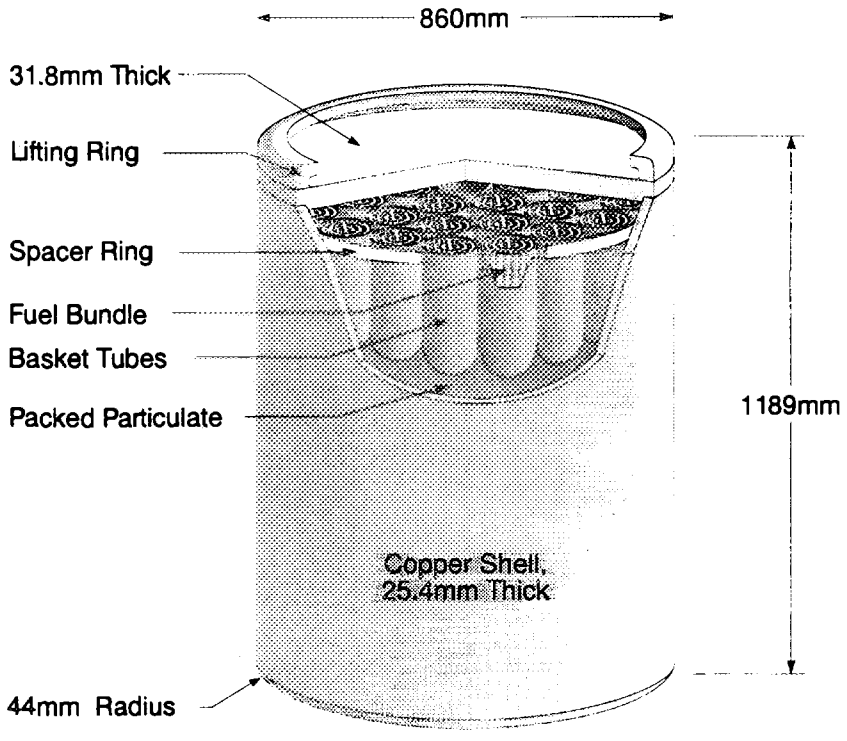

FIGURE 2.2: The Packed-Particulate-Supported Cu-Shell Container

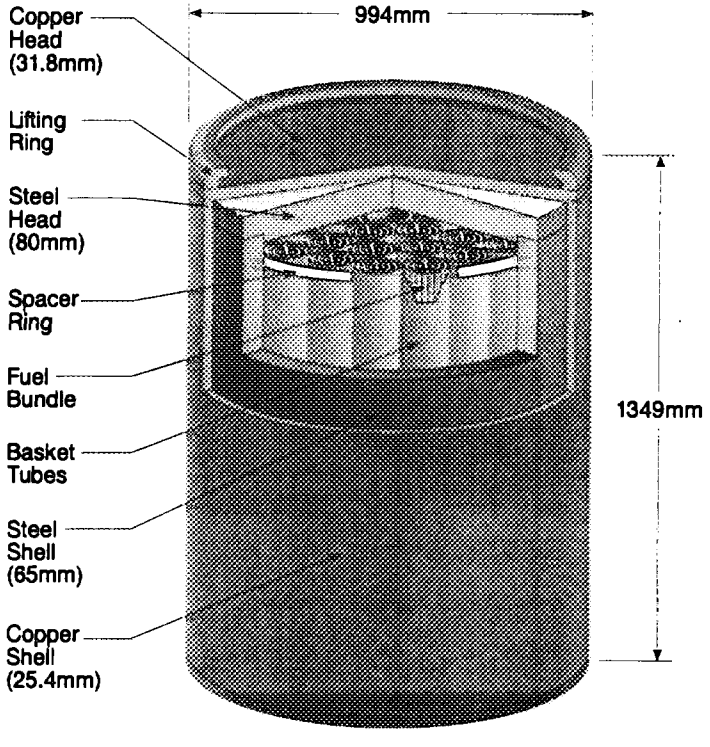

FIGURE 2.3: The Dual-Shell (Fe/Cu) Container

improve vault performance, ensure consistency between the design study and the vault model, or provide flexibility and robustness in the engineered system design. These include:

(1) Replacing the quartz sand in the upper backfill with granite sand. This was proposed to ensure that backfill containing crushed granite would completely surround the buffer. The Fe(II)-bearing minerals in granite promote anoxic conditions and thus ensure that Tc is in its reduced and comparatively immobile state.

(2) Considering the steel-shell supported Cu container design as well as the packed particulate supported design for the assessment calculations. This was undertaken because there is some question whether the latter design would be structurally sound under the potentially high groundwater pressures (~40 MPa) associated with glaciation.

(3) Replacing the silica sand that would fill the gap between the container and buffer with a mixture of granulated bentonite and sand. As discussed in Chapter 3.3.2, radionuclide diffusion through the defect in the container greatly diminishes release. This reduction in mass transport rate can only be assumed if diffusion controls mass transport in the region immediately adjacent to the defect. This is best assured by having bentonite in immediate contact with the container surface.

(4) Using deoxidized, low-phosphorous (DLP) copper for the container shell instead of oxygen-free, electronic (OFE) copper. DLP copper, a high-purity experimental alloy, was proposed for the construction of disposal containers in the Swedish nuclear fuel waste management program, based on that program's long-term mechanical-behaviour investigations of various copper grades (Henderson et al. 1992). This represents a change from the original OFE[3] material specified in Baumgartner et al. (1995). Differences in corrosion performance between the two materials are negligible, as discussed in Chapter 4.4.5.

2.6 THE CONCEPTUAL MODEL OF THE VAULT

In performing calculations with the vault model, we assume that the surface facilities have been removed, that shafts and boreholes leading to the vault have been thoroughly sealed, and that all vault rooms, tunnels and subsurface facilities have been backfilled. Moreover, we assume in the mathematical model that resaturation of the vault is complete

[3] American Society of Testing and Materials (ASTM) material designation number according to the Society's Unified Numbering System (UNS): C10100. The chemical requirements for OFE copper (according to ASTM Specification B 170) are that the minimum copper content shall be 99.99% and that the maximum oxygen content shall be 0.001%.

at the time of closure and that steady-state groundwater flow conditions have been attained. The effects of the unsaturated period have been considered qualitatively for a number of processes in the vault.

The plan area of the disposal vault in the present study occupies about 3.4 km^2 and the surrounding rock exhibits significant spatial variations in its hydrogeological properties, notably groundwater velocities (Stanchell et al. 1996). To account for these variations, we divide the vault into sectors and estimate contaminant releases from each sector. Each sector then serves as a source to a contaminant transport pathway through the geosphere.

The vault model estimates the release of contaminants from each vault sector, by simulating the following processes:

- failure of the copper containers,
- release of contaminants from the used fuel and Zircaloy fuel sheaths to the interior of the container,
- precipitation of contaminants inside the container if solubility limits are exceeded,
- transport by diffusion of dissolved contaminants through a small defect (pinhole) in the container to enter the surrounding buffer, and
- transport by diffusion of contaminants through the buffer, and by convection and dispersion through the backfill and excavation-disturbed zone (EDZ) into the surrounding host rock.

The vault model is also linked to the geosphere model to ensure the two models are consistent. This is achieved in part by dividing the vault into sectors based largely on variations in geosphere properties.

It is expected on the basis of corrosion performance that a 25-mm-thick Cu shell would not fail by corrosion in less than 10^6 a; thus we assume that the only failure mechanism for the copper containers involves undetected fabrication defects. These defects are envisioned to be small, pinhole-sized openings in the outer copper shell that permit the ingress of groundwater and the subsequent escape of contaminants, starting immediately after closure of the vault. The median number of containers that have undetected manufacturing defects is 1 in 5000, resulting in a total of approximately 12 containers failed in the vault. We assume the size of the container defects are time-independent. This last assumption is consistent with the container design option that involves packed particulate to provide internal mechanical support. The design option involving an internal steel shell to provide structural support is expected to have the same failure mechanism, but the size of the defect may be enlarged by internal pressures caused by corrosion-product formation on the steel shell. The likelihood of this effect is expected to

be small and a separate calculation is performed to examine the dose consequences for this case (see Chapters 6.3.2 and 6.5.3.5).

The net release rate of a contaminant from a vault sector is equal to the product of the number of failed containers in that sector and the calculated release rate from one failed container for that sector.

We assume that a failed container fills with groundwater and that all fuel sheaths fail immediately upon closure of the disposal vault. We then estimate releases of contaminants to the water inside the container from the used fuel and from the Zircaloy fuel sheaths. We model two radionuclide release mechanisms: instant and congruent release for the used fuel matrix, and congruent release for the Zircaloy matrix. It is assumed that the fuel sheath does not prevent access of water to the fuel.

Instant release refers to release of contaminants that are not uniformly dispersed in the used fuel matrix. A fraction of the inventory of some contaminants is located in the fuel/sheath gap and at the grain boundaries of the fuel pellets (the remaining inventory is bound in the UO_2 matrix and is released congruently). We assume that this fractional inventory is released to the interior of the failed container at the time of closure of the disposal vault. An important parameter used to model this mechanism is the "instant-release" fraction. In this study, we assume a fraction of the inventory of the following radionuclides undergo instant release: ^{14}C, ^{36}Cl, ^{135}Cs, ^{137}Cs, ^{129}I, ^{126}Sn, ^{79}Se, ^{90}Sr and ^{99}Tc .

Congruent release refers to the release of contaminants that are uniformly dispersed in the host matrix (used fuel or Zircaloy sheaths). We assume a contaminant is released as the matrix degrades, at a rate that is proportional to the contaminant's fractional abundance within the matrix and the rate of dissolution of the matrix as follows:

- The contaminants fractional abundance is given by its initial inventory which is modified (as a function of time) to account for radioactive decay and (for the used matrix) to discount any "instant" release inventory.

- The rate of dissolution of the UO_2 fuel matrix is based on a chemical kinetic (corrosion) model that is strongly dependent on the extent of radiolysis occurring at the fuel surface. At early times, radiolysis of water from α-, β- and γ-radiation causes relatively rapid dissolution rates (calculated using rate data at a conservatively assumed temperature of 100°C). After about 10^3 a, radiation fields would be greatly reduced, but we assume that a minimum rate of dissolution persists to the time limit of the assessment simulations. The congruent-release mechanism is modeled using parameters that include the relative magnitudes and durations of the α-, β- and γ-radiation fields.

- The rate of dissolution of the Zircaloy matrix is determined by two factors: the solubility of zirconium, a sampled parameter, and the rate at which zirconium is removed from the container (by diffusion through the defect in the container).

Many of the parameters used in calculating release rates are described using parameter distribution functions (PDFs) to account for uncertainty. Different values are sampled for each vault sector in a single simulation.

Some contaminants released from the used fuel and Zircaloy to the interior of the container can be sparingly soluble and would precipitate. In this scoping study, we use two different approaches to specify solubility limits:

1. For most chemical elements, we specify a conservative solubility limit. Chemical elements like carbon, chlorine, cesium and iodine are assigned very high solubility limits and would not precipitate; others like palladium and selenium are more insoluble and would likely precipitate in some simulations. Zirconium is expected to precipitate in every simulation because its solubility limit is low and because there is a large mass of zirconium in the Zircaloy matrix. The solubility limit for these elements is defined using PDFs to account for uncertainty.

2. For five elements (neptunium, technetium, plutonium, thorium and uranium), solubility limits are calculated using thermodynamic relationships and a groundwater composition that is representative of the disposal vault (Johnson et al. 1994b). For these elements, uncertainty in solubility is accounted for through the PDFs describing groundwater chemistry.

If the calculated concentration of a contaminant is greater than its effective solubility, we assume a constant-concentration source term in modeling transport from the failed container; otherwise we use a source term based on instant and congruent release. Both types of source terms can apply, but at different times during the simulation. For instance, the concentration of a contaminant might slowly build up to its solubility limit, maintain that limit until the precipitate is completely dissolved, and thereafter decrease to smaller values; we would then have a source term based on instant and congruent release at early times and again at long times, with a constant-concentration source term at intermediate times.

Many of the model parameters used to model precipitation in the container are described using PDFs to account for variability and uncertainty, and separate values are sampled for each vault sector in a single simulation.

We assume that contaminants released to the groundwater inside a failed container diffuse into the surrounding buffer through the small, pinhole-sized defects. These small

defects provide a long-term transport resistance by restricting and delaying the flux of radionuclides out of the container.

The vault model considers two different mathematical solutions to this process, depending on the characteristics of the source term. Contaminants that have precipitated inside the container are modeled using a constant-concentration source term; other contaminants are modeled using a source term based on instant and congruent release. Key model parameters used for these solutions include the contaminant diffusion coefficients (within the pinhole and within the surrounding buffer), the effective radius and length of the pinhole and the internal volume and void porosity of the materials in the container. The effective radius of the pinhole is based on the size of a defect of arbitrary shape. The result of these calculations is the time-dependent rate of release of contaminants into the surrounding buffer.

For mathematical modeling purposes, the complex three-dimensional geometry of the vault is simplified, as illustrated in Fig. 6.1. Thus the containers, buffer, backfill and EDZ are represented as nested cylinders, with adjustments to the radii so as to conserve the volumes of the buffer, backfill and EDZ. The surrounding rock is also treated as an outer cylinder with an infinite radius. We assume the discharge from a failed container can be represented as a point source located along the central axis of the cylinders. This simplification permits the use of a two-dimensional semi-analytical solution, based on the boundary integral method, of contaminant transport through the buffer, backfill and EDZ into the surrounding rock (LeNeveu and Kolar 1996). The adequacy of this two-dimensional mathematical solution has been evaluated by comparisons with a three-dimensional finite element model (LeNeveu and Kolar 1996).

The main output from this component of the vault model is the time-dependent flow ($mol \cdot a^{-1}$) of contaminants out of the vault into the adjoining rock. This is a net flow: it corresponds to the integrated flow over the entire surface of the outer cylinder that represents the EDZ. The final flow rate is derived from calculation of the net flows out of the cylinders representing the buffer and backfill.

Permeability in the buffer is very small and thus we assume that contaminants move only by diffusive transport through this material. However, the permeabilities of the backfill, EDZ and surrounding rock are higher than for the buffer. In these media we assume uniform radial and axial flows within a sector and include both convection and dispersion in calculations of contaminant movement.

The important parameters used to describe contaminant transport through the buffer, backfill and EDZ include diffusion coefficients, capacity factors, thickness (e.g., of the buffer), groundwater velocities and dispersivities in the three media. Other important parameters include diffusion coefficients, groundwater velocities and dispersivities in the surrounding rock. The geosphere model provides information on the direction and magnitude of groundwater flow in the rock immediately surrounding each vault sector (see Fig. 6.2). The geosphere model also provides information on groundwater velocities

through the backfill and EDZ for each vault sector. In this way, we ensure that the estimated flow of contaminants from a vault sector is consistent with the properties of the adjoining rock in the geosphere.

3. EVOLUTION OF NEAR-FIELD CONDITIONS AND MASS TRANSPORT THROUGH SEALING MATERIALS

3.1 INTRODUCTION

In this chapter we describe the properties of the various sealing materials used in the vault and discuss the rationale for the selection of the parameter values used in Chapter 6 to model mass transport of radionuclides in these materials. In addition, we discuss the attributes of the EDZ around the disposal rooms and derive parameters describing its hydraulic behaviour.

3.2 PROPERTIES OF SEALING MATERIALS

The sealing materials used within disposal rooms include:

(i) a floor constructed of low-heat high-performance concrete,

(ii) precompacted blocks of lower (dense) backfill comprising a mixture of clays and crushed granite,

(iii) precompacted blocks of buffer composed of a 1:1 mixture of sand and bentonite, and

(iv) pneumatically emplaced upper (light) backfill, comprising a 1:1 mixture of granite sand and bentonite

The space between the container and the buffer blocks would be pneumatically filled with a mixture of dry quartz sand and dry granular bentonite that would be emplaced at a dry density of 0.9 $Mg \cdot m^{-3}$. The design of a disposal room is shown in Fig. 2.1 and compositions and properties of the sealing materials are given in Table 3-1. The sealing materials and container emplacement operations have been described by Baumgartner et al.(1996).

Other sealing materials would be used in the vault, including concrete and bentonite bulkheads at the entrance to disposal rooms, clay-based backfills to fill tunnels and shafts, shaft seals and exploration borehole seals. The materials and design approaches for these seals have been discussed by Johnson et al.(1994a).

TABLE 3-1

COMPOSITION AND PROPERTIES OF BUFFER AND BACKFILL MATERIALS

	Buffer	Dense backfill	Light backfill
Clay type	Bentonite	Lake Clay/ bentonite	Bentonite
Content (mass %)	50	25/5	50
Aggregate type	Silica sand	Crushed granite	Granite sand
Content (mass %)	50	70	50
Dry bulk density ($Mg \cdot m^{-3}$)	1.67	2.1	1.2
Potential swelling pressure (kPa)	800 - 2000	<50	100 - 200
Free swell (%)	80 - 175	<10	20 - 50
Drying shrinkage (%)	<2	2 - 5	<5
Degree of saturation when placed (%)	80	80	33
Thermal conductivity ($W \cdot m^{-1} \cdot C^{-1}$)	1.7	2.0	0.7
Hydraulic conductivity ($m \cdot s^{-1}$)	$<10^{-11}$	$<10^{-10}$	$<10^{-10}$

In relation to vault performance, the present report describes models only for the performance of the seals used within disposal rooms. Sealing systems in the tunnels, shafts and exploration boreholes are expected to effectively ensure that diffusion dominates mass transport within the boundaries of the excavations in the far field, just as in the case of the near field. As will be seen in Chapter 6, however, significant convective flow occurs throughout the rock surrounding the entire disposal vault.

3.3 THE PRESATURATION PERIOD

3.3.1 Vault Temperatures

Baumgartner et al.(1996) have estimated the disposal container temperature and average disposal vault temperature based on a number of thermal calculations. The projected temperature-time profiles are shown in Fig. 3.1. The maximum container surface temperature of ~75°C is reached at ~10 a.

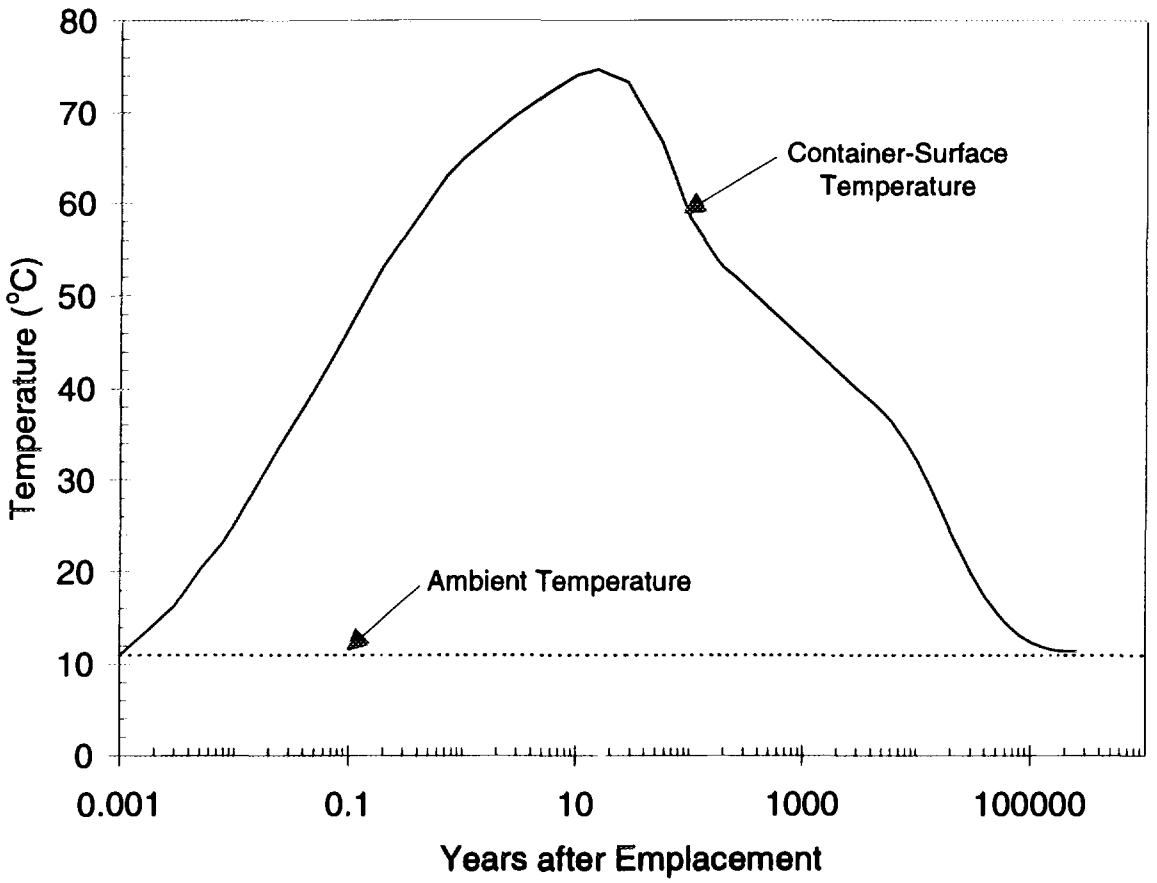

FIGURE 3.1: Variation of Temperature with Time at the Surface of the Disposal Container Located at a Vault Depth of 500 m

3.3.2 Vault Saturation Time

Johnson et al. (1994b) have discussed the moisture content transient that would occur in a disposal vault. They concluded that in very low hydraulic conductivity rock, ($K < 10^{-12}$ m·s^{-1}), buffer and backfill material could take hundreds to thousands of years to saturate. For rock with a hydraulic conductivity of 10^{-10} m·s^{-1}, as assumed in the present study, simple isothermal calculations indicate that saturation could occur in a shorter time.

The water-flow rate, Q, into the container through the defect can be approximated by

$$Q = 2\pi r K h_N \qquad (3.1)$$

where r is the radius of the defect, K is the hydraulic conductivity of the buffer, and h_N is the hydraulic head (Vieno et al. 1992). For maximum expected values[2] of r (1.5 mm) and K(10^{-11} m·s^{-1}) and a hydraulic head of 500 m (disposal vault depth), the volumetric inflow rate is ~2 x 10^{-11} m^3·s^{-1}; thus, the container void space of 118 dm^3 would fill in ~80 a under maximum hydraulic head conditions. This is a very conservative calculation, because the length used to calculate the gradient was chosen conservatively as r/2. More realistic values of hydraulic conductivity of buffer (<<10^{-11} m·s^{-1}, see Chapter 3.5) combined with effect of coupled thermo-hydraulic processes would lead to limited access of groundwater to the fuel for thousands of years. As indicated in Chapter 5.3.2, the dissolution rate of the fuel depends strongly on the radiation field; thus, delays of this magnitude would greatly diminish the extent of dissolution of the fuel. Nonetheless, these delays are not considered in the model, and contact of groundwater with the fuel and radionuclide release are assumed to occur upon emplacement of containers in the vault.

3.4 GROUNDWATER CHEMISTRY

The composition of groundwater at the vault depth of 500 m for the present study has been based on the study by Gascoyne (1996) of groundwaters in the Whiteshell Research Area. The salinity (total dissolved solids) is expected to be 3 to 13 g·L^{-1} in the rock mass at a depth of 150 to 500 m. This range is similar to that used in the previous case study (Johnson et al. 1994b). Measured redox potentials (E_h) for water in fracture zone LD1 are in the range +200 to -100 mV at vault depth. Because of concerns about the possibility that the high assumed flow rates in the rock might draw oxidizing groundwaters to considerable depths, Gascoyne (1996) also measured E_h and dissolved O_2 concentrations in rapidly recharging groundwaters in the WRA. He observed rapid consumption of O_2 in the upper 200 m and measured O_2 concentrations of <1 ppb and redox potentials of <0 mV at a depth of 240 m. These results indicate that groundwaters entering the vault would be essentially reducing, and that the redox chemistry in the vault would be controlled by materials in the vault.

The processes that would control near-field redox chemistry include alteration of minerals such as biotite and magnetite present in the crushed granite in the backfill, oxidation of minerals and organic matter in the glacial lake clay in the backfill and corrosion of the copper containers. Kolar and King (1996a) have examined the kinetics of consumption of oxygen that would be entrapped with the sealing materials for the case of disposal of copper containers using the in-room emplacement concept. They calculated that times to completely consume oxygen could be as long as 670 a at 75°C. The most important O_2 consumption reactions appear to be oxidation of organic matter in clays and corrosion of copper (see Chapter 4.3).

[2] Container defects larger than 3-mm diameter are assumed to be detected during container inspection (see Chapter 4.2)

It is assumed that, once the O_2 is consumed, the porewater in the buffer and backfill will contain enough Fe^{2+} to maintain sufficiently reducing conditions to greatly retard the migration of Tc. This is supported by the observation of significant Fe^{2+} concentrations in the pore water in O_2-free backfill (Sheppard et al. 1996) and by the low Tc diffusion rates observed in deaerated backfill by Oscarson et al. (1994) (see Chapter 3.5).

The parameter characteristics for the groundwater for the present study are given in Table 3-2. These are the same values used in the previous case study (Johnson et al. 1994b). The parameters are used only in the calculation of solubilities of radionuclides, as discussed in Chapter 5.4. The influence of the long-term alteration of the concrete floor of the disposal room on near-field chemistry is discussed in Chapter 3.6.2.

TABLE 3-2

DISTRIBUTION OF GROUNDWATER PARAMETERS

USED IN THE VAULT MODEL

Parameter	Units	Distribution	Minimum	Maximum	Mode
$[CaCl_2]$	$mol \cdot kg^{-1}$	loguniform	$10^{-3.5}$	$10^{-1.0}$	-
[NaCl]	$mol \cdot kg^{-1}$	loguniform	$10^{-2.3}$	$10^{-0.5}$	-
$[Na_2SO_4]$	$mol \cdot kg^{-1}$	loguniform	$10^{-2.2}$	$10^{-1.0}$	-
[tot. inorg. C]	$mol \cdot kg^{-1}$	loguniform	$10^{-3.6}$	$10^{-1.7}$	-
[tot. F]	$mol \cdot kg^{-1}$	loguniform	$10^{-6.0}$	$10^{-2.8}$	-
[tot. inorg. P]	$mol \cdot kg^{-1}$	loguniform	$10^{-8.0}$	$10^{-5.2}$	-
pH		triangular	5.0	10.0	8.0
E_z*(pH = 0)	V	uniform	0.2	0.47	-

* see Chapter 5.4

3.5 MASS TRANSPORT IN BUFFER AND BACKFILL MATERIALS

Based on pressure-gradient measurements, the hydraulic conductivity, K, of compacted bentonitic materials, like buffer, is $<10^{-11}$ $m \cdot s^{-1}$ (Dixon et al. 1987). Recent measurements on compacted bentonite using ultracentrifugation techniques indicate $K < 10^{-16}$ $m \cdot s^{-1}$ at clay densities greater than 0.8 $Mg \cdot m^{-3}$ (Conca et al. 1993). These low K values imply that the hydraulic conductivity for compacted bentonitic materials may be assumed to be zero under the low hydraulic gradients (<0.02 (Chan 1989)) expected in the vault environment. Under these conditions, transport through compacted buffer and backfill will be diffusion controlled, since diffusion processes have been shown to dominate mass transport through earthen materials when K is less than 10^{-10} to 10^{-9} $m \cdot s^{-1}$ (Rowe 1987, Gillham and Cherry 1982).

3.5.1 Diffusive Transport of Radionuclides in Buffer and Backfill Materials

A discussion of diffusion in clay/water systems and the appropriate equations based on Fick's laws is given by Johnson et al. (1994b). Briefly, in the absence of advection, Fick's first law for one-dimensional diffusion adapted to porous media is

$$J = -D_i\left(\frac{\partial C}{\partial x}\right) \tag{3.2}$$

where J is the diffusive flux, D_i the total intrinsic diffusion coefficient, C the concentration, and x the distance. The D_i value is given as

$$D_i = D_o \tau \varepsilon \tag{3.3}$$

where D_o is the diffusion coefficient in bulk water under stationary conditions, τ the pore geometry factor, and ε the effective porosity or the porosity available for diffusion.

In clay/water systems the diffusant often sorbs on the clay; this affects diffusion in the transient state (i.e., until all sorption sites are effectively saturated). Fick's second law, applied to sorption governed by a linear sorption isotherm for porous media, is

$$\frac{\partial C}{\partial t} = D_a\left(\frac{\partial^2 C}{\partial x^2}\right) \tag{3.4}$$

where D_a is the apparent diffusion coefficient and is given as

$$D_a = \frac{D_i}{r} = \frac{D_o \tau \varepsilon}{\varepsilon + \rho_b K_d} \tag{3.5}$$

where r is the capacity factor (the capacity of the solution and solid per unit volume of bulk porous media to hold more of the diffusant as its concentration in the solution phase increases by one unit), ρ_b the dry bulk density of the porous media, and K_d the solid/solution distribution coefficient.

In practice, D_i and D_a are obtained from experiments under steady-state and transient conditions respectively; and r is calculated either from the ratio D_i/D_a or from measured or known values of ε, ρ_b and K_d (Eq. 3.5).

In the mass transport model, D_i and r values are required for radionuclides in both buffer and backfill. Oscarson and Dixon (1989) give the mineralogical and elemental composition of Avonlea bentonite and Lake Agassiz clay, the clay components of buffer and backfill. For transport modeling purposes, the dense and light backfill are assumed to

have the same transport properties, i.e., the ranges chosen for D_i and r are broad enough to apply to both the dense and light crushed granite-based backfills.

In both buffer and backfill saturated with anoxic groundwater at 25°C, D_i values for all radionuclides generally range from 3.2×10^{-4} to 3.2×10^{-3} $m^2 \cdot a^{-1}$ (Oscarson et al. 1995). This range was increased by a factor of four for the present study to account for temperatures up to 90°C. [Diffusion coefficients in the pore solution of compacted clays increase with increasing temperature due to a decrease in solution viscosity; the increase is about a factor of three to four for a temperature increase from 25 to 90°C (Robin et al. 1987)]. As the temperature of buffer and backfill will be <90°C, using D_i values four times greater than those at 25°C is conservative.

Values of r — calculated from the ratio D_i/D_a (Eq. 3.5) — for various elements in buffer and backfill are given in Table 3-3. The number of elements included in Table 3-3 is larger than that for which assessment calculations are performed (see Chapter 6.5). Many of the D_a values (valid for 25°C) used to calculate r were obtained from the compilation of Oscarson et al. (1995), and again, increased by a factor of four to account for temperature effects. If a radionuclide is not included in the compilation of Oscarson et al. (1995), there are no reliable experimental data available for the conditions of interest. In this case, a D_a value was assumed for that radionuclide based on its chemistry, and therefore its likely behaviour in clay/water systems. For example, since there are no reliable diffusion data for Rb and K, they were assumed to have the same diffusivity as Cs for which good data exist.

The data available on diffusive transport in backfill are more limited than those in buffer. However, as Oscarson et al. (1995) noted, the D_a values given for buffer would also likely be appropriate for backfill. This has been shown to be the case where D_a values for several diffusants are available for comparison in both buffer and backfill clays (Oscarson 1994). Hence, where data are not available for backfill, the D_a values given by Oscarson et al. (1995) for buffer are assumed to also apply to backfill.

With the exception of Tc, the r values are the same for buffer and backfill (Table 3-3). For Tc, r ranges from 2 to 20 in buffer and from 1000 to 10 000 in backfill. Crushed granite in backfill is important in slowing the migration of Tc (Oscarson et al. 1994, Hume 1995). In clay/crushed granite barriers, such as the dense and light backfill, Fe(II)-containing minerals in granite, like magnetite and biotite, rapidly consume the dissolved O_2 initially in the pore solution, and Tc(VII) is reduced to Tc(IV) on the surface of these Fe minerals (Oscarson et al. 1994). Reduced Tc species are then strongly sorbed on Fe oxides or other minerals, thus markedly slowing their migration through granite-containing barriers.

There are insufficient data from which to select a probability distribution function for D_i and r. A uniform probability distribution was arbitrarily chosen for all D_i and r values. The ranges of values for D_i and r reflect experimental uncertainties and the potential variability in buffer and backfill density and groundwater salinity.

TABLE 3-3

CAPACITY FACTORS, r, AND TOTAL INTRINSIC DIFFUSION COEFFICIENTS, D_i, FOR RADIONUCLIDES IN BUFFER AND BACKFILL

Element	r[a]
Cs, Rb, K	10 - 100
Sr, Ca, Ra, Be, Cd, Ni, Pd, Pb, Sb, Sn, Cr, Nb, Mo, Si, P, Y	0.5 - 5
Lanthanides & Actinides, Zr	1000 - 10 000
U	100 - 1000
Se, Te	0.1 - 1
C as HCO_3^-	2 - 20
I, Cl, Br, H, Kr, Rn, Ar	0.05 - 0.5
Tc (buffer) (backfill)	2 - 20 1000 - 10 000
D_i $(m^2 \cdot a^{-1})^b$	3.2×10^{-4} - 3.2×10^{-3}

[a] r values are the same for buffer and backfill except for Tc.
[b] D_i values are the same for all radionuclides in buffer and backfill.

By and large, the K_d values recommended for radionuclide/clay systems in waste management programs in other countries (Brandberg and Skagius 1991, Hakanen and Hölttä 1992) give calculated r values [using appropriate ρ_b and ε values (Eq. 3.5)] that fall within the ranges given in Table 3-3.

Some investigators have suggested that surface diffusion, or migration within the electrical double layer next to mineral surfaces, may be an important transport mechanism for some cations in compacted clays (Oscarson 1994 and references therein). Recent studies indicate, however, that surface diffusion is not a significant transport mechanism (Oscarson 1994).

3.5.2 Colloid Transport in Buffer Material

All available data indicate that the transport through buffer of colloidal particles that might be produced upon radionuclide release from used fuel will be extremely slow.

Hence, it was concluded that colloidal transport would not significantly increase the net flow of radionuclides through the buffer; thus, it is not explicitly included in the vault model.

Nowak (1984) reported that colloidal gold (mean particle diameter = 16.4 nm) would not diffuse into bentonite compacted to a density of 0.9 $Mg \cdot m^{-3}$. In addition, the results reported by Vilks et al. (1993) suggest that the clay layer around the Cigar Lake uranium deposit in Saskatchewan, Canada has also been an effective barrier to colloid migration. Moreover, because of size similarities, diffusion measurements of large molecules in compacted bentonite are relevant to an evaluation of colloid transport. Lignosulfonates (molecular weight (MW) = 5600 to 30000 $g \cdot mol^{-1}$), disodium 2,4,5,7-tetrabromo-fluorescein (MW = 646 $g \cdot mol^{-1}$), and sodium anthraquinone-2-sulfonate (MW = 354 $g \cdot mol^{-1}$) have been examined, and the diffusion coefficients determined to be $<3 \times 10^{-8}$ $m^2 \cdot a^{-1}$ (Eriksen and Jacobsson 1982), at least three orders of magnitude lower than those of Cs^+ and Sr^{2+} in this clay. With a diffusion coefficient of $<3 \times 10^{-8}$ $m^2 \cdot a^{-1}$, it would take more than 8 Ma for about half of the initial amount of a diffusant released in a pulse at one side of the buffer to move 0.5 m into the buffer.

The above studies are supported by recent pore-size measurements of Avonlea bentonite, the reference buffer clay, compacted to the reference density (1.67 $Mg \cdot m^{-3}$). Choi and Oscarson (1996) reported that the average pore diameter of this clay is <20 nm. This is smaller than the 100 to 400-nm size range of the most common colloids present in Cigar Lake groundwaters (Vilks et al. 1993). If the colloids present in a disposal vault are similar to, or even considerably smaller than, those present in Cigar Lake groundwaters, they would be completely excluded from, or immobile in, the buffer.

3.6 FACTORS AFFECTING BUFFER AND BACKFILL PERFORMANCE

3.6.1 Self-Sealing Properties of Bentonite-Based Materials

Used nuclear fuel generates heat and will ultimately cause the temperature in the vicinity of the waste containers to rise to about 90°C (Baumgartner et al. 1996). The buffer near the containers could dry, shrink and crack due to heat-induced moisture movement down the thermal gradient away from the containers. Such cracks, if long-lived, could allow advective transport of radionuclides after the containers fail.

The self-sealing properties of dense, cracked bentonitic materials have been examined in several studies. For example, in a natural analogue study, Oscarson et al. (1990) measured the saturated hydraulic conductivity of initially cracked blocks of dense bentonite collected from the Avonlea deposit in south-central Saskatchewan. The clay deposit is 75 to 85 Ma old. The field dry bulk density of the clay ranges from 1.1 to 1.3 $Mg \cdot m^{-3}$, similar to the effective clay dry density of buffer. (Effective clay dry density is defined as the mass of clay divided by the combined volume of clay and voids.) Upon exposure to water, the cracked bentonite blocks swelled, the cracks sealed, and the

material exhibited a hydraulic conductivity similar to that of buffer. This demonstrates that dense Avonlea bentonite maintains a high swelling capacity and a low hydraulic conductivity for tens of millions of years. Pusch et al. (1987) reported similar results for bentonites from other deposits.

In other studies (Oscarson et al. 1996, Dixon et al. 1993), compacted bentonite plugs were either cut with a band saw to produce slots 1 to 2 mm wide in the direction of mass transport (Fig. 3.2A shows an example of a slotted bentonite plug) or cracks were induced by drying. The slotted or cracked plugs were subsequently saturated with groundwater (Fig. 3.2B), and the hydraulic conductivity and diffusivity measured. The slotted buffer plugs had a hydraulic conductivity similar to those of intact (i.e., non-slotted) bentonite plugs (Fig. 3.3). The values of both the slope and intercept obtained from the data (Fig. 3.3) for the slotted buffer plugs fall within the 95% confidence interval of those obtained for the intact bentonite plugs. Hence, the two relationships shown in Fig. 3.3 are not significantly different. We conclude, therefore, that the permeability of the slotted buffer plugs and the intact bentonite plugs is essentially the same. Similar results were obtained for cracked bentonite plugs where the cracks were generated by drying (Dixon et al. 1993). Additional studies of radionuclide diffusion also indicate there is no significant difference in the diffusivity of the slotted and intact plugs (Oscarson et al. 1996).

These studies provide convincing evidence that cracked or fractured, dense bentonitic materials rapidly self-seal upon access to water and maintain a hydraulic conductivity and diffusivity similar to that of intact or uncracked material.

3.6.2 Clay/Concrete Interactions

In the vault design assumed for the present study, a low-heat, high-performance (LHHP) concrete pad is in direct contact with dense backfill (Baumgartner et al. 1996). The primary concern in the interaction of concrete with clay-based barriers is the creation of a high pH (>9) environment in which clay minerals tend to alter to framework silicates, like zeolites (hydrous Na, Ca, Al silicates) (Pusch 1982, Johnston and Miller 1985). The zeolites that may form from Na- and Ca-bentonite precursors, for example, are analcime, phillipsite and natrolite. The conversion of clay minerals to zeolites may occur at either high temperatures (>200°C) or after long periods (500 to 1000 a) when the pH is sufficiently high to promote clay dissolution.

Zeolites are low density, framework silicates with no swelling properties. Their formation from bentonite, for example, could lead to a reduction in plasticity and loss of swelling capacity.

Anderson et al. (1982) reported that after 70 a of contact between bentonite and concrete, mineralogical changes had occurred in the bentonite to a depth of only about 50 μm from the clay/concrete interface. Pusch (1982), on the other hand, found no evidence of zeolite formation in clay in contact with a 70-year-old concrete foundation, nor in laboratory

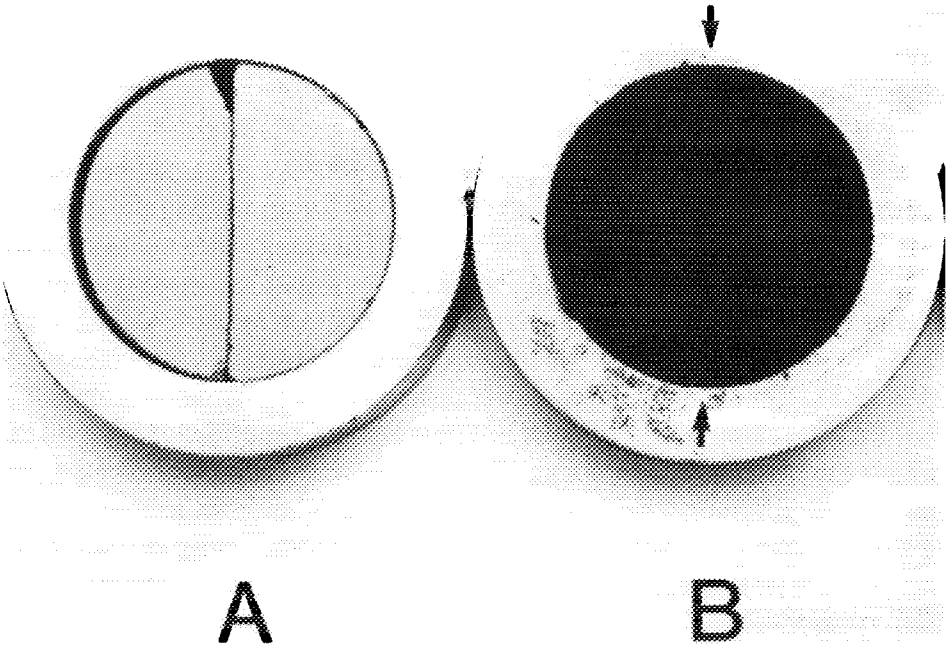

FIGURE 3.2: (A) Slotted Avonlea Bentonite Plug (ρ_c = 1.3 $Mg \cdot m^{-3}$), and (B) Slotted Plug Saturated with a Synthetic Groundwater Solution. The arrows on the ring in B indicate the position of the initial slot. The inside diameter of the ring is 4.1 cm.

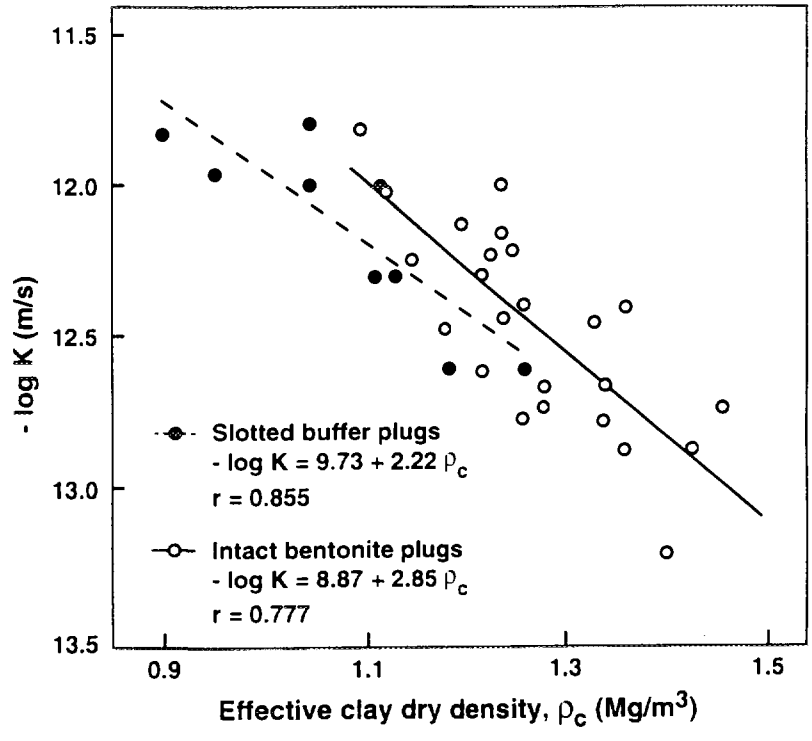

FIGURE 3.3: Hydraulic Conductivity, K, of Slotted and Intact Buffer and Bentonite Plugs

experiments with Na-bentonite plugs reacted with NaOH solution (0.1 mol·L^{-1}, pH 13) (to simulate alkaline concrete leachate) for one year. Moreover, in relatively short-term experiments, mixing $Ca(OH)_2$ (up to 2 wt.%) with bentonite had no significant affect on the hydraulic conductivity and swelling capacity of the subsequently compacted bentonite (Dixon 1995). Pusch (1982) notes that there is no direct evidence of any lattice destruction of smectite clays by OH^- at lower temperatures in compacted bentonite. Nonetheless, following conservative estimates by Neretnieks et al. (1978) that about 10^6 a are required to convert a 1.5-m-thick bentonite layer to analcime, Pusch (1982) concluded that a maximum of 1 cm of bentonite in contact with cement in an underground repository will undergo zeolitization in 500 to 1000 a.

The alkaline environment in cement and concrete is generated, in the long term, by Ca compounds, which produce Ca^{2+} and OH^- ions in aqueous solution. Most cements have Ca/Si ratios >1.5 and therefore the aqueous phase is essentially in equilibrium with solid $Ca(OH)_2$ at pH 12.5 (Atkinson et al. 1991). The Ca/Si ratio of LHHP concrete, however, is <1 and the aqueous phase pH is about 9.5 (Onofrei 1996). Although the pH of the solution in contact with LHHP concrete is lower than that for conventional concretes, the pH is still somewhat higher than that of the equilibrium pore solution of the buffer and backfill, about 7.5 to 8.0 (Oscarson and Dixon 1989).

Studies demonstrate that clay porewaters resist pH changes. This buffering capacity can be attributed largely to ion-exchange processes. Our unpublished data, for example, indicate that suspensions of WN-1 groundwater (Table 3-1a in Johnson et al. 1994b) and Lake Agassiz clay consume approximately 0.2 mol OH^-·kg^{-1} clay before reaching pH 9 from an initial value of about 7.8. (Lake Agassiz clay is the main clay component of dense backfill (Table 3-1)). Others have reported similar clay buffering capacities (Jefferies et al. 1988). Hence, the ability of clays to consume OH^- released from concrete is substantial.

Given that the total mass of Lake Agassiz clay in the dense backfill in a disposal room with a nominal length of 230 m is 506 Mg (Baumgartner 1995)], dense backfill can potentially consume about 1 x 10^5 mol of OH^-, assuming a uniform distribution of OH^- throughout dense backfill, before the porewater pH exceeds 9. This can be compared with the total amount of OH^- that can potentially be released from LHHP concrete. The total mass of LHHP concrete proposed for use in a disposal room is 1094 Mg (Baumgartner 1995), and this material has a maximum $Ca(OH)_2$ content of 0.5 wt.% (Onofrei 1996). [$Ca(OH)_2$ is the main source of OH^- in concrete.] From this, the total amount of OH^- that can potentially be released from the LHHP concrete in a disposal room is 1.5 x 10^5 mol. Hence, the Lake Agassiz clay in dense backfill clay can neutralize the bulk of the OH^- that can potentially be generated by LHHP concrete in a vault. Moreover, the dense backfill also contains 5 wt.% bentonite (Table 3-1) and this clay has about the same buffering capacity as Lake Agassiz clay (Oscarson, unpublished data). Thus, the pH buffering capacity of the dense backfill is even greater than indicated above. This further ensures that the clay will not be markedly altered by contact with LHHP concrete.

The concrete pad is relatively far from the heat-generating waste containers. Therefore, the temperature at the dense backfill/concrete interface will be comparatively low, and clay transformations that are known to occur in high-temperature environments would not occur in a disposal vault. Nevertheless, over long periods of time some alteration of the clay at the dense backfill/concrete interface can be expected. This potential zone of alteration, however, will likely be relatively thin (<1 cm) and will not significantly affect the mass transport properties of the dense backfill.

The buffer and light backfill are also relatively far from the concrete pad. This, combined with the fact that the dense backfill (and the surrounding rock mass) will neutralize most of the OH^- released from the concrete, means that the influence of the concrete on buffer and light backfill will be negligible.

A secondary concern with concrete, and high levels of Ca^{2+}, in the presence of bentonite is the exchange of Ca^{2+} for Na^+ on the exchange complex of bentonite. Complete cation exchange from Na- to Ca-bentonite increases the permeability and diffusivity of compacted bentonite by a factor of two to five (Choi and Oscarson 1996, Pusch 1981). This increase, though, is relatively small and it would not markedly affect the performance of buffer and backfill. Furthermore, in a vault environment it is not possible to get complete exchange, since both Ca^{2+} and Na^+ (as well as other exchangeable cations like Mg^{2+} and K^+) are present in the groundwater, i.e., bentonite will always contain a mixture of several exchangeable cations. Hence, the increase in permeability and diffusivity will be proportionately less than that reported for complete exchange.

On the other hand, the presence of Ca^{2+} on the exchange complex of bentonite retards the illitization process more effectively than Na^+ (Oscarson and Hume 1993, Roberson and Lahann 1981). In this respect, the substitution of Ca^{2+} for Na^+ on bentonite is beneficial. Moreover, Choi and Oscarson (1996) noted that the exchange of Ca^{2+} for Na^+ on compacted bentonite may not alter its fabric (hence its transport properties would not change markedly) because the clay particles have limited mobility in a compacted state, and thus they cannot reorient as the proportion of Ca and Na on the clay changes. This hypothesis requires further study, but if correct, it means that after some exchange of Ca for Na on bentonite has occurred in a vault, the bentonitic barriers would maintain the desirable fabric and transport properties of Na-bentonite, and also have the enhanced stability of Ca-bentonite.

3.6.3 Radiation and Smectite Stability

The radiation field at the surface of a packed-particulate supported copper container is estimated to be ~11 $Gy \cdot h^{-1}$ (Chapter 4.4.6). Johnson et al. (1994b) showed that gamma radiation at these levels does not significantly affect the structure or properties of clay minerals. Other recent work supports this conclusion (Eissa et al. 1994).

The arguments put forward by Johnson et al. (1994b) regarding the insignificant influence of beta and alpha radiation on clay minerals, also apply to the buffer and backfill in the present study.

3.6.4 Gas Generation and Migration

There are several sources of gas production in a disposal vault, as discussed by Johnson et al. (1994b). These include generation of methane and CO_2 in the buffer and backfill as a result of microbial degradation of organic matter, and the production of H_2 from the corrosion of metals and the radiolysis of water.

Sheppard et al. (1996) have measured methane production rates in a number of systems, including natural groundwater alone, backfill and groundwater, and clay and groundwater and metallic iron. They observed methane generation only from systems containing natural groundwater in the absence of clay. No measurable methane production occurred in clay-based systems, even though reducing conditions were achieved. Based on these observations, it has been assumed in the vault model that, if any methane were produced, the rate would be slow enough that it would dissolve and diffuse from the vault without exceeding the solubility of methane in groundwater.

In the assessment of H_2 generation and transport, the present study differs considerably from the previous case study (Johnson et al. 1994b) in two important respects. The first is that no H_2 is produced during corrosion of Cu, as opposed to the low production rate arising from Ti corrosion. Secondly, there are expected to be very few container failures (approximately 12) in the vault, thus, although the production of H_2 from stainless or carbon steel corrosion and radiolysis of water could produce local saturation of H_2 within defective containers, the H_2 will be gradually dissolved as it migrates through the clay barrier materials and into the surrounding rock. The transport of gas through saturated bentonite-based buffer materials has been studied by Pusch et al. (1985) and Kirkham (1995). The former concluded that gas channels would break through when the gas pressure reached the swelling pressure of the buffer. Kirkham (1995), on the other hand, observed breakthrough pressures of at least 10 MPa for buffer material with a swelling pressure of only ~2 MPa. Nonetheless, it is reasonable to assume from these studies that gas travels through the largest capillaries in the clay without significantly affecting the hydraulic and diffusion properties of the buffer. It has thus been concluded that the production and transport of gases would have no significant impact on water movement and contaminant transport in the buffer and backfill.

The production of a gas phase within a failed container could have both beneficial and detrimental effects. Gas could expel contaminated water from the container, thus increasing release rates relative to diffusion. This scenario has effectively been incorporated in the scenario where the pinhole is enlarged by formation of voluminous iron corrosion products (see Chapter 6.5.3.5). An enlarged hole is equivalent to a rapid release of contaminants into the buffer. After expulsion of contaminated water, further

gas production would inhibit release by denying access of water to the used fuel in the container.

3.7 MASS TRANSPORT IN THE EXCAVATION-DISTURBED ZONE (EDZ)

In the present study we consider the EDZ explicitly, and describe quantitatively its effect and relative importance in influencing groundwater flow and radionuclide transport in heterogeneous media. The model for the EDZ encompasses a scale from a few metres to a few hundred metres (the diameter and the length of a room in the vault and adjacent EDZ), and assumes that microscopic material properties can be characterized by macroscopic (continuum) parameters. It employs the equivalent porous medium approach to describe flow and mass transport in the discrete fracture network of the disturbed zone. A key issue in this approach is the formulation of all equivalent properties and the determination of the size of the Representative Elementary Volume (REV) over which the homogenization is valid. The REV is, in effect, a statistical index for the equivalence of properties between a fractured medium and its continuum idealization. The REV itself is not explicitly introduced; instead, the heterogeneities are described in the model as variations in effective values of the EDZ attributes, based on representative, albeit conservative, probability density functions (PDFs).

Permeability, porosity and dispersivity are the characteristics of the EDZ most important to groundwater flow and transport of radionuclides. Whereas the permeability determines the average flux of groundwater through the disturbed zone, the dispersivity determines the spreading of radionuclides. The two attributes are related to each other and both depend on the EDZ geometry. Underlying the choice of the conceptual model for the EDZ is the observation in field studies that fractures occur mainly in the direction parallel (x) and secondarily in a direction perpendicular (y) to the longitudinal axis of the emplacement room.

The porosity affects the radionuclide capacity factor. The porosity in the EDZ is always greater than that of the surrounding rock. The tortuosity would be more important in instances where mass transport is dominated by diffusion.

Selection of both the PDF type and the relevant parameters (location, scale and shape of the EDZ) is based on our understanding of typical ranges and statistics on fractured rock properties. The suggested conceptual model of the EDZ geometry and the PDF assigned to each parameter characteristic are estimates derived from theoretical studies (analytical evaluations), laboratory data and limited field studies. The primary source of information used to derive the input variables required by the Vault Model is data reported in the Stripa Project Reports and SKB Reports (see references in Appendix B).

The suggested values for the vault model inputs are presented in Table 3-4 and further information on the EDZ conceptual model is given in Appendix B.

TABLE 3-4

PARAMETER VALUES FOR TRANSPORT IN THE EDZ[1]

CHARACTERISTIC/ PDF type	Parameters of PDF[2]		Lower Bound	Upper Bound
1) Extent, i.e., thickness (m) / Normal				
	M	SD		
	1.40	0.172	0.884	1.92
2) Permeability (m^2) / Log-normal				
	GM	GSD	Truncated at 1.0×10^{-17}	
a) Axial	1.7×10^{-17}	3.4×10^{1}	1.0×10^{-17}	6.7×10^{-13}
b) Radial	$k_y = k_x / 10$			
3) Dispersivity (m) / Uniform				
	A	B		
a) Axial (x-direction)				
a1) Longitudinal	14.6	45.1	14.6	45.1
a2) Transverse	0.175	0.542	0.175	0.542
b) Radial (y-direction)				
b1) Longitudinal	1.46×10^{-1}	4.51×10^{-1}	1.46×10^{-1}	4.51×10^{-1}
b2) Transverse	1.75×10^{-3}	5.42×10^{-3}	1.75×10^{-3}	5.42×10^{-3}
4) Porosity/Log-normal				
	GM	GSD		
	5×10^{-5}	3.16	1×10^{-5}	1
5) Tortuosity/Triangular				
		Maximum		
		3	2	8

1 See Appendix B for information regarding the derivation procedure, assumptions made and the transformation employed for the $\log_{10}$ distribution; values from the table may differ slightly from the values used in the simulation calculation due to rounding.

2 Where M is the arithmetic mean, SD is the standard deviation of data in the original units, GM is the geometric mean, GSD is the geometric standard deviation, and A and B are the interval limits of a uniform density function.

4. LIFETIME MODEL FOR COPPER CONTAINERS

4.1 INTRODUCTION

The reference container for the present study is based on an outer corrosion barrier of deoxidized low-phosphorus (DLP) copper (see Chapter 2.5). Two conceptual designs for such a container, the packed-particulate and dual-shell container designs, are described in Chapter 2.4. As shown below, failure of these containers as a result of corrosion is not expected in $<10^6$ a (King and Kolar 1995, 1996; Kolar and King 1996b). Therefore, the only containers that would fail before this time are those emplaced with undetected manufacturing defects (Chapter 2.6). More detailed discussion of the corrosion model described below can be found in King (1996a-d) and Kolar and King (1996b).

4.2 CONTAINER DESIGN AND STRUCTURAL PERFORMANCE

The packed-particulate container design for in-room emplacement (Fig. 2.2) is an adaptation of the design described by Simmons and Baumgartner (1994) and has been described by Teper (1992)[3]. In this design, 72 used fuel bundles are placed in stainless steel tubes in two layers of 36 bundles each. The container is shorter and has a larger diameter than the Ti-shell packed-particulate container designed for the previous case study, in which the fuel bundles were in four layers of 18 bundles each. To facilitate horizontal installation of the container into the precompacted buffer, the container-lifting ring attached to the top head is designed to maintain a level profile along the container length. Further details on emplacement procedures are given by Baumgartner et al. (1996).

A structural analysis of the copper-shell packed-particulate design, assuming compacted particulate such as glass beads or silica sand as the supporting material for the shell, was conducted by Teper (1995). In a perfectly packed container (i.e., with no residual void or further settlement of the particulate following container closure) and under 13 MPa external pressure[4], local tensile strains of up to 2.1% can occur by plastic deformation of the shell. Because copper is a ductile material, typically able to deform plastically to uniaxial strains exceeding 30% at its ultimate tensile strength (Kasprick, unpublished data), such strains are well within the limits of acceptability for this container design.

A structural analysis of a container in which an internal void develops through further settlement of the glass-bead particulate was also conducted by Teper (1995). The potential for such settlement is based upon the observation of this phenomenon in the

---

[3] The dimensions shown in Figure 2.2 reflect the effects of certain design changes (Teper 1994, Crosthwaite 1994a) from the original container concept presented in Teper (1992).

[4] Consisting of 10 MPa hydrostatic pressure due to groundwater at a maximum vault depth of 1000 m, plus a maximum of 3 MPa buffer-swelling pressure.

testing of a full-scale titanium-shell packed-particulate container prototype of borehole-emplacement design (Teper 1988, Johnson et al. 1994a). For a volumetric settlement of the same magnitude as that observed in the prototype packed-particulate borehole-emplacement container, the maximum gap height between the container shell and the particulate would be 25.1 mm. Under 13 MPa hydrostatic pressure, the container shell would initially deform to produce a strain of 8.7% and this could, under the effects of material creep, increase to as high as 24%.

Creep tests on DLP copper conducted for the Swedish program (Lindblom et al. 1995) have shown that uniaxial strains to failure of as high as 80% can be achieved under some test conditions. However, other tests incurred strains to failure of as low as 9% and therefore, while DLP copper generally exhibits good creep-rupture ductility, it is currently uncertain whether 24% would fall within acceptance criteria for allowable creep strain. Such acceptance criteria have not yet been established.

Alternative container-design approaches are under investigation, specifically:

(1) Use of alternative particulates (e.g., silica sand) with higher strength and less tendency for additional settlement, and

(2) Use of a carbon-steel inner shell for structural support.

Investigations of alternative particulate materials are focused on the use of graded silica sands. Previous studies (Teper 1987) have shown that such sands have the potential for very high compressive strength (>50 MPa) which, for a container designed with a lifetime of 10^6 a or more, would be able to withstand the combined effects of glacial loading (maximum hydrostatic pressure of 40 MPa) plus the buffer-swelling pressure (2.5 MPa). The current investigations include studies of ease of compaction, short-term mechanical properties, tendencies for further settlement and creep-deformation behaviour. The creep-deformation studies will generate data that will be used to predict the creep-rupture life of the copper shell according to a methodology proposed and described by Dutton (1995).

Investigations of container designs employing a carbon-steel inner shell for structural support are also underway (Garroni et al. 1996). From these studies, a container designed to withstand an external pressure of 50 MPa without collapse has been developed (Fig. 2.3). Note that in this design, the use of a 65-mm-thick inner steel shell would require some increase in the overall container dimensions from those of the packed-particulate design. Studies are underway to determine the creep-rupture life of the copper shell in steel-shell-supported designs.

On the assumption of adequate long-term structural durability, the container-shell lifetime would be limited only by corrosion which would not lead to failure within 10^6 a. Therefore, for periods up to at least 10^6 a (see Chapter 4.5.2), performance assessment of the disposal vault would be based on those containers with an initial undetected defect, i.e., the fraction of containers possessing initial manufacturing defects that have eluded

detection because the combination of their size and population is below the limits of the final-inspection equipments detection capabilities. Based on fabrication development work (Crosthwaite 1994b; Maak 1984, 1987, 1988; Moles 1992), Crosthwaite (1995) has estimated that the range of the diameter of a through-wall hole in a copper-shell container that could elude detection during inspection would be 0.3 to 3 mm. Based on analyses conducted by Doubt (1984), the proportion of finished containers possessing such flaws would be between 1 in 1000 and 1 in 10 000.

4.3 EVOLUTION OF VAULT CONDITIONS

During the lifetime of the containers, the vault environment will evolve from an initial phase of warm, oxidizing conditions to a cool and anoxic period (Fig. 4.1). The corrosion behaviour of the containers will change with time as a result of this evolution in environmental conditions. For the corrosion of Cu, the most important environmental parameters are the availability of oxidants, the restrictive mass-transport conditions and the salinity of the groundwater.

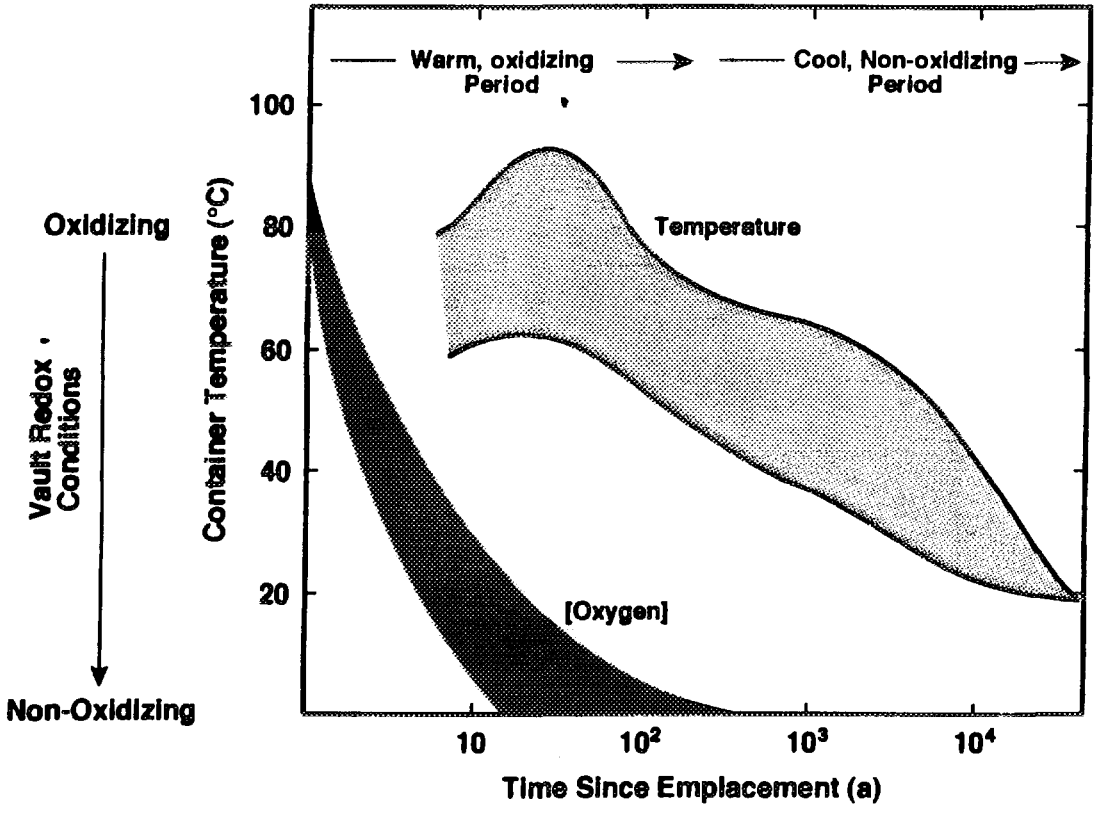

FIGURE 4.1: Schematic Representation of the Evolution of the Vault Environment from an Initial Warm, Oxidizing Period to a Long-term Cool, Anoxic Phase

The major source of oxidant in the disposal vault is the O_2 trapped in the pores of the compacted buffer and backfill materials surrounding the container. For the in-room vault design, the amount of O_2 trapped in the buffer and light and dense backfill layers in the disposal rooms when the vault is sealed is equivalent to ~27 mol·container^{-1}. The only other source of oxidizing species is the γ-radiolysis of water. Gamma-radiation effects will be insignificant after 300 a (equivalent to 10 half-lives of ^{137}Cs) and, even initially, the yield of radiolysis products is expected to be low because of the small absorbed dose rates at the surface of the container (maximum ~11 Gy·h^{-1}). Therefore, the amount of extra oxidants produced by γ-radiolysis will be insignificant compared with the amount of trapped O_2.

The trapped O_2 in the buffer and backfill materials will be consumed by a number of reactions (Kolar and King 1996a): (i) the electrochemical reduction of O_2 on the container surface, (ii) the oxidation of dissolved Cu(I) corrosion products, (iii) the oxidation of organic C, possibly microbially mediated, and other oxidizable impurities (Fe_3O_4, metallic Fe) present naturally in clay (Oscarson and Dixon 1989, Oscarson et al. 1984), (iv) the oxidation of Fe(II) released by the dissolution of biotite, magnetite and pyrite in the crushed granite in the dense and light backfill materials, and (v) diffusion out of the vault into the geosphere where it would be consumed by the oxidation of Fe(II) in the rock. In a conceptual Canadian disposal vault, the trapped O_2 is predicted to be consumed by these reactions in between ~6 and several thousand years, depending on the assumptions made in the calculations (Johnson et al. 1994b, Kolar and King 1996a). Fig. 4.2 shows the predicted evolution of [O_2] within the disposal vault in the case where the O_2 is consumed in ~670 a. This period of ~670 a to consume the O_2 and to establish anoxic conditions within the vault defines the maximum duration of the initial warm, oxidizing phase of the vault evolution.

The variation of vault temperature with time (Fig. 3-1) also affects the evolution of vault conditions. Initially, the buffer material may partially dry out as heat from the container drives moisture away from the surface. In unsaturated buffer, the rate of O_2 transport to the container is higher than in fully saturated buffer (King and Kolar 1995). Corrosion, however, may be limited because insufficient water will be present on the container surface to support aqueous electrochemical reactions (King 1996a). Eventually, the vault is expected to become fully saturated, at a rate that will depend on the relative rates of water movement away from the container due to the thermal gradient and water influx from the surrounding rock. As the vault continues to cool with time (as illustrated by the container surface temperature profile in Fig. 4.1), the rates of chemical and electrochemical reactions and of mass transport processes will decrease.

4.4 THE CORROSION OF COPPER CONTAINERS

4.4.1 Uniform Corrosion

A detailed corrosion mechanism has been proposed for the uniform corrosion of Cu in O_2-containing Cl^- environments (Fig. 4.3). The results of various experimental studies on

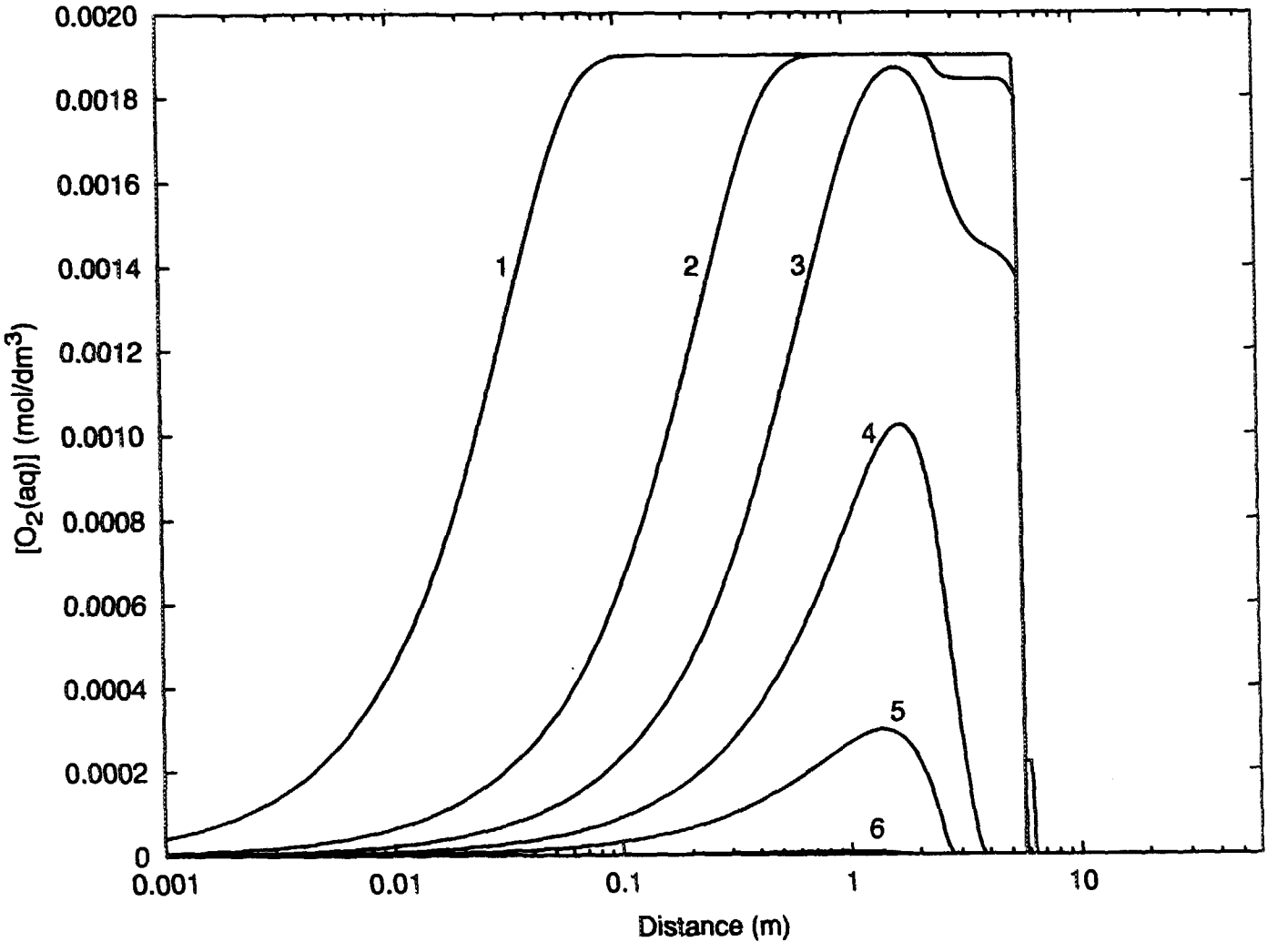

FIGURE 4.2: Predicted Variation of the Dissolved $[O_2]$ in the Vault as a Function of Time. Oxygen trapped in the pores of the sealing materials is consumed by container corrosion and by reaction with Fe(II) in the dense backfill. A constant temperature of 75°C is assumed (Kolar and King 1996b). Curves correspond to periods of (1) 1 month, (2) 4.1 a, (3) 32 a, (4) 174 a, (5) 341 a, and (6) 670 a.

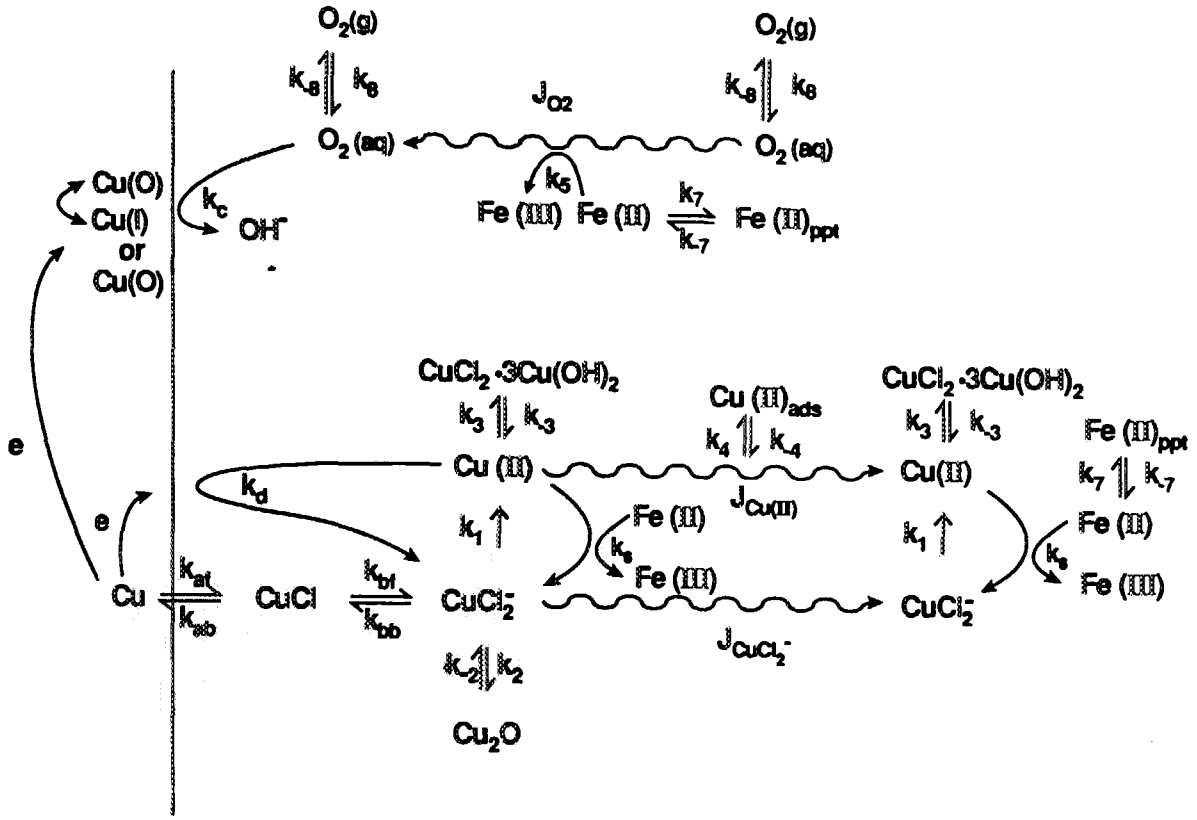

FIGURE 4.3: Mechanism of the Uniform Corrosion of Copper in O_2-containing Chloride Solutions Used to Model the Corrosion of Copper Containers in Compacted Buffer Material

which Fig. 4.3 is based are summarized below, and described in more detail elsewhere (Shoesmith et al. 1995a; King 1996a).

The corrosion behaviour of Cu containers will be affected by the availability of O_2, the low rate of mass transport of species to and from the container surface and the predominance of Cl^- in the pore solution. Figure 4.4 shows the E/pH diagrams for Cu in Cl^-/H_2O for various $[Cl^-]$. The corrosion behaviour of Cu observed under simulated disposal conditions can be rationalised with this relatively simple E/pH diagram, despite the apparent complexity of the corrosion environment. The overall corrosion reaction is not at equilibrium, however, as the use of a thermodynamically based E/pH diagram implies, but Fig. 4.4 is useful for interpretation of the observed behaviour.

The results of corrosion experiments in compacted buffer material show that the corrosion rate of Cu under simulated disposal conditions is controlled by the rate of mass transport of species through the buffer (King et al. 1992). This is hardly surprising since the rates of the interfacial dissolution of Cu and the reduction of O_2 are relatively fast, whereas the diffusion coefficients of dissolved Cu and O_2 in buffer are approximately two orders of magnitude lower than in bulk solution. In aerated buffer material, good agreement is found between the observed corrosion rate and that predicted on the basis that the diffusion of Cu(II) away from the surface is the rate-determining step (rds) (King et al. 1992). At lower $[O_2]$, or in simulated vault environments in which the amount of O_2 is limited, modeling predictions suggest that the corrosion rate is controlled by the rate of supply of O_2 to the Cu surface (King et al. 1996).

The speciation of dissolved and precipitated Cu corrosion products depends on the $[O_2]$ and $[Cl^-]$. In compacted buffer material saturated with various synthetic groundwater solutions, Cu(II) species predominate at high $[O_2]$ and/or low $[Cl^-]$, whereas Cu(I) species predominate at low $[O_2]$ and/or high $[Cl^-]$ (King 1996a). The dominant Cu species can be identified based on (i) the nature of the precipitated corrosion products on the surface of the Cu coupon, (ii) the concentration of Cu in the buffer material close to the corroding surface and (iii) the extent of the Cu diffusion profile in the compacted buffer material. Precipitated Cu(II) species are present as $CuCl_2 \cdot 3Cu(OH)_2$ and Cu(I) as Cu_2O (Litke et al. 1992). The total [Cu] in the buffer next to the corroding surface is high in the presence of Cu(II) because Cu(II) is strongly adsorbed by Na-bentonite (Ryan and King 1994). Similarly, Cu diffusion profiles in the buffer from corrosion experiments are steep and short because adsorption retards the diffusion of Cu(II). On the other hand, when Cu(I) is the dominant soluble corrosion product (stabilized in Cl^- solutions as $CuCl_2^-$, Fig. 4.4) interfacial [Cu] are low and diffusion profiles are shallow and extended because the anionic Cu(I) complexes are not adsorbed by the clay. Cupric species are formed from the homogeneous oxidation of Cu(I) by O_2 (Sharma and Millero 1988). The reaction rate is first order with respect to $[O_2]$ and the value of the rate constant (k_1 in Fig. 4.3) is inversely related to $[Cl^-]$. Thus, at high $[O_2]$ and/or low $[Cl^-]$ Cu(II) species predominate, whereas at low $[O_2]$ and/or high $[Cl^-]$ Cu(I) is stable (King 1996a).

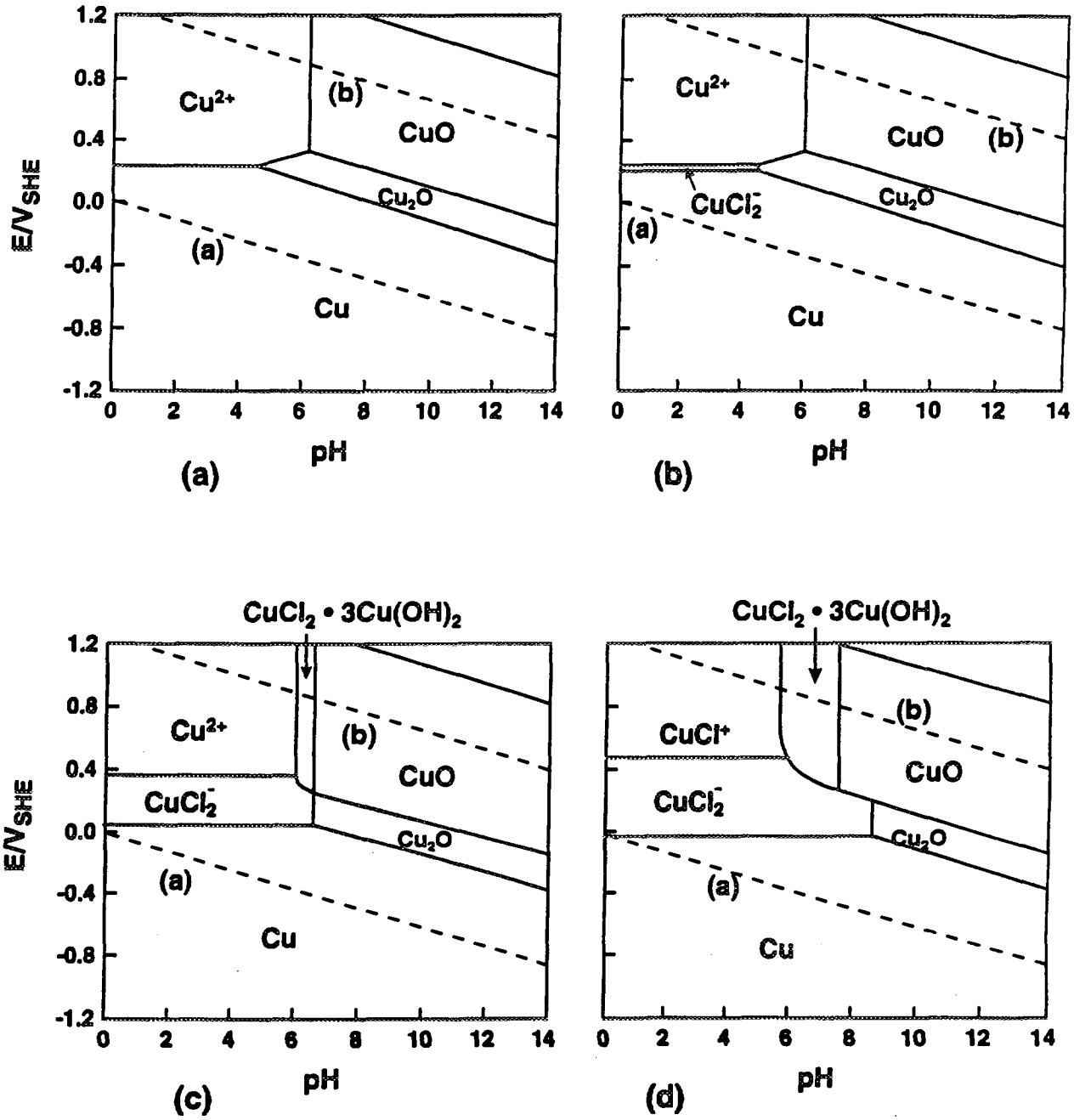

FIGURE 4.4: Potential/pH Diagrams for the $Cu/Cl^-/H_2O$ System at 25°C for Various Chloride Concentrations. (a) 10^{-3} mol·dm^{-3} Cl^-, (b) 10^{-2} mol·dm^{-3} Cl^-, (c) 0.1 mol·dm^{-3} Cl^-, (d) 1.0 mol·dm^{-3} Cl^-. Solution species considered: $CuCl_2^-$, Cu^{2+} and $CuCl^+$, solution activity 10^{-4}; solid species considered: CuCl, Cu, Cu_2O, CuO and $CuCl_2 \cdot 3Cu(OH)_2$.

Under all conditions investigated, precipitated corrosion products were found on the surface of the Cu coupon at the end of the experiments in compacted buffer. In aerated solution, a duplex structure was observed consisting of an inner layer of Cu_2O and an outer layer of $CuCl_2 \cdot 3Cu(OH)_2$ (Litke et al. 1992). In solutions in which Cu(I) was found to predominate, the outer $CuCl_2 \cdot 3Cu(OH)_2$ layer was absent. In all cases, however, neither layer was entirely protective. The outer layer was usually incomplete (King 1996a) and the inner Cu_2O layer contained numerous cracks and defects. Although the mechanism of film formation has not been studied in detail (King 1996a), the Cu_2O layer is most likely formed from the hydrolysis of either a CuCl layer or of dissolved $CuCl_2^-$. The $CuCl_2 \cdot 3Cu(OH)_2$ layer forms by the precipitation of Cu(II), produced from the homogeneous oxidation of Cu(I) by O_2 (King 1996a).

The surface profiles of the corroded coupons were measured after the corrosion products had been stripped. Figure 4.5 shows, on a much expanded vertical scale, that, although the surface was roughened, the corrosion is relatively uniform in nature. In particular, comparison of the corroded profile to that of the original surface shows that all areas of the surface are attacked and that no permanent separation of anodic and cathodic sites, a prerequisite for localized corrosion, takes place.

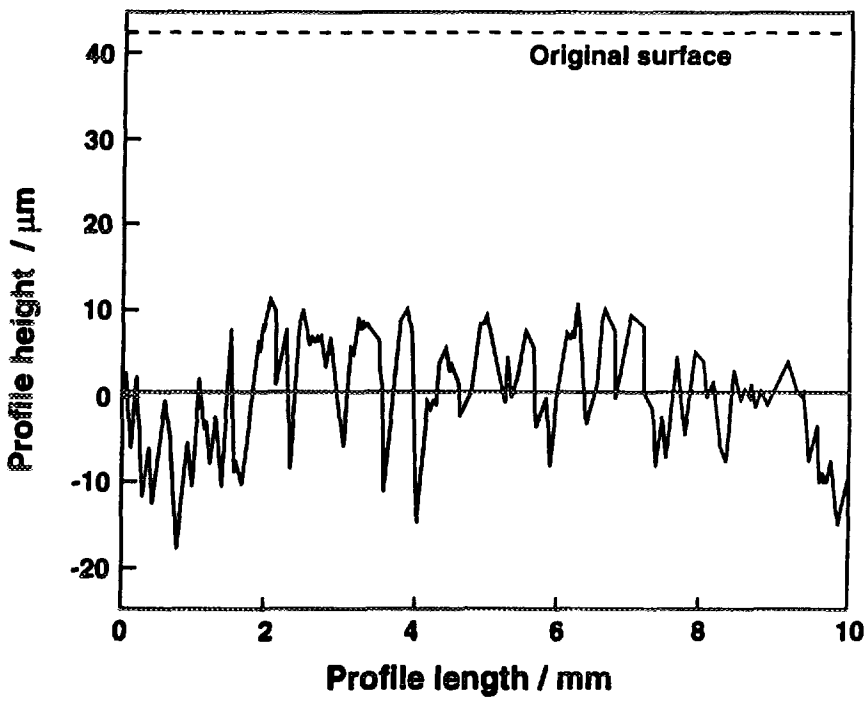

FIGURE 4.5: Typical Surface Profile of Copper Coupon After Exposure to Synthetic Groundwater Solution in Compacted Buffer Material at 100°C (Litke et al. 1992). Note that the entire surface has undergone corrosion to different extents resulting in roughening of the surface. This type of surface roughening is not consistent with pitting involving the permanent separation of anodic and cathodic sites.

Much of the detail regarding the mechanism of the interfacial reactions shown in Fig. 4.3 has come from the results of electrochemical experiments in bulk solution. Thus, Cu anodically dissolves in Cl^- solutions as $CuCl_2^-$ via an adsorbed $CuCl_{ads}$ intermediate (Deslouis et al. 1988, King and Litke 1989)

$$Cu + Cl^- \leftrightarrow CuCl_{ads} + e^- \quad (4.1)$$

$$CuCl_{ads} + Cl^- \leftrightarrow CuCl_2^- \quad (4.2)$$

$$CuCl_2^- \text{ (surface)} \rightarrow CuCl_2^- \text{ (bulk)} \quad \text{rds} \quad (4.3)$$

The major cathodic reaction on the container surface will be the reduction of O_2. In neutral and slightly alkaline (pH 9.2) solution, oxygen reduction occurs primarily by the overall 4-electron pathway to OH^- (Vazquez et al. 1994; King et al. 1995a,b)

$$O_2 + 2H_2O + 4e^- \rightarrow 4OH^- \quad (4.4)$$

Surface redox processes involving Cu(I) species are thought to catalyze the reaction. Only small amounts of peroxide were reported to be formed in both studies.

In O_2-containing Cl^- solutions, Reactions (4.1) to (4.4) describe the interfacial anodic and cathodic reactions that determine the corrosion potential, E_{CORR}. In aerated bulk solution, the anodic reaction is mass-transport controlled at E_{CORR} and the cathodic reaction is controlled by the interfacial step. As the $[O_2]$ is decreased, the cathodic reaction becomes increasingly mass-transport limited, but, because the interfacial rate constant for O_2 reduction is small compared with the rate of mass transport (King et al. 1995a,b), the cathodic reaction does not become totally mass-transport limited, even in nominally deaerated solution (King et al. 1995c). If the rate of mass transport to the corroding surface is reduced by placing a 1-mm-thick layer of compacted bentonite between it and the bulk solution, both reactions become mass-transport limited. Good agreement is observed over a wide range of $[O_2]$ and mass-transport conditions between measured and predicted values of E_{CORR} on the basis of this set of reactions and experimentally measured rate constants (King et al. 1995c).

4.4.2 Pitting

Pitting of Cu, although well known, is a relatively rare phenomenon. The pitting of Cu pipes in potable water has been extensively studied, and various mechanisms proposed (Campbell 1974). This form of pitting is limited to certain types of fresh water found in specific locations and only affects a small fraction of installed pipes (Myers and Cohen 1995). The difference between pitting waters and Canadian Shield groundwaters is the predominance of Cl^- and the absence of O_2 in the latter. As discussed above, Cl^- promotes the active dissolution of Cu. Although Cu_2O films are formed in Cl^- environments, they tend to be porous and extensively defected (King 1996a). Nevertheless, the surfaces of Cu

samples exposed to simulated disposal conditions do exhibit some roughening (Fig. 4.5), and Cu and Cu alloys buried for extended periods also show localized attack (Romanoff 1957; Bresle et al. 1983). Therefore, it is judicious to consider the possible pitting of Cu containers.

Figure 4.6 shows a cross-section through a so-called copper Type I pit (Lucey 1967). Such pits are characterized by a crust of precipitated basic Cu(II) salts and $CaCO_3$ covering a pit containing Cu_2O and CuCl. Initiation involves the formation of a CuCl pocket in a protective Cu_2O layer. The formation of the crust leads to the development of an occluded region and permanent separation of the anodic and cathodic sites. According to Lucey (1967), both the anodic and cathodic sites are located within the occluded region formed by the crust, a porous Cu_2O membrane separating the anodic region underneath from the cathodic region in the top half of the pit. Others suggest a more conventional distribution of anodic and cathodic sites; anodic dissolution within the occluded region being supported by O_2 reduction on Cu_2O-covered surfaces outside the pit (Campbell 1974). Type II pits are covered by a basic cupric sulphate crust, but less mechanistic information is available for this form of pitting (Campbell 1974).

Pitting of these types would not lead to the development of the surface profiles observed under simulated disposal conditions (Fig. 4.5). Types I and II pitting would produce localized penetrations but most of the surface would be unattacked. To explain the form of the profiles in Fig. 4.5, King (1996a) has suggested a mechanism for underdeposit corrosion involving many of the processes included in Lucey's pitting mechanism, but in which propagating pits either die or coalesce. Pit death occurs when the aggressive pit solution

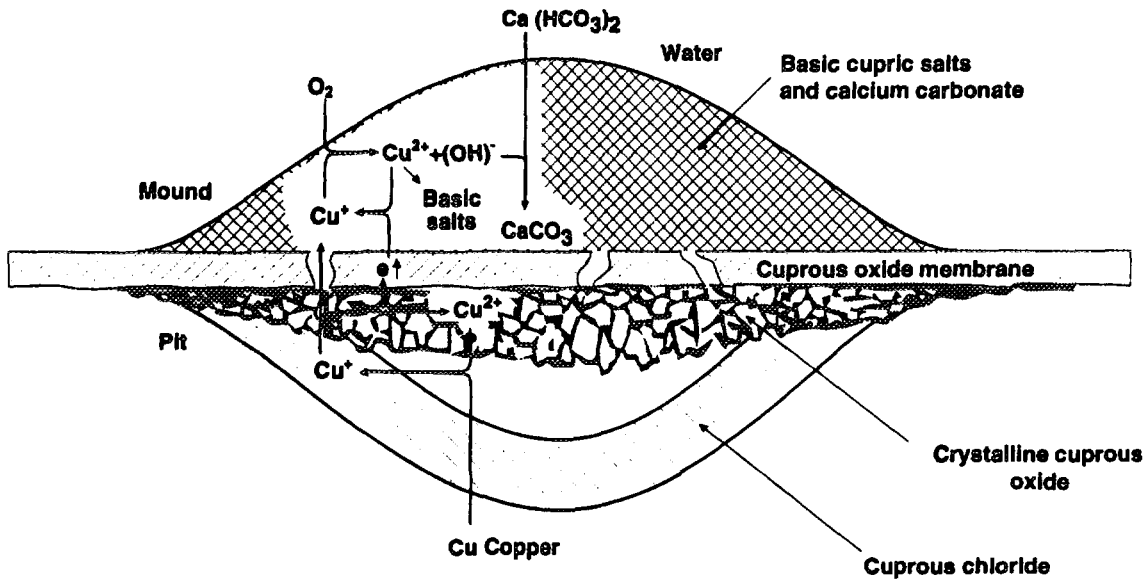

FIGURE 4.6: Cross-section Through a Typical Type-1 Pit on Copper (Lucey 1967)

can no longer be sustained, either because the crust breaks permitting access of the bulk solution or because the slow rate of O_2 supply is insufficient to maintain the necessary rate of Cu dissolution within the pit. Repeated pit initiation, propagation and death events distributed over the entire surface would lead to the type of surface roughening illustrated by Fig. 4.5. At this stage, however, the experimental evidence required to support this type of mechanism is not available. In addition, a model to predict the extent of surface roughening for comparison with experimental surface profiles has not been developed.

Instead, King and LeNeveu (1992) have performed an extreme-value analysis of literature pit-depth data, and applied the results to the prediction of the long-term pitting behaviour of Cu containers. These data (Romanoff 1957; Bresle et al. 1983) were measured on various Cu alloys exposed to different soil types for extended periods (up to ~3000 a). This analysis allows the probability of the maximum pit depth exceeding a given value to be predicted as a function of time. In order to take into account the decreased likelihood of pitting of Cu containers as the vault environment evolves, a maximum pitting period is defined. In their original analysis, King and LeNeveu (1992) assumed that pitting was possible indefinitely because the vault was assumed to be continuously aerated. Nevertheless, the probability of the pit depth exceeding 9 mm on a container in 10^6 a was predicted to be $<10^{-9}$ (a subsequent reanalysis indicates that this probability is in fact $<10^{-21}$). Other criteria for the maximum pitting period are the duration of the warm, oxidizing period (based on the assumption that O_2 is required for pit propagation) or the period over which Cu(II) species are present at the container surface (based on the presumption that the electrochemical reduction of Cu(II) can also support pitting). In a subsequent analysis, King et al. (1994a) estimated that the probability of a pit exceeding 5 mm in depth after 1000 a was $<10^{-11}$. A period of 1000 a exceeds the duration of both the warm, oxidizing period (670 a, Fig. 4.2) and the time required to reduce the $[O_2]$ in the vault below the threshold $[O_2]$ of 3 $\mu g \cdot g^{-1}$, suggested by Myers and Cohen (1995), below which pitting would not occur.

4.4.3 Atmospheric Corrosion

The buffer and backfill materials surrounding the container will be unsaturated for some time following closure of the vault. During this unsaturated period, the corrosion behaviour of the container will depend on the availability of H_2O at the container surface. If the surface of the container is dry, corrosion will take the form of slow gas-phase oxidation. If the container surface is wet, electrochemically based corrosion reactions may be possible (generally, 15 to 90 layers of water are considered necessary for aqueous corrosion, Shreir 1976). Water forms on corroding surfaces in moist atmospheres either through adsorption or because of a lowering of the interfacial water activity through a combination of osmotic and capillary pressures (Shreir 1976). An osmotic pressure can develop because of the precipitation of hygroscopic salts. Capillary forces develop if the corroding surface is covered by a porous corrosion-product or precipitated layer. The same factors (adsorption and osmotic and capillary pressures) acting in the buffer material will tend to prevent H_2O from reaching the container surface. Unsaturated buffer material develops a suction potential, consisting of a matric potential (caused by the capillary pressure generated by the

porous nature of the buffer) and an osmotic potential (due to the presence of solutes in the pore fluids).

It is difficult to predict which of these surfaces (the corroding surface or the surfaces of the clay particles) will be wetted preferentially during the unsaturated phase. The two situations represent opposite extremes in terms of the consequences for container corrosion. Oxidation of the container surface in relatively dry air will be slow (ASM 1987; King 1996a,b), especially at the expected surface temperatures (<80°C). If the container surface is covered by a thin H_2O layer, however, corrosion could be rapid due to the fast supply of O_2 through unsaturated buffer material (King and Kolar 1995). However, although the corrosion rate may be higher in unsaturated buffer material, the total extent of corrosion of the container will be the same because it is limited by the amount of available O_2. Thus, the effect of unsaturated conditions may be to shorten the duration of the initial oxidizing period by using up the O_2 more rapidly (King and Kolar 1995).

4.4.4 Microbially Influenced Corrosion

Although it is now widely accepted that some form of microbial activity within the disposal vault is likely (Stroes-Gascoyne and West 1994), the potential for microbially influenced corrosion (MIC) will be strongly influenced by the evolution of environmental conditions (Chapter 4.3). Initially, conditions would be sufficiently aggressive that no microbial growth will occur close to the container surface (King and Stroes-Gascoyne 1995). The combined effects of heat, γ-radiation and desiccation of the buffer material may even be sufficient to kill microbes close to the container, leading to the formation of a sterilized zone some tens of centimetres thick (King and Stroes-Gascoyne 1995). Therefore, biofilm formation on the container surface is likely to be impossible for several hundred years after emplacement of the container, and may never occur if microbes cannot repopulate the sterilized zone created around the container (Stroes-Gascoyne and West 1994). Further away from the container where conditions will be less aggressive, microbial activity is possible. The type of microorganisms that grow will be affected by the availability of O_2. In the initial aerated phase, the growth of both aerobic and (in anoxic microenvironments underneath biofilms) anaerobic bacteria is possible. Once the trapped O_2 has been consumed, however, only anaerobic bacteria will be viable.

There are numerous reports of MIC of Cu alloys in near-surface environments in the literature, but few of them have direct relevance to the MIC of Cu containers in a deep underground disposal vault (King 1996c). Most literature reports deal with either the MIC of Cu alloys (usually Cu-Ni alloys) in seawater or the microbially influenced pitting of Cu in fresh waters. In all cases, MIC is associated with the formation of a biofilm on the Cu surface. As discussed above, however, these forms of MIC will not occur for some time, possibly never, because of the absence of biofilms on the container surface. In addition, most of the literature reports of MIC involve periodic changes in the aeration of the environment. Thus, the reported cases of MIC of Cu alloys in seawater by sulphate-reducing bacteria (SRB) generally involve heat-exchangers exposed to tidal or estuarine waters, in which the tidal action produces alternating aerobic and anaerobic environments.

As a consequence, SRB-produced HS^- forms sulphide corrosion products during anaerobic periods, which are either sloughed off exposing the underlying metal during subsequent aerobic periods, or catalyze O_2 reduction, also leading to accelerated corrosion (King 1996c). Similarly, periodic stagnant periods interspersed with periods of flowing aerated tap water in institutional buildings is believed to be the cause of the microbially influenced pitting of Cu water pipes in various hospitals, schools and government buildings (Fischer et al. 1988; Chamberlain and Angell 1990).

Since the MIC literature is not particularly useful in determining the possible forms of MIC of Cu containers, the expected behaviour has been assessed based on the known metabolic processes of microbes, the expected evolution of environmental conditions within the vault and the various abiotic and microbial corrosion mechanisms in the literature. No accelerated forms of MIC underneath biofilms are possible for several hundred years after the emplacement of the containers because of the absence of biofilms on the container surface. It is unlikely that metabolic by-products (such as NH_3, HS^- or organic acids) produced in more temperate areas of the vault could reach the container surface during this period, because they would be consumed either by other microbes or by reaction with O_2 or Fe in the buffer before reaching the container surface. At longer times, microbial activity could occur throughout the buffer and backfill materials. However, the restrictive mass-transport conditions in the sealing materials will likely inhibit microbial activity in general, because of the poor availability of nutrients, and prevent repopulation of the sterilized zone around the container in particular, because of the small pore size of the buffer material (Stroes-Gascoyne and West 1994). Therefore, the only form of MIC of concern is that due to the diffusion of microbial metabolic by-products produced in remote locations of the vault to the container surface. Since this would occur during the cool anoxic period in the evolution of vault conditions, it is expected that SRB and the HS^- that they produce will be most likely to lead to corrosion.

It has been shown that HS^- can diffuse through buffer material and affect the corrosion behaviour of Cu (King and Stroes-Gascoyne 1995). Any effect due to sulphide produced by SRB away from the container is likely to be small, however. The maximum steady-state corrosion rate produced by the diffusion of HS^- across a sterile zone 40-cm-thick for a constant $[HS^-]$ of 3 $\mu g.g^{-1}$ is predicted to be only 1×10^{-3} $\mu m \cdot a^{-1}$ (King and Stroes-Gascoyne 1995) (3 $\mu g.g^{-1}$ is the maximimum $[HS^-]$ observed in our MIC experiments (King and Strandlund unpublished data)). Gascoyne and Kamineni in a 1992 study report no detectable sulphide in groundwaters at the URL. More recently, Gascoyne et al. (1995) reported measurable sulphide in a number of URL samples, but the sulphide may have been produced by microbial contamination caused by the sampling procedure.). Therefore, even if sufficient nutrient were available to support microbial activity at a rate of 1×10^{-3} $\mu m \cdot a^{-1}$ for 10^6 a, the maximum additional damage to the container would only amount to ~1 mm. Consequently, because of the limited impact of MIC on container lifetimes, we have chosen not to include MIC in the current version of the corrosion model.

4.4.5 Stress-Corrosion Cracking

Stress-corrosion cracking (SCC) would lead to relatively rapid failure of the container if cracking were to initiate and if conditions were suitable for crack propagation. Therefore, it must be demonstrated that SCC will either not initiate or that the conditions necessary for crack propagation will not exist. The SCC literature on α-brass in ammonia solutions and on Cu in ammonia, nitrite and organic acids has been reviewed and the potential for SCC of Cu containers assessed (King 1996d). Three main mechanisms have been proposed to explain the SCC of Cu: (i) a film-rupture/anodic dissolution model, in which the crack advances by anodic dissolution at the bare crack tip following rupture of a protective film, (ii) a tarnish-rupture mechanism, in which crack advance occurs by rupture of a tarnish (oxide) film, and (iii) a film-induced cleavage model, in which a brittle cleavage-like crack is initiated in a thin surface layer and then propagates for a significant distance into the underlying metal.

The major argument against SCC of the containers is that the necessary combination of stress and a suitable corrosive environment will not be present simultaneously in the vault (King 1996d). In particular, all three proposed mechanisms require a certain degree of crack-tip strain in order for the crack to propagate. In the film-rupture/dissolution and tarnish-rupture mechanisms, crack-tip strain is required to fracture the Cu_2O film at the crack tip. In the case of cracking by a film-induced cleavage mechanism, crack-tip strain is not only required to initiate the crack in the surface layer but is also necessary to continuously fracture load-bearing ligaments between the cleavage-like facets. Without continuous straining, cleavage cracks in Cu stop after propagating 20 μm (Sieradzki et al. 1984). For the two container designs presented in Chapter 2.4, rapid strain of the Cu shell will only occur as the hydrostatic and buffer swelling pressures are imposed on the container, and then only until such time that the gap between the outer Cu shell and either the inner C-steel liner or packed particulate is closed. The long-term strain of the Cu shell due to creep of the packed particulate would involve strain rates much lower than those at which SCC has ever been observed to occur (perhaps 10^{-10} s^{-1}, governed by the creep rate of the particulate). SCC is probably not possible at such low strain rates because the time interval between film rupture events (determined by the strain rate and the critical strain required for film fracture) becomes so long that the crack is stifled by oxide growth or blunted by dissolution of the crack walls.

As well as a sufficient strain rate, the environment must meet certain requirements for SCC to occur. The environment must be able to support either dissolution at the crack tip or the formation of a brittle oxide or tarnish layer. As discussed above, the amount of available oxidant is limited, so that these latter requirements are also only met for a limited period of time. The presence of Cl^- is also expected to inhibit SCC, either because of the formation of a protective layer of $CuCl_2 \cdot 3Cu(OH)_2$ which prevents further oxide growth or because Cl^- increases the pore size in the surface layer through surface diffusion of copper atoms, destroying the microporosity believed to be a requirement for the surface layer that initiates cleavage cracks (King 1996d). Chloride will also be incorporated into the Cu_2O layer, which may affect its critical fracture strain and its

ability to initiate cleavage cracks. One or more of these effects may be responsible for the observation that Cl^- inhibits the SCC of α-brass in ammonia solutions (King 1996d).

In addition to the effects of Cl^- and the lack of oxidant, the environment will not support SCC because of the absence of known agents for SCC of Cu, since, unlike stainless steels, chloride does not induce SCC of Cu. Microbial activity within a biofilm could conceivably result in the formation of NH_3, NO_2^- and organic acids, all of which have been shown to cause the SCC of Cu (King 1996d). As argued above, however, biofilms will not be present on the container surface during the critical period for SCC when O_2 will be available and when the container is undergoing strain. Alternatively, these species could be produced by the γ-radiolysis of moist air during the unsaturated phase, although the formation of NO_2^- or organic acids is unlikely (King 1996d). However, the quantities of radiolysis products will be small because of the small radiation fields (~11 $Gy \cdot h^{-1}$). Although a small amount of NH_3 could be produced by radiolysis (King 1996d), moist air will only be present before the imposition of the external loads, so that, apart from the effect of any residual manufacturing stresses, the container will not be undergoing strain during this period.

Phosphorous-containing Cu alloys, such as the DLP alloy specified for the container, have been shown to have an increased susceptibility to SCC in tarnishing ammonia atmospheres (Thompson and Tracy 1949). Increased susceptibility was observed for P contents >40 $\mu g \cdot g^{-1}$ compared with a current specification of 50 $\mu g \cdot g^{-1}$ P for DLP Cu. Refinement of this experimental alloy could presumably result in a lowering of the P content below that found to increase the SCC susceptibility. In all other respects, the corrosion behaviour of DLP Cu is expected to be the same as that of oxygen-free electronic Cu (OFE, UNS 10100), on which much of the supporting experimental evidence is based.

In general, therefore, SCC of Cu containers is extremely unlikely because: (i) the container will undergo significant strain for only a limited period of time, (ii) known SCC agents are unlikely to form in sufficient quantities; and, even the small amount formed will not be present during the period of container strain, and (iii) the general lack of oxidant in the vault and the inhibitive effects of Cl^- further reduce the likelihood of SCC.

4.4.6 Effect of γ-Radiation

Radiolysis of the environment by γ-radiation could potentially alter the corrosion behaviour of the container by producing aggressive species and by acting as an additional source of oxidants. In general, however, the effect of these processes, in particular the production of oxidants, is expected to be small because of the low absorbed dose rates.

During the unsaturated phase, the radiolysis of moist air may lead to the fixation of nitrogen. Reed and Van Konynenburg (1991) have considered the possibility of N-acid, N-oxide and NH_3 formation. The yield of NO_3^- depends on the availability of H_2O, having a

maximum value at 50% relative humidity (RH). At lower RH, HNO_3 decomposes to NO_2 and H_2O (Jones 1959), so that the yield of nitric acid near the container may be limited by the availability of H_2O. Nitrous acid is rarely identified as a major product. In either case, the acidification due to radiolytically produced N-acids (or the alkalization due to NH_4OH) would be offset by the pH-buffering capacity of the Na-bentonite clay surrounding the container. The formation of N-oxides, such as NO, N_2O and NO_2, although reported, would be unlikely to have any effect on the corrosion of the container since they do not appear to participate in interfacial reactions. Ammonia is observed as a product of moist air radiolysis, even though the production of OH radicals from H_2O would suggest that conditions would be too oxidizing to fix nitrogen in the reduced form. Reed and Van Konynenburg (1991) report a maximum concentration 0.0026 mol% (26 vppm) at an absorbed dose of ~9 x 10^4 Gy. At higher doses, the [NH_3] decreased, being only 7 vppm at 4 x 10^5 Gy. For comparison, these doses would be achieved at the surface of a Cu container after ~0.9 and 4.4 a, respectively (assumed absorbed dose rate 11 Gy·h^{-1}, $t_{1/2}$ = 30 a), after which the [NH_3] will decrease as it is consumed in further radiolysis reactions.

After saturation of the vault, the radiolysis of the liquid phase will become more important. However, the significance of liquid-phase radiolysis reactions will depend on the time for saturation. If saturation is delayed for, say, 120 a (four times the half life of ^{137}Cs), the maximum surface absorbed dose rate will have decayed to ~0.7 Gy·h^{-1} and any effect on the corrosion behaviour of the container will be minimal. King and Litke (1987) did not observe a positive shift in E_{CORR} of Cu in deaerated synthetic groundwater at 150°C when irradiated at a dose rate of 27 Gy·h^{-1} (at least 2.5 times the maximum dose rate for a container), and hence concluded that there was no significant formation of oxidizing radiolysis products at such dose rates.

In support of these arguments, no deleterious effect of γ-radiation (dose rate 5 Gy·h^{-1}) has been observed during long-term (up to 5 a) irradiated corrosion tests under simulated Canadian disposal conditions (King and Ryan, unpublished data). Stressed samples (U-bends and creviced double U-bends) showed no sign of SCC when exposed to either a vapour phase, compacted buffer material or bulk solution. No crevice corrosion was observed on the creviced U-bend and non-stressed crevice samples, the extent of corrosion being limited to the formation of interference colours.

4.4.7 Corrosion of Welds

Testing of electron-beam welded Cu samples has consisted of exposing planar welded specimens to irradiated environments consisting of a saturated vapour phase, synthetic groundwater, and compacted buffer material (King and Ryan, unpublished data). In the tests completed to date, no preferential corrosion of the welded samples has been observed.

4.4.8 Other Forms of Corrosion

The only major type of corrosion that has not been considered here is crevice corrosion (CC). Crevice corrosion of Cu alloys is usually associated with the formation of a

differential copper-ion concentration cell, rather than the classic type of CC involving differential aeration (ASM 1987), regions of the surface in contact with a low copper-ion concentration acting as the anode, with regions of high concentration acting as the cathode. Thus, the reduction of copper ions on cathodic sites drives copper dissolution in anodic regions. This form of CC is self limiting, however, the concentration of dissolved copper increasing in anodic regions until the differential concentration cell no longer exists. For this reason, practical cases of CC of Cu alloys, when observed, are usually limited to <400 μm in depth (ASM 1987). However, in long-term (up to 5 a) irradiated corrosion tests under simulated disposal conditions, no CC was observed on either creviced U-bend or creviced planar specimens (King and Ryan, unpublished data).

Unlike many materials, hydrogen (whether formed radiolytically or by corrosion) has little effect on the mechanical properties of Cu. The only known cause of failure due to hydrogen is the so-called "hydrogen sickness" that affects oxygen-containing alloys when exposed to hydrogen atmospheres at temperatures above the critical point of water (ASM 1987). Oxygen-free Cu alloys, such as OFE and DLP, are immune.

4.4.9 Natural Analogues

One of the benefits of Cu as a candidate container material is that there are natural analogues that can be used as evidence to justify long-term corrosion predictions. These analogues are in the form of native Cu deposits and man-made Cu and bronze artifacts.

Two studies of man-made analogues have been used in our assessment of the long-term corrosion behaviour of Cu containers. One of these studies (King 1995) has been used to justify the corrosion mechanism on which the long-term prediction of the behaviour of Cu containers is based (Fig. 4.3). This involved the reanalysis of a study of a bronze cannon that had been submerged in seabed clay sediments in the Baltic Sea for 316 a, and which has been used as an analogue in the Swedish program (Hallberg et al. 1988). In particular, the reanalysis suggested the importance of the interfacial production of $CuCl_2^-$ species as included in our corrosion mechanism (k_{af}, k_{ab}, k_{bf} and k_{bb}, Fig. 4.3). By considering the formation of $CuCl_2^-$, King (1995) was able to account for the layered $Cu_2O/CuCO_3{\cdot}Cu(OH)_2$ corrosion product observed on the cannon (analogous to reactions k_2/k_{-2} and k_3/k_{-3} in Fig. 4.3). The major oxidant for the cannon was not O_2, as is expected for the container, but Cu(II) dissolved from CuO inclusions in the bronze matrix. The dissolution of these inclusions via the $CuCl_2^-$ species, as proposed by King (1995), is analogous to the dissolution of $CuCl_2{\cdot}3Cu(OH)_2$ and the reduction of Cu(II) on the container (k_{-3} and k_d, Fig. 4.3). Further support for the mechanism in Fig. 4.3 came from the observed [Cu] profiles in the clay sediments surrounding the cannon. The observed profiles were similar to those found experimentally for Cu coupons in contact with compacted buffer material, and confirmed the importance of Cu(II) adsorption on clay (k_4/k_{-4}, Fig. 4.3). King (1995) was able to show that the value of the apparent diffusion coefficient of Cu(II) derived from the observed profiles fitted the same temperature dependence as that for values measured experimentally from Cu corrosion (Litke et al.

1992) and diffusion experiments (King and Ryan, unpublished data). Finally, by assuming a Cu(II)-diffusion rds, King et al. (1994b) were able to predict the corrosion rate to within a factor of 6 of the value estimated from the analysis of the cannon (Hallberg et al. 1988).

The other analogue study that has been used is the analysis of the pit depths on a collection of Swedish bronze-age artifacts (Bresle et al. 1983). These artifacts had been exposed to near-surface burial conditions for periods of up to 3000 a. Although the burial conditions differ from those expected in a disposal vault, it was judged that the data were useful for predicting the long-term pitting behaviour of a container because of the length of the exposure period. In fact, it can be argued that the exposure conditions and range of alloy types made the artifacts more susceptible to pitting than the containers. The artifacts would have been exposed to continuously aerated low-Cl^-/high-HCO_3^- waters, which increases the susceptibility to pitting (King 1996a; Sridhar and Cragnolino 1993). Furthermore, although the Cu content of many of the artifacts was unusually high (Bresle et al. 1983), the presence of alloying elements and inclusions and the use of crude metallurgical procedures may have rendered the artifacts more susceptible to pitting than modern oxygen-free Cu alloys.

Along with long-term pitting data from a study by Romanoff (1957), these archaeological pit-depth data have been used in a statistical extreme-value analysis (Chapter 4.4.2). This analysis forms the basis of the prediction of the maximum pit depth on a container in the disposal vault. Pitting is most likely in the presence of O_2, which will have been consumed within a period of 3000 a. The benefit of using data collected over a period of up to 3000 a for this analysis, therefore, is that the prediction is based on an interpolation of measured data, rather than an extrapolation.

4.5 CORROSION AND MATHEMATICAL MODELS

The corrosion model described in this section is used to predict the long-term corrosion behaviour of Cu containers,. The model concludes that uniform corrosion and pitting corrosion will not lead to failure in $<10^6$ a. As a result, the container failure model in SYVAC PR4 describes only those containers failing as a result of initial fabrication defects (see Chapter 6.3.1).

In the corrosion model, it is assumed that failure could occur as a result of uniform corrosion or pitting. The container is considered to have failed if 16 mm of the Cu shell has been uniformly corroded (approximately two-thirds of the minimum 25 mm wall thickness), failure due to buckling occurring at this point. Alternatively, the container is considered to fail by pitting if the maximum pit depth plus the depth of uniform corrosion equals the minimum wall thickness of 25 mm. The full wall thickness is used for the pitting allowance because it is considered that localized penetration of the container over a relatively small surface area will not result in mechanical instability.

4.5.1 The Corrosion Model

The reaction mechanism describing the electrochemical, chemical and mass-transport processes involved in the uniform corrosion of Cu is illustrated in Fig. 4.3. This mechanism is based on the results of our own experimental program and those of other workers and from analogue studies, as described in this Chapter and in more detail elsewhere (King 1996a-d). In addition to identifying the important processes, these studies have also provided values for many of the rate constants (designated as k in Fig. 4.3) needed for the mathematical model. All processes included in the model are described by kinetic expressions, thus avoiding the necessity to assume that the reactions are at equilibrium. The Cu surface is assumed to be uniformly accessible so that the anodic and cathodic interfacial reactions can occur over the whole surface.

The interfacial electrochemical reactions included in the model are the anodic dissolution of Cu (k_{af}/k_{ab}, k_{bf}/k_{bb}), the cathodic reduction of O_2 to OH^- (k_c) and the cathodic reduction of $Cu^{2+}$to Cu(I) k_d. The precipitation and dissolution of Cu_2O and $CuCl_2 \cdot 3Cu(OH)_2$ are included (k_2/k_{-2} and k_3/k_{-3}, respectively), as observed experimentally. Redox reactions involving O_2, Cu(I)/Cu(II) and Fe(II) are also considered. The homogeneous oxidation of Cu(I) by O_2 (k_1) is the reaction via which Cu(II) is produced. Oxygen is also consumed by reaction with Fe(II) (k_5). The other redox reaction included is the reduction of Cu(II) by Fe(II) (k_6). This reaction is believed to partly explain the large observed temperature dependence of the apparent diffusion coefficient of Cu(II) (King 1995), and may be significant during the cool, anoxic period in the evolution of vault conditions.

Mass transport (J_{O2}, $J_{Cu(II)}$, $J_{Cu(I)}$) through the porous layers surrounding the container is assumed to occur by diffusion. Diffusion of these species through the buffer and backfill materials is treated in a similar manner to that of radionuclides (Chapter 3.5). Adsorption is treated somewhat differently, however, by using kinetic expressions rather than an equilibrium distribution coefficient. The only species considered to adsorb on the negatively charged clay particles is Cu(II). A kinetic Langmuir expression is used to describe the adsorption and desorption of Cu(II) (k_4/k_{-4} in Fig. 4.3).

The effect of the unsaturated period on the corrosion behaviour of the container can be simulated. Oxygen is assumed to diffuse through both the vapour and solution phases in partially saturated buffer material, with dissolved and gaseous O_2 connected through partitioning rate constants (k_8/k_{-8}).

4.5.2 The Mathematical Model and Predictions

The mathematical model is based on the corrosion model in Fig. 4.3 and a 1-dimensional (1-D), multi-layer description of the various materials surrounding the container (King and Kolar 1995, 1996; Kolar and King 1996b). In this version of the model, up to four layers are considered: buffer material, light or dense backfill material, the EDZ, and the fractured rock. Thus, the model simulates the effects of both the vault environment and that of the surrounding geosphere. The properties of the EDZ and fractured-rock layer are varied to

simulate the effect of a permeable geosphere. No credit is taken for the mass-transport properties of the 500 m of rock.

Mass-balance equations are written for the various diffusing and non-diffusing species considered in the model, of the general forms

$$\varepsilon_a \frac{\partial C}{\partial t} = \frac{\partial}{\partial x}\left(\varepsilon \tau D_o \frac{\partial C}{\partial x}\right) + \varepsilon_a R + R' \tag{4.7}$$

$$\frac{\partial C}{\partial t} = \varepsilon_a R + R' \tag{4.8}$$

where ε_a is the accessible porosity (King et al. 1996), R and R' are terms describing the rates of homogeneous reactions and the other terms have been defined in Chapter 3.5. The ten species considered in the model are: dissolved O_2, O_2 in the gas phase, dissolved Cu(I) (as $CuCl_2^-$), precipitated Cu(I) (as Cu_2O), dissolved Cu(II) (as Cu^{2+}), precipitated Cu(II) (as $CuCl_2 \cdot 3Cu(OH)_2$), adsorbed Cu(II), Cl^-, dissolved Fe(II), and precipitated Fe(II). In addition, a heat-conduction equation is also included to simulate the effect of varying temperature within the vault.

The mass-balance equations are solved using finite-difference techniques subject to a set of boundary and initial conditions. The boundary conditions (bc) for O_2, $CuCl_2^-$ and Cu^{2+} and Cl^- at x=0 are defined by electrochemical expressions. To ensure that there is no net loss or gain of electrons, the total cathodic current for the reduction of O_2 and Cu^{2+} must equal the anodic current for Cu dissolution as $CuCl_2^-$. The anodic and total cathodic current densities are equal to the corrosion current density i_{CORR} (in A per unit area), which is proportional to the corrosion rate in $\mu m \cdot a^{-1}$. The rates of electrochemical reactions are potential dependent and, under naturally corroding conditions, the balance of the anodic and cathodic rates defines E_{CORR}. Dissolved Fe(II) is assigned a zero-flux boundary condition at x=0 and, since the remaining species do not diffuse, the respective mass-balance equations can be used as boundary condition for these species. At the far boundary, corresponding to the EDZ/rock interface, the diffusing Cu species are assigned a zero concentration boundary condition, and O_2, Fe(II) and Cl^- have constant-concentration boundary condition determined by the composition of the groundwater.

The initial conditions depend on the system being modeled. Invariably, the layers are taken to be initially free of all Cu species. In the example shown here, we assume the vault immediately saturates with incoming groundwater from the surrounding rock. The groundwater is assumed to be essentially deaerated ($[O_2] < 3 \times 10^{-8}$ mol·dm^{-3} or < 1 ng·g^{-1}, Gascoyne 1996). The incoming groundwater is diluted by the fresh water used to compact the buffer and backfill materials. These materials are compacted at either 80% (buffer and dense backfill) or 33% (light backfill) of their saturated moisture contents. Therefore, there is significant air-filled void space in these layers. Here, the initial distribution of O_2 in the

various layers is determined assuming the gaseous O_2 immediately dissolves in the pore solutions, in addition to that already present in the aerated water used for compaction.

The use of a 1-D model has certain limitations. For instance, it is impossible to account for the non-uniform distribution of the various buffer and backfill materials around the container (Fig. 2-1). We can only simulate diffusion in a radial direction. Therefore, when light backfill is used as the second layer, we simulate diffusion from the container towards the top of the room through the buffer and light backfill layers. When using dense backfill as the second layer, we simulate diffusion in the opposite direction. Neither is it possible to take into account the influence of neighbouring containers on the development of concentration gradients in the various layers. Despite these limitations, a simple 1-D mass-transport model was chosen so that as many of the reactions and processes involved in the corrosion process as possible could be included in the mathematical model.

Apart from the simplifications inherent in assuming 1-D mass-transport and the assumption that the mechanism in Fig. 4.3 adequately describes the corrosion behaviour of Cu, there are relatively few assumptions made in the model. Although for the simulations described here, we assume (i) fully saturated buffer and backfill materials and (ii) the absence of γ-radiation, the effects of these variables are described elsewhere (King and Kolar 1995) or will be included in future versions of the model. The effect of unsaturated buffer is to increase the rate of corrosion, since O_2 diffuses to the container faster through vapour-filled pores, but the extent of corrosion is the same as in saturated buffer, because it is limited by the quantity of available oxidant, which is the same in both cases. Experimental studies show that the effect of irradiation leads to lower corrosion rates (King 1996a). Therefore, present exclusion of these two effects will not invalidate the prediction of this version of the model. We do assume, however, a constant pH (pH 7) throughout the simulation and the mass-transport effects of the precipitate layers that first grow on, and then dissolve from, the container surface are not included. The effects of these surface layers on the rate of the cathodic interfacial reactions are accounted for by using values for the electrochemical rate constants appropriate for film-covered surfaces. We do not, however, scale the rates of the interfacial anodic or cathodic reactions for partial coverage of the container surface by porous corrosion products.

The extent of pitting is calculated outside this model. As described in Section 4.4.2, the probability of the deepest pit exceeding a given depth after a given period is predicted using extreme-value analysis of literature pit-depth data. A probability of 10^{-11} is used, which corresponds to a probability of $<10^{-6}$ that the maximum pit depth on any of the ~60 000 containers in the disposal vault will exceed the predicted value. Fig. 4.7 shows the extreme-value distributions for the maximum pit depth on a Cu container as a function of exposure time predicted from the extreme-value analysis of the bronze-age and buried Cu objects (King and LeNeveu 1992). The distributions do not represent the distribution of pit depths on a container; rather, they represent the probability F(x) that the maximum pit depth on a container will exceed a depth x. For the condition $1\text{-}F(x) < 10^{-11}$, x varies from 4.5 mm to 6.0 mm for times of 100 a and 10^6 a respectively. Thus, for pitting periods up to 10^6 a, the maximum pit depth on any container is < 6 mm. Since the difference between the pitting

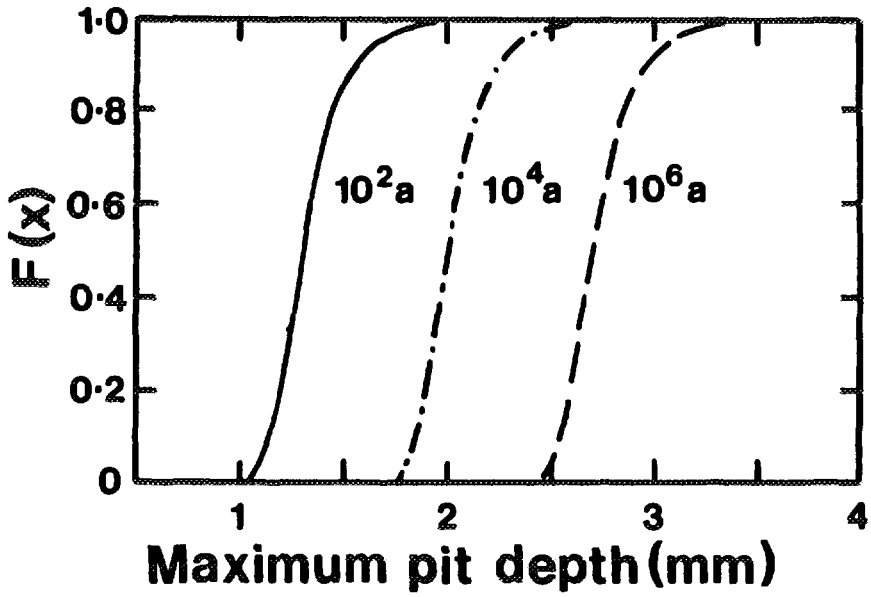

FIGURE 4.7: Predicted Cumulative Probabilities (F(x)) for Maximum Pit Depths (x) on Copper Containers as a Function of Exposure Time (King and LeNeveu 1992). F(x) is the cumulative probability that the deepest pit on a container will be less than or equal to x.

plus uniform corrosion allowance (25 mm) and the uniform corrosion allowance (16 mm) is 9 mm and the maximum pit depth on any of the containers is < 6 mm for times up to 10^6 a, container failure by corrosion will only occur within this period if the uniform corrosion allowance of 16 mm is breached.

Figure 4.8 shows the predicted variation of E_{CORR} and i_{CORR} with exposure time for the case of dense backfill as the second layer. These predictions illustrate one of the fundamental properties of the vault - the evolution from oxidizing to anoxic conditions as the O_2 initially trapped in the pores of the buffer and backfill materials is consumed. In terms of the corrosion behaviour of the container, this evolution in redox conditions results in a decrease in both E_{CORR} and i_{CORR} with time. After all the O_2 is consumed, E_{CORR} increases as Cu(II) is reduced to $CuCl_2^-$ by reaction with Fe(II) (King and Kolar 1995, 1996; Kolar and King 1996b). Most importantly, the corrosion rate decreases from an initial value of 1.3 $\mu m \cdot a^{-1}$ (equivalent to $i_{CORR} = 5.5 \times 10^{-8}$ $A \cdot cm^{-2}$) to virtually zero after 2640 a. (The period of corrosion in this simulation is longer than the period of 670 a to consume the O_2 in Fig. 4.2 because the spatial and temporal variation of temperature was included in the present calculation instead of the constant temperature of 75°C used for Fig. 4.2). The integrated corrosion current density is shown in Fig. 4.9, which more clearly shows that the extent of corrosion is limited by the total amount of O_2 in the vault - i.e., once the initially trapped O_2 is consumed, corrosion virtually ceases. The maximum wall penetration due to uniform

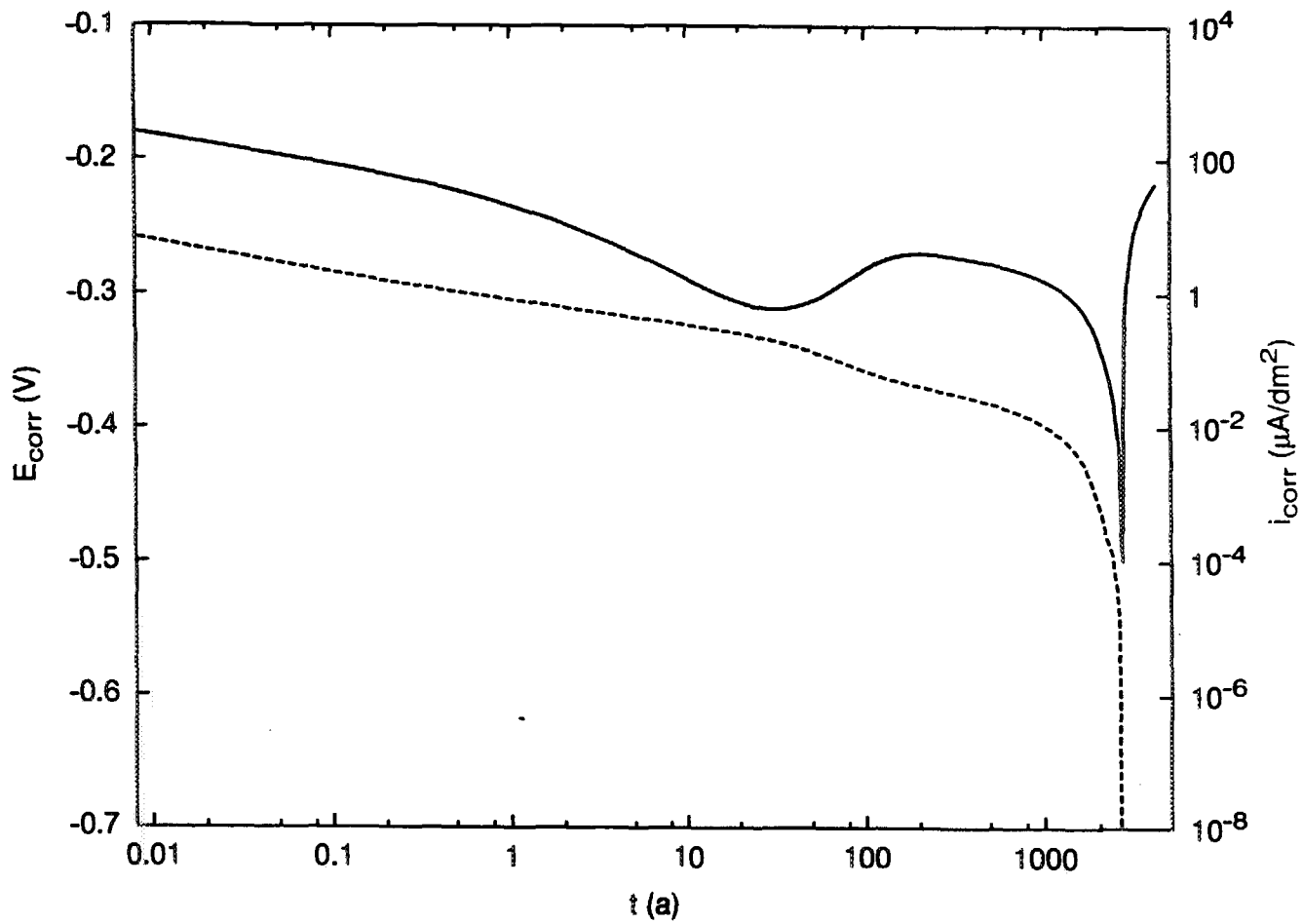

FIGURE 4.8: Predicted Variation of the Corrosion Potential (E_{CORR}) and Corrosion Current Density (i_{CORR}) as a Function of Time for a Copper Container in a Disposal Vault. In this 1-D simulation, the container is assumed to be surrounded by a layer of compacted buffer material, a layer of dense backfill and the excavation-damaged zone. No credit is taken for the rest of the geosphere as a mass-transport barrier. E_{CORR} ——— , i_{CORR} ----------

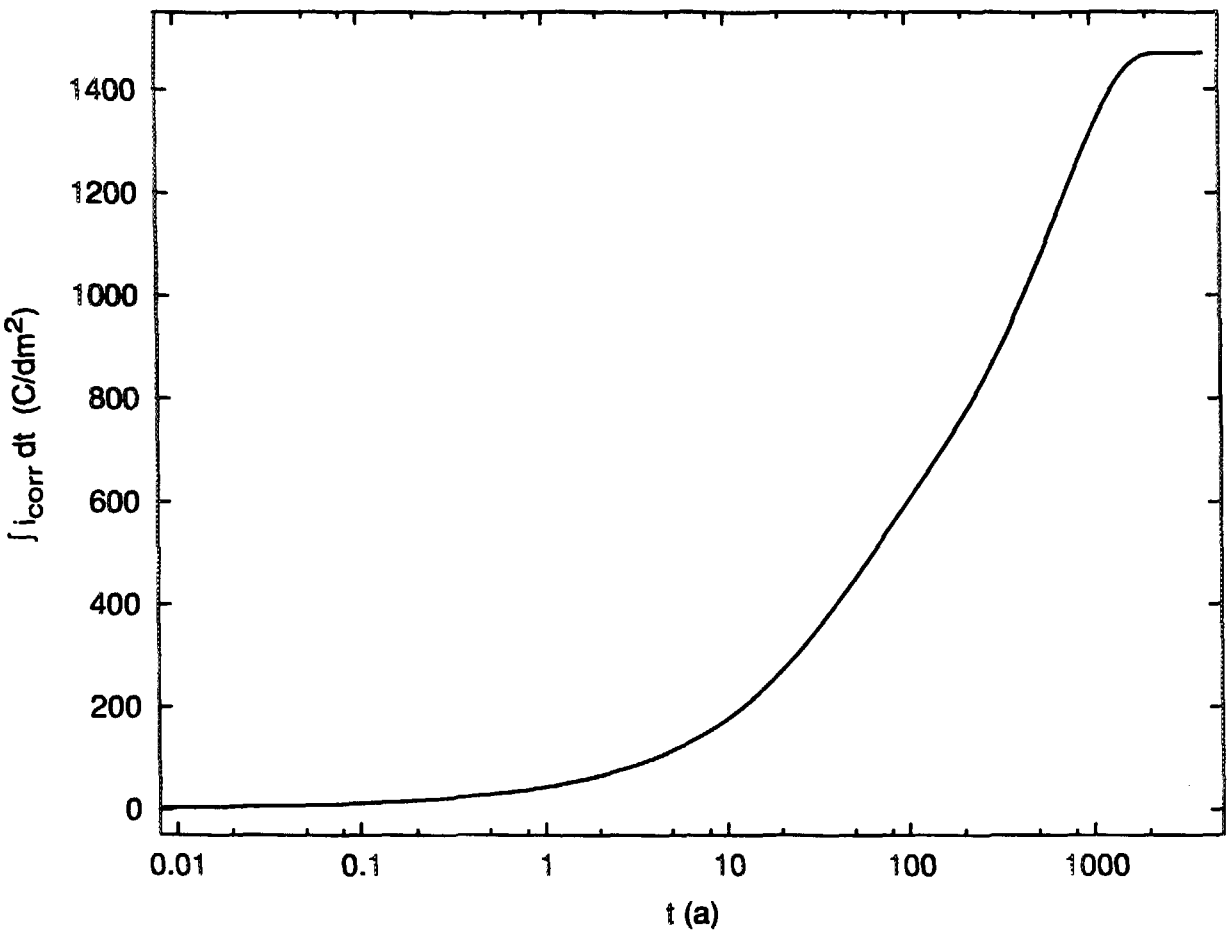

FIGURE 4.9: The Variation of the Integrated Corrosion Current Density with Time for the Simulation Shown in Fig. 4.8. The integrated current density is proportional to the depth of uniform corrosion. This figure illustrates that corrosion of the container effectively stops once the initially trapped O_2 is consumed. The maximum integrated current density is equivalent to a penetration of 11 μm.

corrosion is 11μm. Thus, uniform corrosion will not result in container failure in periods $< 10^6$ a.

As shown in Fig. 4.3, Cu dissolution proceeds via the Cu(I) state. Homogeneous oxidation by O_2 results in the formation of Cu(II) species. Figure 4.10 shows the predicted concentration profiles for various Cu species in the buffer material surrounding the container as a function of time. The Cu species included in this figure are dissolved $CuCl_2^-$, precipitated Cu_2O, dissolved Cu^{2+}, precipitated $CuCl_2 \cdot 3Cu(OH)_2$ and adsorbed Cu^{2+} (in the model, precipitation reactions are allowed to occur throughout the layers, although the amount of material precipitated is small). Of the total amount of Cu shown in Fig. 4.10, >99% comprises the various Cu(II) species, of which >98% is adsorbed Cu(II). This predominance of adsorbed Cu(II) and the resultant [Cu] profiles are consistent with the results of Cu corrosion experiments in compacted buffer (King et al. 1992; Litke et al. 1992) and the observation of [Cu] profiles around the bronze cannon analogue (Hallberg et al. 1988; King 1995).

More details of these and other simulations can be found elsewhere (King and Kolar 1995, 1996; Kolar and King 1996a,b; King et al. 1996).

The results of the detailed mathematical model can be compared to the maximum depth of corrosion estimated from the known amount of O_2 in the vault and an empirically determined pitting factor. On this basis, the maximum depth of uniform corrosion would be ~176 μm. This value exceeds the value of 11 μm calculated above because, in the detailed model, most of the O_2 is consumed by reaction with Fe(II) minerals and because the detailed calculation above does not take into account the O_2 trapped in the light backfill material or in the non-accessible pores of the buffer and backfill materials, which is unavailable for corrosion of the container (King et al. 1996, Kolar and King 1996a). The pitting factor is the ratio of the maximum pit depth to the depth of uniform corrosion. In the Swedish program, a pitting factor of 3 to 5 is used (Swedish Corrosion Institute 1983). In contrast, our statistical treatment of pitting giving a maximum pit depth of 6 mm is equivalent to a pitting factor of 550.

It should also be remembered that this prediction corresponds to a groundwater containing 1 $ng \cdot g^{-1}$ O_2 and no Fe(II). Such conditions are far more oxidizing than those found at depth in the Canadian Shield, and corresponds to an E_h of +0.76 V_{SHE} at pH 7 and 25°C. This redox potential compares with observed E_h values for fracture zone LD1 of between +0.20 and -0.10 V_{SHE} (Chapter 3.4) and the range of redox potentials used to calculate radionuclide solubility of 0.06 to -0.21 V_{SHE} at pH 7 (Table 3-2). The observed redox potentials are much lower than the calculated value of 0.76 V_{SHE} because redox couples other than O_2/H_2O (such as Fe(II)/Fe(III)) control the redox potential and the system is essentially O_2-free

Despite the use of a more conservative corrosion model than that used in the Swedish program, the detailed model described here suggests that failure of Cu containers from corrosion will not occur in a Canadian disposal vault in less than 10^6 a. This claim is

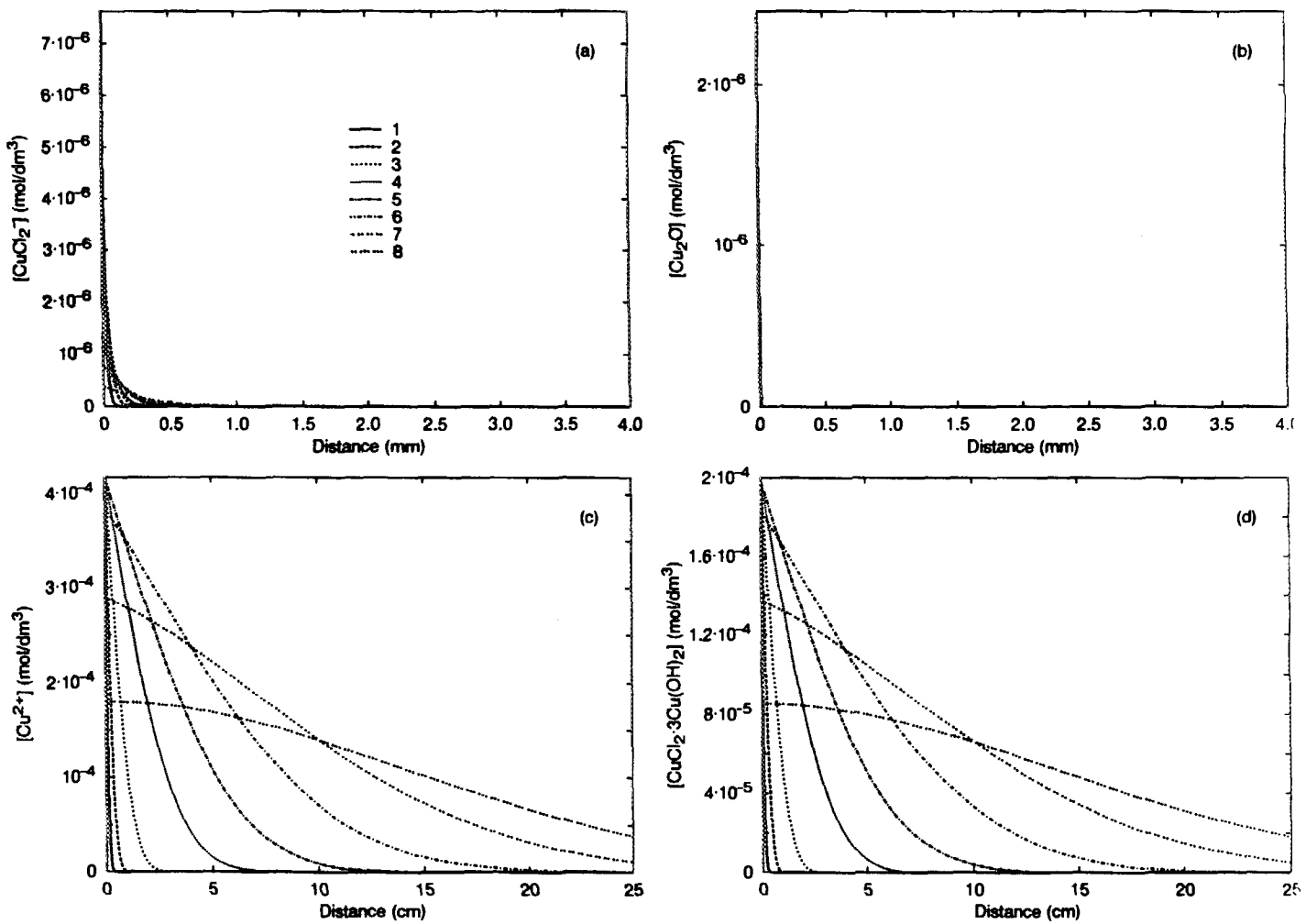
(a)
[CuCl2-] (mol/dm3)
7·10-6
6·10-6
5·10-6
4·10-6
3·10-6
2·10-6
10-6
0
0 0.5 1.0 1.5 2.0 2.5 3.0 3.5 4.0
Distance (mm)
1
2
3
4
5
6
7
8
(b)
[Cu2O] (mol/dm3)
2·10-6
10-6
0
0 0.5 1.0 1.5 2.0 2.5 3.0 3.5
Distance (mm)
(c)
[Cu2+] (mol/dm3)
4·10-4
3·10-4
2·10-4
10-4
0
0 5 10 15 20 25
Distance (cm)
(d)
[CuCl2·3Cu(OH)2] (mol/dm3)
2·10-4
1.6·10-4
1.2·10-4
8·10-5
4·10-5
0
0 5 10 15 20
Distance (cm)

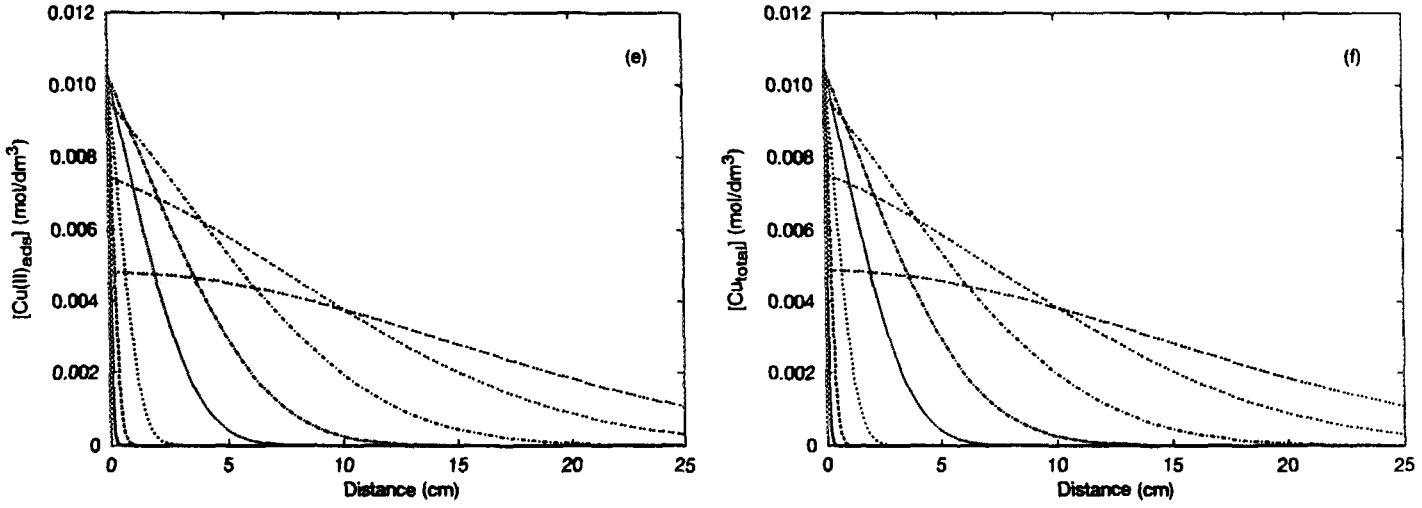

FIGURE 4.10: The Predicted Distribution of Various Copper Species in the Buffer Material as a Function of Time for the Simulation Shown in Fig. 4.8. The Cu species considered are: (a) dissolved $CuCl_2^-$, (b) precipitated Cu_2O, (c) dissolved Cu^{2+}, (d) precipitated $CuCl_2 \cdot 3Cu(OH)_2$, (e) adsorbed Cu(II), and (f) the sum of the all Cu species. Note various concentration and distance axes used. Profiles shown for times of (1) 1 month, (2) 11 months, (3) 5.8 a, (4) 32.2 a, (5) 124 a, (6) 478 a, (7) 1312 a and (8) 2572 a.

supported by the results of an extensive experimental program, from information available in the literature, and from natural analogue studies.

4.6 THE IMPACT OF CORROSION ON THE CONTAINER PERFORMANCE ASSESSMENT MODEL IN SYVAC

Although the corrosion model described here is not used directly in the SYVAC PR4 simulations, corrosion of the container could have an impact on the performance assessment model for initially defected containers. In particular, corrosion might increase the radius of the pinhole defect, currently assumed to be in the range 0.15 to 1.5 mm. According to the predictions above, uniform corrosion could increase this range by 11 μm, to between 0.161 and 1.51 mm. Since the release rate is proportional to the area of the defect (see Chapter 6.5.2.6), this increase in radius could result in a 1 to 15% increase in release. However, not included in this calculation is the effect of corrosion product deposition within the defect. Since some of the dissolved Cu will precipitate as Cu_2O or $CuCl_2 \cdot 3Cu(OH)_2$ in the defect, both of which have higher molar volumes than Cu, corrosion will actually result in a decrease in the defect size and hence, a reduction in the release rate. To maintain a conservative approach, the effect of corrosion product formation in the defect is not included in the SYVAC PR4 predictions and the defect size is assumed not to change with time.

5. THE USED FUEL DISSOLUTION MODEL

5.1 INTRODUCTION

Here we present the characteristics of the reference used CANDU fuel and the conceptual and mathematical models for dissolution of used fuel and radionuclide release into the groundwater entering the defective containers. The linkage of the radionuclide concentrations in the porewater inside a defective container with the model for mass transport of radionuclides from within the container, through the defect and into the surrounding buffer is discussed in Chapter 6.

Before describing the radionuclide inventories and the models for radionuclide release, it is necessary to briefly review the scenario under consideration. The vast majority of containers are expected to survive intact for periods in excess of 10^6 a. Between 6 and 20 containers of the total of 60,000 in the vault might be expected to be defective when emplaced (see Chapter 6.3.1), most likely because of weld defects that could escape detection. Such defects are assumed to have a diameter of 0.3 to 3 mm. Conceptually, it is expected that groundwater from the surrounding rock would gradually be taken up by buffer and backfill materials and would enter the defect very slowly as the hydrostatic head in the vault is restored. Oxygen trapped within the container would be consumed relatively rapidly (within days) by oxidation of copper and steel once water started to enter the container, although this would take longer (probably decades to hundreds of years) in the surrounding buffer and backfill.

Before radionuclides could be released from the fuel in significant quantities, there would have to be through-wall corrosion of the Zircaloy sheath. Some sheaths (approximately 1 in 10 000 to 1 in 100 000) would have failed previously in-reactor. For the remainder, corrosion failures from uniform corrosion upon exposure to groundwater would be negligible because of the corrosion resistance of the oxide film on Zircaloy. Crevice corrosion would be extremely difficult to support because of the rapid consumption of residual oxygen within the container. We therefore expect that hydrogen-induced cracking is the most likely form of sheath failure. On the basis of available information, it is not possible to predict times to failure for this mechanism. No evidence of such failures or of Zircaloy corrosion by other processes has been found in studies of the durability of used fuel bundles over periods of up to 10 a in dry or moist air storage at 150°C (Wasywich 1993) or 25 a in wet storage (Wasywich 1992). Consequently, we expect minimum lifetimes of decades for Zircaloy sheath, with a reasonable likelihood that lifetimes could exceed thousands of years. Once fuel sheaths fail, the groundwaters could rapidly leach out the instant release fraction of a number of radionuclides, including ^{137}Cs, ^{135}Cs, ^{90}Sr, ^{129}I, ^{36}Cl, ^{99}Tc, ^{79}Se, ^{126}Sn, ^{14}C and ^{3}H.

In summary, it is expected that groundwater would be unlikely to enter the defective containers for hundreds of years, and, once in contact with the fuel sheaths, would be unlikely to contact the UO_2 fuel itself for an even longer period of time. This delayed contact of groundwater with the fuel would have a major impact on the rate of dissolution of the fuel matrix. As will be discussed in Chapter 5.3, the dissolution of the UO_2 matrix is sensitive to the beta/gamma dose rate, which drops by several orders of magnitude within the first 300 a to levels that have a negligible effect on the dissolution rate. Consequently, it is reasonable to expect that the actual dissolution rate of the fuel would be similar to that described in the previous case study (Johnson et al. 1994b) and that dissolution of the UO_2 matrix would make a small contribution to radionuclide release.

In spite of the arguments above that imply a delay of many hundreds of years before water would contact the UO_2 fuel, we have chosen to model radionuclide release based on water saturating the buffer and backfill and the pore space within the defective containers immediately upon emplacement, along with immediate failure of all fuel sheaths. Such assumptions undoubtedly lead to a great overestimate of the extent of fuel matrix dissolution, but they avoid the problem of mathematically modeling a complex scenario and assure that fuel matrix dissolution rates are modeled conservatively.

5.2 COMPOSITION AND DECAY CHARACTERISTICS OF CANDU FUEL

The isotopic composition of 37-element Bruce fuel bundles for a reference burnup of 685 GJ·(kg U)$^{-1}$ has been reported by Tait et al. (1989). This composition was used to define source terms for a previous case study (Johnson et al. 1994b), describing the performance of a reference disposal system for borehole emplacement of titanium containers. The average burnup of CANDU fuel has increased slightly to 720 GJ·(kg U)$^{-1}$ (Floyd et al. 1992). Based on this revised burnup, ORIGEN-S calculations have been

performed to define the decay heat and radionuclide inventories for the present case study.

In addition to revising the burnup, the pre-irradiation concentrations of various light elements have been examined and adjusted (Tait and Theaker 1996) to ensure that activation products arising from their presence during in-reactor irradiation are incorporated in assessment calculations. Of particular note is the inclusion of ^{36}Cl inventories in used fuel bundles, based on recent measurements (Johnson et al. 1995).

The present assessment focuses only on the group of radionuclides identified in a screening study (Goodwin et al. 1996a) that have the highest estimated dose consequence. Some calculations have also been performed for the actinides, as discussed in Chapter 6.5.4.

The inventories of radionuclides in used CANDU fuel for the revised reference burnup of 720 GJ·(kg U)$^{-1}$ are given in Table A-1 of Appendix A. As discussed in Chapter 6.5.1, of the total number of radionuclides, only sixteen fission and activation products and three actinide decay chains were examined in the present study.

5.3 THE DISSOLUTION OF USED FUEL

Extensive studies of the dissolution of used fuel in groundwater have established that radionuclide release is dominated by the rapid release of a small fraction of the inventory of a selected group of radionuclides, including ^{137}Cs, ^{129}I, ^{14}C and ^{36}Cl (Johnson et al. 1994b, 1995). The release of radionuclides contained within the fuel matrix , the dissolution rate of which depends on redox conditions, is a much less significant contributor to risk from disposal provided containment is provided for approximately 1000 a. This is because matrix dissolution is expected to be driven largely by the effects of beta and gamma radiolysis of water which declines by orders of magnitude within this time frame (see Chapter 5.3.2.9).

5.3.1 The Instant Release Fraction

The fraction of the radionucide inventory released rapidly upon exposure to water is referred to as the instant-release fraction (IRF). The IRF comprises release both from the fuel to sheath gap and from the grain boundaries in the fuel. The assumption that release from the grain boundaries is instantaneous is clearly conservative (Stroes-Gascoyne submitted). The IRF values for various important radionuclides adopted in the previous case study (Johnson et al. 1994b) are given in Table 5-1 along with their PDF characteristics. Table 5-1 also contains revised values based on new inventory and release measurements for some radionuclides and new data for others that were not included in the previous case study. The rationale for the PDF characteristics and the reasons for the revisions are discussed below. The revised values in Table 5-1 are used in the assessment calculations discussed in Chapter 6.

TABLE 5-1

PARAMETER DISTRIBUTION FUNCTIONS FOR

INSTANT-RELEASE FRACTIONS FOR SELECTED RADIONUCLIDES

Radio-nuclide	Case Study 1*				Present Study			
	μ (%)	σ (%)	Cutoffs (%)	Distri-bution	μ (%)	σ (%)	Cutoffs (%)	Distri-bution
^{135}Cs	8.1	1.0	1.2-25	normal	8.1	1.0	1.2-25	normal
^{137}Cs	-	-	-	-	8.1	1.0	1.2-25	normal
^{129}I	8.1	1.0	1.2-25	normal	8.1	1.0	1.2-25	normal
^{14}C	-	-	1-25	uniform	2.7	1.6	0.05-7.5	normal
^{36}Cl	-	-	-	-	8.1	1.0	1.2-25	normal
^{90}Sr	-	-	0.001-0.3	uniform	2.5	0.8	0.1-49	normal
^{99}Tc	6.0	1.0	-	normal	6.0	1.0	1.2-25	normal
^{3}H	-	-	30-40	uniform	-	-	10^{-3}-10^{-1}	uniform
^{79}Se	8.1	1.0	1.2-2.5	uniform	8.1	1.0	1.2-2.5	uniform
^{126}Sn	8.1	1.0	1.2-2.5	uniform	8.1	1.0	1.2-2.5	uniform

* Goodwin et al. 1994.

5.3.1.1 The IRF for ^{135}Cs and ^{137}Cs

The mean IRF value of 8.1% used in the previous case study for ^{135}Cs is also assumed for the present study for both ^{135}Cs and ^{137}Cs. Review by Stroes-Gascoyne (submitted) of a significant body of data indicates that this value appears to overestimate the IRF by a factor of up to 4.

5.3.1.2 The IRF for ^{14}C

The principal route of production of ^{14}C in used fuel is the $^{14}N(n,p)$ reaction. At the time of the previous assessment study (Goodwin et al. 1994), neither the inventory nor the release fraction of ^{14}C for CANDU fuel were well known. As a result, an IRF range of 1 to 25% was adopted (Johnson et al. 1994b) based on a limited number of measurements of release made for light water reactor (LWR) fuel. For CANDU fuel, Stroes-Gascoyne et al. (1994) reported a series of measurements of ^{14}C from both crushed fuel samples and from clad fuel element sections. No correlation of total ^{14}C release with fuel burnup or power rating was observed. The mean release from crushed fuel samples, based on measurements on fifteen fuel samples was 2.7%, with an estimated standard deviation of 1.6% (Table 5-1). These figures represent the total gap plus grain boundary inventory of ^{14}C in the fuel.

In addition to determining the instant release fraction, Stroes-Gascoyne et al. (1994) also measured the total ^{14}C inventory of a number of used fuel samples. These results showed that the total inventories were also significantly overestimated in the previous case study. This appears to have arisen because a nitrogen impurity level of 100 $\mu g \cdot g^{-1}$ was used for ORIGEN-S calculations that determined the ^{14}C inventories resulting from the $^{14}N(n,p)$ reaction (Tait et al. 1989). Measured ^{14}C inventories are more than ten times lower than those calculated using the 100 $\mu g \cdot g^{-1}$ assumed nitrogen impurity level, implying that the nitrogen impurity level in UO_2 fuel is much smaller. For the present study, the ^{14}C inventory in the reference fuel was revised accordingly.

5.3.1.3 The IRF for ^{36}Cl

Johnson et al. (1995) reported on the results of a radiological assessment of ^{36}Cl for the disposal of CANDU fuel. Several analyses of the Cl impurity levels in fuel indicate values of less than 5 ppm. Preliminary measurements of the release of ^{36}Cl from used fuel samples give fractional releases that are similar to those obtained for ^{129}I. For the purposes of the present study we have assumed that the IRF of ^{36}Cl is the same as that of ^{129}I (see Table 5-1) and that the inventory of ^{36}Cl in used fuel is 4.22×10^5 Bq $(kg\ U)^{-1}$, consistent with a pre-irradiation chlorine impurity level of 5 $\mu g \cdot g^{-1}$.

5.3.1.4 The IRF for ^{90}Sr

Stroes-Gascoyne (submitted) reviewed the data from a number of studies of dissolution of used CANDU fuel and concluded that the study of Johnson et al. (1994b) underestimated the IRF for ^{90}Sr. The previous range of 0.001 to 0.3% was largely based on leaching of fuel fragments; thus, the results represented release from the gap region. The more recent results of Stroes-Gascoyne (submitted) (μ = 2.5%, σ = 0.8%) represent releases from both the gap and grain boundary regions.

5.3.1.5 The IRF for ^{3}H

Johnson et al. (1994b) used an IRF range of 30 to 40% in a previous assessment study. As they reported, this was based on a misprint in the paper of Ohuchi and Sakurai (1988). The revised range of 10^{-3} to 10^{-1}% (Table 5-1) is based on the values reported by Goode and Cox (1970) and the corrected value from the study of Ohuchi and Sakurai (Kempe 1992).

5.3.1.6 Other IRF Values

IRF values for ^{99}Tc, ^{79}Se, ^{87}Rb, ^{126}Sn, ^{39}Ar, ^{42}Ar, Br, ^{40}K, ^{85}Kr and ^{81}Kr remain the same as those used in the previous case study (Johnson et al. 1994b).

5.3.2 Dissolution of the Used Fuel Matrix

5.3.2.1 Introduction

In the previous case study, the model for radionuclide release from used fuel consisted of two separate components: an instant-release model, in which the radionuclides trapped in the fuel cladding gap and in the grain boundaries are combined in a single term; and a matrix dissolution or congruent-release model, in which the remaining radionuclides are released at the same fractional rate as that at which the UO_2 fuel matrix dissolves (Johnson et al. 1994b). This matrix dissolution process was assumed to be limited by the solubility of UO_{2+x} (up to U_4O_9) and the diffusional transport of uranium away from the surface of the fuel. The solubility of uranium was calculated using a thermodynamic model by sampling from a range of concentrations of groundwater species and E_h (oxidation potential) and pH values. This model is applicable providing E_h is not positive to the U_4O_9/U_3O_7 boundary (Johnson et al. 1994b). However, any model of fuel dissolution within a prematurely failed container must take into account the fact that, initially, the redox conditions will be oxidizing , due to the presence of dissolved oxygen and the production of oxidizing radiolysis products. Under these conditions, oxidation beyond the U_4O_9/ U_3O_7 boundary is inevitable and the dissolution rate will be determined by kinetic factors.

The oxidants available to drive oxidative dissolution are: (i) dissolved oxygen trapped inside the container when the container is sealed; (ii) oxygen which diffuses into the container once it has failed, and (iii) the products of water radiolysis due to the decay of radionuclides within the fuel. Therefore, the fuel dissolution rate will be a function of the oxygen concentration and the combined effects of the radiation dose rates due to gamma, beta and alpha radiolysis.

5.3.2.2 Need for an Electrochemical Model

For a thermodynamically-based model to be appropriate, the composition of the fuel surface must be in equilibrium with the surrounding redox environment; i.e., the corrosion potential at the fuel surface must equal the redox potential in the surrounding environment (E_h). While evidence is available to indicate such a state may be achievable providing the surface of the fuel is not oxidized beyond $UO_{2.33}$ (Sunder et al. 1992a), there is a large body of evidence demonstrating that for more oxidizing conditions, the dissolution of fuel must be considered as an electrochemical process and therefore treated kinetically (Shoesmith and Sunder 1991). Under these conditions, a difference in potential, the driving force for the electrochemical dissolution process, exists across the dissolving solid-solution interface, Fig. 5.1. The dissolution reaction is now a coupled process involving the oxidative dissolution of the UO_2 and the reduction of the available oxidant.

$$UO_2 \rightarrow UO_2^{2+} + 2e^- \quad (5.1)$$

$$Ox + ne^- \rightarrow Red \quad (5.2)$$

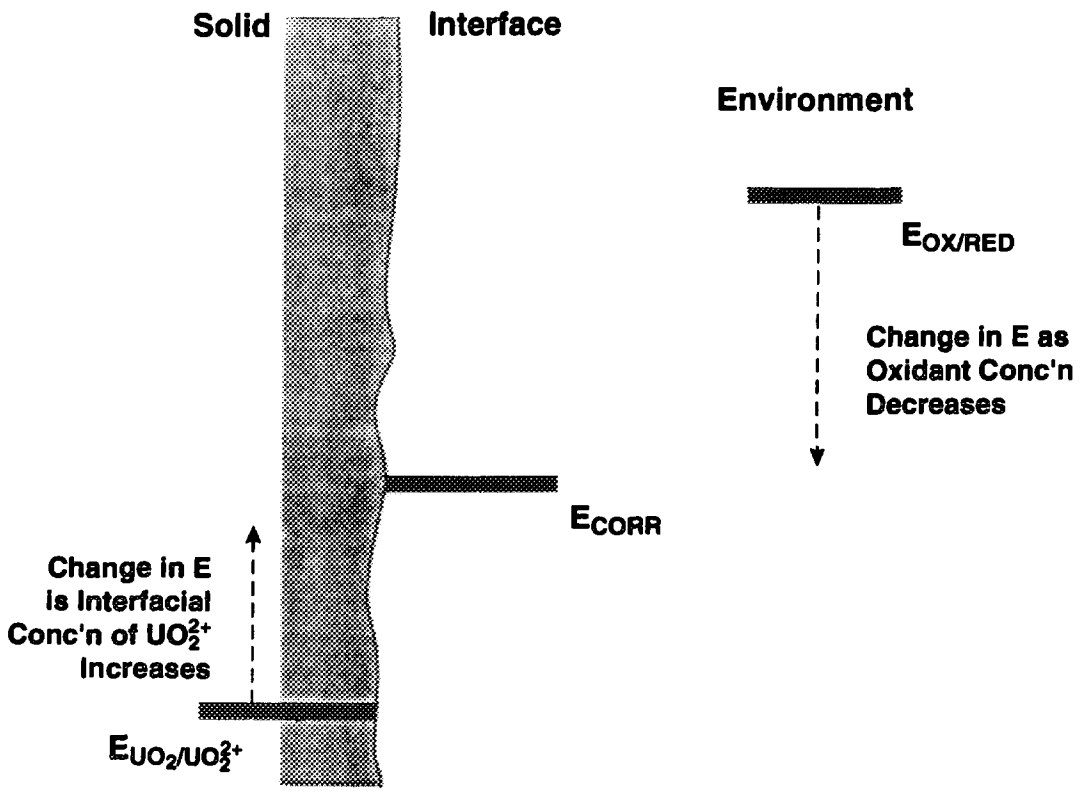

FIGURE 5.1: Relationship Between Potentials When the Surface of the Fuel Is Not in Equilibrium With Its Environment and an Electrochemical Driving Force for Corrosion Exists

Depending on the relative kinetics of these two half reactions, the dissolving surface will adopt a potential, known as the corrosion potential (E_{CORR}), between the equilibrium values for the two reactions. Under these conditions, dissolution will occur with both reactions away from equilibrium, and the fuel can be said to be undergoing corrosion. As corrosion proceeds, the increase in the surface concentration of dissolved uranium will lead to an increase in the equilibrium potential of the surface reaction, and the consumption of the oxidant will cause a fall in the value of E_h; i.e., the potential difference driving the corrosion reaction will decrease as oxidant is consumed. Consequently, if available oxidants are consumed, and not replenished, and corrosion products accumulate in the vicinity of the fuel surface, the need for a model based on the kinetics of the corrosion process will diminish. Providing the potential difference across the solid/solution interface is eventually reduced to zero, then the reapplication of the solubility-based, transport-limited dissolution model would be appropriate. The overall fuel reaction is appropriately considered as a corrosion reaction when $E_h > E_{CORR}$ but as a dissolution reaction when $E_h \sim E_{CORR}$. We conservatively assume that equilibrium would never be established and use a constant corrosion rate that would persist at long times.

5.3.2.3 Evolution of Redox Conditions in the Failed Container

The evolution in redox conditions within the container will be determined by the sum effects of oxygen consumption and the decay of radiation fields within the fuel. The oxygen concentration will decrease at a rate determined by its rate of consumption by the fuel and by other oxidizable materials in the container, especially the copper walls of the container itself. The gamma-, beta- and alpha-radiation fields at the surface of the fuel will decay with time at a rate determined by the nature of the fuel and its in-reactor history. Radiolytically produced oxidants could also be consumed by reaction with the copper container. For alpha and beta radiolysis, oxidants will be produced locally at the fuel surface and must be transported to the walls of the container. Garisto (1989) has calculated that >90% of the α-particle energy will be deposited within 20 μm of the fuel surface. For gamma radiolysis, the production of oxidants will be more widely dispersed and reaction with the container would be less affected by transport processes. As these oxidants are consumed, redox conditions will become controlled by a complex suite of redox reactions involving the products of corrosion processes [on copper (Cu^{I}/Cu^{II} species) and any iron-containing structural components (Fe^{II}/Fe^{III} species) within the container] and the oxidized products of fuel corrosion (U^{VI} species).

5.3.2.4 Procedure to Calculate Fuel Corrosion and Dissolution Rates as a Function of Evolving Redox Conditions

In this report we calculate the fuel corrosion rates based on our recently developed electrochemical model (Shoesmith and Sunder 1991). In this model the rates are predicted as a function of redox conditions by extrapolating steady-state electrochemical currents for the anodic dissolution of UO_2 to the corrosion potentials measured in solutions containing the various available oxidants. This procedure is illustrated schematically in Fig. 5.2, and leads to corrosion rates expressed as corrosion currents, which are easily converted to the units used in this report by the application of Faraday's law (Shoesmith et al. 1989). (A corrosion current of 1 $\mu A \cdot cm^{-2}$ is equivalent to a corrosion rate of 1.35 $mol \cdot m^{-2} \cdot a^{-1}$.).

These corrosion rates are then combined with a knowledge of the evolution of redox conditions within the container to predict the change in fuel corrosion rate with time. This requires that the rate of consumption of oxygen and the radiation decay profile as a function of age of the fuel be known. This procedure is illustrated schematically in Fig. 5.3. Once the electrochemical driving force disappears (Chapter 5.3), then the rate of corrosion will fall to a low value. Below this threshold value, indicated by the dashed line in Fig. 5.3C, the process can be considered as a dissolution reaction, and a solubility-based, transport-limited model would be as appropriate as an electrochemical one (Shoesmith and Sunder 1991), although we have adopted the more conservative approach by using a corrosion rate-based model.

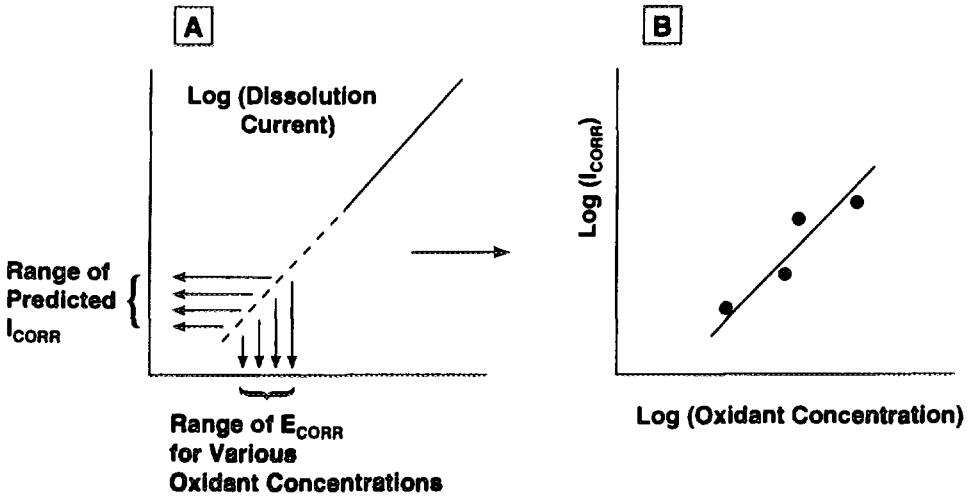

FIGURE 5.2: Illustration of the Procedure Used to Obtain Values of Corrosion Current (I_{CORR} ≡ Corrosion Rate) for the Corrosion of UO_2 Fuel: A - Tafel Relaltionship Relating Anodic Dissolution Currents to the Applied Electrochemical Potentials. The dashed section of the line shows the extrapolation of measured currents to the measured corrosion potential (E_{CORR}) to obtain the values of corrosion current plotted as a function of oxidant concentration shown in B.

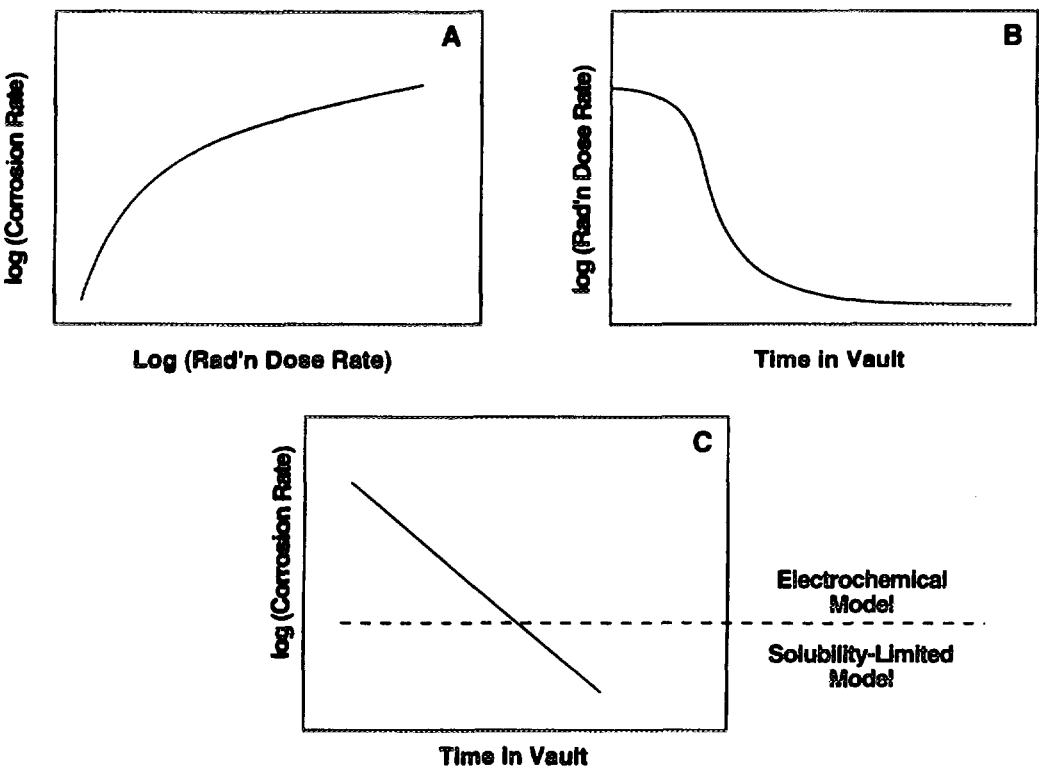

FIGURE 5.3: Illustration of the Procedure Used to Determine Fuel Corrosion Rates as a Function of Time in the Vault (C) from a Knowledge of Corrosion Rates as a Function of Radiation Dose Rate (A) (from the Procedure Illustrated in Fig. 5.2) and the Calculated Radiation Dose Rate Decay Curves (B) (Fig. 5.4)

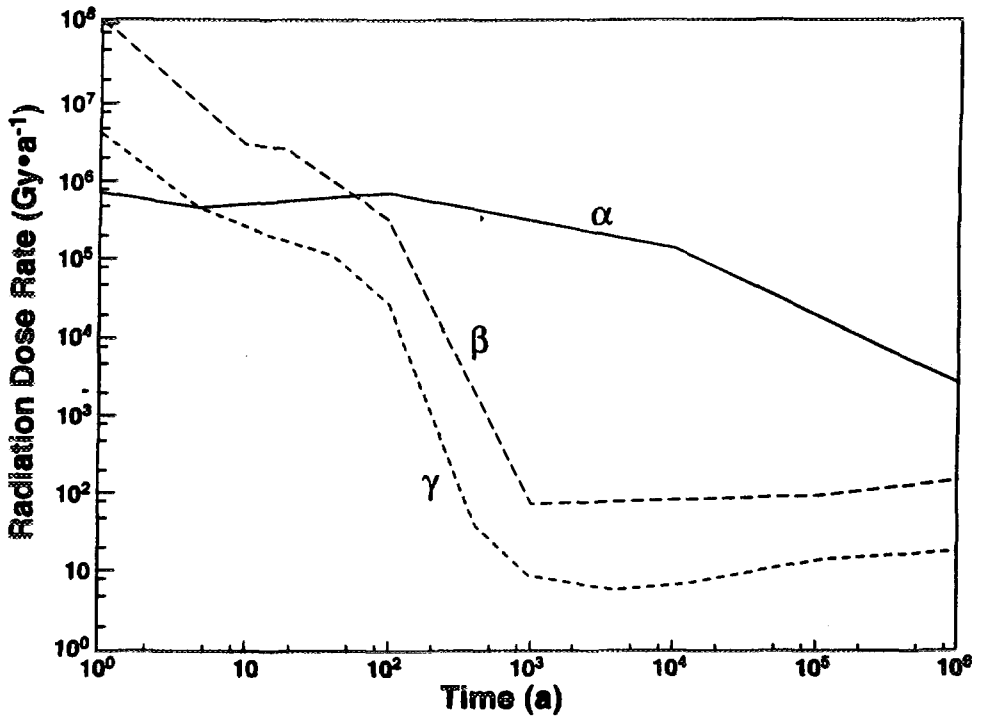

FIGURE 5.4: Decay Curves Calculated for Alpha, Beta and Gamma Radiation (Chapter 5.4.6 and Appendix G) for the Reference Spent Fuel

5.3.2.5 Corrosion Due to Dissolved Oxygen

The amount of oxygen available to cause corrosion of the fuel can be calculated from the volume of air originally trapped within the container. This assumes no more oxygen will diffuse into the container through the defect. This is a reasonable assumption for two reasons: (i) the defect will be small, and (ii) corrosion of the outside of the container will reduce the concentration of oxygen close to the container to a small value (Kolar and King 1996a). More detailed calculations using the data of these authors predict an oxygen concentration of $<3.5 \times 10^{-6}$ mol·L^{-1} will be achieved at a distance of 0.1 mm from the container surface only one month after emplacement in the vault. Consequently, the flux of oxygen into the container through the defect will be negligible.

The inventory of available oxygen has been calculated to be 1.01 mol based on the amount of oxygen trapped in the void volume (118 L) within the container (Appendix C). If all of this oxygen were to cause oxidation of the fuel according to the reaction

$$UO_2 + 1/2\ O_2 = UO_3 \qquad (5.3)$$

then the maximum amount of fuel oxidized would be about 2.016 mol (~544 g) of UO_2. Since a container will contain 72 bundles, each comprising 21.3 kg of fuel, this amounts to only a very small fraction (0.00035) of the 1534 kg of fuel. A possibility is that the oxygen

could be used in the dry oxidation of the fuel prior to wetting. This can be shown to be very slow (Appendix D) and would not significantly affect the subsequent rate of corrosion, according to the results of Gray and Thomas (1992, 1994).

While the available oxygen can only cause a limited amount of fuel oxidation, the presence of dissolved oxygen while radiation fields endure, especially gamma and beta, can lead to a significant increase in the rate of fuel corrosion due to the production of the oxidizing products of water radiolysis (Shoesmith and Sunder 1991). To determine whether this effect need be considered, we have calculated the relative rates of oxygen consumption by corrosion of the fuel and by corrosion of the copper container (Appendix E). This comparison shows that the rate of consumption by reaction with copper is ~ 10^4 times higher than that by reaction with UO_2 leading to the consumption of all the oxygen in the container in ~1.4 days (Appendix E).

Since the oxygen will be rapidly consumed by the copper container we need only consider corrosion driven by the radiolysis of deaerated solutions. This is a significant advantage since the predicted corrosion rates in deaerated solutions are much lower than in oxygenated solutions (Shoesmith and Sunder 1991).

5.3.2.6 Radiation Dose Rates for Used Fuel as a Function of Time

Despite the rapid consumption of dissolved oxygen by the corrosion of the container, the redox conditions of the groundwater initially contacting the used nuclear fuel will be modified due to the radiolysis of water by the ionizing radiation from the fuel. The radiolysis of water produces both molecular and radical oxidants and reductants (Spinks and Woods 1990), and the concentration of the different species formed depends on both the nature of the ionizing radiation and the dose rate to the water. It is well known that low linear energy transfer (LET) radiation (beta and gamma) produces more radicals (e.g., H , O_2^-) than high LET radiation (alpha) which results predominantly in the formation of molecular radiolysis products (e.g., H_2O_2). The consumption of these radiolytic oxidants by reaction with the container will not prevent radiolytically induced corrosion of the fuel. Due to the short range of alpha and beta particles in water, they will only produce oxidants close to the fuel surface, and the radicals (the main oxidants formed by gamma and beta radiolysis) are too reactive to escape the reaction layer at the fuel surface (Christensen and Sunder 1995).

To evaluate the effects of water radiolysis on the fuel corrosion rate, it is necessary to know the dose rate to the water in the container due to the different types of ionizing radiation. Here, we consider the effects of beta and gamma radiation together since both are low LET radiations likely to affect corrosion at relatively short times compared to alpha radiation. We have calculated alpha, beta and gamma dose rates in water in contact with the reference used fuel (burnup of 720 GJ·(kg U)$^{-1}$) (Sunder 1995). Figure 5.4 shows the various dose rates in water, for a *single* fuel bundle, as a function of time. The procedure and data used to obtain these results are described in Appendix F. Since alpha and beta radiations produce oxidants only in the vicinity of the surface from which they are emitted, their dose rates are independent of the number of fuel bundles in the container. However, for gamma radiation the irradiation of

adjacent surfaces will occur and the dose rate to the water at the fuel surface will depend both on the number of fuel bundles in the container and on their placement geometry. We estimate that the average gamma dose rate in the container will be about 4 to 7 times that calculated for a single bundle in Fig. 5.4 (Appendix G).

5.3.2.7 Corrosion Rates Used in the Model

Since the oxygen within the container will be consumed rapidly, only the corrosion rates due to the radiolysis of deaerated solutions need be used to predict radionuclide release rates. Figure 5.5 shows these rates as a function of gamma and alpha dose rates at room temperature (22°C). The data used in these figures were recorded in 0.1 mol·L^{-1} $NaClO_4$ (pH = 9.5), a solution typical of the non-complexing groundwaters expected under waste vault conditions, and have been

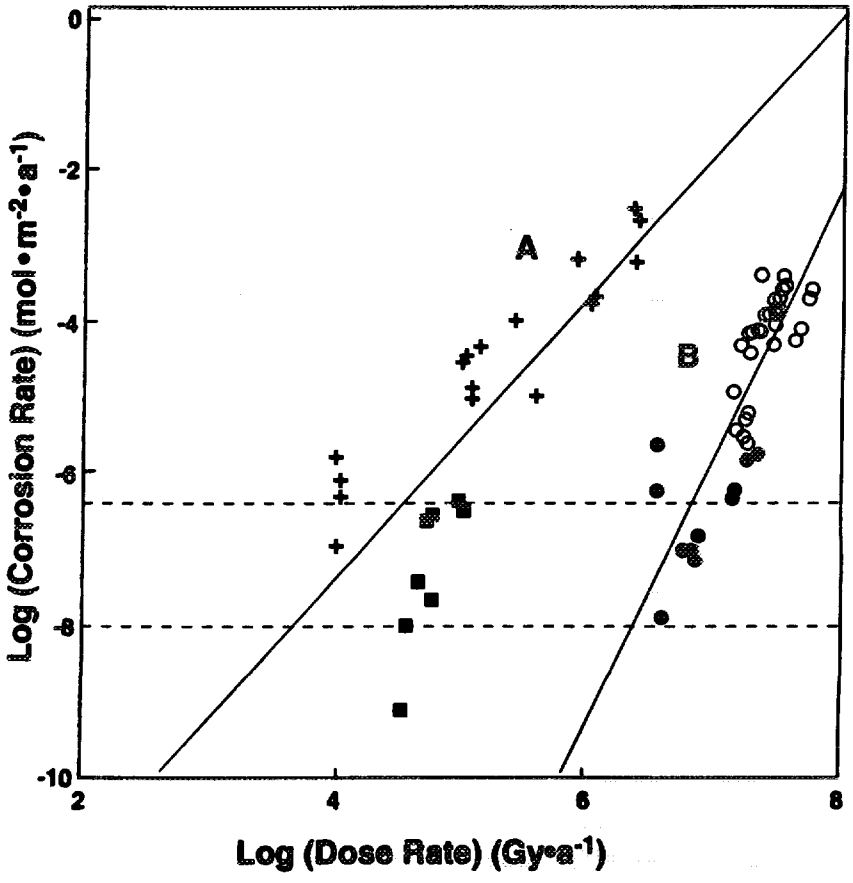

FIGURE 5.5: Fuel Corrosion Rates Predicted for Neutral Non-complexing Solutions (0.1 mol·L^{-1} $NaClO_4$; pH = 9.5) at Room Temperature (~22°C) Using the Procedure Outlined in Fig. 5.2. The results for gamma radiolysis (line A) are from Shoesmith and Sunder (1991) and those for alpha radiolysis (line B) from Sunder et al. (1996). Values plotted with closed symbols are eventually not used in calculations (Appendix I). The upper and lower horizontal lines show the predicted corrosion rates for corrosion potentials of -100 mV and -200 mV (vs. SCE), respectively.

published elsewhere (Shoesmith and Sunder 1991, Sunder et al. 1995). In the calculations which follow, the corrosion rates due to beta radiolysis are assumed to be the same as those due to gamma radiolysis since both are low LET radiations (Chapter 5.3.2.6). The rates for alpha radiolysis shown in Fig. 5.5 are from experiments carried out in crevices 30 μm in width and are, therefore, representative of the behaviour expected in narrow cracks or at the fuel/cladding interface. A more extensive discussion of the application of the electrochemical model to obtain the rates in Fig. 5.5 and of their reliability is given in Appendix H.

The upper horizontal dashed line in Fig. 5.5 represents the corrosion rate (3.52×10^{-7} mol·m^{-2}·a^{-1}) predicted by our model for a corrosion potential of -100 mV (vs. SCE), the potential at which our electrochemistry/XPS results tell us the surface composition is $UO_{2.33}$ (Shoesmith and Sunder 1992, Sunder et al. 1992b). Above this value, the $UO_{2.33}$ film achieves a constant thickness and, under steady-state conditions, the rate of its formation is balanced by the rate of its oxidative dissolution; i.e., steady-state corrosion conditions are achieved (Shoesmith et al. 1996). Below this potential, the degree of oxidation of the surface is determined by the potential achieved, and a state of redox equilibrium appears to prevail (Sunder et al. 1992a). Consequently, we have taken this value as a threshold above which the application of a corrosion model, as opposed to a transport-limited solubility-based model, is essential (Shoesmith and Sunder 1991). For values below this threshold the process should be considered as a dissolution reaction. The lower horizontal line represents the corrosion rate (3.79×10^{-9} mol·m^{-2}·a^{-1}) predicted by our model for a corrosion potential of -200 mV (vs. SCE), the highest value observed in deaerated solutions. Inevitably, corrosion potentials are <-200 mV in deaerated solutions making the value at -200 mV a conservative estimate of the maximum rate of dissolution under deaerated conditions in the absence of any radiation field. We consider this rate to be the lower limit of applicability of our corrosion model. Consequently, the need for a corrosion model disappears once the corrosion rate falls to a value somewhere in the range between these bounding values. In our calculations, once this occurs, we assume that further dissolution of the fuel will continue indefinitely at this constant threshold rate. This threshold value is chosen assuming a loguniform distribution of possible values within this range.

An alternative approach once the redox conditions have become sufficiently "non-oxidizing", and a corrosion model is no longer essential, would be to return to the transport-limited, solubility-based model used in the previous case study (Johnson et al. 1994b). However the transition from a kinetic to a thermodynamically based approach is complicated and the effort necessary to implement such a transition hard to justify. This is because the corrosion product, U^{VI} (in the form of hydrolyzed UO_2^{2+} species) is not inert but can become involved in redox reactions with various components of the system, particularly the copper container and the products of its corrosion, and any iron/iron oxides. This will lead to a period when the redox potential of the system is buffered by a complex set of reactions, culminating eventually in conditions for which the application of the transport-limited, solubility-based model is appropriate. In the absence of a much more extensive kinetic database, it is impossible to calculate how long this period of redox adjustment would take.

5.3.2.8 The Effect of Temperature on the Corrosion Rate

The corrosion rates plotted in Fig. 5.5 were measured at room temperature (~22°C) whereas the temperature in the container will be above this value for nearly 10^5 a (Appendix I). Based on the calculations of Wai and Tsai (1995) and Baumgartner (1995), we have taken the temperature in the container to be a conservatively constant 100°C when calculating the corrosion rate of the fuel driven by the radiolysis of water. However, by the time fuel corrosion rates fall to values below our threshold value (Chapter 5.3.2.7), which is expected to occur after a few hundred years, the temperature will have fallen to between 60°C and 50°C. Consequently, we have taken a temperature of 55°C to calculate the threshold dissolution rate.

A value of 33.45 $kJ \cdot mol^{-1}$ has been chosen for the activation energy for the dissolution rate of used fuel based on our review of published activation energies (Sunder and Shoesmith 1991) and some recently reported measurements (Shoesmith et al. 1995b). This value is the largest reported for non-complexing solutions (i.e., in solutions containing $<10^{-3}$ $mol \cdot L^{1}$ total carbonate) and is appropriate for two reasons: (i) the groundwaters which will flood the container are not expected to contain significant concentrations of complexing agents such as carbonate; and (ii) the electrochemical dissolution currents and corrosion potentials upon which our model is based were measured in such non-complexing solutions. A more extensive justification for choosing this activation energy is given in Appendix I.

5.3.2.9 Calculation of Fuel Corrosion Rates and the Fraction of Fuel Dissolved in a Failed Waste Container

Figures 5.6A and 5.6B show the corrosion rates used in our calculations plotted logarithmically as a function of radiation dose rate for a temperature of 100°C. The reasons for using only the limited data sets plotted in Figs. 5.6A and 5.6B in our calculations are discussed in Appendix H. Also shown on these figures are the ranges of gamma, beta and alpha dose rates expected over the first 1000 a assuming the fuel is 10 a old when emplaced in the vault. For alpha radiolysis, to predict used-fuel behaviour it is necessary to extrapolate to dose rates lower than those used in experimental measurements, Fig 5.6A. For gamma/beta radiolysis, our experimental data cover the high dose rate range expected at short times and extrapolation is only required for the lower dose rates prevailing at longer times. The chosen fits to these data, and the errors associated with their extrapolation are discussed in Appendix J.

The corrosion rate of fuel inside an instantaneously failed container can now be calculated by the procedure outlined in Fig. 5.3 using the fitted relationships for fuel corrosion rates as a function of radiation dose rate (Fig. 5.6) and the calculated decay curves for alpha, beta and gamma radiation (Fig. 5.4).

The total fuel corrosion rate per unit area of the corroding surface, c(t) ($mol \cdot m^2 \cdot a^{-1}$), is given by the sum of the rates due to each radiation source and the threshold dissolution rate value (R_c),

$$c(t) = 10^{b_\alpha} \{\alpha(t+t_c)\}^{a_\alpha} + 10^{b_\beta} \{\beta(t+t_c)\}^{a_\beta} + 10^{b_\gamma} \{F\gamma(t+t_c)\}^{a_\gamma} + R_c \quad (5.4)$$

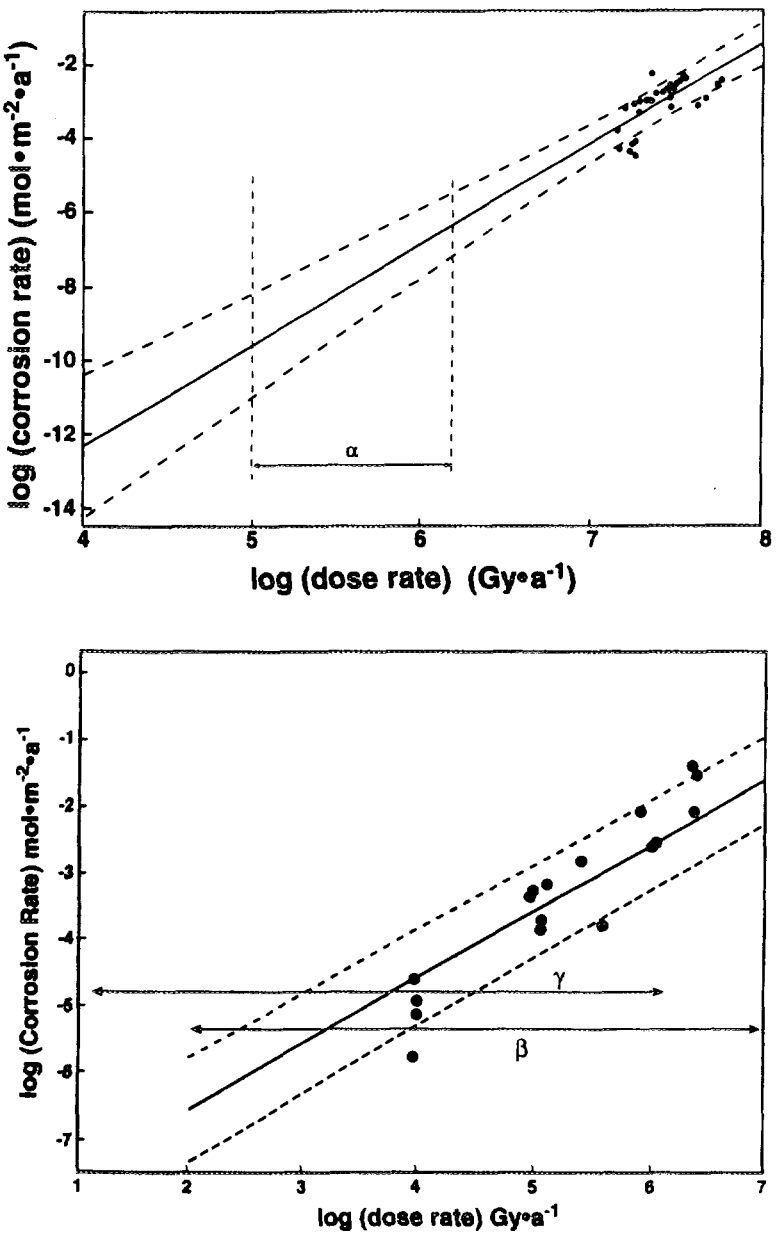

FIGURE 5.6: Fuel Corrosion Rates Used in Predictions (Calculated for 100°C) Plotted Logarithmically as a Function of Radiation Dose Rate: A - Rates Used for Alpha Radiolysis; B - Rates Used for Gamma/Beta Radiolysis. The solid lines are the fitted lines and the dashed lines the $\pm 1\sigma$ values of this fit. The fitted parameters are given in Table 5-2. The horizontal lines show the range of dose rates between fuel ages of 10 a and 1000 a for alpha (α), beta (β) and gamma (γ) radiation, respectively.

TABLE 5-2

PARAMETER VALUES USED IN CALCULATING

USED FUEL DISSOLUTION RATES IN A FAILED CONTAINER

Parameter	Symbol	Units	Value	Distribution Type	Upper Bound	Lower Bound	Reference
Mass of fuel per container	m	kg	1533.6	constant			
Area of fuel per container	A	m^2	306.72	constant			Appendix E
Maximum temperature	T	°C	100	constant			Appendix I
Chemical diss'n rate at 55°C	R_c	mol m^{-2} a^{-1}	2.20×10^{-7}	loguniform	1.39×10^{-6}	3.47×10^{-8}	
Alpha fuel dose exponent	a_α		2.7172	constant			Equation 5.4
Alpha fuel rate convert factor	b_α		-23.1434	constant			Equation 5.4
Beta fuel rate convert factor	b_β		-8.5426	constant			Equation 5.4
Gamma fuel rate convert factor	b_γ		-8.5426	constant			Equation 5.4
Alpha dose vary factor			1.00	triangular	1.66	0.77	Appendix F
Beta dose vary factor			1.00	triangular	1.41	0.75	Appendix F
Gamma dose vary factor			5.5	uniform	7.0	4.0	Appendix G

where $\alpha(t)$, $\beta(t)$ and $\gamma(t)$ are the alpha, beta and gamma dose rates to water at the surface of a single fuel bundle, and F is the factor for gamma radiation to convert the dose rate for a single fuel bundle to that expected in the container (Appendix G); $t = 0$ corresponds to the time at which water enters the container and t_c is the time since discharge of the fuel bundle from the reactor. The terms a_α, a_β, a_γ and b_α, b_β, b_γ are the fitting parameters for the slopes and intercepts, respectively, of the lines plotted through the data in Fig. 5.6. The procedure used to fit the data to obtain values of a and b is described in Appendix J.

The range of values for R_c is shown in Fig. 5.7 and discussed in Chapter 5.3.2.7. In these calculations we used a conservative assumption of constant fuel surface area, which is a good approximation until most of the fuel has dissolved. The values of parameter and the types of distribution used to calculate the rate are given in Table 5-2.

The corrosion rate, c(t), (from Eq. (5.4)) for ten-year old fuel ($t_c = 10$ a), the range of values of R_c and the breakdown into contributions from alpha, beta and gamma radiolysis is shown in Fig. 5.7. Figure 5.8 shows the fraction of used fuel dissolved for the median values of

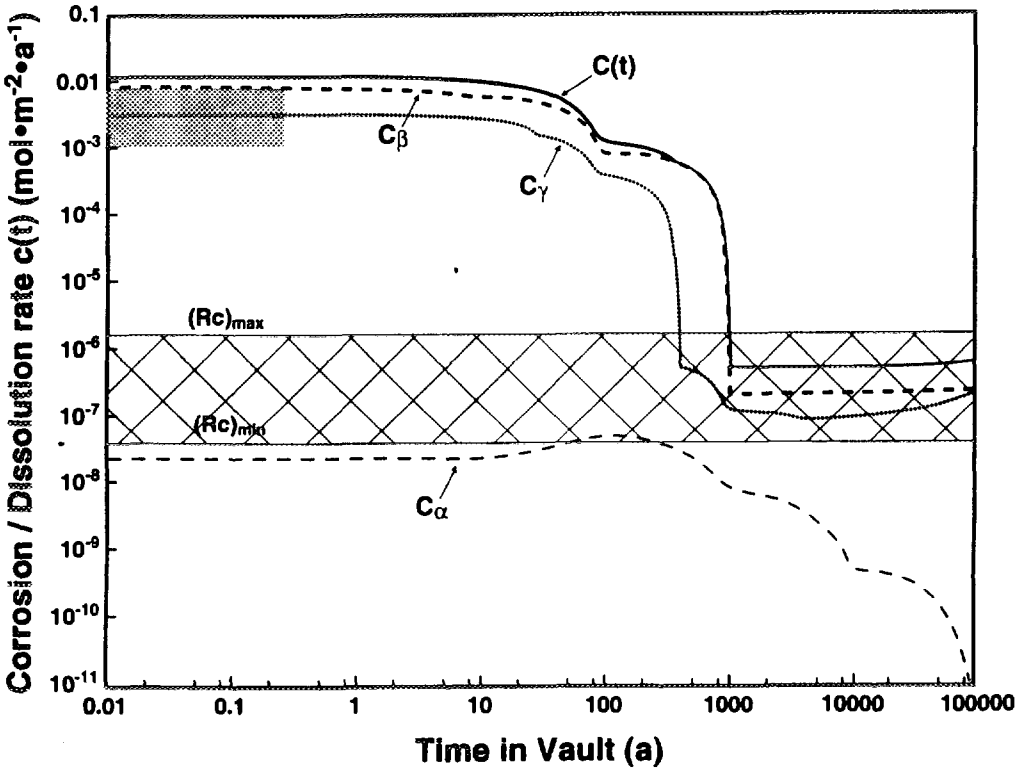

FIGURE 5.7: Predicted Corrosion Rates for the Reference Fuel (Assuming a Constant Vault Temperature of 100°C) as a Function of Time of Emplacement in the Vault Assuming the Container Fails at t = 0: (————) total (c(t)); (- - - - -) rate due to β radiolysis (c_β); (·····) rate due to gamma radiolysis (c_γ); (— — —) rate due to alpha radiolysis (c_α). The lower shaded area is the range of threshold dissolution rate values (Chapter 5.3.2.7). The upper shaded area is the range of measured fuel corrosion rates (Chapter 5.4.9 and Table 5-3).

parameters (solid line) as well as for a number of other example simulations. Figure 5.9 shows the distribution of fuel fractions dissolved after 10^4 a of emplacement in the vault determined from ~250 simulations with the used fuel dissolution model.

According to the predictions of Fig. 5.7 , corrosion due to alpha radiolysis will be insignificant since the rate is always less than the range of threshold values for the solubility-limited dissolution rate, shown as the lower shaded area in the figure. By contrast, corrosion rates due to beta and gamma radiolysis are predicted to exceed the threshold value for ~1000 a, due predominantly to the high dose rates for beta radiation for this period (Fig. 5.4). If we were to consider gamma radiation only, then corrosion rates would fall below the threshold value in 200 to 300 a, consistent with our previous calculations for the effects of gamma radiation only (Shoesmith and Sunder 1991).

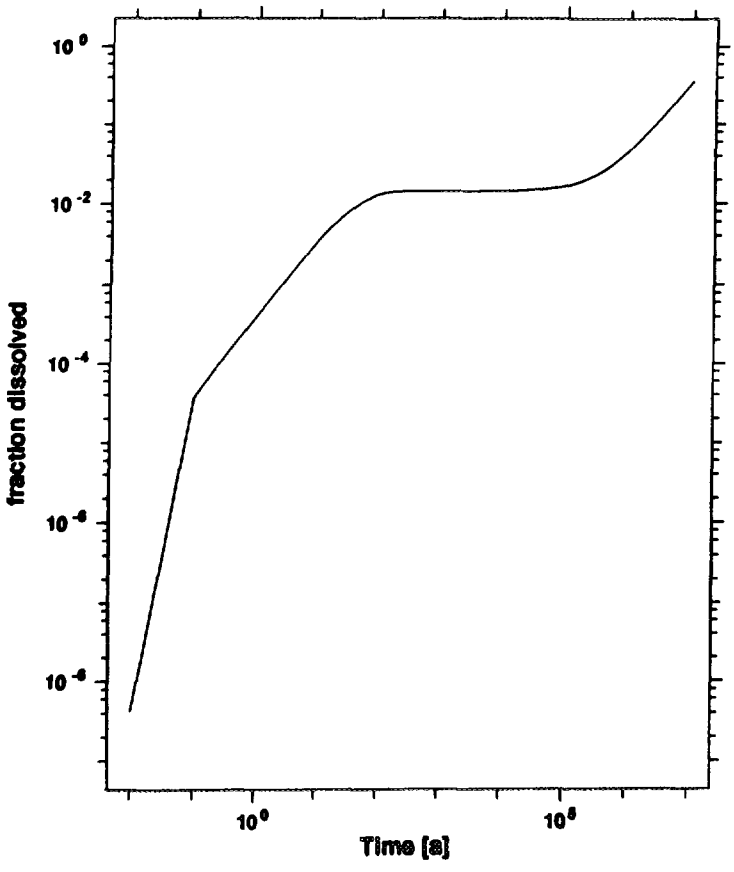

FIGURE 5.8: Fraction of Used Fuel Dissolved for the Median Values of Parameters (from Table 5-2)

Also plotted in Fig. 5.7 is a shaded area (the upper area) showing the experimental values observed for the corrosion of used fuel with a burnup higher than that for the reference fuel used in our calculations. The upper bound of this area is the rate at 100°C ($9.4 \pm (4.8)$ x 10^{-3} mol·m^{-2}·a^{-1}) calculated from the rate measured at 22°C in neutral non-complexing solution ($0.54 \pm (0.28)$ x 10^{-3} mol·m^{-2}·a^{-1}) using our activation energy of 33.5 kJ·mol^{-1} (Shoesmith et al. 1995b). The lower bound is for a rate one order of magnitude lower. This range represents the uncertainties encountered in measuring the surface area of spent fuel specimens (Shoesmith et al. 1995b).

The characteristics of used fuel used in the dissolution rate experiments have been compared to those of the reference used fuel considered in our calculations (Table 5-3). Of greatest importance when attempting to predict the corrosion rate is the sum of the beta and gamma dose rates since it is the oxidants produced by these two processes which have the major influence (the effect of alpha radiolysis is negligible). Consequently, we would predict approximately the same corrosion rate for both fuels since this sum is nearly the same for both fuels (Table 5-3). The predicted and experimental values are surprisingly close though this may be fortuitous, since the experimental rate chosen for the comparison is the upper limit of the range of possible rates.

TABLE 5-3

CHARACTERISTICS OF THE REFERENCE USED FUEL USED FOR THIS ASSESSMENT AND THAT USED IN EXPERIMENTS

Parameter	Reference Used Fuel	Experimental Used Fuel
Age (a)	10	11
Burnup ($GJ \cdot (kg\ U)^{-1}$)	720	~1110
Dose Rate *($Gy \cdot a^{-1}$)		
alpha	5.2×10^5	9.39×10^5
beta	3.3×10^6	4.65×10^6
gamma	1.4×10^6	1.2×10^4
Experimental Corrosion Rate ($mol \cdot m^{-2} \cdot a^{-1}$)	-	$9.4 \pm (4.8) \times 10^{-3}$
Predicted Corrosion Rate ($mol \cdot m^{-2} \cdot a^{-1}$)	13.42×10^{-3}	13.25×10^{-3}

* Includes the factor F (~5.5) to calculate the gamma dose rate in the array of fuel bundles within the container.

If we were to accept a larger value for the surface area of fuel used in dissolution experiments then a lower corrosion rate (within the range shown in Fig. 5.7) would be obtained, and the margin of overprediction by our model would be greater.

5.3.2.10 Reliability of Predicted Corrosion Rates

A number of features of the calculations of corrosion rate require discussion. The prediction that corrosion due to alpha radiolysis is insignificant can be attributed to two factors: (i) the corrosion rate strongly depends on alpha dose rate (the slope (a) of the fitted line in Fig. 5.6a is 2.7 (Table 5-2)); and (ii) the alpha dose rates for the reference used fuel are 1 to 2 orders of magnitude less than those used experimentally to determine corrosion rates (Fig. 5.6). This large slope of 2.7 is not consistent with a simple dependence of corrosion rate on the concentration of oxidants produced by alpha radiolysis. A possibility is that the dependence of corrosion potential on alpha source strength on which these predictions are based is determined by a combination of both corrosion of the fuel and decomposition of the radiolytically produced hydrogen peroxide. If the latter process becomes more dominant at lower source strengths then we would observe a dramatic decrease in corrosion rate as the source strength decreases. This situation has been discussed in more detail elsewhere (Shoesmith et al. 1985, Sunder et al. 1987, Sunder et al. 1995) but a thorough understanding remains to be developed.

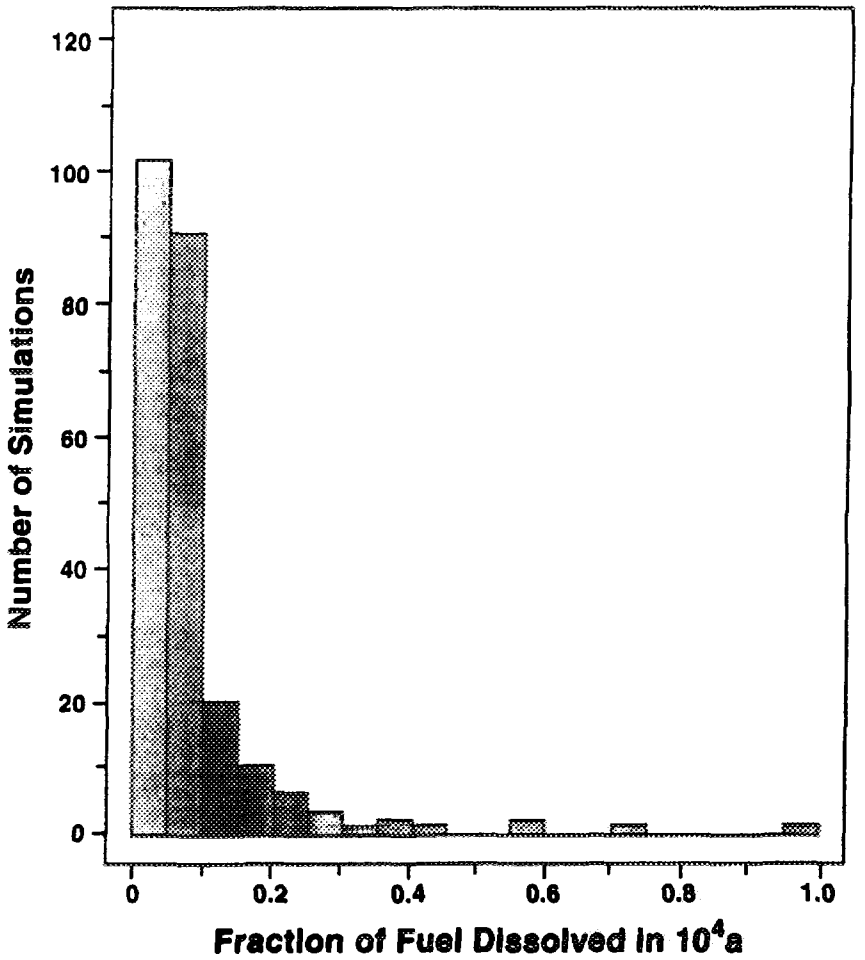

FIGURE 5.9: Distribution of Fuel Fraction Dissolved after 10^4 a in the Vault

Experimental measurements to determine corrosion rates due to alpha radiolysis were made in a thin crevice (Chapter 5.4.7) (Sunder et al. 1995) making the concentration of radiolytic oxidants at the fuel surface dependent on the balance between their radiolytic production and their rate of loss by diffusive flux out of the crevice. Intuitively, we would expect this surface concentration to be larger the narrower the width of the crevice since this would reduce their rate of diffusive loss. Consequently, our predictions could underestimate the effects of alpha radiolysis in tight wet cracks in the fuel but would overestimate their effects on open surfaces with unconfined geometry.

While the agreement between predicted and measured fuel dissolution rates is gratifying, this may be partly fortuitous for a number of reasons. When applying our electrochemical model we chose to extrapolate the highest values of anodic dissolution current recorded. The experimental data show that a less conservatively chosen extrapolation (Fig. H-1, Appendix H) could yield corrosion rate values one to two orders of magnitude lower than those used in our calculations. This, coupled with the uncertainties involved in defining the corrosion rate of used fuel (due to

the difficulties in measuring/estimating surface areas) shows that considerable uncertainties still exist in predicted corrosion rate values.

Despite these uncertainties, we have good grounds to believe that our predictions do not underestimate fuel corrosion rates. A major problem in defining both electrochemical dissolution currents and used fuel corrosion rates in neutral non-complexing solutions is the unpredictable accumulation of corrosion products (e.g., $UO_3 \cdot 2H_2O$) on the dissolving/corroding surface, and the extent to which they block the corrosion process. The irreproducibility of this process is thought to account for the scatter in current values in Fig. H-1 (Sunder et al. 1996) and for the problems encountered when trying to perform corrosion measurements on actual used fuel specimens (Shoesmith et al. 1996). By extrapolating line 1 in Fig H-1 to predict corrosion rates we have tried to avoid the effects of blockage of the corrosion process by deposited corrosion products.

5.4 RADIONUCLIDE SOLUBILITIES

Precipitation of some radionuclides within the disposal container is accounted for in the vault model in the same fashion as in the previous case study (Johnson et al. 1994b), with the following modifications:

(1) Thermodynamic data for Tc have been modified based on recent measurements (Lemire and Jobe 1996).

(2) The solubility of U is calculated in the same fashion as Th, Pu, Np and Tc, by sampling over the groundwater parameter ranges given in Table 3-2. Unlike the previous case study, U concentrations do not affect the dissolution rate of the fuel. This is because the matrix dissolution rate in the present study is based on corrosion rates rather than on equilibrium solubility of U coupled to U mass transport.

(3) The E_h range sampled varies from 0.20 (magnetite/hematite) to 0.47 V (magnetite/goethite) at pH = 0. This range of potentials is expected to reasonably represent the environment within a disposal container that contains large quantities of stainless or carbon steel. Conditions would likely evolve from the higher end of this range to 0.20 V or less as all O_2 was consumed by corrosion of Cu and steel.

(4) The solubility of Zr is calculated as described in Appendix A of Johnson et al. (1995).

(5) For a number of radionuclides, concentration limits are determined by fixed solubility limits. For radionuclides expected to be highly soluble (including I, Cs and Rn), and for those for which the chemistry in natural systems is complex to predict or is not well understood (including Ca, Cd

and Po), the limiting solubility was fixed conservatively at a very high value, 2 $mol \cdot L^{-1}$, to ensure that the precipitation which could delay transport would not occur. On the basis of thermodynamic stabilities and observed behaviour in natural and experimental systems, many of the remaining radionuclides are expected to have limited, though measurable, solubilities. For each of these radionuclides, a fixed solubility limit is specified separately on the basis of its known and modeled chemical behaviour over the range of expected vault conditions. Where thermodynamic data are available, solubility estimates first were calculated by a set of scoping calculations using the geochemical modeling code HARPHRQ (Brown et al. 1991) and the HATCHES thermodynamic database (Cross and Ewart 1990) to determine the concentration of the radionuclide in equilibrium with groundwater for a range of pH and redox conditions. The calculated concentrations then were compared with tabulated estimates of concentration limits at similar geochemical conditions (Berner 1995, SKB 1992) and were revised upwards where more conservative estimates were indicated. The results are summarized in Table 5-4.

Several redox-sensitive radionuclides are expected to be largely insoluble under reducing conditions in a vault, but different solubility-limiting solid phases could become stable under oxidizing conditions. This would result in increased aqueous concentrations. For simplicity, the maximum solubility estimates for the elements Pd, Pa, Sb and Se were based only on oxidizing conditions. This is a conservative assumption because concentrations would be much less under reducing conditions.

5.5 MICROBIAL EFFECTS ON USED FUEL DISSOLUTION

Under oxidizing conditions, microbially mediated oxidation of UO_2 to U(VI) by Fe(III) can occur at pH values below 2.5 (Tuovinen 1990). The bacterial creation of acidity under disposal vault conditions could only arise from the oxidation of pyrite (FeS_2). Although pyrite is present in granite in small quantities (<0.1 wt.%) and could become oxidized during the aerated phase of the vault, the small amount of acid produced by its oxidation would be rapidly neutralized by the clays used in the backfill and buffer. Thus, although Fe(III) oxides might be expected to form when aerated water enters the defective container, the pH would be in the neutral region. Consumption of oxygen within the container as a result of corrosion of copper (see Appendix E) and steel would occur rapidly at their expected corrosion rates. In addition, the presence of an intense γ-radiation field within a defective disposal container shortly after emplacement would essentially eliminate microbial activity near or on the fuel while radiation fields remain high (Stroes-Gascoyne et al. 1995). Once reducing conditions are attained, oxygen is no longer available for the microbially mediated oxidation of UO_2 to U(VI).

TABLE 5-4

SOLUBILITIES OF RADIONUCLIDES USED IN THE VAULT MODEL

	Solubility	Berner (1995) (pH 9, E_h -400 mV)		Comments
	($mol \cdot L^{-1}$)	"Realistic" ($mol \cdot L^{-1}$)	"Conservative" ($mol \cdot L^{-1}$)	
Np		1×10^{-10}	1×10^{-8}	calculated as described
Pu		1×10^{-8}	1×10^{-6}	by Johnson et al. (1994b)
Tc		1×10^{-7}	---	
Th		5×10^{-9}	1×10^{-7}	
U				
Ac	2	not.lim.	not lim.	unrevised[¥]
Be	2	not lim.	not lim.	unrevised
Ca	2	not lim.	not lim.	unrevised
Cd	2	not lim.	not lim.	unrevised
Cs	2	not lim.	not lim.	unrevised
H	2	not lim.	not lim.	unrevised
Hf	2	not lim.	not lim.	unrevised
I	2	not lim.	not lim.	unrevised
K	2	not lim.	not lim.	unrevised
Mo	2	not lim.	not lim.	unrevised
Ni	2	not lim.	not lim.	unrevised
Po	2	not lim.	not lim.	unrevised
Rb	2	not lim.	not lim.	unrevised
Re	2	not lim.	not lim.	unrevised
Rn	2	not lim.	not lim.	unrevised
Sr	2	not lim.	not lim.	unrevised
Am	1×10^{-5}	1×10^{-5}	1×10^{-5}	
Be	4×10^{-5}	4×10^{-6}	4×10^{-6}	
C 14	5×10^{-2}	5×10^{-2}	5×10^{-3}	calcite precipitation
Cm	1×10^{-5}	1×10^{-5}	1×10^{-5}	
Nb	1×10^{-3}	1×10^{-3}	1×10^{-3}	
Pb	1×10^{-5}	1×10^{-5}	1×10^{-5}	
Ra	1×10^{-5}	1×10^{-5}	1×10^{-9}	co-precip'n with calcite
REE's*	1×10^{-4}	1×10^{-4}	1×10^{-5}	
Si	5×10^{-2}	5×10^{-2}		SiO_2 am
Sn	1×10^{-4}	1×10^{-4}	11×10^{-5}	
Zr	1×10^{-3}			Johnson et al. (1995)
Pd	2×10^{-6}	1×10^{-11}	2×10^{-6}	
Pa	1×10^{-6}	1×10^{-10}	1×10^{-7}	
Sb	2	6×10^{-5}	6×10^{-5}	
Se	2	1×10^{-4}	---	

[¥] unrevised from values used in Johnson et al. (1994b)

* = La, Ce, Pr, Nd, Pm, Sm, Eu, Gd, Dy

5.6 RADIONUCLIDE RELEASE FROM THE ZIRCALOY SHEATH

The corrosion behaviour of Zircaloy has been discussed by Johnson et al. (1994b). It is expected that activation products in the Zircaloy would be uniformly distributed; thus they could only be released by congruent dissolution. The adherence of the corrosion product to the zirconium metal suggests that radionuclides would be incorporated into the oxide film as corrosion progresses. As a result, they would only be released when the oxide dissolves.

In the vault model, the rate of dissolution of the Zircaloy is determined by the solubility of Zr and the rate of diffusion of dissolved Zr from the container. The solubility of Zr is sampled from a lognormal distribution with a geometric mean of 1.8×10^{-9} mol·L^{-1} and a maximum of 10^{-3} mol·L^{-1} as described in Johnson et al. (1995). An alternative approach would be to use a corrosion rate model, conservatively assuming that radionuclides are released at the rate of corrosion. For a conservatively estimated corrosion rate of 0.01 μm·a^{-1}, the fuel sheath would release all its inventory of ^{36}Cl and ^{14}C in several tens of thousands of years, considerably faster than with the solubility model. Nonetheless, this would make very little difference to the dose estimate results presented in Chapter 6.5. This is because the total inventory of ^{36}Cl in the fuel is ~8 times larger than in the sheath and the total release of ^{36}Cl in 10^4 a from the fuel is typically 10 to 15% of the total inventory. For ^{14}C, total releases would likely be slightly larger with a corrosion rate model, but the overall impact would be small because ^{14}C is a small contributor to overall dose.

5.7 SUMMARY OF THE FUEL DISSOLUTION MODEL

In the present assessment, the only container failures expected to occur are those arising from manufacturing defects. The model developed for radionuclide release from used fuel describes two processes occurring in such containers. The first involves instant release of a fraction of the inventory of some radionuclides. This model remains the same as described in detail in the previous case study (Johnson et al. 1994b), and only data changes were made where new information was available (see Table 5-1).

The second process, which applies to both the used fuel matrix and the Zircaloy sheath, involves congruent release of radionuclides. For the dissolution of the fuel matrix, the possibility of groundwater contacting the fuel shortly after container emplacement leads to the need for a kinetic dissolution model that takes into account the effects of radiolysis of water on fuel dissolution rates. For this model, the dissolution rates have been derived from an electrochemical model that takes into account the oxidizing effects of gamma, beta and alpha radiolysis. The rate therefore decreases with time as radiation fields decrease. The model conservatively assumes that water enters the container immediately upon container emplacement and that sheath failure also occurs immediately. After approximately 1000 a, the fuel dissolution rate reaches a low value, which is assumed to remain constant thereafter. For the early stages of matrix dissolution, the results obtained with this model are similar to those obtained in a preliminary calculation discussed in

Johnson et al. (1994b, p. 267). In the long term, however, the use of a constant low dissolution rate, as opposed to the assumption of redox equilibrium in Johnson et al.(1994b), leads to complete dissolution of the fuel in ~10^6 to 10^7 a. Natural analogue studies (Cramer 1994) suggest that the long-term predictions of the model are extremely conservative. By choosing a very conservative constant lower limit for the fuel dissolution rate, we have drastically overemphasized the long-term extent of fuel corrosion. The rate chosen really only represents the lower limit of reliability of our model and ignores the effect on the corrosion rate of the long-term decay in radiation dose rates which would occur in the time period 10^3 to 10^6 a (Johnson et al. 1994a, Fig. 2.5). Since dose rates in the used fuel will approach those in natural uranium ore deposits within approximately 10^5 a, this neglect of the decay will clearly lead to a major overestimate of the extent of fuel dissolution.

The rate of dissolution of the Zircaloy matrix is determined by two factors: the solubility of zirconium and the rate at which zirconium is removed from the container (by diffusion through the defect in the container). For the Zircaloy matrix, the congruent-release mechanism is modeled using a solubility parameter for zirconium and by parameters that describe mass transport from a failed container.

Radionuclides released from the fuel are assumed to dissolve in the pore water within the container. For Pu, Th, Tc, U and Np, solubilities are calculated by sampling over the expected range of groundwater chemistry parameters and precipitation may occur. For other elements, conservative upper bound solubilities have been estimated and are used to determine if precipitation occurs.

6. THE RADIONUCLIDE RELEASE AND MASS TRANSPORT MODEL

6.1 INTRODUCTION

We describe here the key features of the vault model for the in-room emplacement design considered in this study. The model simulates radionuclide release from the used fuel and Zircaloy sheaths to the interior of the container, precipitation inside the container for radionuclides whose solubilities have been exceeded, mass transfer of radionuclides through a pinhole in a small number of initially defected containers, through the buffer, backfill and EDZ into the surrounding rock. Various aspects of the model such as the Boundary Integral Model (BIM) for mass transport (Kolar and LeNeveu 1995, LeNeveu and Kolar 1996) and the pinhole defect model (LeNeveu 1996) have been previously described. In this document, the model is presented at the conceptual level. Readers are referred to the above reports for the mathematical development of the model.

The vault design for in-room emplacement consists of a series of elliptical cross-section tunnels excavated into the rock at 500 m below the surface (Fig. 2.1). Two container designs are being considered: a single copper shell container supported internally by packed

particulate, and a dual copper/carbon steel shell design (see Chapter 4.2). Successive layers of buffer and backfill surround the containers and fill the disposal rooms. An EDZ is assumed to exist around the excavated room. The vault model for a room consists of nested cylindrical regions of container with a pinhole-size defect (point source) buffer, backfill and EDZ surrounded by rock. The model geometry for a vault room is contrasted with the design of a vault room in Fig. 6.1.

6.2 INTERFACE WITH THE GEOSPHERE MODEL

To account for the variability in the hydrogeological properties of the rock, and for differences in room lengths, the vault is divided into twenty-four sectors (Fig. 6.2). The rock associated with each vault sector is assumed to have uniform hydrogeological properties. The rooms in each sector are of a constant length. Each room within a vault sector is assumed to be enveloped by an EDZ. The EDZ is considered to be a necessary feature of the vault model because of the relatively large groundwater velocities assumed in the system assessed. The vault model determines the outward radionuclide flux integrated over the entire surface of the EDZ from a single failed container within the room. Should more than one container fail within a vault sector, the integrated flux for a single container is multiplied by the number of failed containers. The total integrated flux from each vault sector is the source for the geosphere model.

The vault model requires as input a number of parameters that are related to the properties of the geosphere (the rock surrounding each disposal room comprising the vault). These are the porosity, the axial and radial components of the dispersion length (or coefficient), and the average Darcy groundwater velocity in all media.

The radial dispersion length a_{RR}, must be comparable to the thickness of the EDZ, and is, thus, chosen to be a fraction of the axial dispersion length, a_{yy};

$$a_{RR} = \frac{1}{100} a_{yy} \quad . \tag{6.1}$$

The transverse dispersion length due to radial flow, a_{Ry}, in the EDZ is expressed as a fraction of the transverse dispersion length due to axial flow, a_{yR};

$$a_{Ry} = \frac{1}{100} a_{yR} \quad . \tag{6.2}$$

The porosity in the EDZ, ε_D, is sampled separately from its PDF, however, it is not allowed to be less than the porosity in the rock (ε_R). Thus, if the sampled porosity is ε_D^S, the value used in the vault model would be

$$\varepsilon_D = \max(\varepsilon_D^S, \varepsilon_R) \quad . \tag{6.3}$$

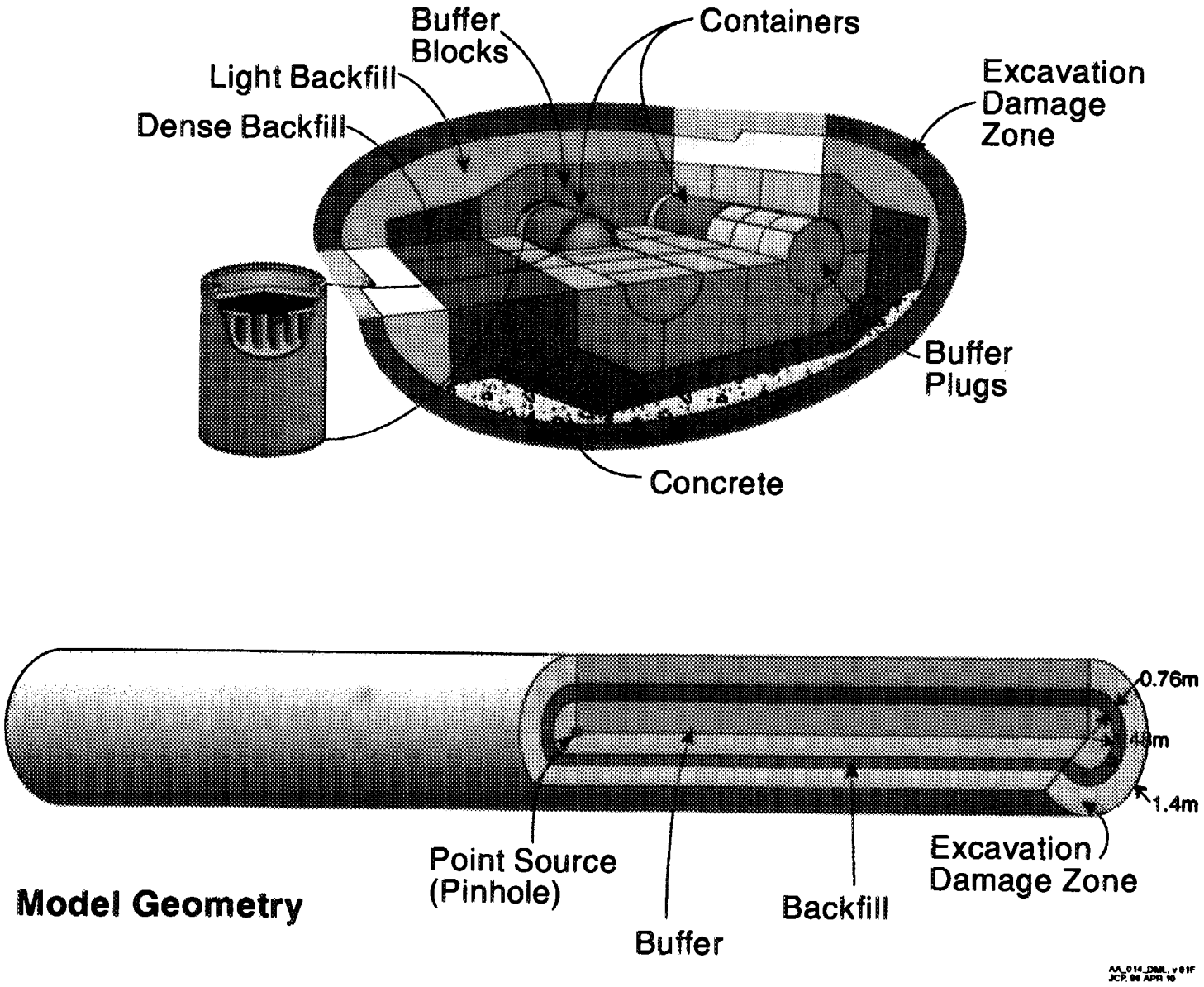

FIGURE 6.1: Physical Layout of Disposal Room

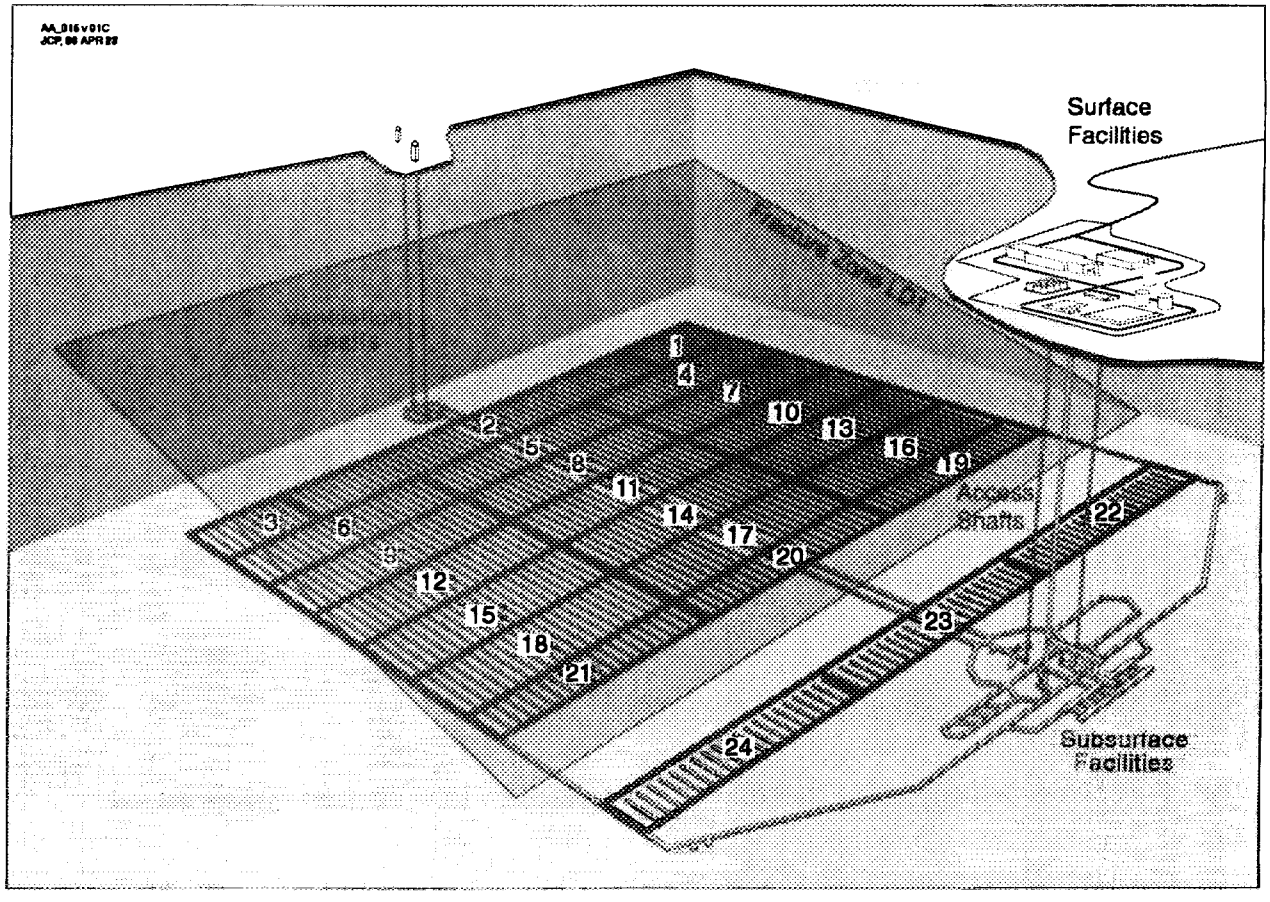

FIGURE 6.2: Model Geometry at the Interface Between the Vault and the Geosphere

All other porosities and dispersion coefficients are uncorrelated and their sampled values are used unmodified.

The components of the average Darcy velocity in different media (i.e., the backfill and EDZ) are all proportional to the Darcy velocity in the surrounding rock (i.e., to the hydraulic conductivity and gradient in the vicinity of the room). The formulas expressing this proportionality were obtained using simplified concepts of the distribution of the groundwater flow among the different media based on the resistance (permeability) of each medium to the water flow.

The radial (i.e., representing the velocity component perpendicular to the long axis of the room) Darcy velocity in the EDZ, V_Z^T, calculated by an equivalent resistor model, is

$$V_Z^T = \frac{k_Z^T V_R^T}{A_F k_F + A_Z k_Z^T + (1 - A_F - A_Z - A_B) k_R} \quad . \tag{6.4}$$

where A_Z, A_F and A_B are related to the cross-section of the EDZ, backfill and buffer as determined from

$$A_j = \frac{2T_j}{S} \tag{6.5}$$

where T_j is the thickness of the buffer, backfill or EDZ and S is the centre to centre spacing of the disposal rooms. In Eq. (6.4), k_R and k_F are the permeability in the rock and backfill, k_Z^T is the radial permeability in the EDZ and V_R^T is the component of the Darcy velocity in the rock, orthogonal to the long axis of the disposal room. The value of k_Z^T should not exceed the permeability of the rock; it is given by:

$$k_Z^T = \max\left(\frac{1}{10} k_Z^A, k_R\right) \quad , \tag{6.6}$$

where k_Z^A is the axial permeability of the EDZ.

The radial Darcy velocity in the backfill, V_F^T, calculated by an equivalent resistor model is:

$$V_F^T = \frac{k_F V_R^T}{A_F k_F + A_Z k_Z^T + (1 - A_F - A_Z - A_B) k_R} \quad . \tag{6.7}$$

The axial Darcy velocity in the room is given by the minimum of the Darcy velocity determined by water collection (Pusch et al. 1991, Harr 1962) and that determined from direct application of Darcy's law.

The axial Darcy velocity in the EDZ, V_{CZ}^A, as determined by water collection from a hemisphere of radius $10R_Z$ at the incoming end of the room, is given by

$$V_{CZ}^A = \frac{20 V_R^A (L + 10R_Z) R_Z k_Z^A}{9(B_F k_F + B_Z k_Z^A)} \quad . \tag{6.8}$$

Here, B_F is the cross-sectional area of the backfill and B_Z is the cross-sectional area of the EDZ; R_Z is the outer radius of the EDZ and V_R^A is the component of the Darcy velocity in the rock parallel to the axis of the disposal room.

The axial Darcy velocity in the backfill, V_{CF}^A, also determined by water collection from the region at the end of the room, is given by

$$V_{CF}^A = \frac{20V_R^A(L+10R_Z)R_Z k_F}{9(B_F k_F + B_Z k_Z^A)} \quad . \tag{6.9}$$

The axial Darcy velocity in the EDZ from Darcy's law, V_{DZ}^A, is:

$$V_{DZ}^A = \frac{k_Z^A}{k_R} V_R^A \quad . \tag{6.10}$$

The axial Darcy velocity in the backfill from Darcy's law, V_{DF}^A, is:

$$V_{DF}^A = \frac{k_F}{k_R} V_R^A \quad . \tag{6.11}$$

Thus, the axial Darcy velocity used in the vault model in the EDZ, V_Z^A is given by

$$V_Z^A = \min(V_{CZ}^A, V_{DZ}^A) \quad . \tag{6.12}$$

The axial Darcy velocity used in the vault model in the backfill zone, V_F^A is given by:

$$V_F^A = \min(V_{CF}^A, V_{DF}^A) \quad . \tag{6.13}$$

The Darcy velocity in the buffer is assumed to be zero (see Chapter 3.5).

It will be shown in Chapter 6.4 that the values of the components of Darcy velocity as given by Eqs. (6.4), (6.7), (6.12) and (6.13) compare favourably with the volume average values obtained in a three-dimensional finite element model of an emplacement room and its surrounding rock.

6.3 MODEL SYNOPSIS

The five main components of the vault model are:

1) container failure,

2) release of radionuclides from the used fuel and Zircaloy to the interior of the container following failure,

3) release of radionuclides from the container defect into the buffer,

4) solubility constraints on the radionuclide release rates into the buffer, and

5) mass transport of radionuclides across the buffer, backfill and EDZ.

The following summarizes the approach used in each of these areas. More detail, including the mathematical formulations, is given in LeNeveu (1996) and LeNeveu and Kolar (1996).

6.3.1 Container Failure

The vast majority of containers are expected to survive intact for $>10^6$ a. The migration of radionuclides is assumed to take place only from containers with initial fabrication defects. The median probability of failure is sampled from a truncated lognormal distribution (Johnson et al. 1994b), with a median value of 2×10^{-4}. The number of containers failing in a given sector is determined by random sampling from a binomial distribution according to the number of containers in each sector and the probability of fabrication defects.

6.3.2 Radionuclide Release from the Used Fuel and Zircaloy to the Interior of the Container

For both the packed particulate container and the dual-shell container (Figs. 2.2 and 2.3), there is assumed to be a continuous diffusion path from the fuel through a defect in the copper shell to the buffer. For the dual-shell container, the inner carbon steel shell is assumed to fail immediately after emplacement in a manner similar to the copper shell (Chapter 2.6). It is assumed that the defected containers become saturated with water immediately upon failure. This is a very conservative assumption. To saturate the material in the container, water from the rock must first saturate the buffer and backfill and then pass through the small defect to fill the container. These processes could take a very long time depending on the hydraulic conductivity of the various media in the system and the supply of water from the geosphere. The time required for saturation of clay-based materials in the vault and the time to fill a defective container are discussed in more detail in Chapter 3.3.2. Calculations indicate that the defect size would not increase significantly over the time of the assessment (See Chapter 4.6)

Another case is evaluated that applies only to the dual shell container. It is assumed that the inner steel shell remains water-tight for about one thousand years. This is based on a conservative estimate of the average corrosion rate of carbon steel under anaerobic conditions of ~10 $\mu m \cdot a^{-1}$ (Blackwood et al. 1994). It is assumed that magnetite film growth from anaerobic corrosion in the space between the two shells ultimately causes the failure of the internal steel shell; thus, the defect in the Cu shell could become significantly larger (Garroni et al. in preparation), although studies suggest that this is unlikely (Hoch and

Sharland 1993). However, the extent to which this might occur is difficult to estimate. To provide a bounding analysis, the defect size is made equal to the external surface area of the container. This large size prevents the defect from restricting mass transfer from the container to the buffer.

After ingress of water, radionuclides are released from the fuel into the interior of the container by two mechanisms, instant release and congruent release. Instant release refers to the rapid release of the inventory of radionuclides in the fuel-sheath gaps and on the grain boundaries of the used fuel (Chapter 5.3.1). It is assumed that this inventory is immediately dispersed into the water-filled interior of the defected containers.

Congruent release refers to the relatively slow release of radionuclides immobilized in the matrix of the used fuel and the Zircaloy sheaths. These radionuclides are released according to the degradation rate of the matrix and the fractional abundance of the radionuclide within the matrix. The degradation of the used fuel is determined by radiolysis of water occurring at the fuel surface. Radiolysis and the subsequent rate of degradation decrease with time. At very long times, when radiolysis effects would be very small, the degradation rate of the fuel is determined by an assumed constant rate of chemical dissolution. These processes are described in more detail in Chapter 5.3.2. The degradation of the Zircaloy sheath is determined by the solubility of zirconium. This solubility is sampled from a distribution, as described in Johnson et al. (1995). The solubility-controlled degradation rate of the sheath is determined by the rate of mass transfer of the dissolution products through the defect in the container. Equations describing this phenomenon are given in LeNeveu (1996).

6.3.3 Release from the Container Defect to the Buffer

A response function has been developed for the diffusion of a radionuclide through a container defect into the buffer due to a unit impulse discharged into the interior of the container (LeNeveu 1996). To obtain the total release rate of a radionuclide from the defect into the buffer, the sum of the instant and congruent release rates into the interior of the container are convoluted with the response function. The convolution process is a mathematical means by which the release rate from the defect to the buffer due to a series of unit impulses discharged at separate times into the container are combined. The sum of all the unit impulses constitute the instant and congruent release rate of a radionuclide into the interior of the container. The total mass of radionuclides accumulated inside the container during this process is determined, taking into account nuclear transformations.

6.3.4 Solubility Constraints on the Release Rates into the Buffer

Equations have been developed that describe the diffusion of a radionuclide through a container defect into the buffer for radionuclides whose concentrations in the interior of the container remains constant at their solubility (LeNeveu 1996). These equations provide an upper limit on the rate at which a radionuclide can be released from the defect into the buffer. Should the instant and congruent release rates from the defect to the buffer as

determined by the convolution process, exceed the solubility-controlled release rate from the defect to the buffer, the radionuclide is precipitated inside the container. The release rate from the defect to the buffer is determined by the solubility of the precipitate until such time as the precipitate has been completely dissolved. At this time the release rate from the defect to the buffer reverts to the rate determined by the convolution process. The effect of nuclear transformations are accounted for in this process.

The solubility of five elements, Th, U, Np, Pu and Tc are determined by thermodynamic equations developed by Lemire and Garisto (1989). The reference groundwater compositions used to calculate solubilities is given in Table 3.2. Updates to the thermodynamic data for Tc required for these calculations are described by Lemire and Jobe (1996). An upper limit on the solubility of the other elements has been estimated with the aid of chemical speciation codes (See Chapter 5.4). Effective solubilities of isotopes were determined by multiplying the element solubility pertaining to the isotope by the time-varying isotopic ratio.

The solubility-controlled release rate from the defect forms the input to the buffer, backfill and EDZ.

6.3.5 Mass Transfer Across the Buffer, Backfill and EDZ

Using the boundary integral method, response functions for a decay chain have been developed that describe the integrated flux over the outer surface area of a disposal room due to a unit impulse of radionuclide discharged from a point along a central axis through the buffer (LeNeveu 1996). The point is assumed to correspond to a small defect in a container. The response functions are for nested cylindrical regions composed of buffer, backfill and EDZ surrounded by rock infinite in radial extent. The EDZ is considered to be part of the room.

The space occupied by the containers in the room is excluded from the model. This is appropriate because the container surface remains intact for virtually all the containers, preventing radionuclides from diffusing into the space occupied by the containers. The radius of the buffer and backfill are chosen to conserve the volumes of these materials. In the Boundary Integral Model (BIM) incorporated into the vault model the rooms are cylindrical whereas the vault design calls for rooms with an elliptic cross-section. Comparisons of the BIM with a three dimensional finite-element model that uses rectangularly shaped rooms indicate that the shape of the room is not important as long as volumes of the buffer, backfill and EDZ are conserved (Chapter 6.4 and Kolar and LeNeveu 1995). The finite-element model spreads the initial source over a small spatial element rather than concentrating the source at a point. The comparison between the two models indicates that the use of a point source rather than a small elemental source is unimportant. The finite-element model also uses a finite external rock region rather than an infinite region as employed by the vault model. The comparison between the two models indicates that beyond about 150 m from the room boundaries, the spatial extent of the external rock is

not an important factor. The comparisons with the finite-element model are discussed in more detail in Chapter 6.4

The presence of the concrete along the floor of the room is not included in the model. This should be a conservative assumption because the concrete would serve as an additional barrier to groundwater and radionuclide movement. The model does not discriminate between light and dense backfill. This is justified because light and dense backfill have similar mass transport properties even though their compositions are different (see Chapter 3.5).

Continuity of flux and concentration integrated over the interface between adjoining regions is used as the interfacial boundary condition between media in the BIM. Should it be necessary to know the concentration or flux at every point along the room boundaries, a more detailed boundary condition that required continuity of flux and concentration at all points at the interface between adjoining media would be required. In the vault model, the integrated flux over the entire room surface is used as a source term for the geosphere model. Thus the spatial detail of mass transport over the boundary surfaces is not required. One consequence of using integrated continuity conditions is that the model becomes insensitive to the position of the source within the room. Comparisons with the finite element model, which exhibits sensitivity to the position of the point source, indicate that for the parameter values typical of this assessment, integrated room release is not very sensitive to source position. In any case, any dependence on source position would tend to be averaged over many simulations. Since the vault model uses an averaging procedure in a single simulation, the average dependence of source position should be adequately represented.

The boundary condition employed at the ends of the room in the BIM sets the flux equal to the product of the concentration of the radionuclide and one half of the Darcy velocity. It is assumed that the concentration is uniform over the end surfaces of the room. This is a convective type boundary condition that will allow radionuclides transported to the ends of the room to escape providing there is an axial groundwater velocity in the medium. For zero groundwater velocity, there will be no release from the ends of the room. This is reasonable considering the rooms would be sealed at the ends with low permeability bulkheads and grout. Furthermore, the area of the room ends is very small compared to that of other surfaces and, thus, their capacity for mass transfer is correspondingly small. In addition, in the presence of a strong convective, near vertical, groundwater flow field, as assumed in this assessment, the radionuclides will tend to be transported outwards into the rock before they can migrate throughout the room.

The vault model assumes that the groundwater velocity is negligible in the buffer but uses spatially uniform radial and axial components of groundwater velocities in the backfill, EDZ and surrounding rock. In reality the groundwater could have a vertical upward or downward component within the room rather than a radial component and would be spatially variable. Use of a radial velocity component should be a conservative assumption because radionuclides would be carried outwards in all directions. A vertical velocity, on

the other hand, would tend to move radionuclides outward in some parts of the room and inwards in other parts. Comparisons with the finite-element model MOTIF indicate the use of a uniform radial component to represent a vertical flow field is a good approximation. These comparisons also indicate that the use of spatial uniformity in the velocities is a good approximation (see Chapter 6.4)

The axial and radial components of velocity in the backfill and EDZ are determined from the unperturbed groundwater velocities in the geosphere. The equations and assumptions used in determining these velocities are described in Chapter 6.2.

To obtain the total release rate to the surrounding rock from a single defected container within the room, the previously determined release rate from the defect to the buffer is convoluted with the response functions for the disposal room.

6.4 VERIFICATION WITH MOTIF

Here we describe the verification of the approximate equations for the Darcy velocity components of Chapter 6.2, and of the BIM of Chapter 6.3.5 for the calculation of the integrated flux from a failed container into the geosphere.

These verifications are done by comparing the results of the finite element code MOTIF with those obtained with the BIM. The finite element model of the disposal room and its surrounding rock is the same for both cases (i.e., for the Darcy velocity determination and the integrated flux calculation). The disposal room is modeled by three nested (coaxial) regions of square cross-section, the innermost one representing the buffer around the containers, the next one the backfill, and the outer one the EDZ. The volumes of these three regions are the same as in the BIM (Fig. 6.3). We use two finite element models. The first was chosen so that it resembled the simplified BIM geometry as closely as possible (200 m of rock along the four long sides of the room and no rock at the ends; constant Darcy velocity in each medium (LeNeveu and Kolar 1996)). This is called the "fat" model. In the second, we model a typical disposal room that is flanked by two other rooms with the centre-to-centre distance between the rooms being only 30 m. As it would be difficult to model more than one disposal room, we have to use symmetry, and place the outer auxiliary boundary of the MOTIF finite element model at the plane half-way between the centres of two adjacent rooms. We refer to this model as the "slim" model to distinguish it from the "fat" model in which the presence of neighbouring rooms is neglected, and rock of equal thickness is placed on the sides of the room and below the room. The orientation of the x and z coordinate axes for the purposes of verification calculations is shown in Fig. 6.3. The y axis is identical to the long axis of the room. The room dimensions corresponding to the current assessment case are given in Table 6-1.

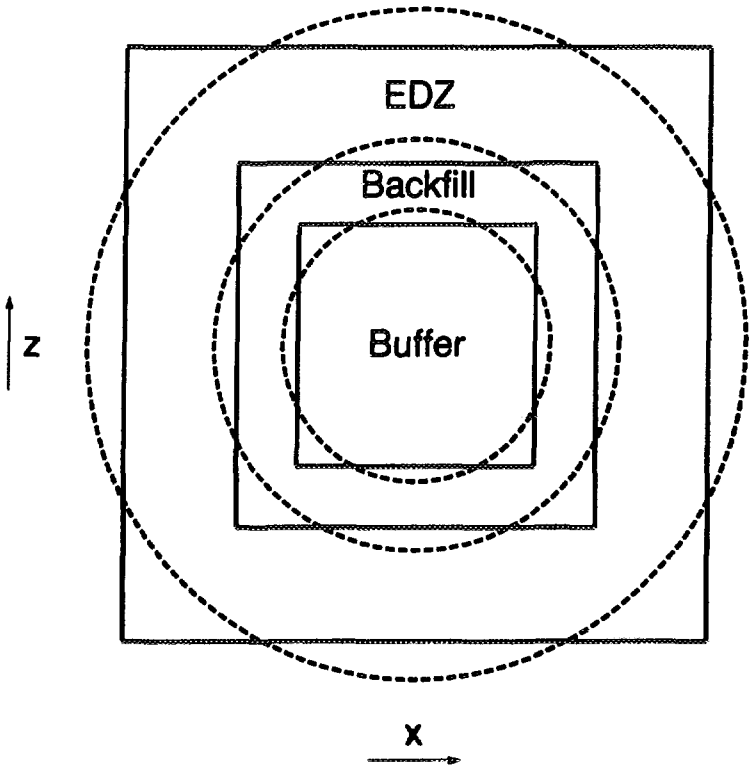

FIGURE 6.3: Comparison of the MOTIF (Solid Line) and BIM (Dashed Line) Disposal Room Models for Dimensions of Table 6-1.

TABLE 6-1

BIM TO MOTIF CONVERSION OF

THE DISPOSAL ROOM DIMENSIONS (m)

Region	BIM	MOTIF
	diameter	side of the square cross-section
buffer	2.96	2.62
	radial thickness	thickness
backfill	0.76	0.67
EDZ	1.4	1.24
Room length = 206		

All of these dimensions are fixed by the vault design, except for the EDZ thickness which may vary. For the dimensions in Table 6-1 (corresponding to the mean value of the EDZ thickness), there is thus (in the x direction) only 11.8 m of intact rock between the outer

boundary of the EDZ and the symmetry plane between the two rooms in the "slim" model. For this plane to be the actual symmetry plane for all the aspects of modeling, there must be no groundwater flow across this plane, i.e., the component of the hydraulic gradient (Darcy velocity) perpendicular to this plane must be zero. This limits somewhat the class of cases that can be treated using this model. However, this limitation is not severe because the orientation of the hydraulic gradient in the other two directions can be arbitrary. At this symmetry plane we use the zero-gradient boundary condition, $\partial C/\partial x = 0$. Above the room we consider the rock to extend only to the distance of 50 m where the position of a major fracture is assumed. Here we require the swept-away boundary condition $C = 0$. Below the room and at its ends we again put 200 m of rock. Here, we assume the form of the diffusion boundary condition is not too important, and we use the conservative $C = 0$ condition.

The flow field in each medium is inhomogeneous, generated self-consistently by MOTIF using suitable boundary conditions. We need an interface between a large scale model for groundwater flow in the disposal system (Stanchell et al. 1996) and its small subset, a disposal room and its surrounding rock. An obvious way is to prescribe the values of hydraulic heads at all nodes on all outer surfaces of the room-scale model. This is done in the following way. We assume that in the absence of the disposal room (rooms), there would be a locally homogeneous flow field in the rock corresponding to the local value of the hydraulic gradient. In such a flow field the hydraulic heads are constant on the planes perpendicular to the direction of the hydraulic gradient. In the presence of the room, we simply require that the values of the hydraulic head on the outer boundaries of a MOTIF finite element model are the same as they would be in the unperturbed rock. This is expressed by the following formula:

$$h(X_1,X_2,X_3)=h(O_1,O_2,O_3)+\sum_i g_i\ (X_i-O_i)\ . \qquad (6.14)$$

Here (X_1,X_2,X_3) are the coordinates of an arbitrary surface node of the local model, $h(X_1,X_2,X_3)$ is the value of the hydraulic head at this node, (O_1,O_2,O_3) is a reference point (e.g., the centre or a corner of the room), $h(O_1,O_2,O_3)$ is the value of the hydraulic head at this reference point in the absence of the room, and (g_1,g_2,g_3) are the components of the hydraulic gradient (in the original large-scale model). Using Eq. (6.14) everywhere gives satisfactory results only if the local model is such that the flow at its outer boundaries is not modified noticeably by the added inhomogeneities. This condition is not satisfied in the "slim" model described above, in the region between two rooms, even if we limit ourselves to the cases with $g_1 = 0$ as explained above. The solution is to use Eq. (6.14) only on those boundary surfaces that are far away from the room, and to use the no-water-flux boundary conditions for the flow at the symmetry planes between the rooms (at the left and right model boundaries).

Finite elements for this model range typically from 0.44 x 0.44 x 2 m inside the buffer to irregular hexahedral elements with some of their edges many tens of metres long near the bottom of the model. For $g_1 = 0$ and the radionuclide source (failed container) positioned on the axis of the buffer, both the flow field and the concentration profiles must also be

symmetric with respect to the vertical symmetry plane of the room (corresponding to x = 0). Using this symmetry, one needs only one half of the model, e.g. the region $0 < x < 15$ m, which typically requires a grid with 17 937 nodes and 15 612 different hexahedral elements of the above size. We have verified, in one case, that the MOTIF results obtained in this way are the same as those obtained in the full model (with 31 224 elements).

All the pertinent parameters for the current assessment case are listed in Table 6-2 as parameter set 1. Parameter set 2 was used for preliminary calculations prior to the definition of parameter set 1.

TABLE 6-2

PARAMETER VALUES FOR MOTIF AND BIM COMPARISONS

Parameter Name	Parameter Values		Units
	Set 1	Set 2	
radial thickness of buffer (BIM)	1.48	1.47	m
radial thickness of backfill (BIM)	0.76	0.805	m
radial thickness of EDZ (BIM)	1.40	1.13	m
length of room	206	214	m
capacity factor of I in buffer	0.275	0.241	
capacity factor of I in backfill	0.275	3.47	
capacity factor of I in the EDZ	5.0×10^{-5}	0.05	
capacity factor of I in rock	1.0×10^{-5}	0.003	
decay constant of ^{129}I	4.41×10^{-8}	4.41×10^{-8}	a^{-1}
total intrinsic diffusion coefficient in buffer	6.93×10^{-3}	6.30×10^{-4}	$m^2 \cdot a^{-1}$
total intrinsic diffusion coefficient in backfill	6.93×10^{-3}	6.30×10^{-4}	$m^2 \cdot a^{-1}$
total intrinsic diffusion coefficient in the EDZ	1.38×10^{-7}	9.25×10^{-6}	$m^2 \cdot a^{-1}$
total intrinsic diffusion coefficient in rock	2.76×10^{-8}	5.55×10^{-7}	$m^2 \cdot a^{-1}$
axial dispersion length in backfill	0.345	10.5	m
axial dispersion length in the EDZ	29.8	10.5	m
axial dispersion length in rock	30.5	10.5	m
transverse dispersion length for axial flow in backfill	5.00×10^{-3}	1.05	m
transverse dispersion length for axial flow in the EDZ	0.362	1.05	m
transverse dispersion length for axial flow in rock	3.05	1.05	m
radial dispersion length in backfill	0.345	10.5	m
radial dispersion length in the EDZ	0.298	10.5	m
radial dispersion length in rock	30.5	10.5	m
transverse dispersion length for radial flow in backfill	5.00×10^{-3}	1.05	m
transverse dispersion length for radial flow in the EDZ	3.62×10^{-3}	1.05	m
transverse dispersion length for radial flow in rock	3.05	1.05	m
viscosity of water	9.72×10^{-4}	1.47×10^{-3}	$kg \cdot m^{-1} \cdot s^{-1}$
density of water	1000.3	1000.0	$kg \cdot m^{-3}$

6.4.1 Verification of the Darcy Velocity Components of Chapter 6.2

It is much faster (in terms of the CPU time) to generate only the stationary flow field in the above model than to perform the subsequent transient calculation of the concentration profiles for a given radionuclide source. Using the slim model described above, we have thus performed a verification of Eqs. (6.4), (6.7), (6.12) and (6.13). The following parameters were chosen for this verification: the value of the hydraulic gradient of 0.00520 for a 28 000 $m^3 \cdot a^{-1}$ 100 m-deep well case was used (Stanchell et al. 1996). This corresponds to a value of the Darcy velocity in the intact rock of 1.65 $m \cdot a^{-1}$. The prevailing direction of the groundwater flow in the large scale geosphere model is upwards in most of the vault. We have thus used in Eq. (6.14) a hydraulic gradient inclined only slightly, by 10°, from the vertical direction, i.e., g = 0.00520 (0, cos 10°, -sin 80°). The permeability of rock, k_R, was isotropic, equal to 10^{-17} m^2. The same value was used for the x and z component of the permeability of the EDZ. All dimensions were fixed and the same as in Table 6-1, except for the radial thickness of the EDZ which could assume one of the following five values: 0.9, 1.2, 1.4, 1.6 and 1.9 m. The y (axial) component of the permeability of the EDZ , k_Z^A, was also varied through the following five discrete values: 10^{-17}, 5 x 10^{-17}, 10^{-16}, 10^{-15}, 6.7 x 10^{-13} m^2 (see Table 3-4). The isotropic permeability of the backfill, assumed one of the following three values: 7.5 x 10^{-18}, 2.37 x 10^{-17} and 7.5 x 10^{-17} m^2. These three parameters that were varied represent those that are expected to influence most the value of the Darcy velocities. The range of their variation was chosen to cover the range of the respective sampling distributions in the vault and geosphere models. Using all the values listed above gives 75 cases altogether. For all 75 cases MOTIF was used to generate the flow field in the slim model described above. For each case, the volume average values of the components of the Darcy velocity were calculated in each of the three different regions of the model (backfill, EDZ and intact rock). The mean Darcy velocity in the intact rock was in all 75 cases equal to 1.65 $m \cdot a^{-1}$ as given by Darcy's law. This indicates that the model used was large enough that the assumption that the flowfield at the outer boundary is unperturbed by the presence of the room is justified. The other mean values obtained by MOTIF are denoted as follows: the axial component of the Darcy velocity in the backfill is $q_{F,y}$; the respective vertical component is $q_{F,z}$; the axial component of the Darcy velocity in the EDZ is $q_{Z,y}$, and the respective vertical component is $q_{Z,z}$. These are compared in Figs. 6.4 through 6.7 with the values obtained by the simple approximate formulas of Chapter 6.2. If the two sets of results were identical, all the points would lie on the displayed straight lines. One can see that the difference between the approximate formulas of Chapter 6.2 and the "realistic" results obtained by MOTIF is rather small as all the points in the four figures lie very close to the straight identity lines. This difference is mostly conservative because most of the points lie above the straight identity lines, which means that larger than real (as obtained by MOTIF) velocity values are used in the vault model (which give larger radionuclide releases). This is confirmed by the histograms in Figs. 6.8 and 6.9 where the distribution of the ratio of the magnitudes of the approximate and real velocities among the 75 cases is shown. In most of the cases, the ratio is close to 1 or larger than 1. The following definitions are used:

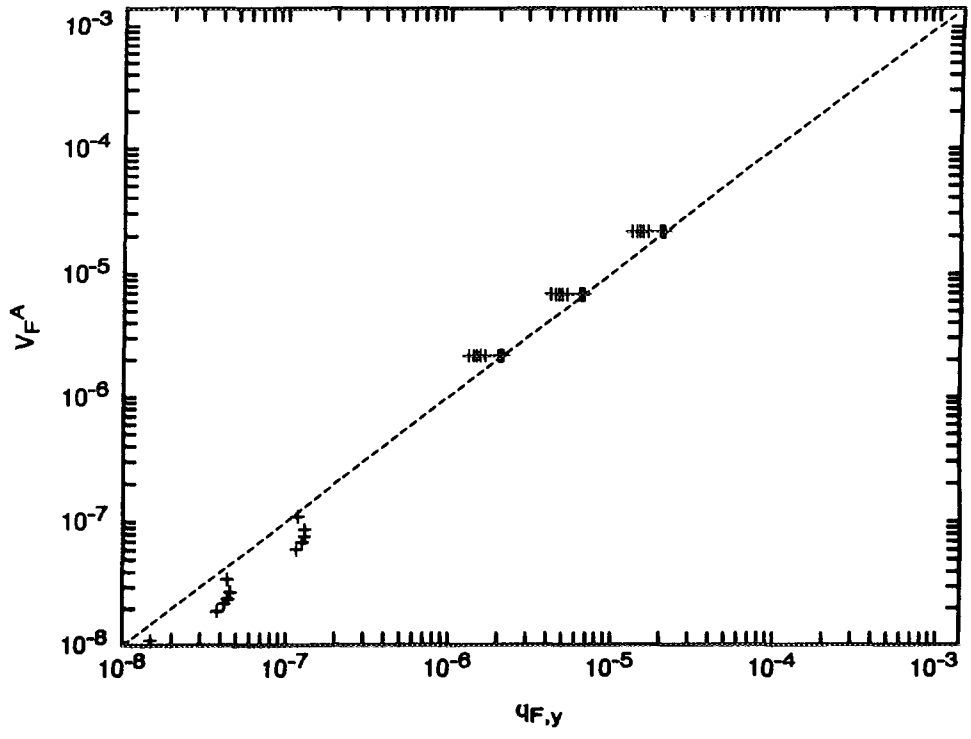

FIGURE 6.4: Comparison of the Approximate and the Mean Axial Component of the Darcy Velocity in the Backfill

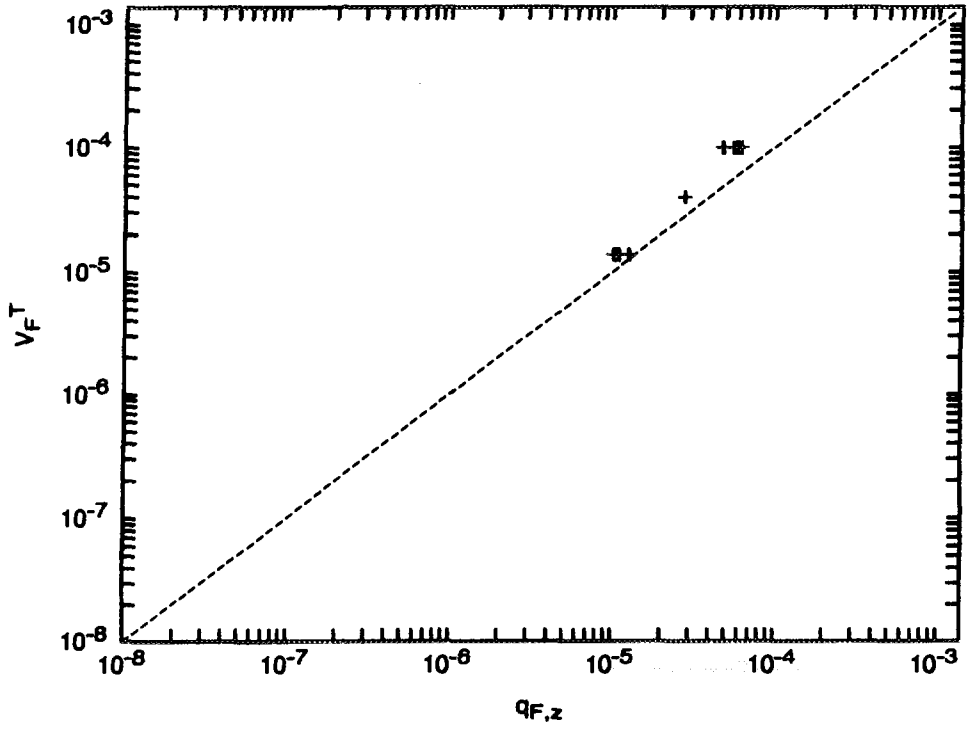

FIGURE 6.5: Comparison of the Approximate and the Mean Vertical Component of the Darcy Velocity in the Backfill

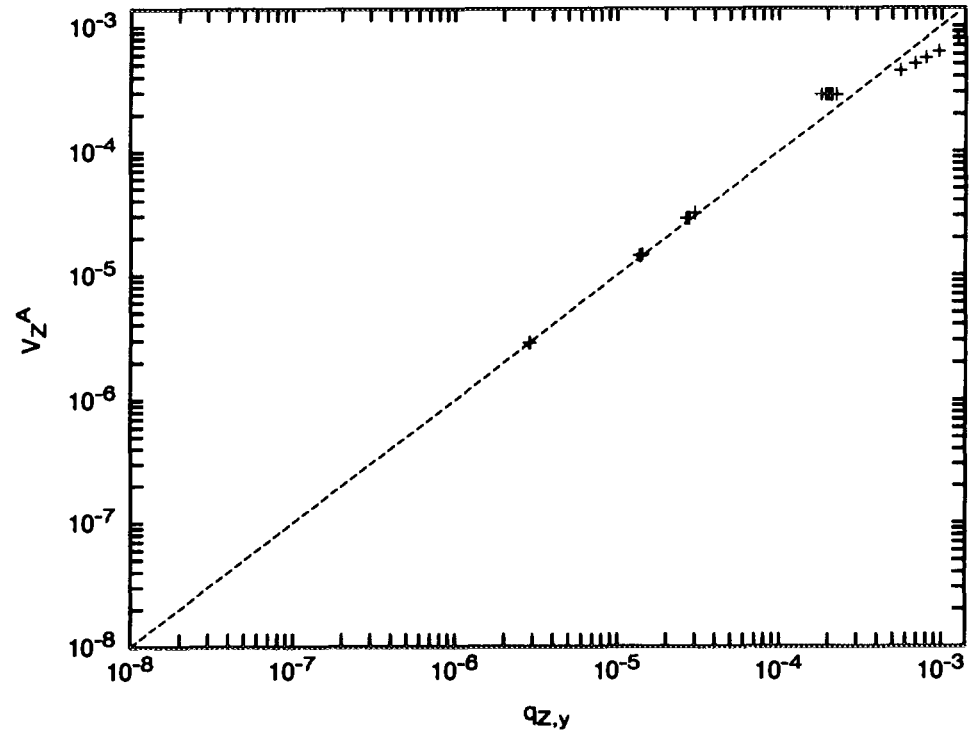

FIGURE 6.6: Comparison of the Approximate and the Mean Axial Component of the Darcy Velocity in the EDZ

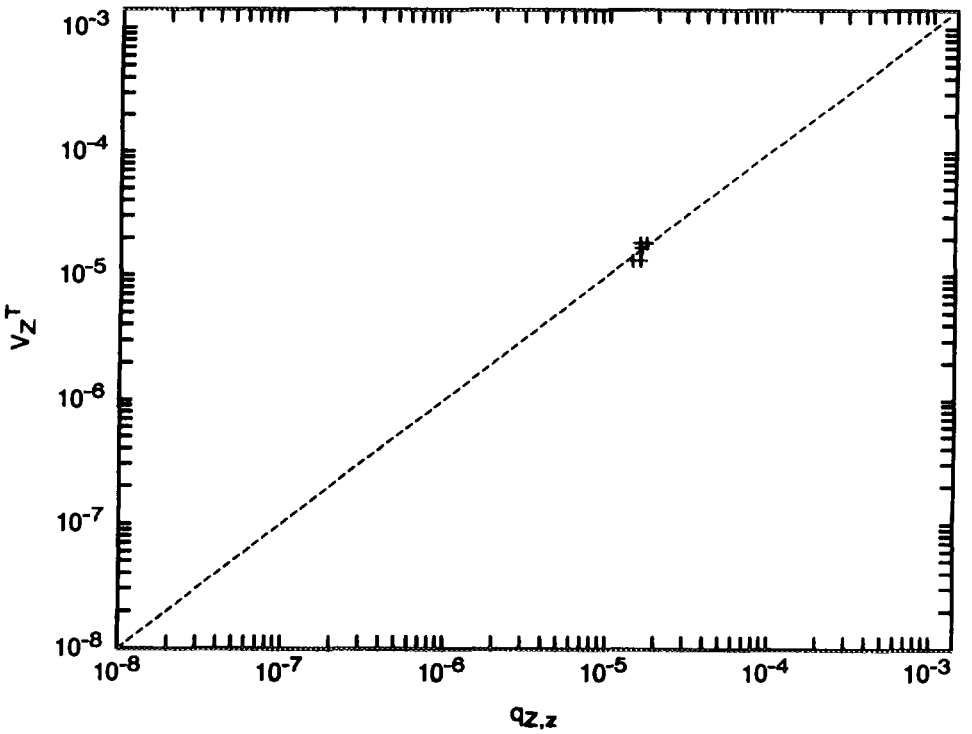

FIGURE 6.7: Comparison of the Approximate and the Mean Vertical Component of the Darcy Velocity in the EDZ

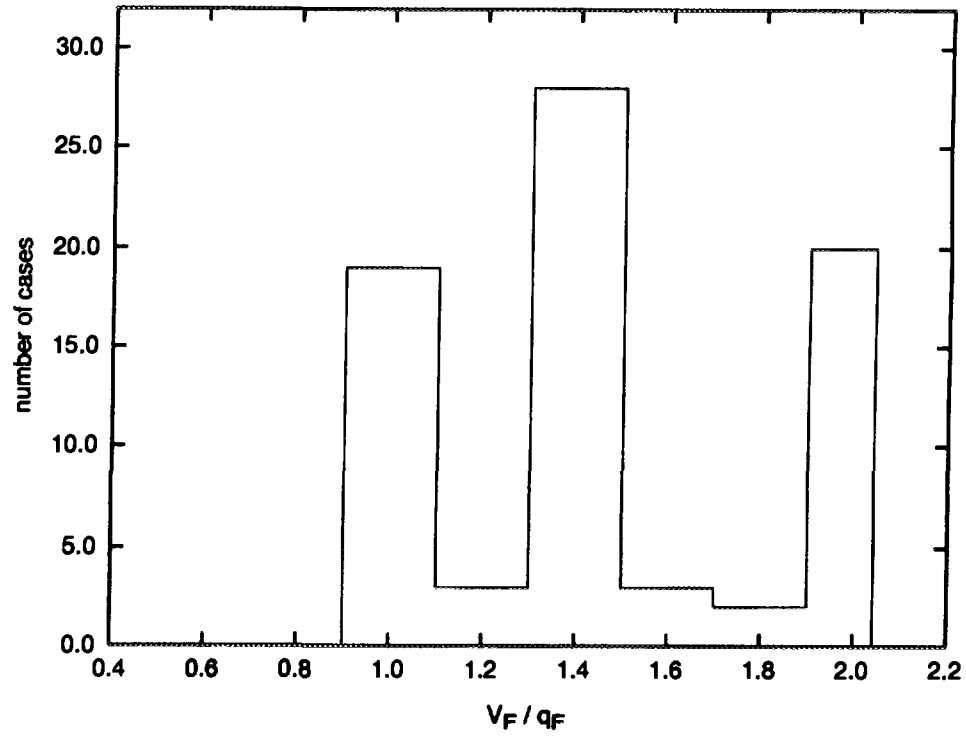

FIGURE 6.8: Distribution of the Ratio of the Magnitude of the Approximate and the Mean Darcy Velocity in the Backfill

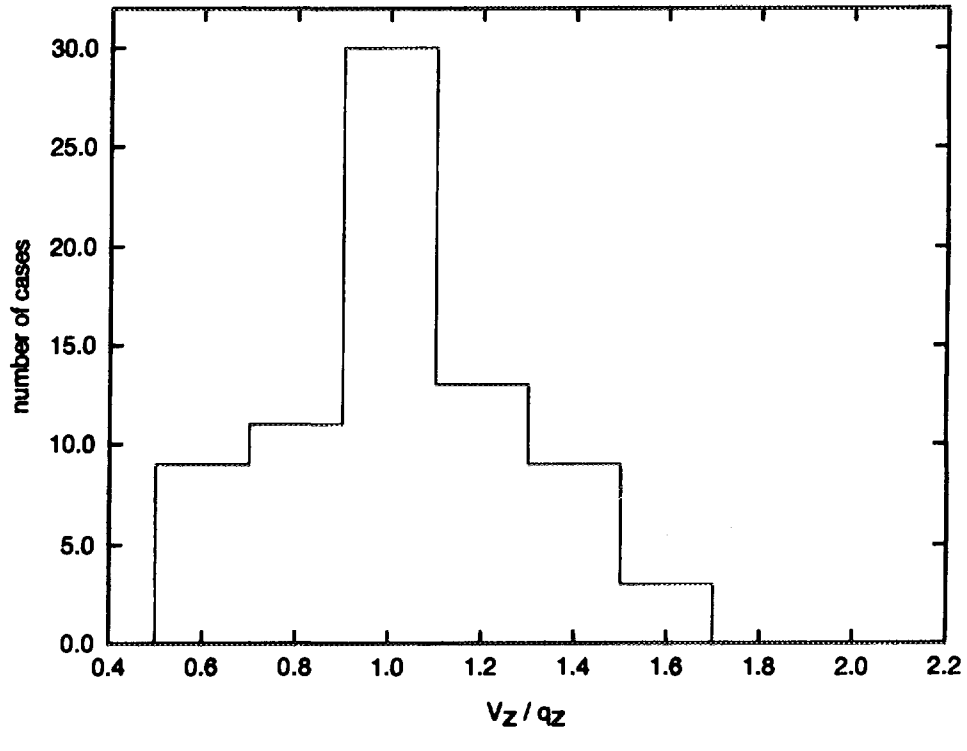

FIGURE 6.9: Distribution of the Ratio of the Magnitude of the Approximate and the Mean Darcy Velocity in the EDZ

$$q_F = \left[\left(q_{F,y}\right)^2 + \left(q_{F,z}\right)^2 \right]^{1/2} \quad \text{and} \quad q_Z = \left[\left(q_{Z,y}\right)^2 + \left(q_{Z,z}\right)^2 \right]^{1/2} \qquad (6.15)$$

and similarly for the approximate values:

$$V_F = \left[\left(V_F^A\right)^2 + \left(V_F^T\right)^2 \right]^{1/2} \quad \text{and} \quad V_Z = \left[\left(V_Z^A\right)^2 + \left(V_Z^T\right)^2 \right]^{1/2} \qquad (6.16)$$

6.4.2 Verification of the BIM results of Chapter 6.3.5

The process of verification of the BIM calculation of the integrated flux into the geosphere is in many respects a two-way process of mutual verification (or calibration) of the MOTIF code as applied to the solute transport modeling, and of the approximations used to make the BIM approach feasible. Up to now, MOTIF has been applied primarily to groundwater flow and heat transport problems, and its application to diffusive or convective solute transport is inherently accompanied by the appearance of oscillations in the calculated concentration profiles, especially in the vicinity of the concentration front, that can lead to negative values of concentrations or unphysical reversals in diffusive fluxes. Thus in the process of verification we have to show first that the presence of these oscillations does not compromise the MOTIF results.

This process of two-way verification has been a rather lengthy one with many comparisons being done before the values of parameter set 1 in Table 6-2 were finalized. Therefore, many of the comparisons discussed below used variations of the parameter values from parameter set 2 of Table 6-2.

The verification was done for ^{129}I which has the longest half-life of all the readily leachable radionuclides. The source unit of ^{129}I is always situated on the long axis of the disposal room. It is simulated with a nonzero concentration in a single node.

When used for the solute transport calculation (in a given or internally calculated groundwater flow field), the MOTIF program provides the pore-water concentration of ^{129}I, C(x,t), as a function of position, x, and time, t. For the comparison with the BIM results, the total flux integrated over the outer surface of each region is needed. Let us denote integrated flux through the outer surface of buffer, backfill and EDZ by $F_1(t)$, $F_2(t)$ and $F_3(t)$, respectively. Let us further denote the total mass of ^{129}I in the buffer, backfill and EDZ by $M_1(t)$, $M_2(t)$ and $M_3(t)$, respectively. Thus,

$$M_i(t) = r_i \int_{V_i} C(x,t)dx\,, \qquad i = 1,2,3 \qquad (6.17)$$

Here r_i is the capacity factor of the i-th medium, and V_i is the volume of this medium. Then the following global mass-balance equations hold:

$$\Phi_1(t)=M_1(0)-M_1(t)-\lambda\int_0^t M_1(\tau)d\tau, \qquad (6.18a)$$

$$\Phi_2(t)=\Phi_1(t)+M_2(0)-M_2(t)-\lambda\int_0^t M_2(\tau)d\tau\,, \qquad (6.18b)$$

$$\Phi_3(t)=\Phi_2(t)+M_3(0)-M_3(t)-\lambda\int_0^t M_3(\tau)d\tau\,. \qquad (6.18c)$$

Here λ is the decay constant of ^{129}I, and

$$\Phi_i(t)=\int_0^t F_i(\tau)d\tau;\ i=1,2,3 \qquad (6.19)$$

is the flux integrated over the outer surface of the i-th medium, integrated further over time. Equations (6.17) and (6.18) represent a link between the MOTIF output and the integrated fluxes $F_i(t)$ to be used for the comparisons with the BIM results. In the figures below, we compare directly the doubly integrated fluxes $\Phi_i(t)$ (integrated over space and time).

The BIM described in Chapter 6.3.5 (for more detail, see LeNeveu and Kolar 1996) should give exact results for the integrated flux in the absence of groundwater flow. This fact can be used for assessing the degree of precision that can be obtained in MOTIF. In Fig. 6.10, the integrated contaminant fluxes for MOTIF and BIM are compared for the case of identically zero groundwater velocity and also of zero decay constant. This figure contains two sets of MOTIF results corresponding to different boundary conditions. This is due to the fact that for a finite-element model, an auxiliary outer boundary somewhere in the rock surrounding the disposal room has to be specified, and suitable boundary conditions specified on this boundary. In the case of Fig. 6.10, this auxiliary boundary is rather close to the room on all sides except at the ends, where there is no rock at all (here we again use the "fat" model of the same type as in Leneveu and Kolar (1996), in an effort to emulate the BIM geometry as close as possible). Using the C=0 boundary condition everywhere is evidently more conservative because it forces the radionuclide out of the whole model, and therefore also out of the room, faster than it would happen in an infinite rock. On the other hand, the zero-flux boundary condition retains the radionuclide inside the MOTIF model (in this case of no decay, the final state is given by a constant C throughout the model; only a fraction of the total mass of ^{129}I diffuses through the EDZ/rock boundary; this corresponds to the zero-flux curve for $\Phi_3(t)$ in Fig. 6.10 leveling off at a value less than one; one corresponds to a unit source). The true curve for $\Phi_i(t)$ should thus lie between the two MOTIF curves corresponding to the two kinds of boundary conditions. This is what we see in Fig. 6.10, where the true curve is in

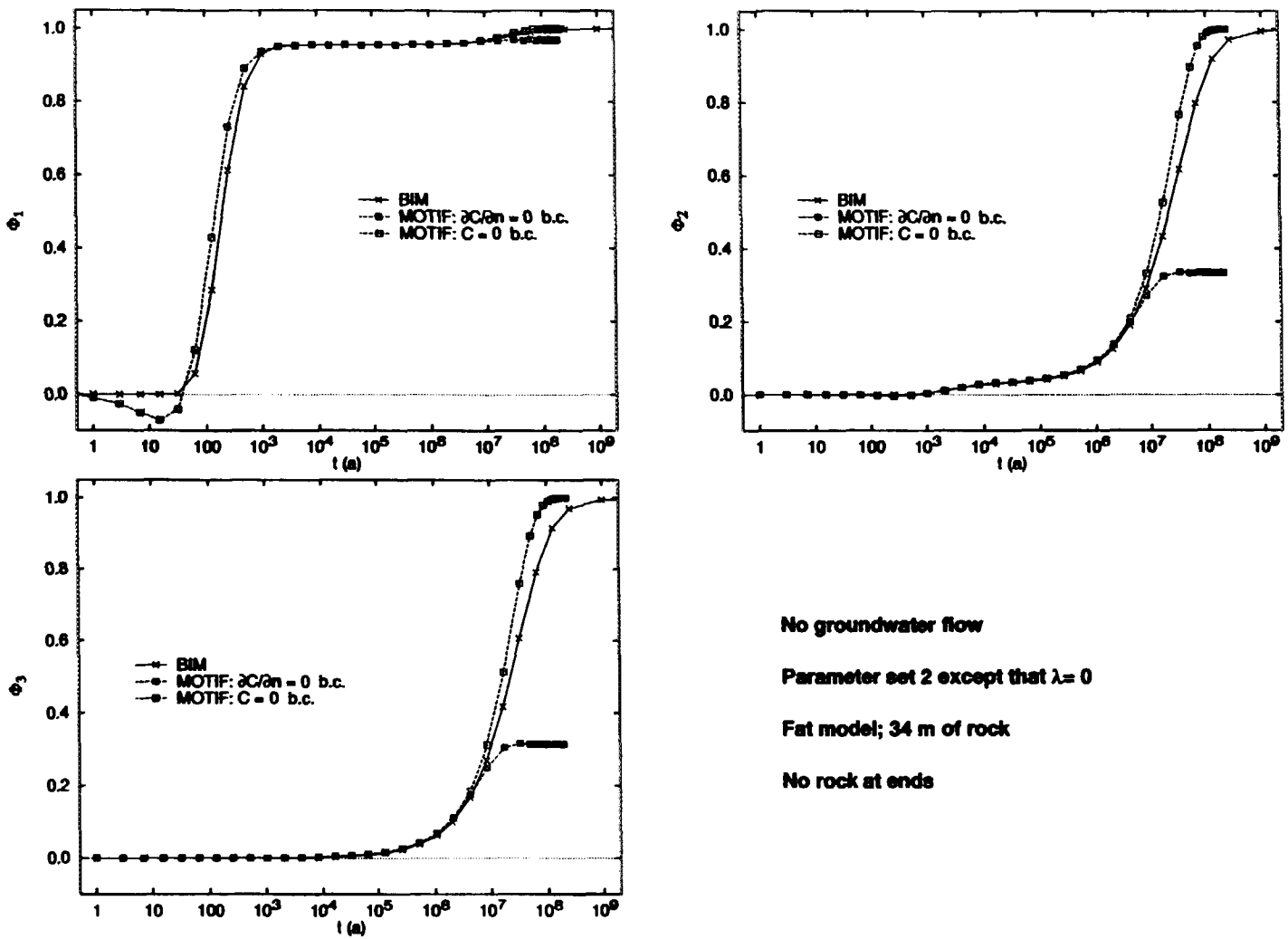

FIGURE 6.10: Comparison of the BIM Model with the Fat MOTIF Model With No Rock at the Ends in the Absence of Groundwater Flow and Radioactive Decay. Φ1, Φ2, and Φ3 represent the integrated fluxes of contaminant from the buffer, backfill and EDZ, respectively.

this case exactly given by the BIM curve. This is in spite of the rather large spurious oscillations in C(x,t) that are responsible for the negative minimum in the $\Phi_1(t)$ curve corresponding to the passage of the oscillation front from the buffer into the backfill. It thus seems that the MOTIF oscillations have little or no effect on the results for the integrated flux, $\Phi_3(t)$, through the outer surface of the EDZ.

Figure 6.11 refers to the same MOTIF geometry as Fig. 6.10, except that the calculations are done for ^{129}I and for axial groundwater flow with the same constant Darcy velocities as in BIM. Two different thicknesses of rock around the disposal room are used in MOTIF, 34 and 50 m. One can see that the separation between the curves obtained with the two types of boundary condition as described above quickly decreases as the thickness of rock is increased. For the thickness of 150 or 200 m being used in further comparisons, the type of boundary condition becomes practically irrelevant. The two different curves (marked by filled squares and diamonds) for the zero-flux boundary condition were obtained with rather different finite-element grids and different sizes of initial time steps. Nevertheless, both curves are practically identical. In general, MOTIF results were found to be very robust with respect to the variation of the spatial grid (the size and shape of the finite elements) and the size of the time steps. On the negative side, this means that it is impossible to get rid of the unphysical oscillations in the MOTIF concentration, that give rise to the negative integrated flux $\Phi_1(t)$ (see the behaviour of $\Phi_1(t)$ at very short times in most of Figs. 6.10 through 6.16). Fortunately, as indicated by Figs. 6.10 and 6.11, this phenomenon does not seem to have much effect on the flux through the outer surface of the EDZ, $\Phi_3(t)$, which is of main concern in our comparisons. Thus, we can conclude that MOTIF results for the integrated flux, especially for $\Phi_3(t)$, reasonably represent reality and can be used to test the BIM results in the more complicated cases that follow.

In Fig. 6.11, $\Phi_3(t)$ levels off before reaching the value of one because, for the smaller groundwater velocities, a significant part of ^{129}I decays inside the room before it can be carried away. MOTIF results depend on the source position. As the source position approaches that end of the room towards which the groundwater flow is directed, all the MOTIF curves in Fig. 6.11 move up and end up slightly above the BIM curve. For much higher Darcy velocities this is shown in Fig. 4 of LeNeveu and Kolar (1996), but it also happens for the parameters of Fig. 6.11. However, as will be discussed below in relation to Figs. 6.15 and 6.16, in more realistic calculations using the slim model and MOTIF-generated flow fields, the MOTIF release is delayed with respect to that from a fat model with constant velocities and rock at the ends. As a result, BIM seems to be always conservative with respect to the more realistic MOTIF results. The absence of rock at the ends will speed up considerably the release from the room by convection through the backfill and EDZ, when the source is near the end towards which the axial water flow is directed. (When rock is present at the ends, the flow field in this region is highly nonuniform, because there must be a transition from high water velocities in the backfill and EDZ to much smaller velocities in the rock outside; the presence of this transitional region will slow down the convection.) On the other hand, the averaging approximation

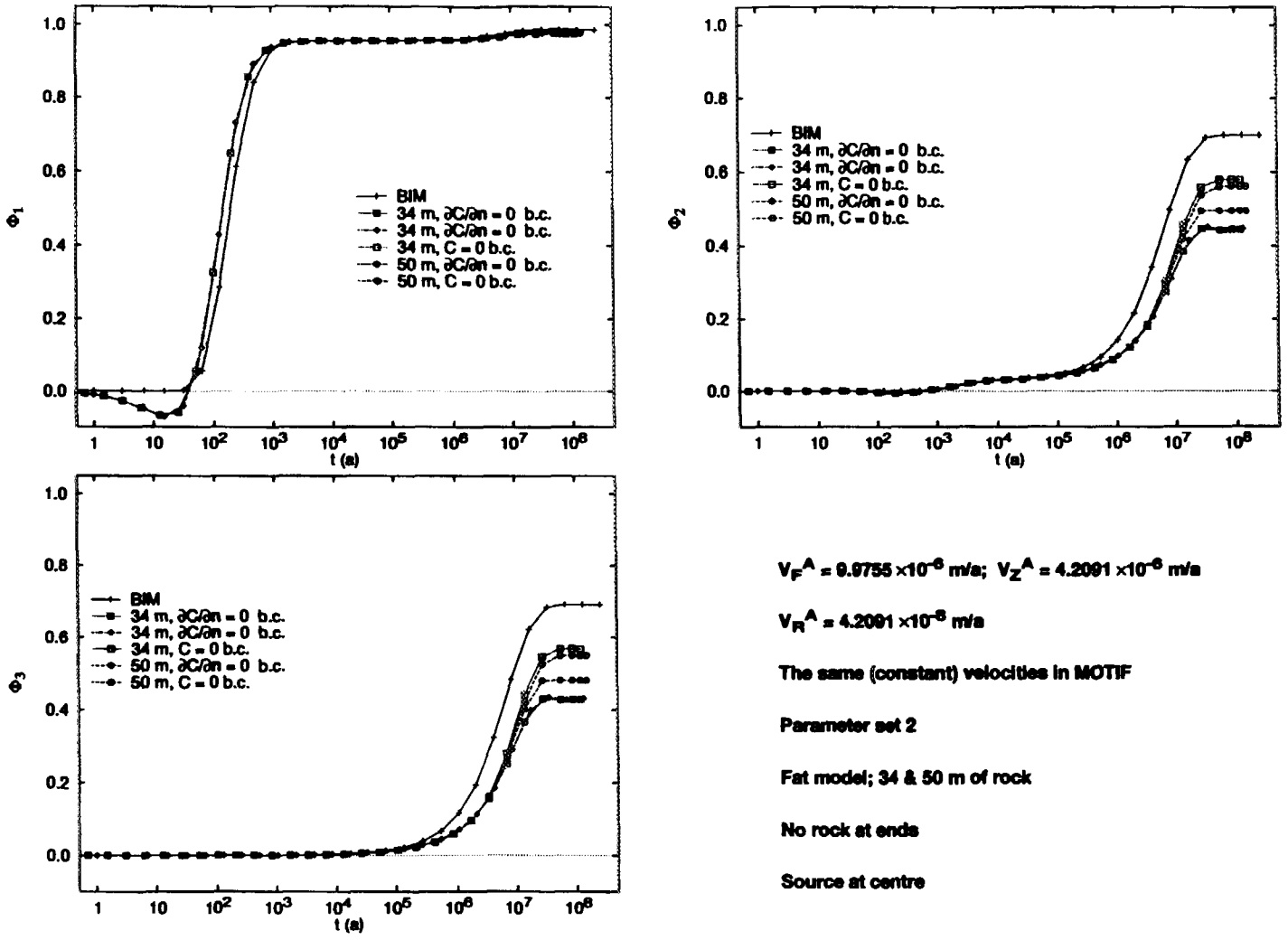

FIGURE 6.11: Comparison of the BIM Model with the Fat MOTIF Model With No Rock at the Ends Using Constant Darcy Velocities. Φ1, Φ2, and Φ3 represent the integrated fluxes of contaminant from the buffer, backfill and EDZ, respectively.

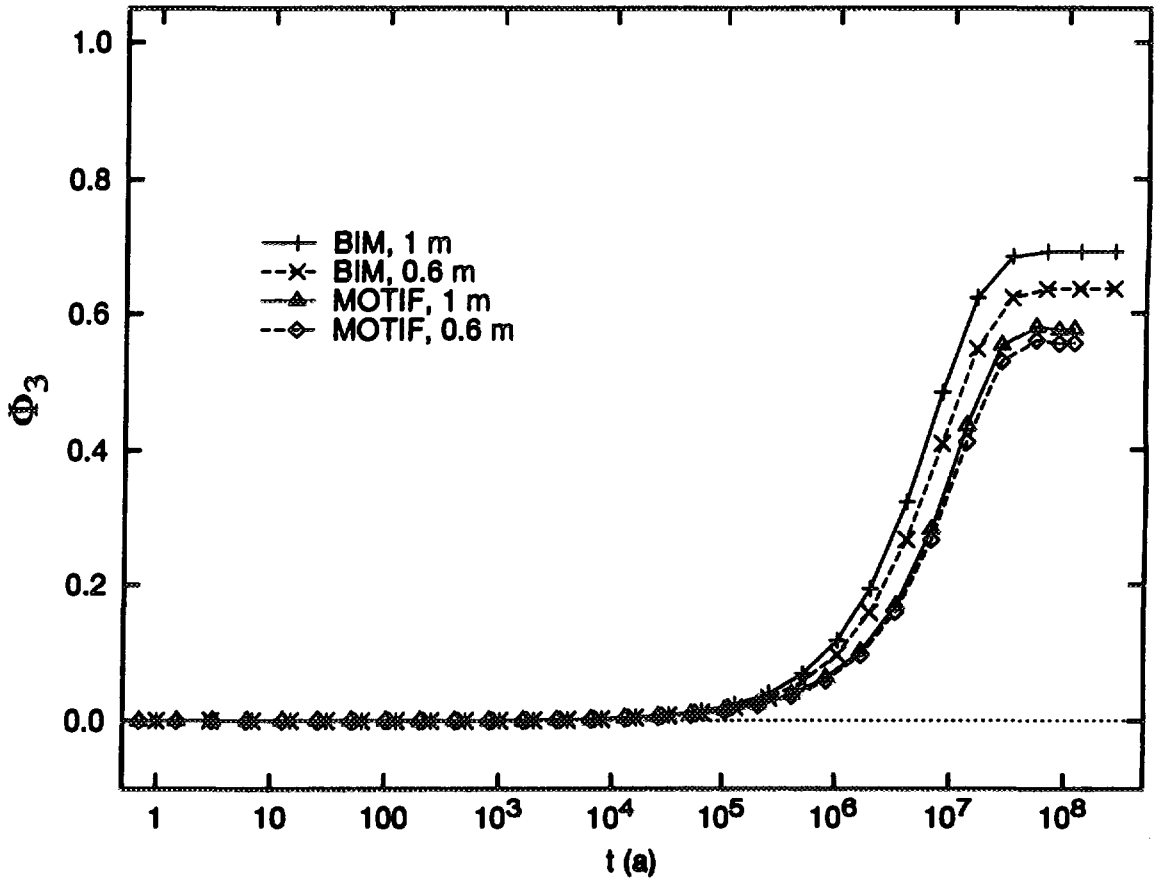

FIGURE 6.12: Dependence of the Integrated Flux of Contaminant Φ3 on the EDZ Thickness. Φ3 represents the integrated flux of contaminant from the EDZ. MOTIF uses the fat model with 50 m of rock above the room and 150 m of rock in all other directions. MOTIF calculates spatially varying velocities. The source for MOTIF is in the centre of the room.

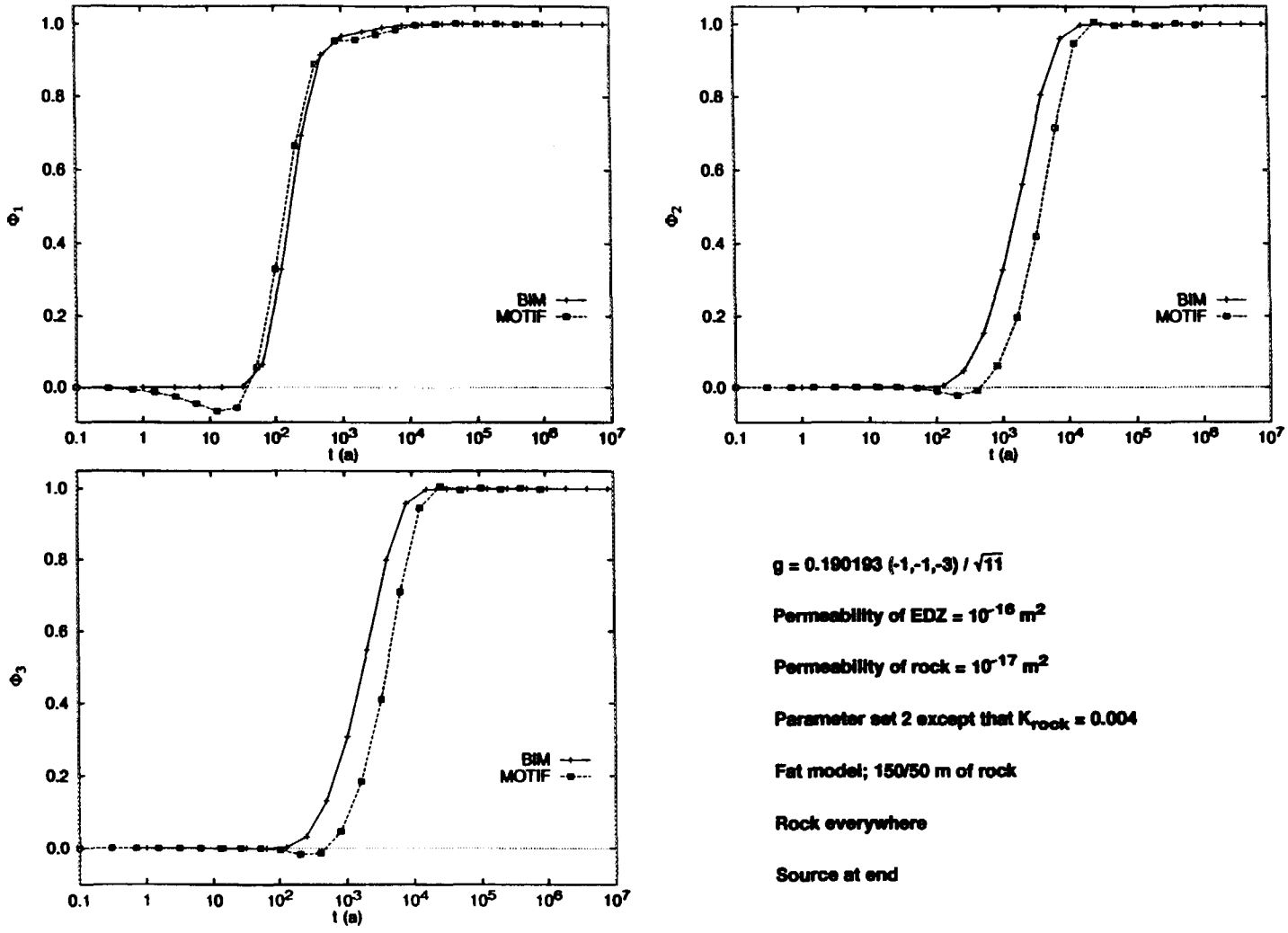

FIGURE 6.13: Comparison of the BIM Model with the Fat MOTIF Model Using Realistic Flow Field for a Very High Hydraulic Gradient of General Orientation. Φ1, Φ2, and Φ3 represent the integrated fluxes of contaminant from the buffer, backfill and EDZ, respectively.

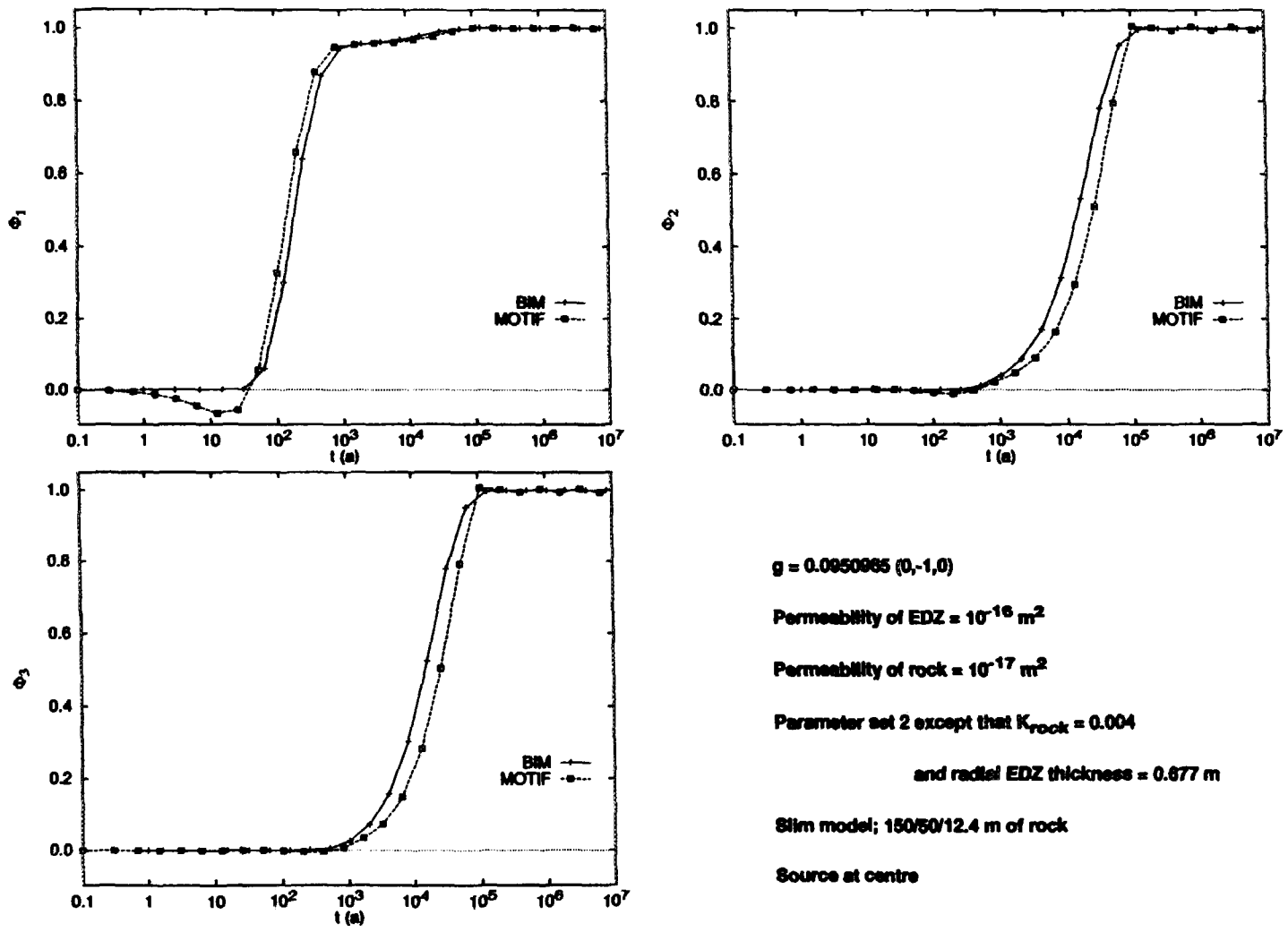

FIGURE 6.14: Comparison of the BIM Model with the Slim MOTIF Model Using Realistic Flow Field for a Very High Axial Hydraulic Gradient Orientation. Φ1, Φ2, and Φ3 represent the integrated fluxes of contaminant from the buffer, backfill and EDZ, respectively.

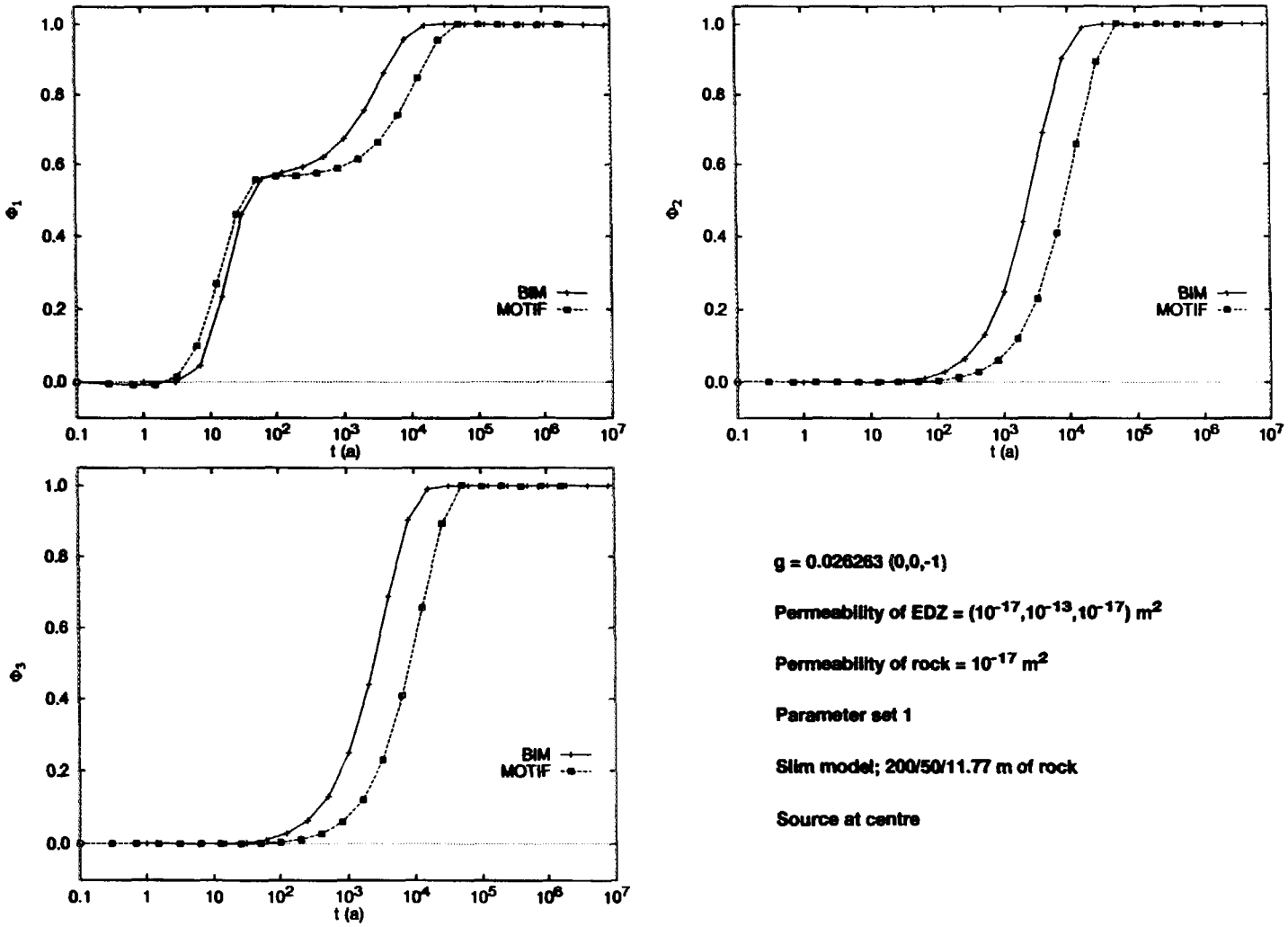

FIGURE 6.15: Comparison of the BIM Model with the Slim MOTIF Model Using Realistic Flow Field Corresponding to a Purely Vertical Hydraulic Gradient in the Presence of Anisotropic EDZ. Φ1, Φ2, and Φ3 represent the integrated fluxes of contaminant from the buffer, backfill and EDZ, respectively.

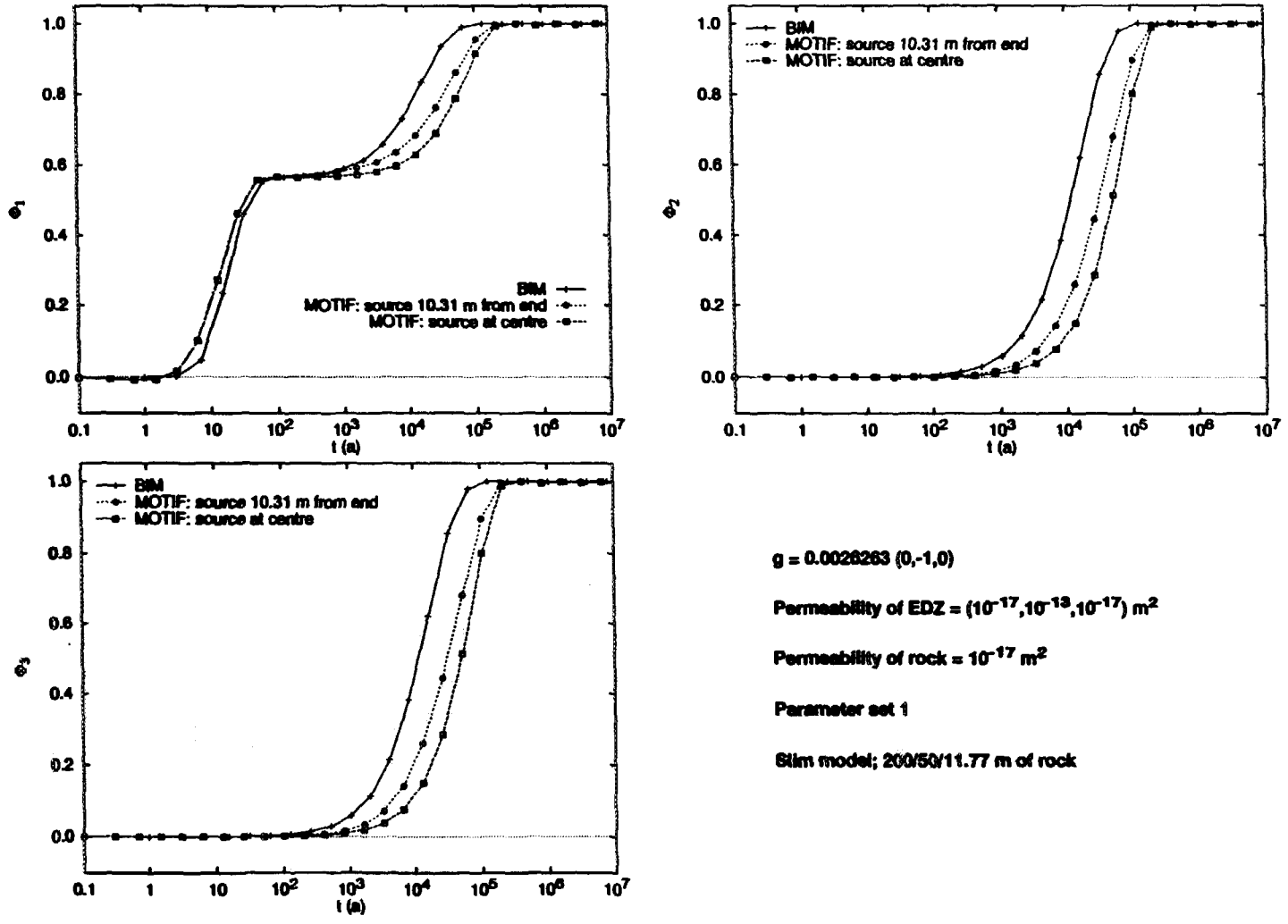

FIGURE 6.16: Comparison of the BIM Model with the Slim MOTIF Model Using Realistic Flow Field Corresponding to a Purely Axial Hydraulic Gradient in the Presence of Anisotropic EDZ. Φ1, Φ2, and Φ3 represent the integrated fluxes of contaminant from the buffer, backfill and EDZ, respectively.

used in the BIM decreases the release relative to when the source is near the outgoing end of the room because this approximation tends to spread the concentration evenly over the surface of a medium. The effect of these two approximations (absence of rock at the ends and surface averaging) apparently partially cancel each other in such a way that the BIM release is always slightly higher than the real release for any source position when there is rock at the ends.

The constant Darcy velocities in Fig. 6.11 correspond almost exactly to using the axial hydraulic gradient of 0.002 and the isotropic permeabilities $k_F = 2.37 \times 10^{-17}$ m^2, $k_Z = 10^{-17}$ m^2, and $k_R = 10^{-19}$ m^2, in Eqs. (6.12) and (6.13). Figure 6.12 shows the first realistic MOTIF results (by realistic we mean here that MOTIF generates the flow field itself as described in the beginning of this section - see Eq. (6.14)). The above values of hydraulic gradient and permeabilities are used together with parameter set 2 of Table 6-2 (except that the EDZ thickness is varied as indicated in Fig. 6.12 where the MOTIF EDZ thickness is given: parameter set 2 corresponds to the MOTIF EDZ thickness of 1 m) in a fat model with 150 m of rock in all directions, with the unit source at the centre. Mixed boundary conditions are used: the C = 0 swept-away boundary condition on the top (representing a major fracture zone) and $\partial C/\partial \mathbf{n} = 0$ everywhere else. (These mixed boundary conditions are also used in Figs. 6.13 through 6.16. As mentioned above, the type of boundary condition really does not matter for a thickness of rock of 150 m. The results are affected, however, when the distance to the fracture zone above the room is only 50 m, as in all the cases that follow. Then the C = 0 boundary condition on the top plane is important.) Comparing Figs. 6.11 and 6.12 shows that the MOTIF results for the 1 m case are almost the same, indicating that at least for this case the MOTIF geometry and the way of generating the flow field is not very important.

Figure 6.12 shows that the BIM and the MOTIF results change in the same direction when the thickness of the EDZ is changed. A proper treatment of the EDZ in the BIM model is important because its properties have a considerable influence on the release from the room. The results show that the integrated release increases as the thickness of the EDZ increases. Thus, the EDZ does not act as a barrier, but as a preferential pathway for transport out of the room. The thicker the EDZ, the faster the transport.

Figure 6.13 compares the BIM and MOTIF results for an oblique angle of the hydraulic gradient. This comparison can be done only in the fat model, thus neglecting the presence of the neighbouring rooms, as discussed in the introduction to this section. The gradient is oriented mainly downward, resulting in a primarily upward flow, but it also has an axial (y) and a transverse horizontal (x) component. In BIM the transverse (x and z) components are represented by the radial flow. The permeability of the backfill is again $k_F = 2.37 \times 10^{-17}$ m^2; it is the same in all the comparisons made here. Again, there is 150 m of rock on the five sides of the room and only 50 m above the room. All other parameters are indicated in the figure. The agreement between the BIM and MOTIF results seems to be very satisfactory for this very large hydraulic gradient ($V_R = 0.000605$ m·a^{-1}) which is much larger than what one expects to encounter even in the present case of the very permeable host rock. This agreement suggests that the BIM

model representation of the transverse components of the real flow by a radial flow works very well.

Figure 6.14 compares the results of the two approaches for another unrealistically high value of the hydraulic gradient. This time the flow is purely axial and the slim model (with only 12.4 m of rock on the sides), taking into account in an approximate way the presence of the neighbouring rooms, is used. In this case, because of the very high axial groundwater velocities, MOTIF shows some oscillations at about 10^5 a, but the agreement between the two approaches is very good.

In Figs. 6.15 and 6.16, the same BIM results as in Figs. 2 and 4 of LeNeveu and Kolar (1996) are used, and compared with realistic MOTIF calculations. The corresponding hydraulic gradients are at the higher end of the range of values one can encounter in the present geosphere. Figure 6.15 is for purely vertical flow, and again confirms the conclusion that the BIM representation of the transverse flows is adequate.

Figure 6.16 shows that, unlike the constant-velocity fat MOTIF calculations of Fig. 4 of LeNeveu and Kolar (1996), the realistic MOTIF calculations seem to yield release that is always (i.e., for an arbitrary source position) delayed with respect to the BIM release (see also the discussion of Fig. 6.10 above). It thus seems that the BIM model always gives results that are conservative.

6.4.3 Justification of the Use of BIM

We wish to employ the best available technology to model radionuclide release and mass transport in the vault. The finite-element method is well developed but is unsuitable for a detailed probabilistic assessment of the proposed disposal system for several reasons. Some of these reasons have been discussed above. Because of the resolution and scale problems inherent in the finite-element method, it is only possible to simulate a small number of disposal rooms. In fact, a model of a single room, as reported above, strained the capabilities of the technique. Since the method is finite in nature it is necessary to impose artificial boundary conditions on the external surfaces of the model. In the room-scale finite-element model, above, both zero-flux and zero-concentration boundary conditions were applied. Neither is really appropriate. The rock is essentially semi-infinite in extent with spatially variable properties, bounded above by the surface biosphere. The finite-element method suffers from unquantified inaccuracies as evidenced by the oscillations in the solutions as reported above. In our experience, the computer resources required to implement the finite-element method are so large as to render probabilistic assessments impossible. To apply the method for a daughter radionuclide would require the input of sources at every node in the model derived from the solution of the system for the parent. This process would have to be repeated for each chain member. The method is not sufficiently accurate or economical on computational resources for simulations of decay chains to be feasible. It would also be very difficult to implement the variety of source conditions used in the vault model, such as congruent dissolution, solubility-controlled release, and precipitation within the container.

The BIM is more than 10^4 times computationally more efficient than the finite-element method for this simulation system. With the BIM we are able to perform a probabilistic assessment. The BIM is semi-infinite in spatial extent. Artificial boundary conditions are imposed only at the ends of the room where their ability to distort the solution are very limited. Provided the occurrence of changing medium properties in the surrounding rock occur sufficiently far away from the room, BIM is well suited for this disposal geometry and is inherently more accurate than the finite-element method. Inaccuracies arise primarily in the inversion of the Laplace transform solution and these inaccuracies are quantified with an explicit error estimation. A further quality assurance and accuracy check has been implemented into the BIM by comparing the time-integrated area under the response functions for the buffer, backfill and EDZ with a separate solution to the time-integrated area provided by direct numerical inversion of the Laplace transform solution of this area. The BIM uses some approximations, namely, use of integrated continuity conditions at the boundaries between different media, a cylindrical room cross-section rather than an oval cross-section, and constant medium parameters such as groundwater velocity which would otherwise be spatially variable. These approximations have, by comparison to the finite-element solution, been shown to be acceptable. With the BIM we have simulated twenty four vault sectors, for twenty eight radionuclides, and three decay chains. We have repeated these simulations thousands of times to attain a reliable estimate of dose consequence and have encountered no significant inaccuracies or numerical instabilities in any of these simulations.

6.5 RESULTS FROM EXAMPLE SIMULATIONS

6.5.1 Introduction

To illustrate the vault model, four example simulations have been analyzed in some detail. The first is a median value simulation where all input parameters were fixed at their median values except those parameters controlling container failure. The parameters controlling container failure were adjusted so that one container failed in each of the twenty-four vault sectors. The other three simulations presented here are the ones giving the highest, second highest and lowest maximum dose consequences from thirty-two simulations where the input parameters were sampled from a fractional-factorial latin hypercube design (FFLH). These four simulations are referred to as the median simulation, simulation 27, simulation 31, and simulation 3, referring to the median value, highest dose FFLH, second highest dose FFLH and lowest dose FFLH simulations, respectively. These are the same system simulations referred to by Goodwin et al. (1996a). In the four example simulations, sixteen fission products and activation products and three actinide decay chains (4n+1, 4n+3, and 4n+2) were simulated. Radionuclides in the used fuel and Zircaloy are treated as separate species. For instance ^{14}C from used fuel, is differentiated from ^{14}C from Zircaloy which is designated as $^{14}C(Z)$. The fission products and activation products simulated are: ^{14}C, $^{14}C(Z)$, ^{36}Cl, $^{36}Cl(Z)$, ^{135}Cs, ^{137}Cs, ^{129}I, ^{93}Zr->^{93m}Nb, ^{107}Pd, ^{79}Se, ^{126}Sn=^{126}Sb, ^{90}Sr=^{90}Y and ^{99}Tc. The equal sign (=) indicates that the radionuclides were modeled as being in secular equilibrium. The arrow (->) indicates that the radionuclides were modeled as being in a decay chain.

The actinides simulated are:

4n+1 chain: ^{241}Am->^{237}Np->^{233}Pa->^{233}U->^{229}Th=^{225}Ra=^{225}Ac

4n+3 chain: ^{243}Am=^{239}Np->^{239}Pu->^{235}U->^{231}Th->^{231}Pa=^{227}Ac=^{227}Th=^{223}Ra

4n+2 chain: ^{238}U=^{234}Th->^{234}U->^{230}Th->^{226}Ra=^{222}Rn=^{210}Pb=^{210}Bi=^{210}Po.

Twenty-four vault sectors were used for these example simulations. These interface with twenty-four geosphere segments (Stanchell et al. 1996). Thus, the spatial discretization of the vault model was the same as the discretization used in the geosphere model. The simulations were carried out to ten million years.

In addition to these simulations, which assumed that the copper container defect size remains constant with time, example simulations were done for the case where the inner carbon-steel shell remains watertight for 1000 a and the defect in the copper shell becomes enlarged due to corrosion-product formation (see Chapter 2.6).

Table 6-3 gives the maximum dose rates of the four highest contributors within ten million years for the four example simulations.

TABLE 6-3

HIGHEST CONTRIBUTORS TO MAXIMUM DOSE ($Sv \cdot a^{-1}$)

FOR THE EXAMPLE SIMULATIONS

Median		Simulation 27		Simulation 31		Simulation 3	
^{129}I	4.6×10^{-6}	^{129}I	1.3×10^{-5}	^{129}I	1.2×10^{-5}	^{36}Cl	6.9×10^{-9}
^{36}Cl	1.1×10^{-7}	^{79}Se	6.3×10^{-8}	^{36}Cl	1.5×10^{-7}	^{129}I	4.0×10^{-9}
^{79}Se	6.5×10^{-8}	^{36}Cl	7.9×10^{-8}	^{126}Sn	6.9×10^{-9}	^{126}Sn	1.4×10^{-12}
^{126}Sb	3.1×10^{-8}	^{126}Sb	4.8×10^{-8}	^{126}Sb	2.9×10^{-9}	^{135}Cs	9.7×10^{-13}

Table 6-3 illustrates that there is some variability in the contributors to maximum dose rate. Further analysis of a large number of simulations reveals that ^{129}I is, on average, the largest contributor to maximum dose consequence up to 10^7 years, followed by ^{126}Sb, ^{99}Tc, ^{79}Se, and ^{90}Sr (Goodwin et. al. 1996a). Based on these results only the following seven fission products and actinides are discussed in detail here: ^{129}I, ^{90}Sr, ^{36}Cl, ^{99}Tc, ^{79}Se, ^{126}Sn, and ^{135}Cs. Analysis of ^{126}Sb is not necessary because it is assumed to be in secular equilibrium with ^{126}Sn.

6.5.2 Model Inputs

In this section, we attempt to explain the results from the vault model in terms of the inputs to the model. This is a difficult task given the fact that there are more than five thousand input parameters for the system model. Four simulations are inadequate to elucidate the sensitivity of the system to the input parameters; however some understanding of the behaviour of the models can be gained by examining the four example simulations in detail. We focus here on the input parameters to the vault model, which are:

parameters determining the number of failed containers
initial inventories of the radionuclides
instant release fraction
parameters determining radiolytic dissolution of used fuel
solubility of zirconium
effective radius of defect in container
length of the pinhole
internal volume of container
internal porosity of container
total intrinsic diffusion coefficient in pinhole
porosity of pinhole
disposal room length
total intrinsic diffusion coefficient in buffer
radial and axial components of Darcy velocity in backfill, EDZ and rock
radionuclide capacity factors in buffer, backfill, EDZ and rock
radionuclide diffusion coefficient in free water
radionuclide decay constants
tortuosity of rock and EDZ
porosity of rock and EDZ
parameters determining solubility
parameters determining groundwater velocities in the media.
number of vault sectors

Some of the above parameters are constant such as:

length of the pinhole
internal volume of the container
porosity of the pinhole
internal porosity of the container
disposal room length
number of vault sectors and
radionuclide decay constants.

Although the features of the physical system for the model are, in part, determined by the constant parameters, the results from the model will not be sensitive to these parameters because they do not vary. For this reason we focus the discussion on those parameters that

do vary. The overall system sensitivity analysis, discussed by Goodwin et al. (1996a), indicates that two sets of vault parameters can be discerned as being important to dose consequence: (i) parameters determining the number of failed containers and (ii) parameters determining the amount of used fuel dissolved. The axial permeability of the EDZ is also an influential parameter. We attempt to explain these sensitivities as well as the overall behaviour of the vault model, with reference to each of the variable parameters listed above.

6.5.2.1 Parameters Determining the Number of Failed Containers

Two sampled parameters and a constant parameter determine the number of containers having initial defects. They are the probability of failure for a single container, a binomial probability variate and the number of containers in a sector (LeNeveu 1994). In the median simulation, the first two of these parameters were adjusted so that one container failed in each vault sector. The number failing in other simulations varies. The number of failures in each sector in the four example simulations is illustrated in Fig. 6.17. As discussed earlier, sensitivity analysis indicates that the number of containers failing is important in determining the dose consequence.

6.5.2.2 Initial Inventories for the Radionuclides

The probability distributions describing the initial radionuclide inventories are described in Appendix A. The variability in initial inventories for the four example simulations is illustrated in Fig. 6.18, which shows it to be very small; thus, intial inventories are determined not to be important parameters in the overall sensitivity analysis. Although not important, the relative initial inventory, radiotoxicity, mobility and half-life determine the overall dose potential of a radionuclide. For instance, ^{129}I has a relatively large initial inventory, is very mobile and very long-lived. These factors account for its major contribution to dose consequence. Technetium-99 has a larger initial inventory than ^{129}I and is more radiotoxic but less mobile; therefore, ^{99}Tc does not have as large an influence on dose consequence. The radiotoxicity is generally related to the half-life. Fission products and activation products with short half-lives tend to be more radiotoxic; however, many of these will decay in the vault before causing any consequence to man and the accessible environment.

6.5.2.3 Instant-Release Fractions

The input distributions for the instant release fractions are given in Chapter 5.3.1. The values in the four example simulations are shown in Fig. 6.19. The variability in the values of the instant release fractions as shown by Fig. 6.19 is quite small. A substantial portion of the fuel, relative to the instant release, dissolves as a result of beta and gamma radiolysis at relatively short times. Because of these two factors, dose consequence is not very sensitive to the instant release fraction.

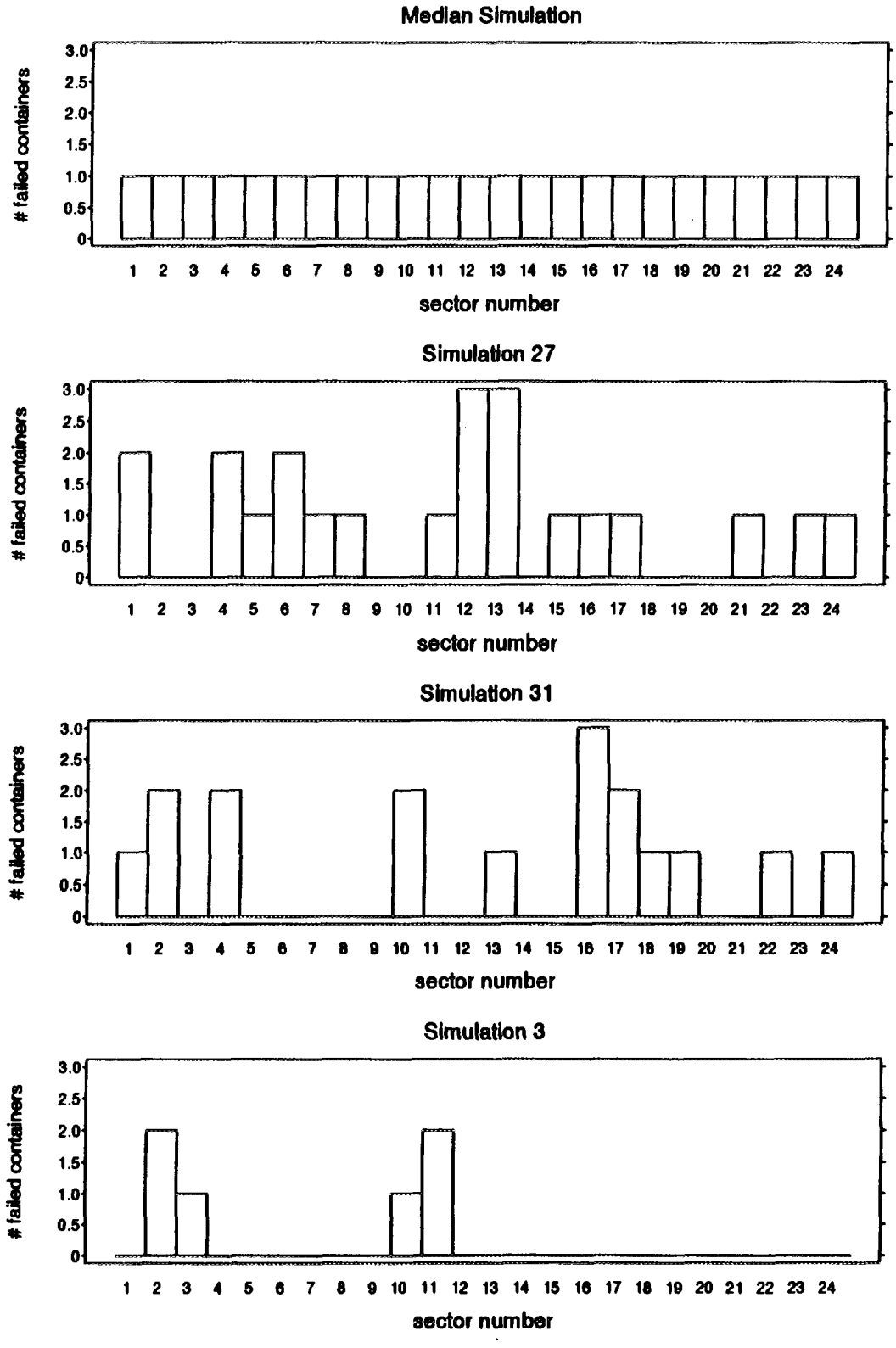

FIGURE 6.17 Number of Containers Failing in Each Sector for Four Simulations

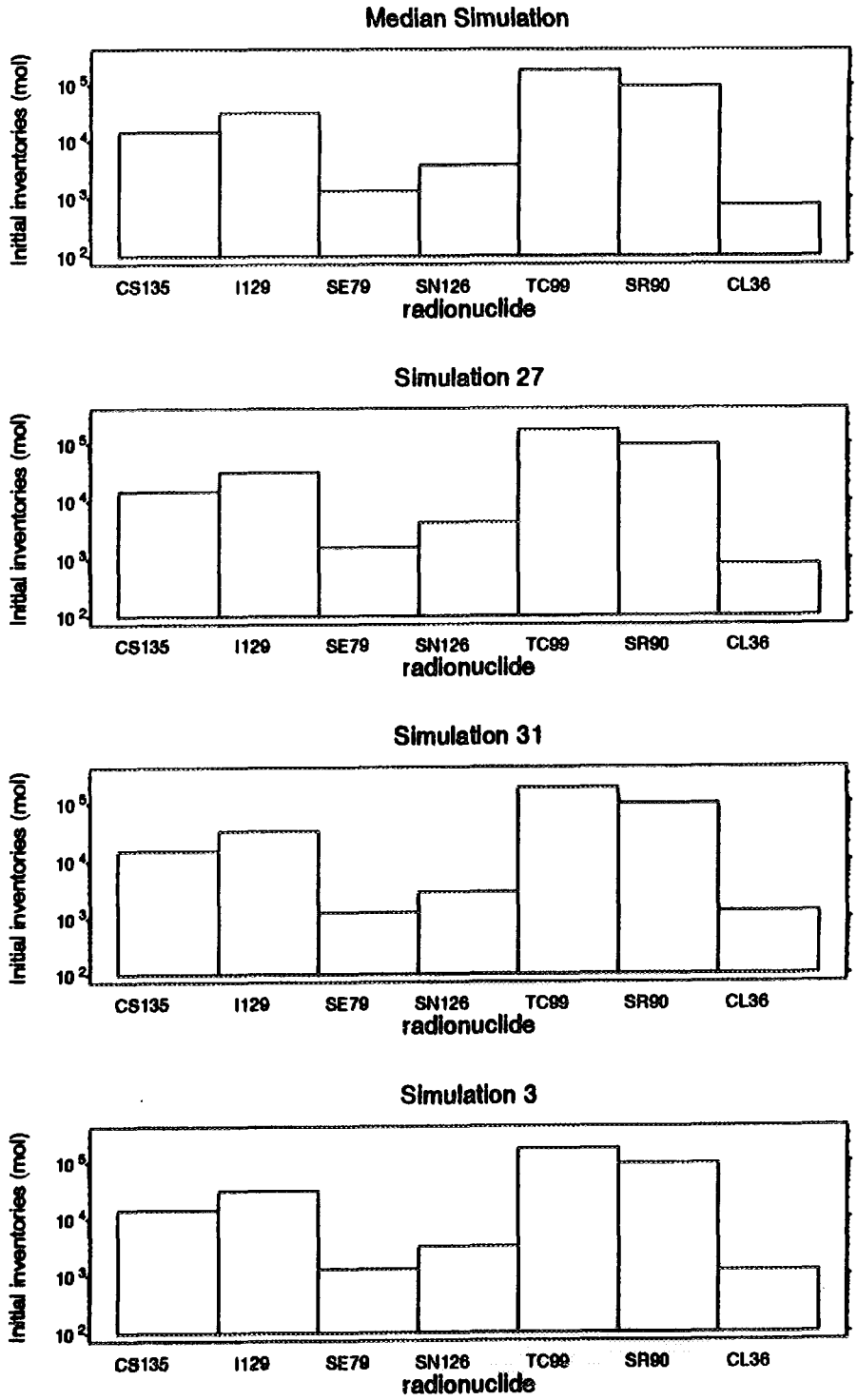

FIGURE 6.18: Initial Inventories of ^{135}Cs, ^{129}I, ^{79}Se, ^{126}Sn, ^{99}Tc, ^{90}Sr and ^{36}Cl for Four Simulations

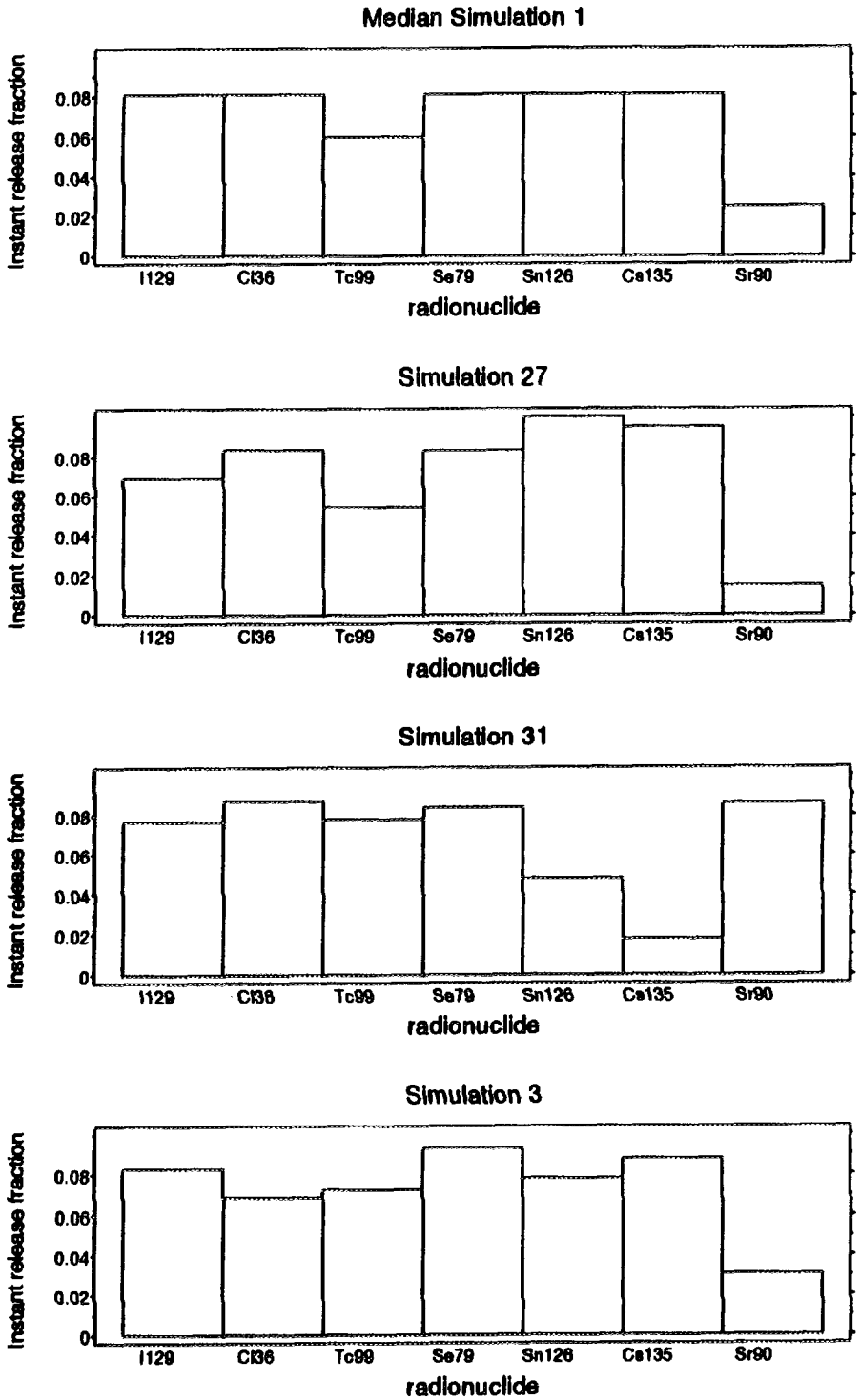

FIGURE 6.19: Instant Release Fraction for Four Simulations

6.5.2.4 Radiolytic Dissolution of Used Fuel

There are many parameters that determine the corrosion rate of used fuel (see Chapter 5.3). A single calculated variable, the total fraction of the fuel matrix dissolved up to 10^7 a captures the effect of these parameters. The fraction of fuel dissolved for the four example simulations is given in Table 6-4 below.

TABLE 6-4

FRACTION OF FUEL DISSOLVED UP TO 10^7 YEARS FOR THE EXAMPLE CALCULATIONS

median simulation	3.6×10^{-1}
simulation 27 (highest dose)	8.9×10^{-1}
simulation 31 (second highest dose)	5.6×10^{-1}
simulation 3 (lowest dose)	1.0

Although there is considerable variability associated with this parameter, the simulation giving the highest dose to the critical group is not the same as the simulation having the highest amount of fuel dissolved. The main reasons for this are that the large variability in some parameters in the bioshpere model tends to overwhelm the impact of the relatively small range in dissolution fraction and that four simulations are inadequate to determine sensitivity in this complex system. Sensitivity analysis based on many more simulations reveal that parameters determining the amount of fuel dissolved are important in determining dose consequence (Goodwin et al. 1996a).

The fraction of the fuel dissolved can be quite large, to the extent that in one simulation the entire amount of used fuel dissolves before 10^7 a. This is a reflection of the very conservative nature of the dissolution model and is somewhat misleading. Figure 6.20 shows the fraction of fuel dissolved as a function of time for the four example simulations. Between about 10^2 a and about 10^5 a the fraction dissolved remains at a relatively constant plateau value. Since the peak release rate from the vault for most of the major contributors to dose consequence has occurred before this time it is the plateau value that is important in influencing the dose. The plateau values of the fraction of fuel dissolved are about the same as the instant release fractions or smaller. We might expect that these two parameters would be equally important in determining dose consequence. Because the fraction of fuel dissolved has much more variability than the instant release fraction, sensitivity analysis determines parameters controlling the fraction of fuel dissolved to be important and the instant release fraction to be unimportant. At very long times the conservative use of a corrosion rate model that neglects back reaction and resulting equilibrium conditions results in a large portion of the fuel being dissolved.

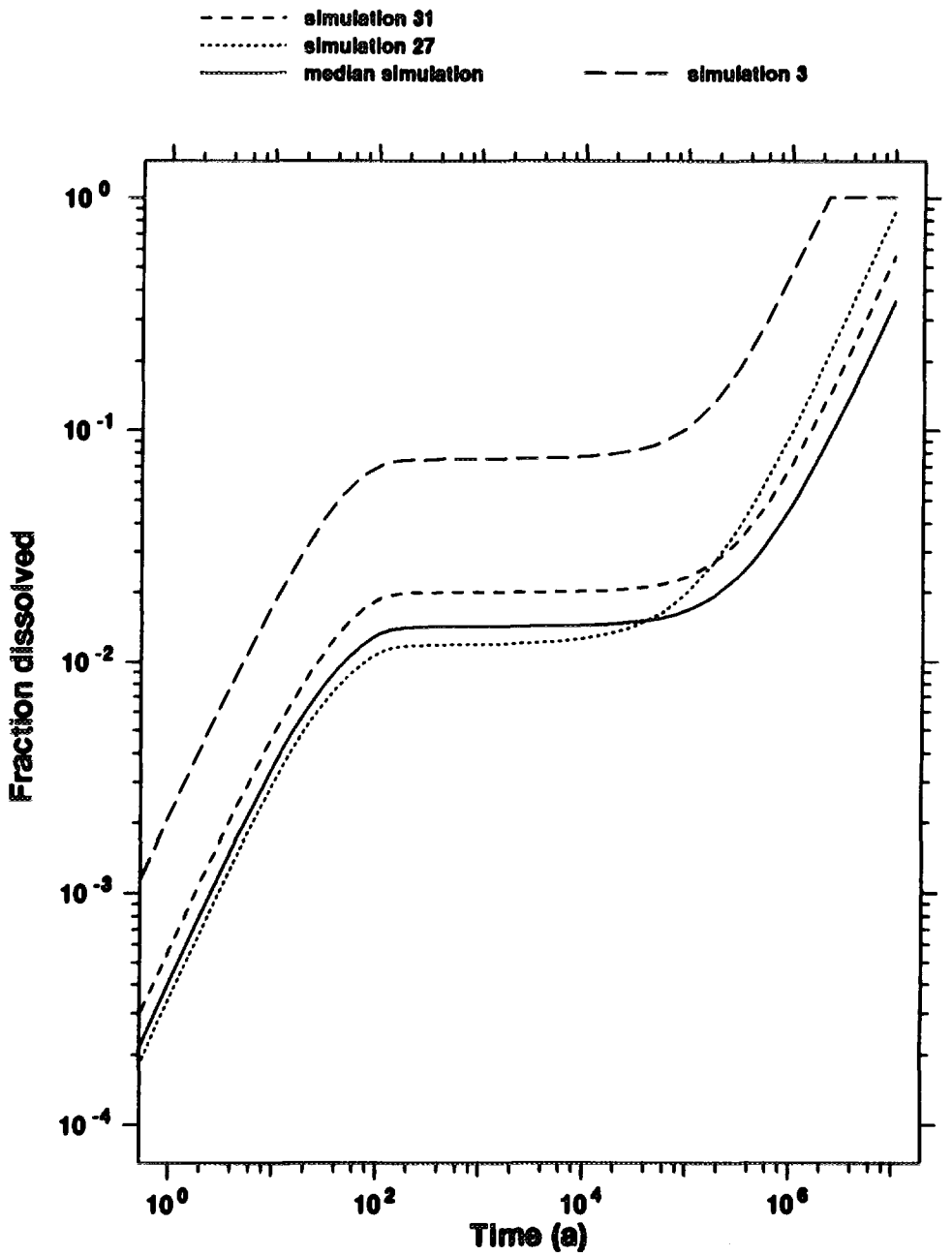

FIGURE 6.20: Fraction of Fuel Dissolved as a Function of Time for Four Simulations

6.5.2.5 Solubility of Zirconium

The radionuclides in the zirconium matrix are insignificant contributors to the dose consequence and thus do not warrant further analysis at this time.

6.5.2.6 Effective Radius of the Defect in the Container

This is the most important parameter controlling the mass transfer rate through the pinhole defect because the other parameters are either constant, such as length of the pinhole, or have small variability, such as diffusion coefficients in the buffer and in the pinhole. The defect radius is varied from sector to sector for each simulation and also from simulation to simulation. The variability for the four example simulations is illustrated in Fig. 6.21. This parameter is important in determining the maximum release rate from each vault sector. This is discussed in more detail later in this section. It is not very important, however, in the overall sensitivity analysis because the variability in defect radius over all sectors tends to average out and thereby diminish the influence of this parameter on the dose consequence.

6.5.2.7 Dispersion and Diffusion Coefficients

Dispersion coefficients are determined from diffusion coefficients and groundwater velocities according to the following simplified formula:

$$D_i = D_I + a_T V_i + a_L V_i \qquad (6.20)$$

Here D_i is the ith component of the dispersion coefficient, V_i is the ith component of the Darcy velocity, D_I is the total intrinsic diffusion coefficient, a_T is the transverse dispersion length and a_L is the longitudinal dispersion length. The distributions for the dispersion lengths in the backfill and EDZ are given in Appendix B. Dispersion lengths in the rock are a sampled fraction of the segment length in the geosphere (Stanchell et. al. 1996).

Since no groundwater movement is assumed to occur in the buffer and in the pinhole, the total intrinsic diffusion coefficients in the pinhole and in the buffer control mass transport in these media. The variability in the values of the total intrinsic diffusion coefficients in the pinhole and buffer for the four example simulations is given in Table 6-5.

The variability of the intrinsic diffusion coefficients in the pinhole and buffer is small for these simulations (less than a factor of 2 in the pinhole and a factor of five in the buffer). These parameters are not found to be important in the overall sensitivity analysis.

The diffusion coefficients in the backfill, EDZ and rock are inconsequential because, with the relatively large convective flow field associated with this assessment, the diffusion coefficients have a negligible contribution to the dispersion coefficients. The probability distributions for parameters determining diffusion and dispersion are discussed in more

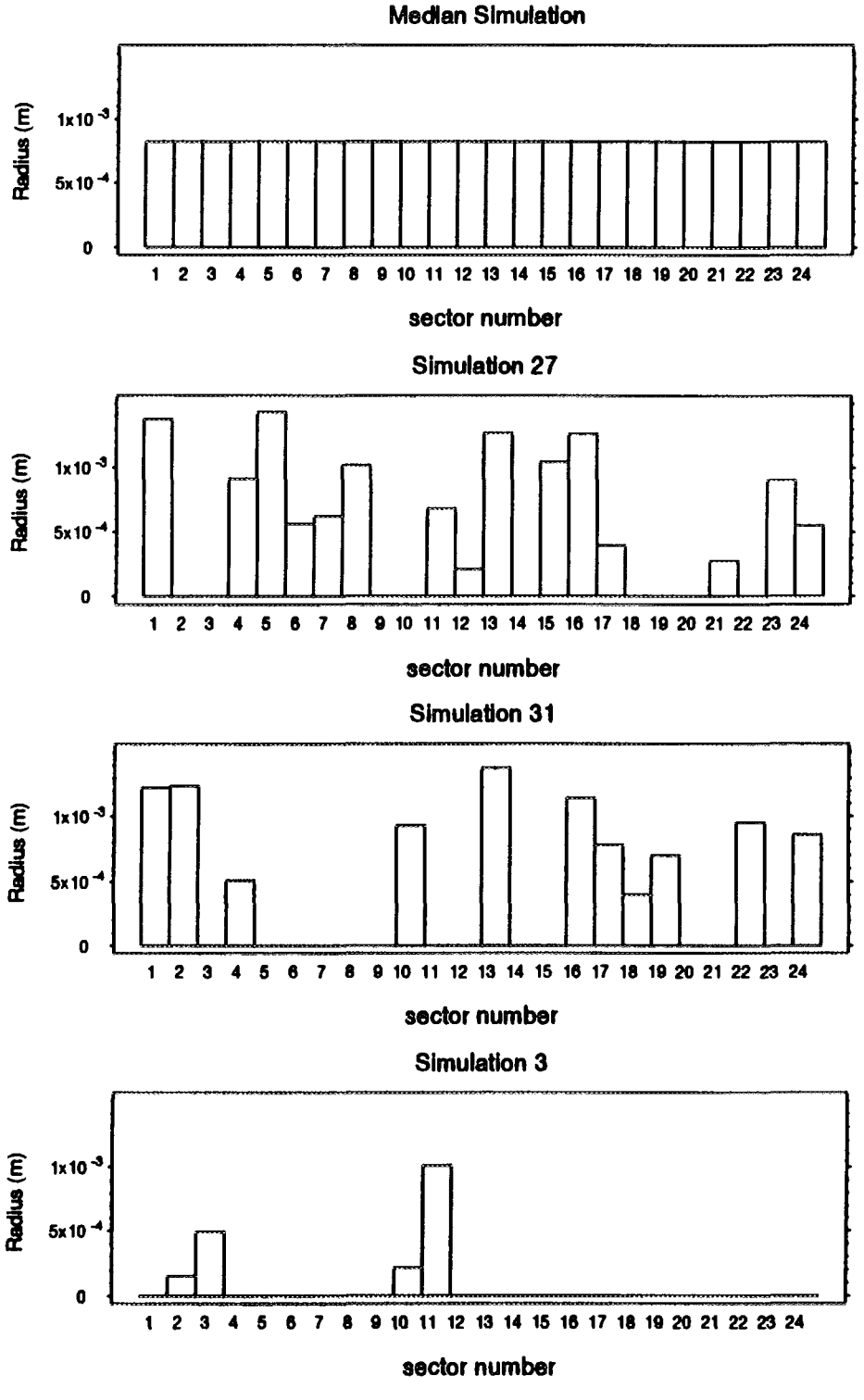

FIGURE 6.21: Effective Radius of Defect in Container for Four Simulations

TABLE 6-5

INTRINSIC DIFFUSION COEFFICIENTS FOR THE EXAMPLE SIMULATIONS

Simulation	Pinhole ($m^2 \cdot a^1$)	Buffer ($m^2 \cdot a^1$)
median simulation	9.4×10^{-2}	6.9×10^{-3}
simulation 27 (highest dose)	1.0×10^{-1}	5.3×10^{-3}
simulation 31 (second highest dose)	1.0×10^{-1}	1.1×10^{-2}
simulation 3 (lowest dose)	1.0×10^{-1}	2.2×10^{-3}

detail in Appendix B. The value of the dispersion coefficient depends on the groundwater velocities as well as dispersion lengths. Thus, variability and importance of dispersion coefficients is related to the variability and importance of groundwater velocity. The variability in groundwater velocities for the four example simulations is illustrated in Figs. 6.22 to 6.26 for the rock, EDZ and the backfill.

6.5.2.8 Capacity Factors

Capacity factors and solubilities determine the relative mobility of the radionuclides. As discussed previously, relative mobility together with intial inventory and radiotoxicity determine the relative importance of the radionuclides. Capacity factors are chemical element and media specific and vary from simulation to simulation. The general formula for determination of capacity factors, r is:

$$r = \varepsilon + \rho_b K_d \qquad (6.21)$$

Here K_d is the radionuclide and medium-specific distribution coefficient, ρ_b is the bulk dry density of the medium, and ε is the porosity of the medium.

The variability of capacity factors for the elements, I, Cl, Tc, Se, Sn, Cs and Sr in the buffer, backfill, EDZ and rock for the four example simulations are illustrated in Fig. 6.27. The variability in this parameter for different radionuclides can be very large, spanning many orders of magnitude. Chlorine and iodine are not sorbed in any of the four media so the respective capacity factors depend only on the porosity of the media. The porosity of the EDZ is about three orders of magnitude smaller than that of the buffer and backfill. Technetium is moderately sorbed in the buffer, strongly sorbed in the backfill and not sorbed in the EDZ and rock. Selenium is slightly sorbed in all the media. Tin is moderately sorbed in all the media. Strontium is moderately sorbed in the buffer and backfill and weakly sorbed in the EDZ and rock. Cesium is quite strongly sorbed in all media.

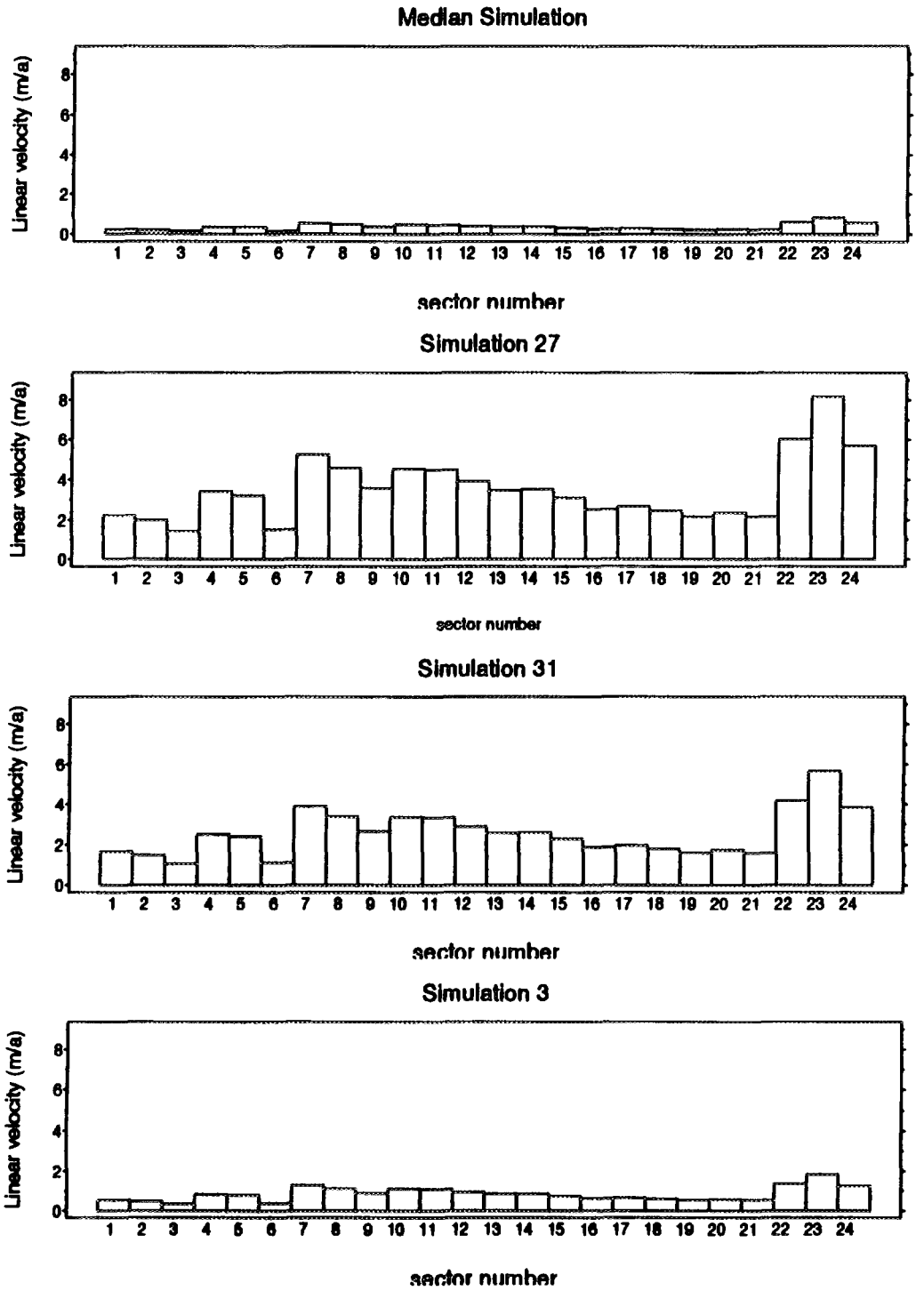

FIGURE 6.22: Average Linear Velocities in the Rock for Four Simulations

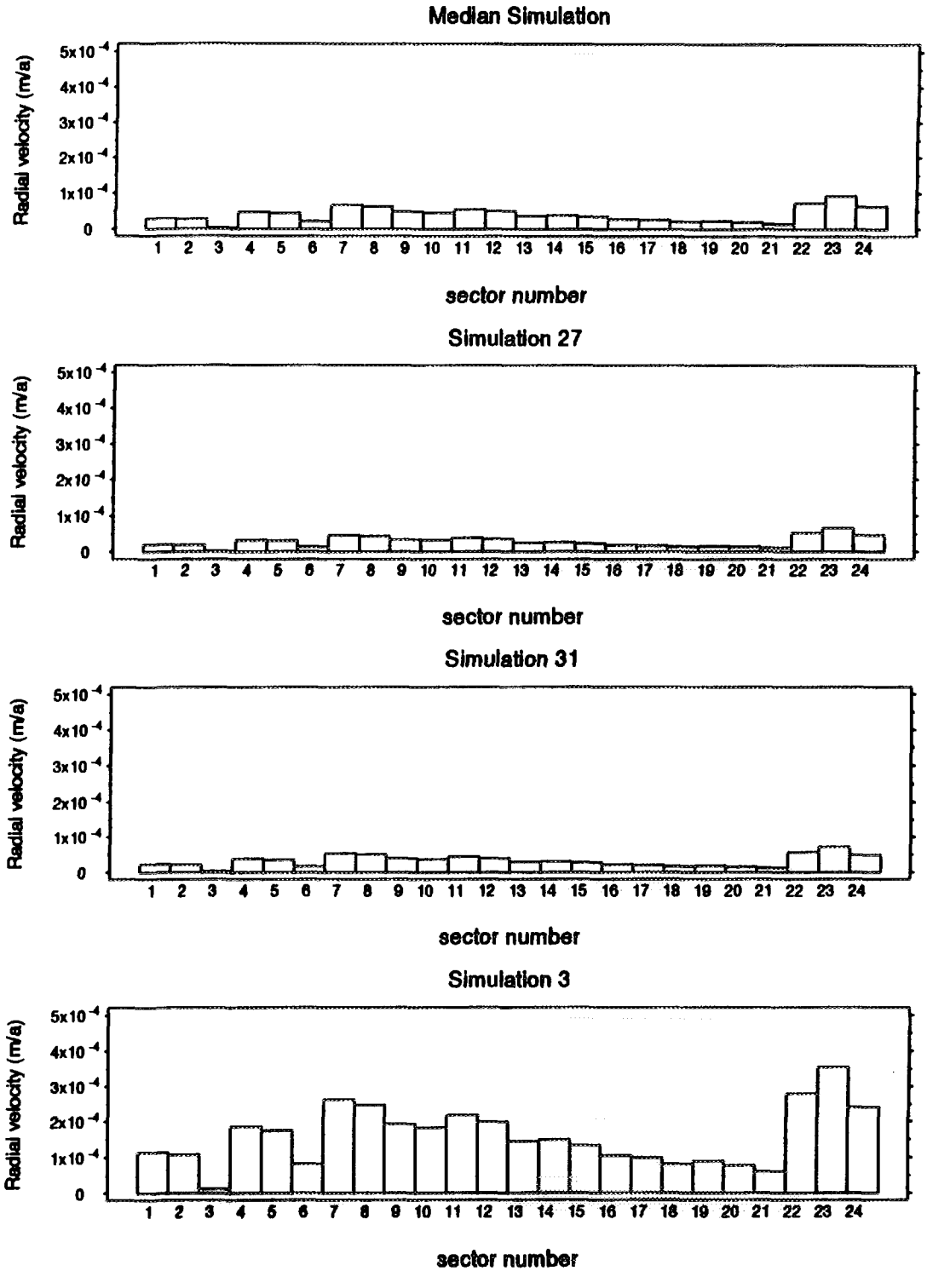

FIGURE 6.23 Radial Darcy Velocities in the EDZ for Four Simulations

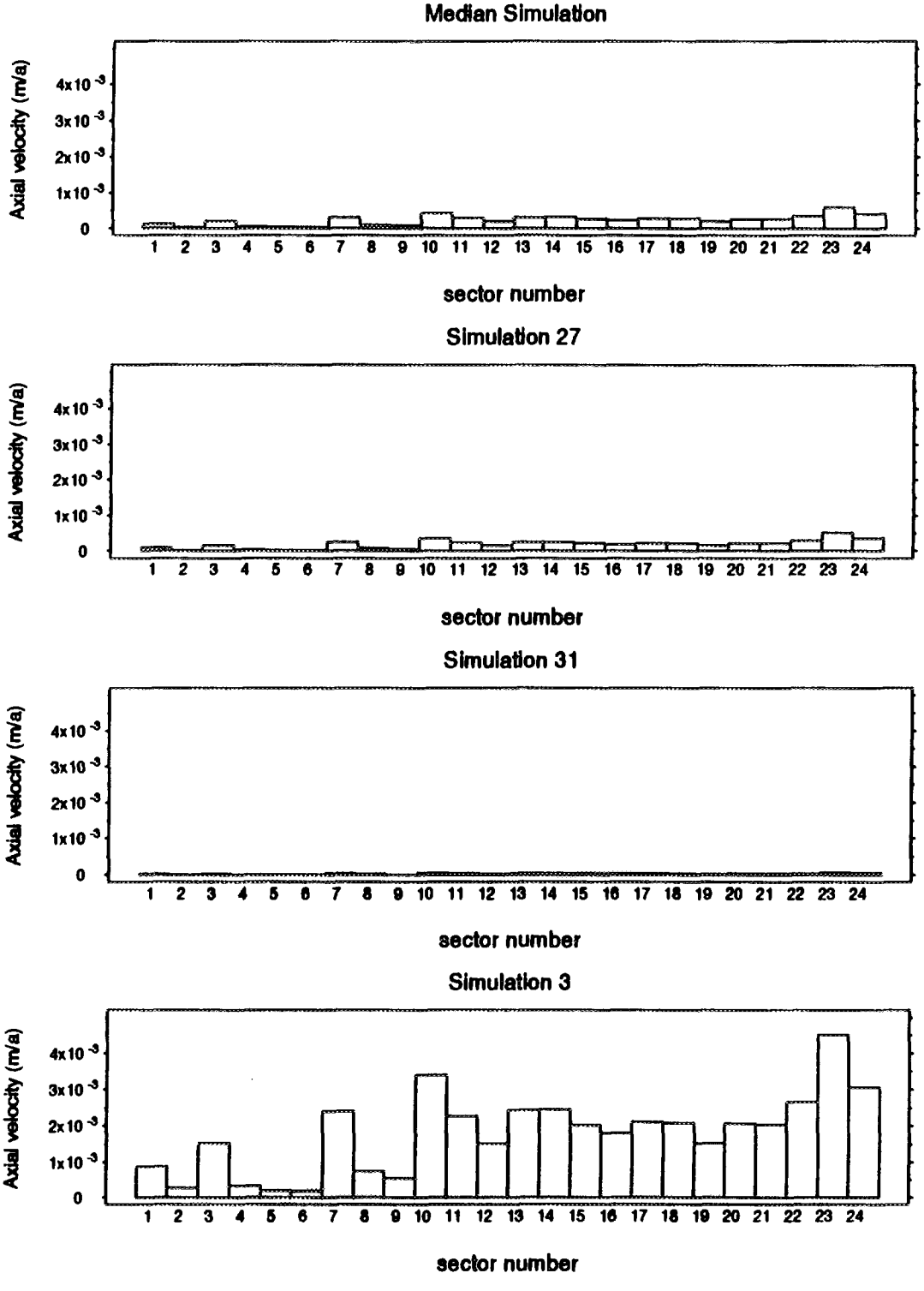

FIGURE 6.24 Axial Darcy Velocities in the EDZ for Four Simulations

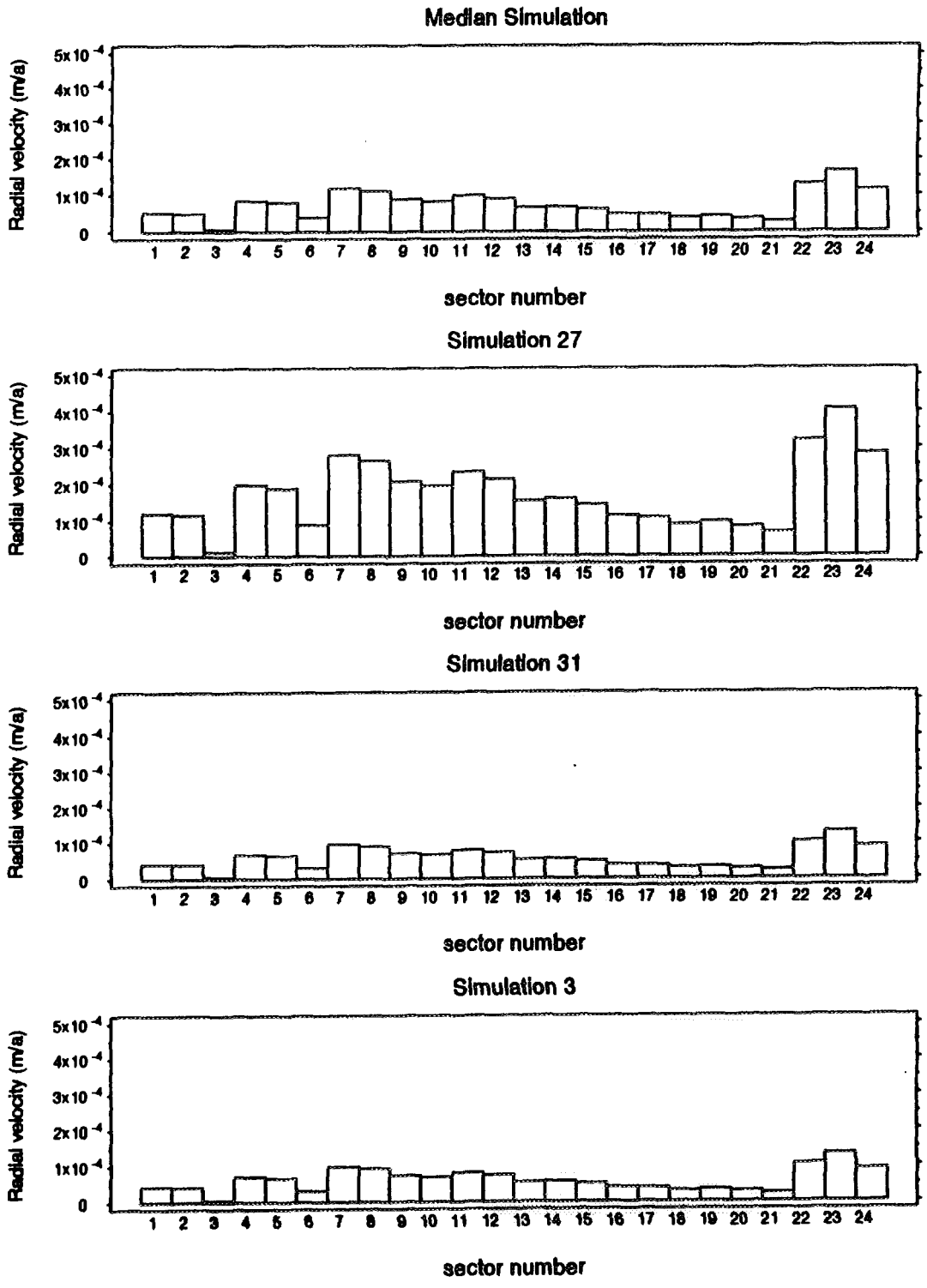

FIGURE 6.25: Radial Darcy Velocities in the Backfill for Four Simulations

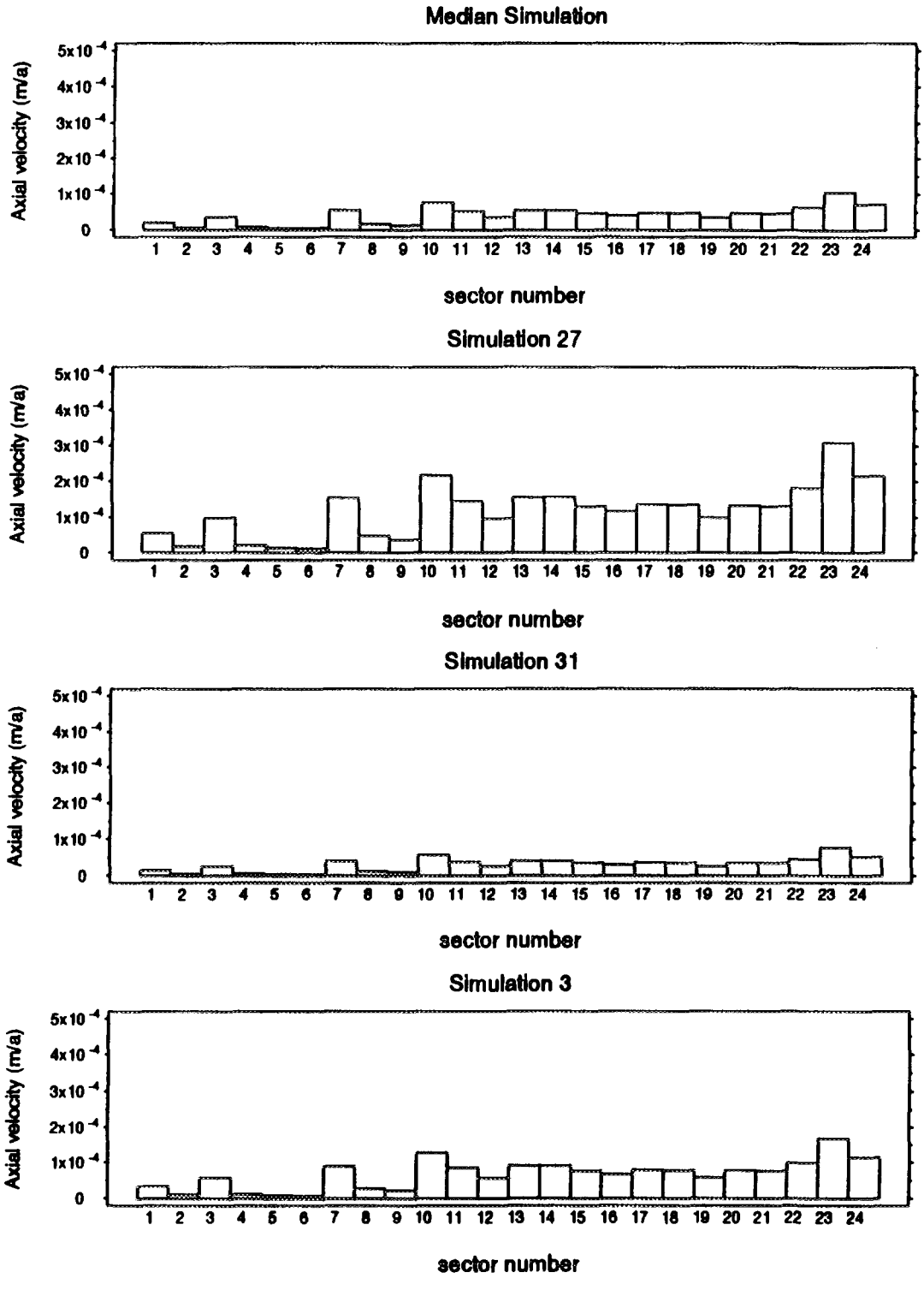

FIGURE 6.26: Axial Darcy Velocities in the Backfill for Four Simulations

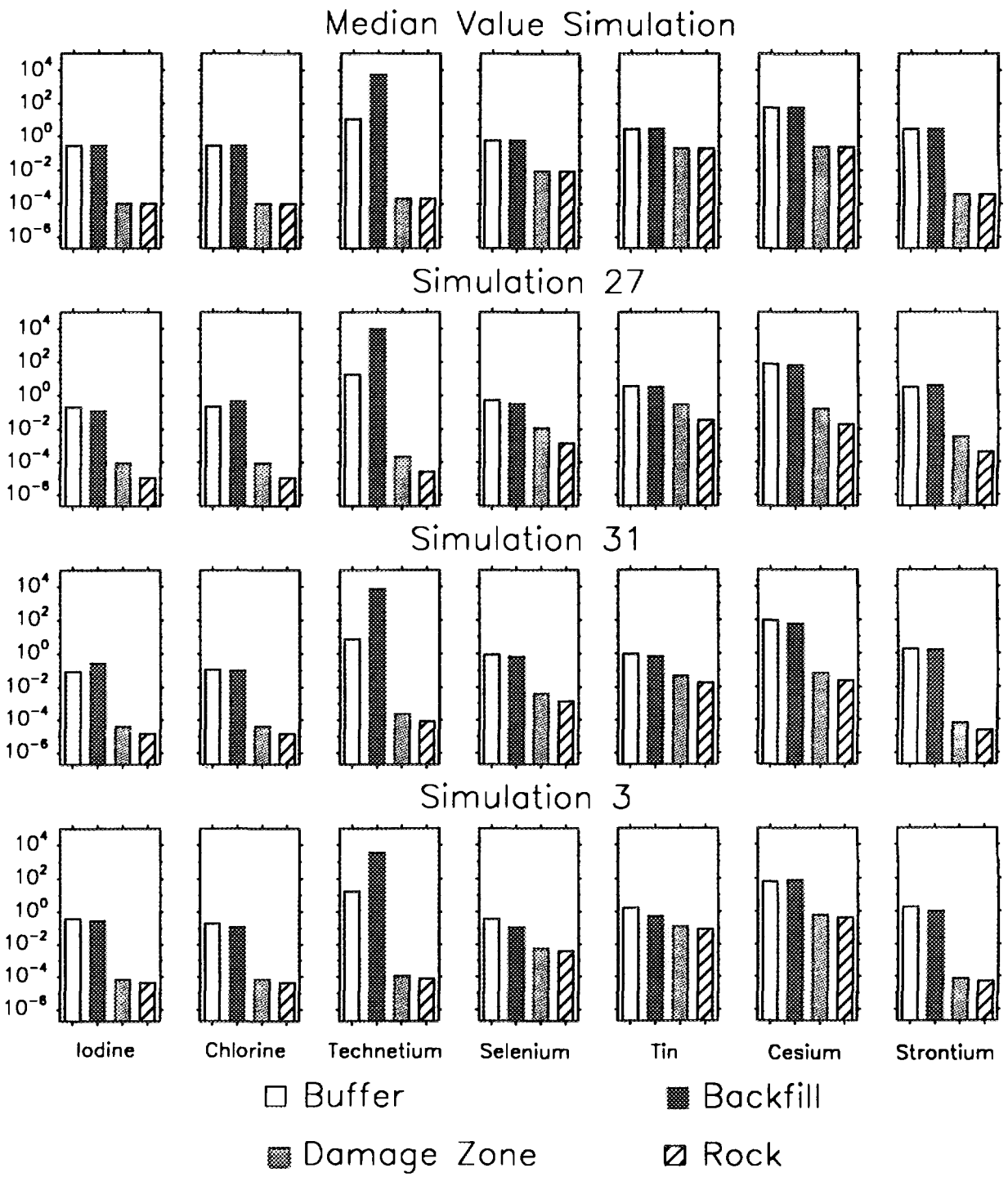

FIGURE 6.27: Capacity Factors In and Around a Vault Room for Four Simulations

6.5.2.9 Tortuosity

The tortuosity of the EDZ and rock affect the total intrinsic diffusion coefficients of radionuclides in these media. As discussed earlier the total intrinsic diffusion coefficients make a negligible contribution to dispersion coefficients and thus should not effect the release from the vault. Tortuosity of rock has an influence in determining effective pathlengths in the geosphere model, and therefore this parameter could potentially have some importance in the performance of the geosphere. In fact the overall sensitivity analysis does not reveal tortuosity of the rock as an important parameter. This is discussed further by Goodwin et al. (1996a). The tortuosity of the EDZ is not an important parameter because convection dominates mass transport in this region of the vault.

6.5.2.10 Porosity

The porosity of the EDZ and rock is used to determine capacity factors and to determine average linear groundwater velocities. The variation in porosities for the four example simulations is given in Table 6-6.

TABLE 6-6

POROSITIES IN THE EDZ AND ROCK FOR THE EXAMPLE SIMULATIONS

	EDZ	Rock
median simulation	1.0×10^{-4}	1.0×10^{-4}
simulation 27 (highest dose)	8.6×10^{-5}	1.0×10^{-5}
simulation 31 (second highest dose)	3.9×10^{-5}	1.4×10^{-5}
simulation 3 (lowest dose)	6.4×10^{-5}	4.4×10^{-5}

In this assessment the Darcy velocities in the rock are constant from simulation to simulation. The porosity of the rock and EDZ are sampled. This means that the average linear velocity, obtained by dividing the Darcy velocity by the porosity, varies from simulation to simulation. This is illustrated in Fig. 6.22. Since the porosity of the EDZ and rock influence both capacity factors and velocities, we might expect that the porosity of the EDZ and rock would have some influence on dose consequence. Overall sensitivity analysis, however, indicates that the influence of these parameters is not large.

6.5.2.11 Solubilities

As discussed earlier, solubilities for five elements, Tc, Pu, Th, U and Np are calculated based on a large number of sampled thermodynamic and geochemical parameters. The remainder of the elements, except for Zr which is sampled from a truncated normal distribution, are given constant maximum solubilities as discussed in Chapter 5.4. Of the fission products and activation products, only the solubility of Tc is small enough to lead to

precipitation. The values of the solubility of Tc in the four example simulations is given in Table 6-7.

TABLE 6-7

SOLUBILITIES OF Tc FOR THE EXAMPLE SIMULATIONS

	solubility ($mol \cdot m^{-3}$)
median simulation	1.53×10^{-3}
simulation 27 (highest dose)	5.06×10^{-5}
simulation 31 (second highest dose)	3.29×10^{-5}
simulation 3 (lowest dose)	3.04×10^{-2}

6.5.2.12 Groundwater Velocities

The Darcy velocities in the rock are determined from the finite-element code MOTIF (Stanchell et al. 1996) and are constant for all simulations. The porosity of the rock is sampled; thus, the average linear velocity in the rock varies from simulation to simulation and from segment to segment as shown in Fig. 6.22. The radial and axial components of the Darcy velocities in the EDZ and backfill are determined from the components of the Darcy velocities in the rock as explained in Chapter 6.2. Their pattern of variation from sector to sector matches the pattern of variation in the linear velocities in the rock. The radial and axial Darcy velocities in the EDZ and backfill vary from simulation to simulation because the parameters used in their determination are sampled. The variation of the components of the Darcy velocities in the EDZ and backfill are illustrated in Figs. 6.23 to 6.26.

These figures show that the Darcy velocities in the EDZ are about one order of magnitude higher than in the backfill and about two orders of magnitude higher than in the rock. The axial velocities in the EDZ are larger than the radial, while the radial velocities in the backfill are larger than the axial. These patterns are consistent with the values of the hydraulic head gradients and the relative permeabilities in the media. In particular, the EDZ is anisotropic having a greater permeability in the axial direction. The backfill and rock have isotropic permeabilities. The backfill has a somewhat larger permeability than the rock. Vertical head gradients tend to be larger than horizontal in the vicinity of the vault.

The other notable feature of these velocity patterns is that when the Darcy velocities in the EDZ are relatively small in a simulation, the backfill Darcy velocities are relatively large. As explained in Chapter 6.2, Darcy velocities in the EDZ and backfill are determined by water mass balance with the Darcy velocities in the rock. The EDZ and backfill tend to share the available water so that the relative velocities in these two media tend to complement each other. Overall sensitivity analysis indicates that the axial permeability of

the EDZ is an influential parameter. Both the axial and radial velocities in the EDZ are dependent on this parameter.

6.5.3 Fission-Product and Activation-Product Release Rates from Vault Barriers

In this section, we discuss release rates of various radionuclides through the vault barriers. After failure of the container, the vault barriers can be classified as, the used fuel, the defect in the container, the precipitate, the buffer, the backfill and the EDZ.

Release rates for the median simulation from these barriers are illustrated in Figs. 6.28 through 6.34 for the fission and activation products ^{129}I, ^{36}Cl, ^{90}Sr, ^{79}Se, ^{126}Sn, ^{135}Cs and ^{99}Tc. The general behaviour of the first six of these radionuclides is similar.

6.5.3.1 Release from the Used Fuel and Zircaloy into the Container

The release rate from the used fuel and Zircaloy into the interior of the container is the sum of the instant and congruent release. The instant release is shown as a narrow pulse at the left-hand side of the figures. The area under the pulse is equal to the instant-release inventory. The congruent release rate is governed largely by radiolysis. Initially, the dissolution rate due to oxidant production from beta and gamma radiolysis is relatively high but after a few hundred years it diminishes. Subsequently, (except for ^{90}Sr which decays relatively soon) there is a period of relatively constant release rate caused by alpha radiolysis and a low constant dissolution rate of the fuel. Ultimately the congruent release rate drops off sharply due to radioactive decay except for ^{129}I which has a half-life greater than the simulation time.

6.5.3.2 The Release Rate Out of the Container Without Solubility Constraints

The release rate out of the container for radionuclides that do not have solubility constraints is determined by mass transfer through the pinhole. The pinhole offers a very large mass transfer resistance and provides a large reduction in maximum radionuclide release rate.

6.5.3.3 The Release Rate Out of the Container With Solubility Constraints (Precipitation)

Of the seven example fission products and actinides, precipitation occurs only for ^{99}Tc because of its relatively low solubility. The release from the precipitate remains constant at a small value until the amount of precipitate in the container becomes exhausted. At this time the release rate drops sharply becoming equal to the release rate from the pinhole in the absence of precipitation. Precipitation significantly reduces release rates from the container when it occurs.

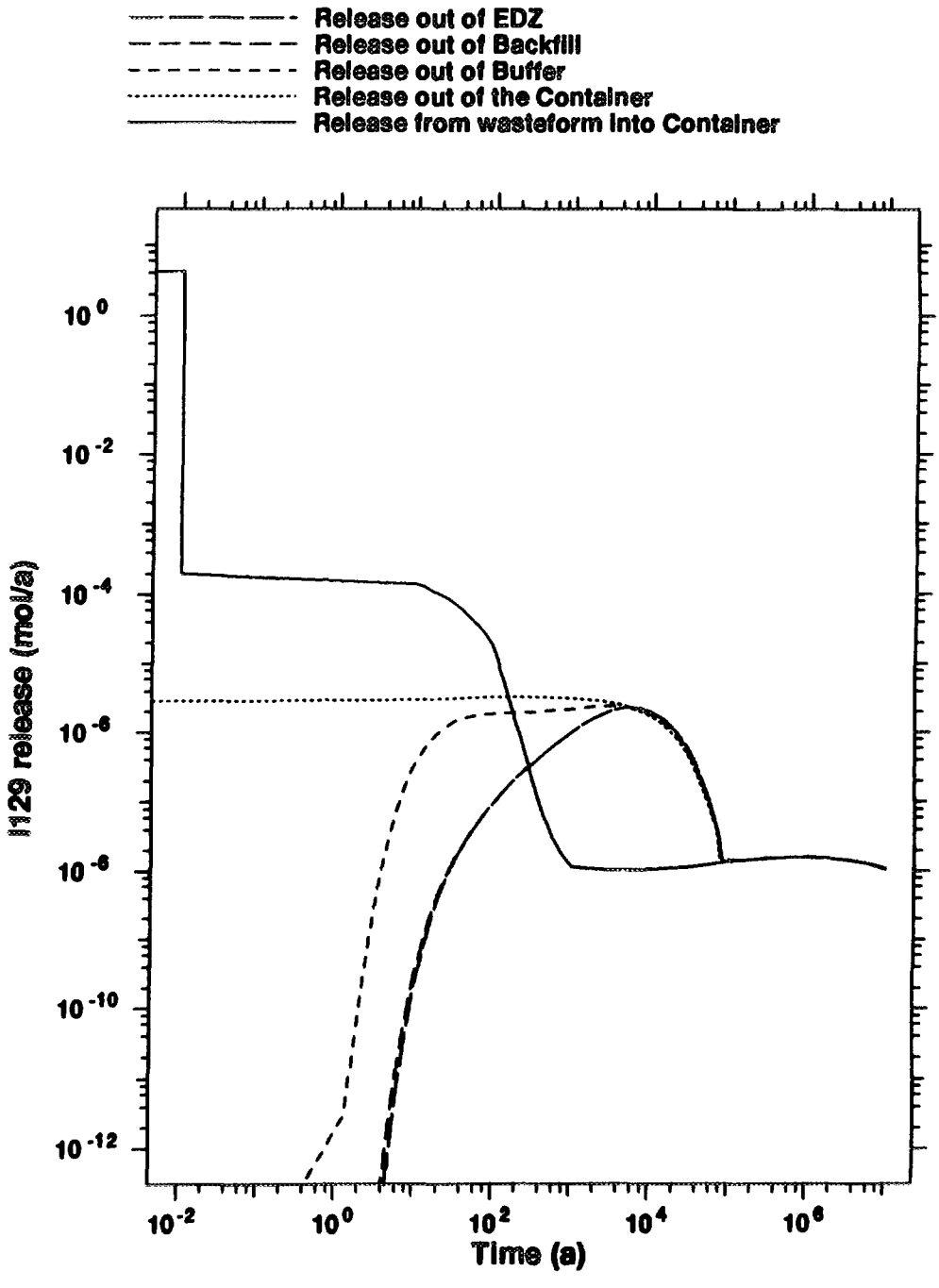

FIGURE 6.28: Release Rates of ^{129}I from Vault Sector 11 for the Median Simulation

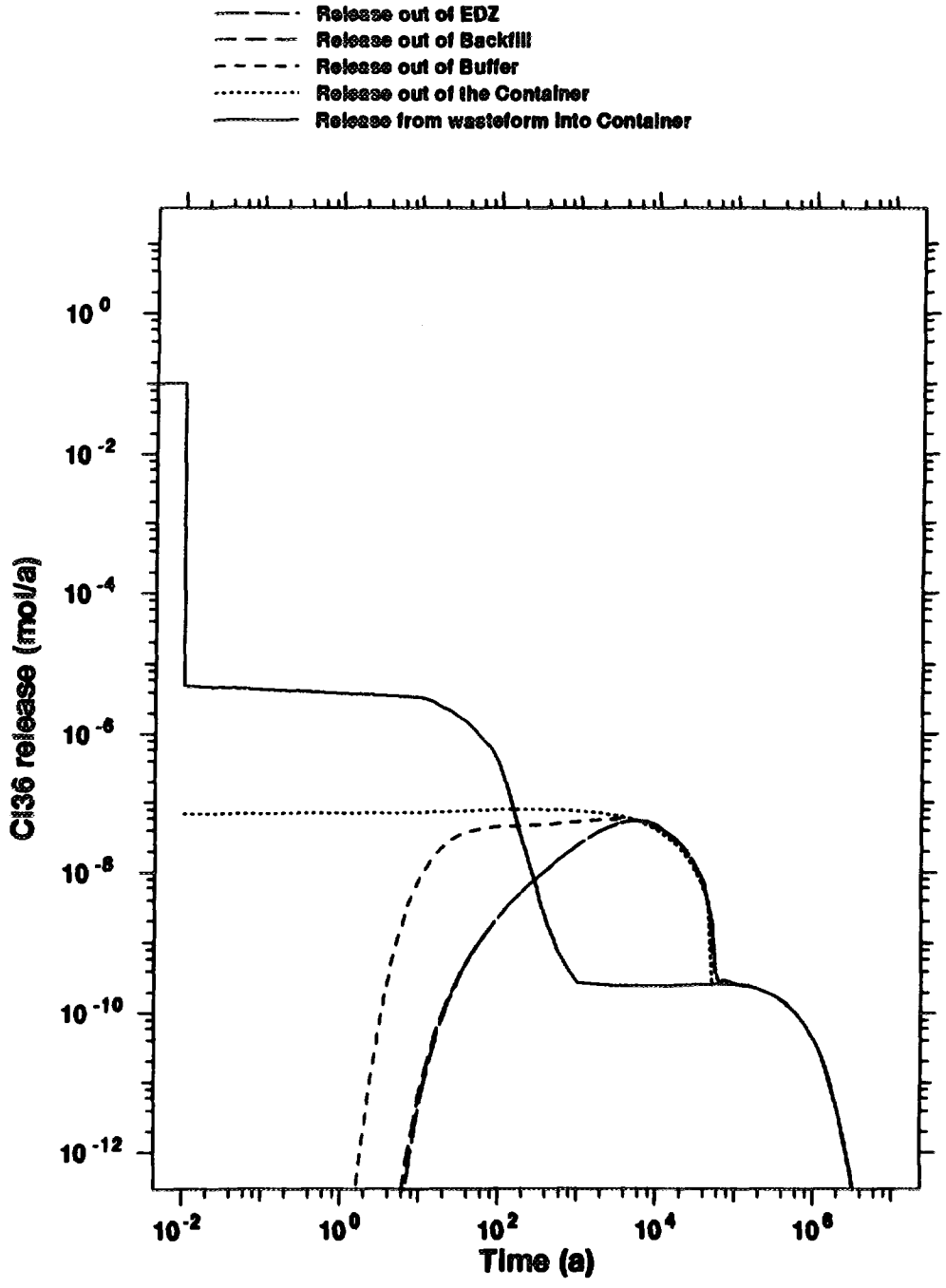

FIGURE 6.29 Release Rates of ^{36}Cl from Vault Sector 11 for the Median Simulation

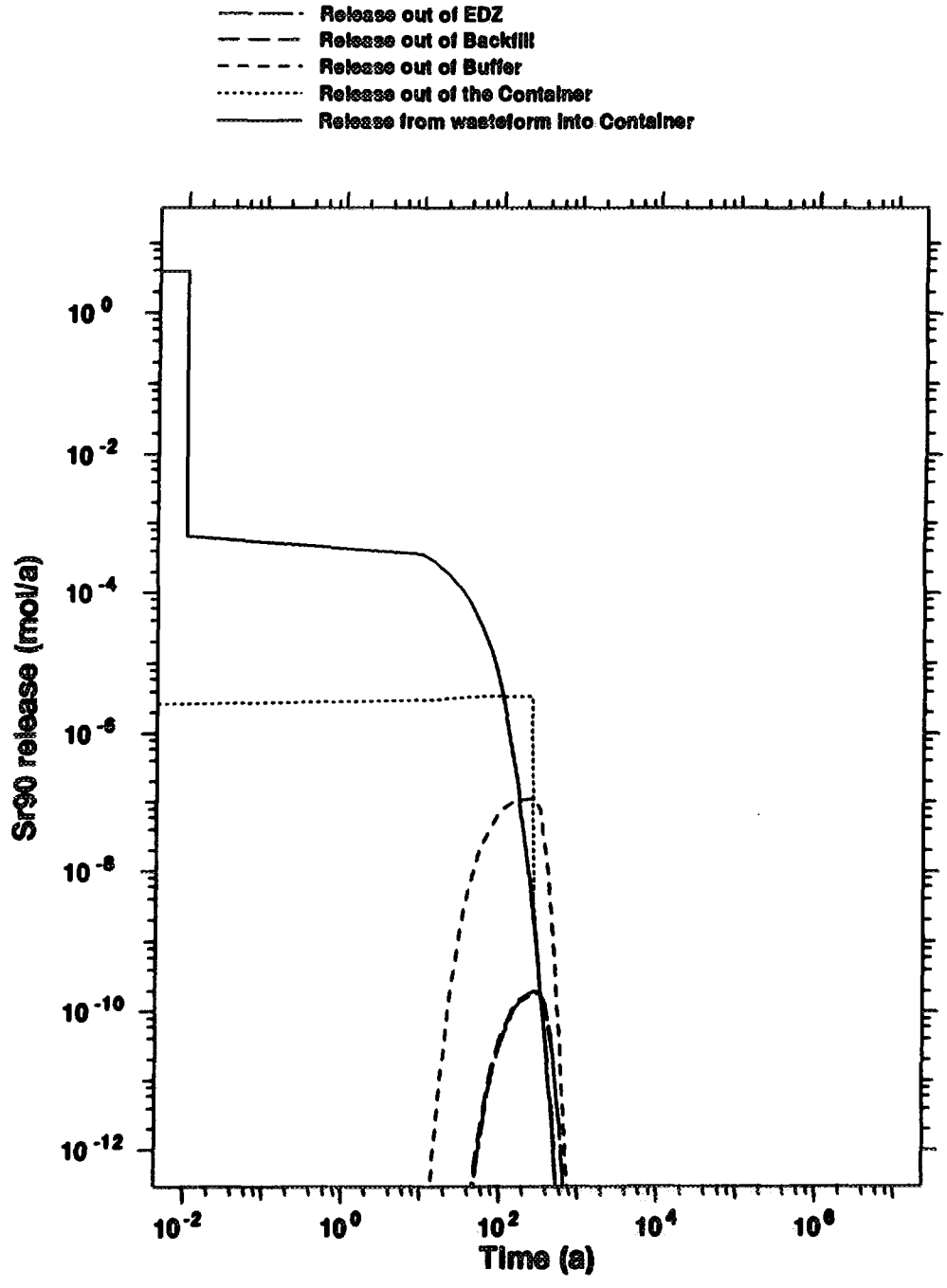

FIGURE 6.30: Release Rates of ^{90}Sr from Vault Sector 11 for the Median Simulation

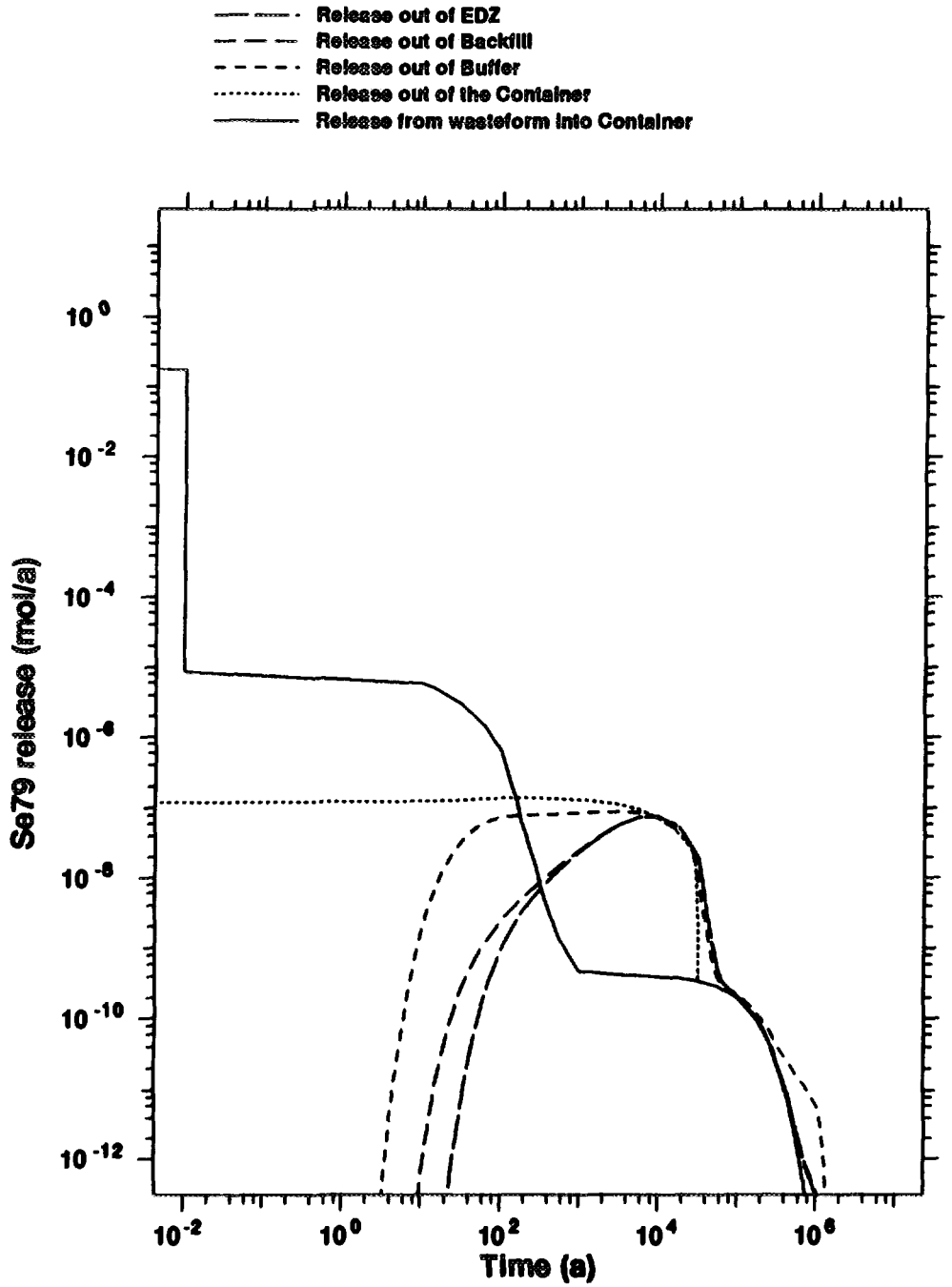

FIGURE 6.31: Release Rates of ^{79}Se from Vault Sector 11 for the Median Simulation

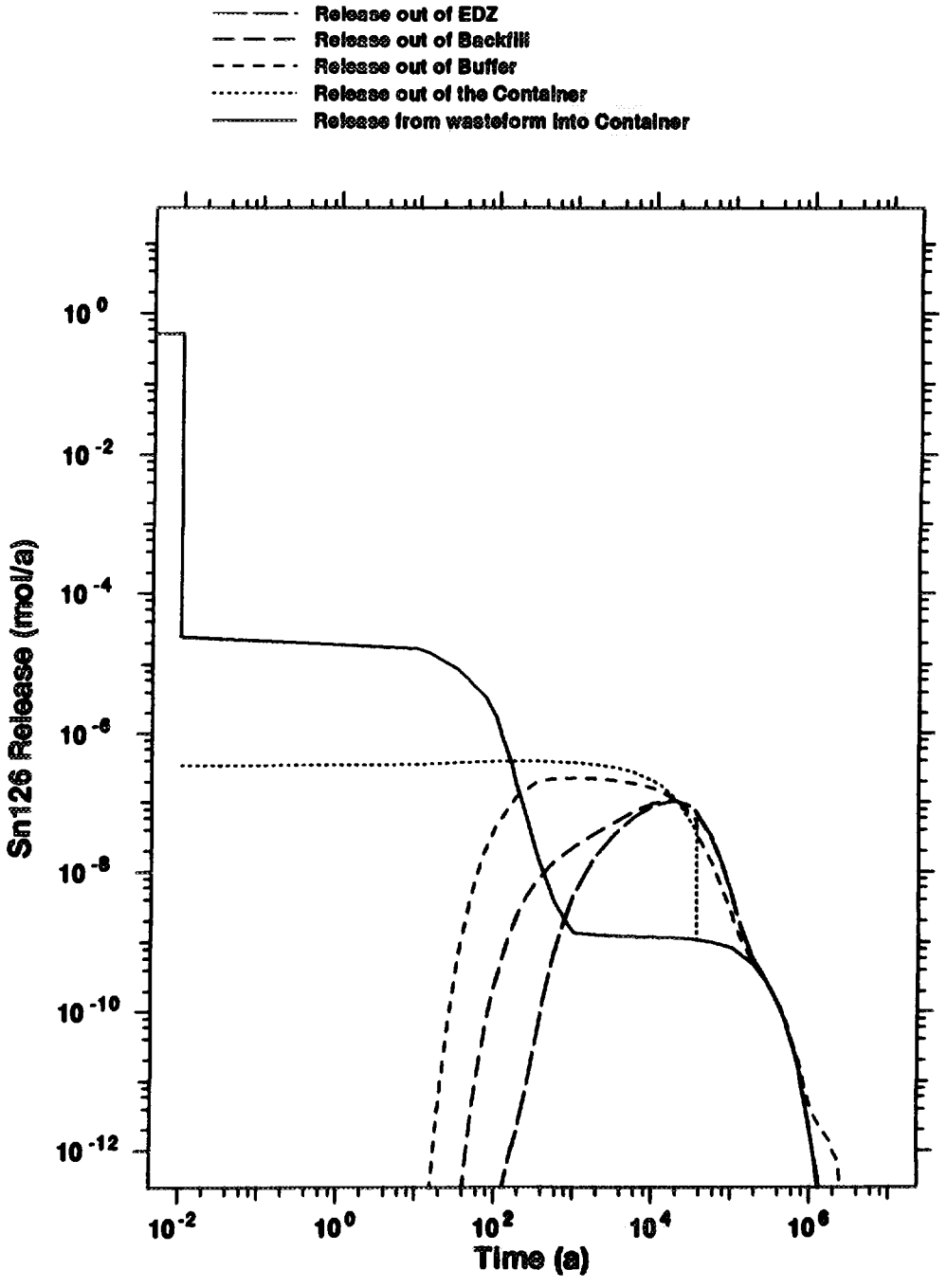

FIGURE 6.32: Release Rates of ^{126}Sn from Vault Sector 11 for the Median Simulation

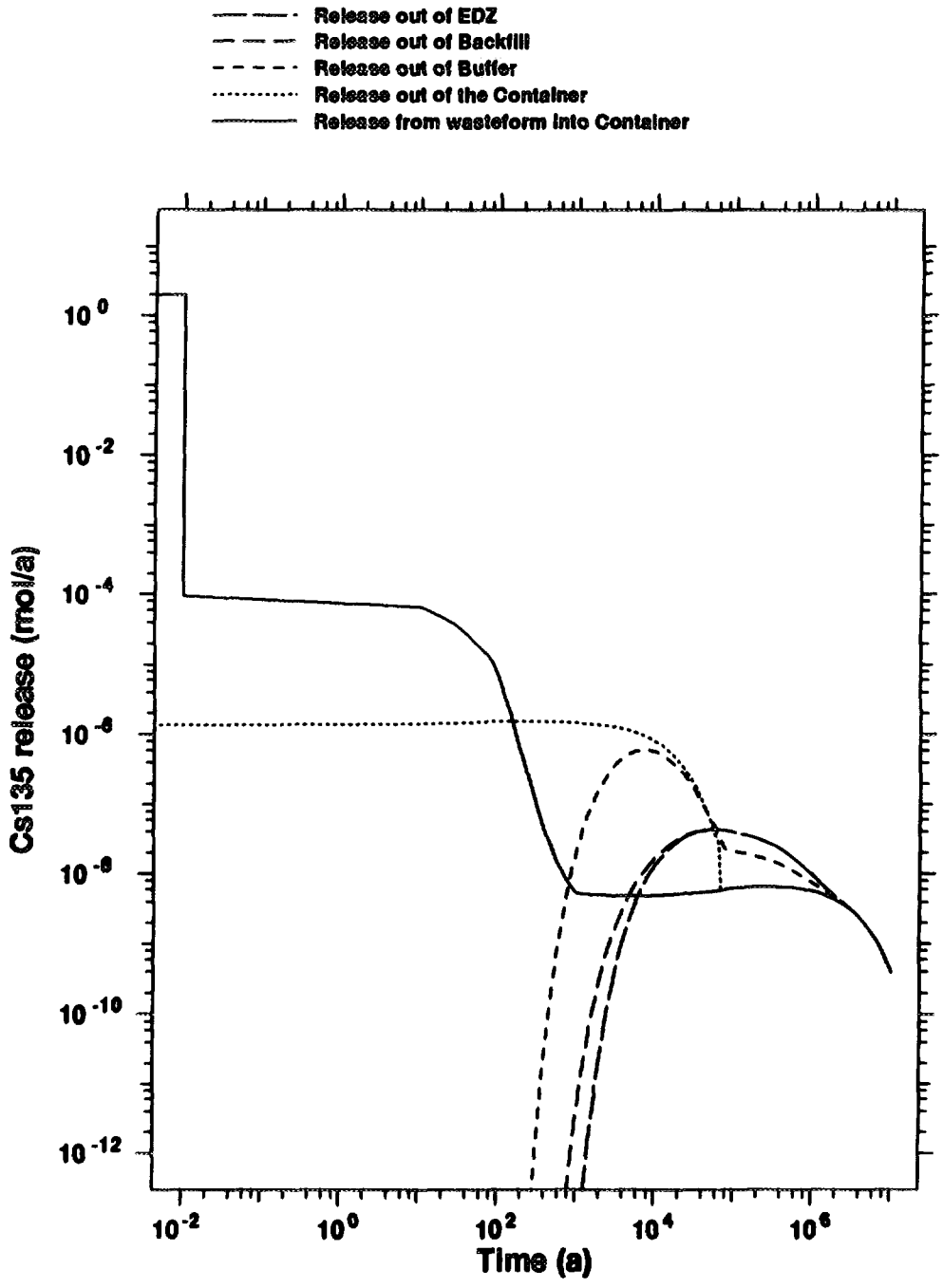

FIGURE 6.33: Release Rates of ^{135}Cs from Vault Sector 11 for the Median Simulation

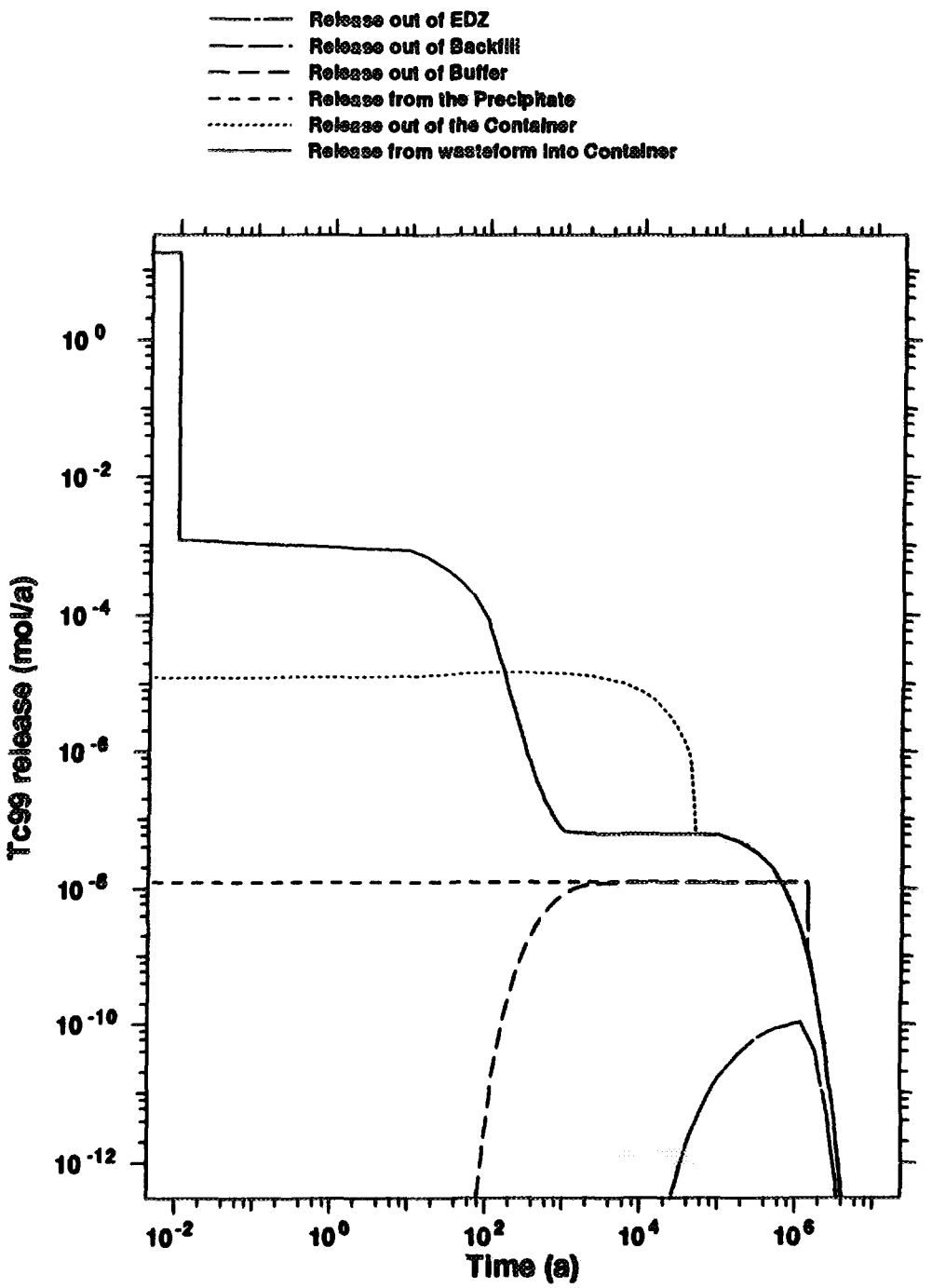

FIGURE 6.34: Release Rates of ^{99}Tc from Vault Sector 11 for the Median Simulation

6.5.3.4 Mass Transport in Buffer, Backfill and EDZ

The mass transfer resistance of the buffer, backfill, EDZ and rock are interrelated. The reduction in maximum release rate in traversing the buffer and backfill is very small for the poorly sorbed radionuclides ^{129}I, ^{36}Cl and ^{79}Se (see Figs. 6.28, 6.29 and 6.31). The reduction is more significant for ^{135}Cs which is strongly sorbed in all the media (Fig. 6.33), for ^{99}Tc which is strongly sorbed in the backfill (Fig. 6.34) and for ^{90}Sr which is retarded enough by sorption that it decays substantially in the buffer and backfill (Fig. 6.30). Tin-126 is moderately sorbed and experiences a small reduction in maximum release rate in traversing the buffer and backfill (Fig. 6.32). The EDZ does not offer significant resistance to mass transport in any simulations but is nonetheless important. Because of its relatively large permeability, groundwater velocities are largest in the EDZ. These large velocities draw radionuclides out of the backfill as soon as they appear at the boundary with the EDZ and carry the radionuclides relatively quickly through the EDZ. When groundwater velocities decrease toward zero, the mass transfer resistance of the buffer, backfill and EDZ increases dramatically, to the extent that ^{129}I decays substantially in the room as shown in Fig. 1 of LeNeveu and Kolar (1996) and Fig. 6.11 of this report.

Examination of the results of other simulations shows that they have the same general behaviour as the median simulation.

6.5.3.5 Dual-Shell Container With Enlarged Pinhole

Figure 6.35 illustrates the barrier release rate for ^{129}I for the dual-shell container with an enlarged pinhole in the Cu shell for the median simulation for the case where failure of the steel shell is assumed to occur at 1000 a. In this simulation, the pinhole offers negligible resistance compared to the buffer and backfill; however, the maximum release rate from the EDZ to the rock is only a factor of six larger than in the case with a small pinhole. This shows that the buffer and backfill are redundant barriers to the pinhole and are almost as effective as the pinhole in restricting release rates. In the enlarged pinhole scenario, short-lived radionuclides like ^{90}Sr decay to insignificant levels by the time the inner steel shell fails. Iodine-129 remains as the major contributor to dose consequence. Although the release rates and subsequent dose consequence for ^{129}I are about a factor of six larger, the AECB risk criteria is not exceeded in 32 FFLH simulations for the enlarged pinhole scenario.

6.5.3.6 Maximum Release Rates from Each Vault Sector

Maximum release rates from each vault sector for ^{129}I for the four example simulations are illustrated in Fig. 6.36. The maximum release rates are largest in simulation 31, the simulation giving the second highest dose consequence of the 32 FFLLH simulations performed. Overall sensitivity analysis indicates that in simulation 31 the variability in the biosphere parameters tends to dominate over the parameters from the vault and geosphere models masking the effect of the higher release rates from the vault. Similar results to Fig. 6.36 are obtained for the other fission products, with the exception of ^{99}Tc.

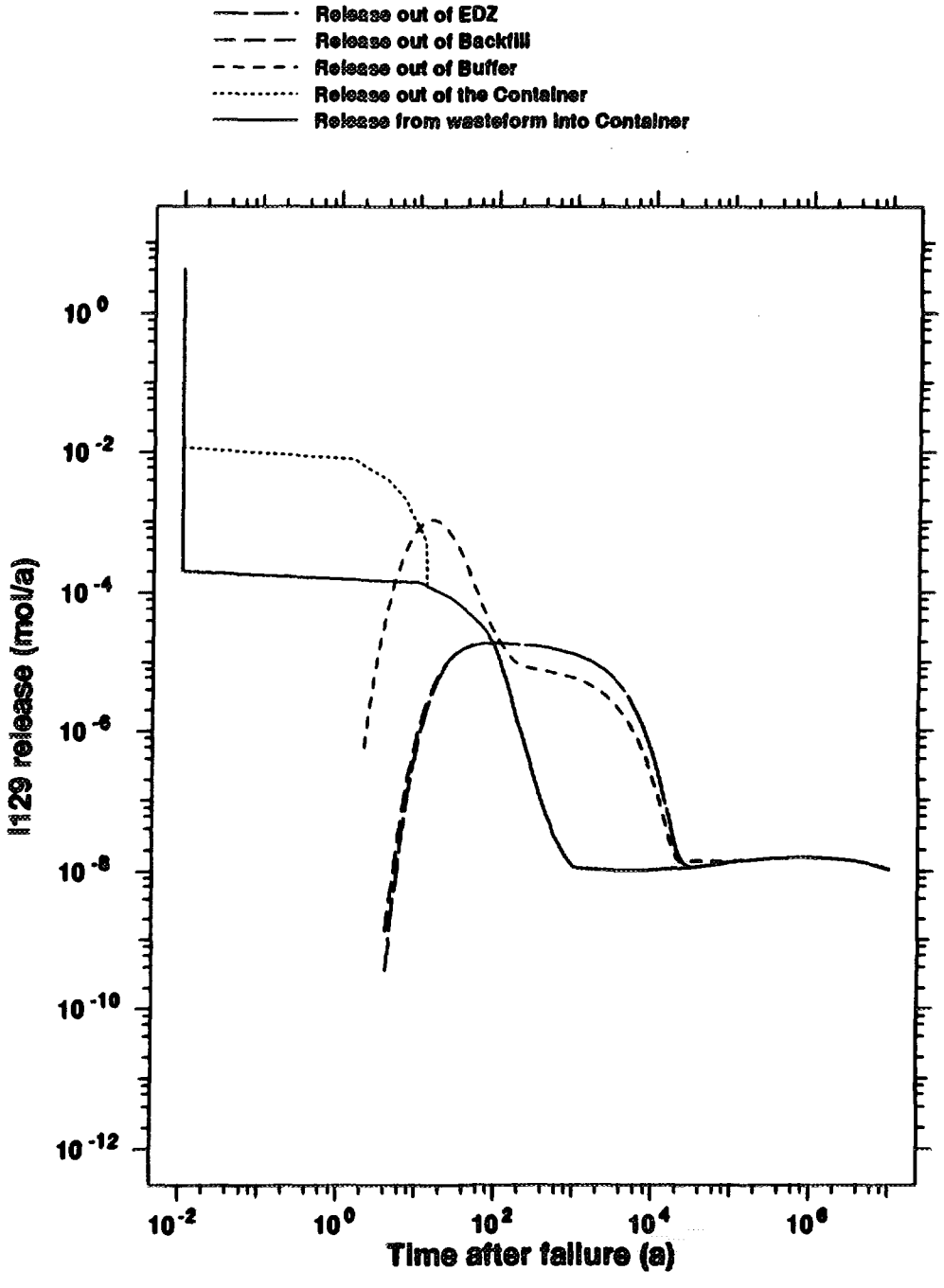

FIGURE 6.35: Release Rates of ^{129}I from Vault Sector 11 for the Median Simulation for an Enlarged Pinhole

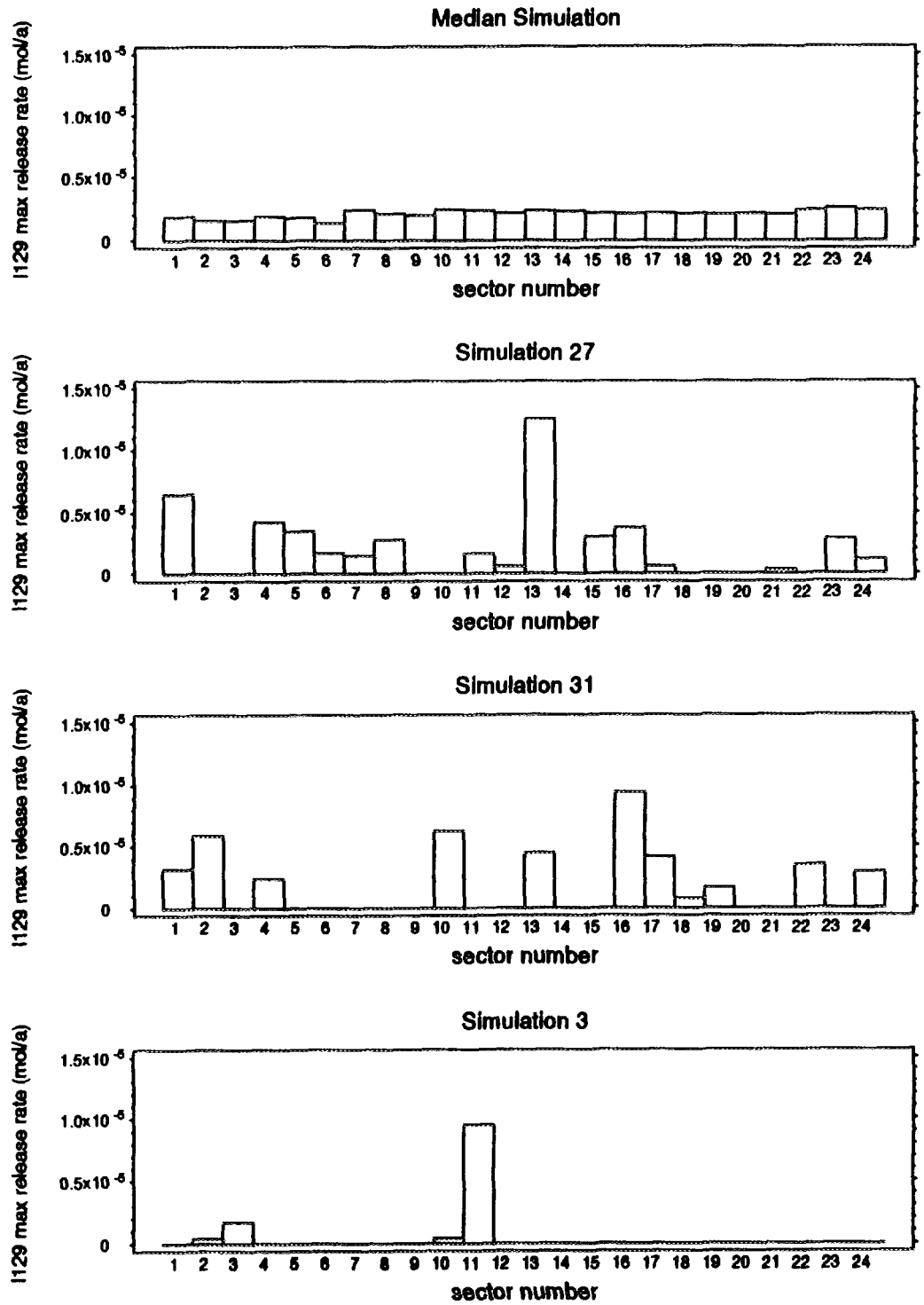

FIGURE 6.36: Maximum Release Rate of ^{129}I from Each Vault Sector

The median simulation is noteworthy because the sector to sector pattern follows that of the average linear groundwater velocity in the rock (Fig. 6.22). This behaviour is apparent only in the median simulation because the defect radius and number of containers failed are equal in every sector.

In simulations 27, 31 and 3 the pattern of maximum release rates reflects both the pattern of number of failed containers and of the defect size. The variation with groundwater velocity is no longer apparent indicating its effect is not as strong. In general, the larger the number of failures in each sector and the larger the defect radius, the larger the maximum sector release rate.

For ^{99}Tc, the pattern of maximum release rates from simulation to simulation follows closely the pattern of solubilities (Fig. 6.37). The larger the solubility in a given simulation, the larger the maximum release rates.

6.5.3.7 Summary for Fission Products and Activation Products

In summary, the number of failed containers and the amount of fuel dissolved by oxidants produced by radiolysis are most influential in determining the relative magnitude of the source term for radionuclide mass transport. The pinhole in the container is the most effective barrier in restricting mass transport from failed waste containers. The buffer, backfill, EDZ and rock act together as a redundant barrier that is almost as effective as the pinhole in restricting mass transport. The permeability of the EDZ is influential in determining radionuclide release rates from the vault and subsequent dose consequences.

The relative dose potential of the various radionuclides depends mainly on three factors, the initial inventory, the mobility and the radiotoxicity.

6.5.4 The Actinides

Three actinide chains, designated 4n+1, 4n+2 and 4n+3, were simulated (Chapter 6.5.1). The actinides are not among the major contributors to dose consequence. For example, the largest actinide dose in the 32 FFLH simulations is 3.4×10^{-7} Sv·a^{-1} from ^{237}Np. In general, the actinide dose rates are lower because the actinides are strongly sorbed in the buffer, backfill and rock.

The release rates of actinides through the vault barriers can be quite different than for the fission products and activation products. These differences can be attributed to a number of factors: (i) there is no instant release fraction for the actinides, (ii) most actinides precipitate in the container, and (iii) many actinides increase in inventory as a result of nuclear transformations. Figure 6.38 illustrates these effects for ^{230}Th. The release rate from the used fuel shows the high release rate caused by the oxidative effects of beta and gamma radiolysis but is missing the pulse from instant release. The beta and gamma radiolysis begins to diminish after about ten years. This is followed by a long period where the release rate increases as a result of ingrowth of ^{230}Th from parents. The release rate out of the

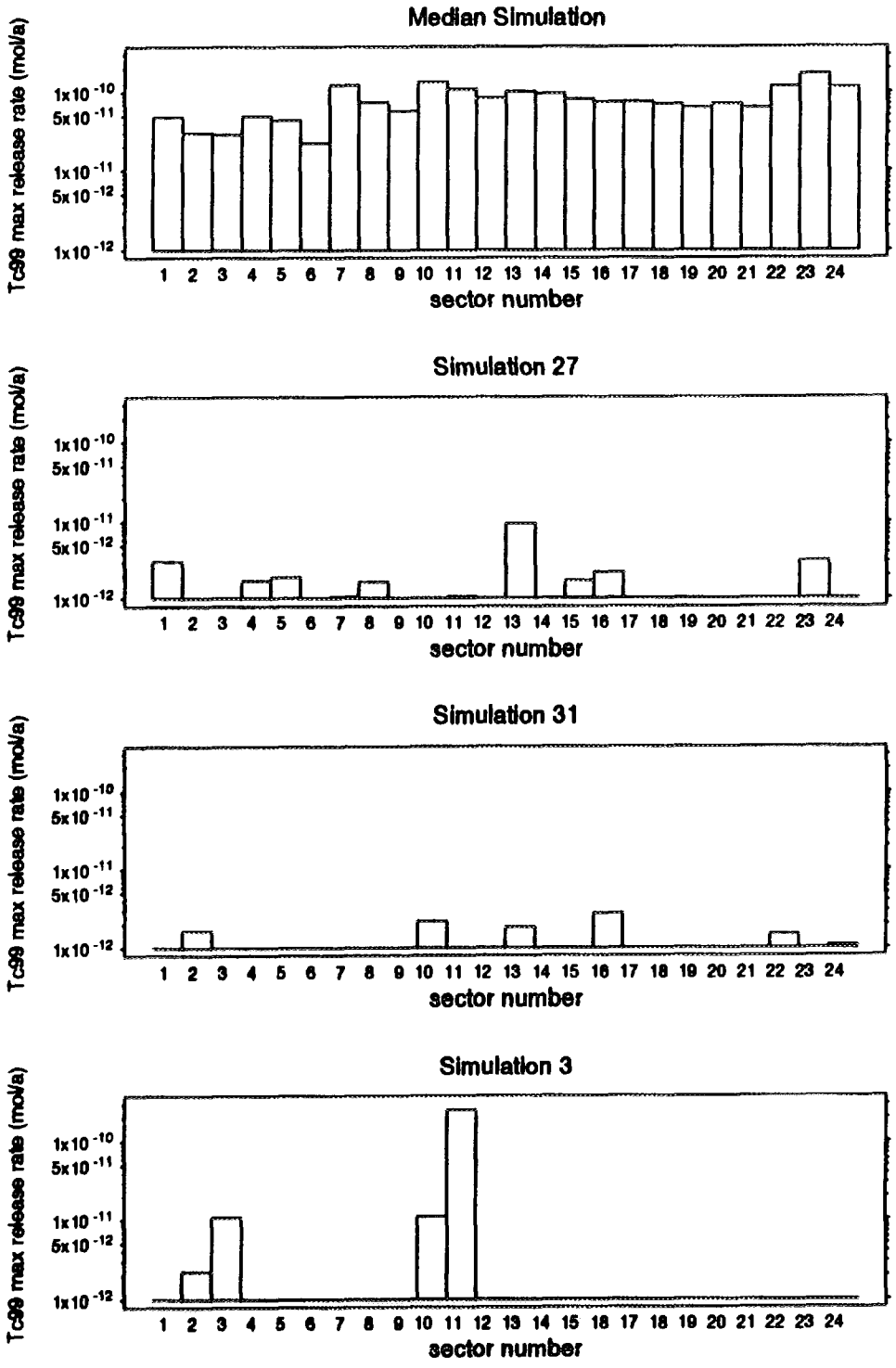

FIGURE 6.37: Maximum Release Rate of ^{99}Tc from Each Vault Sector

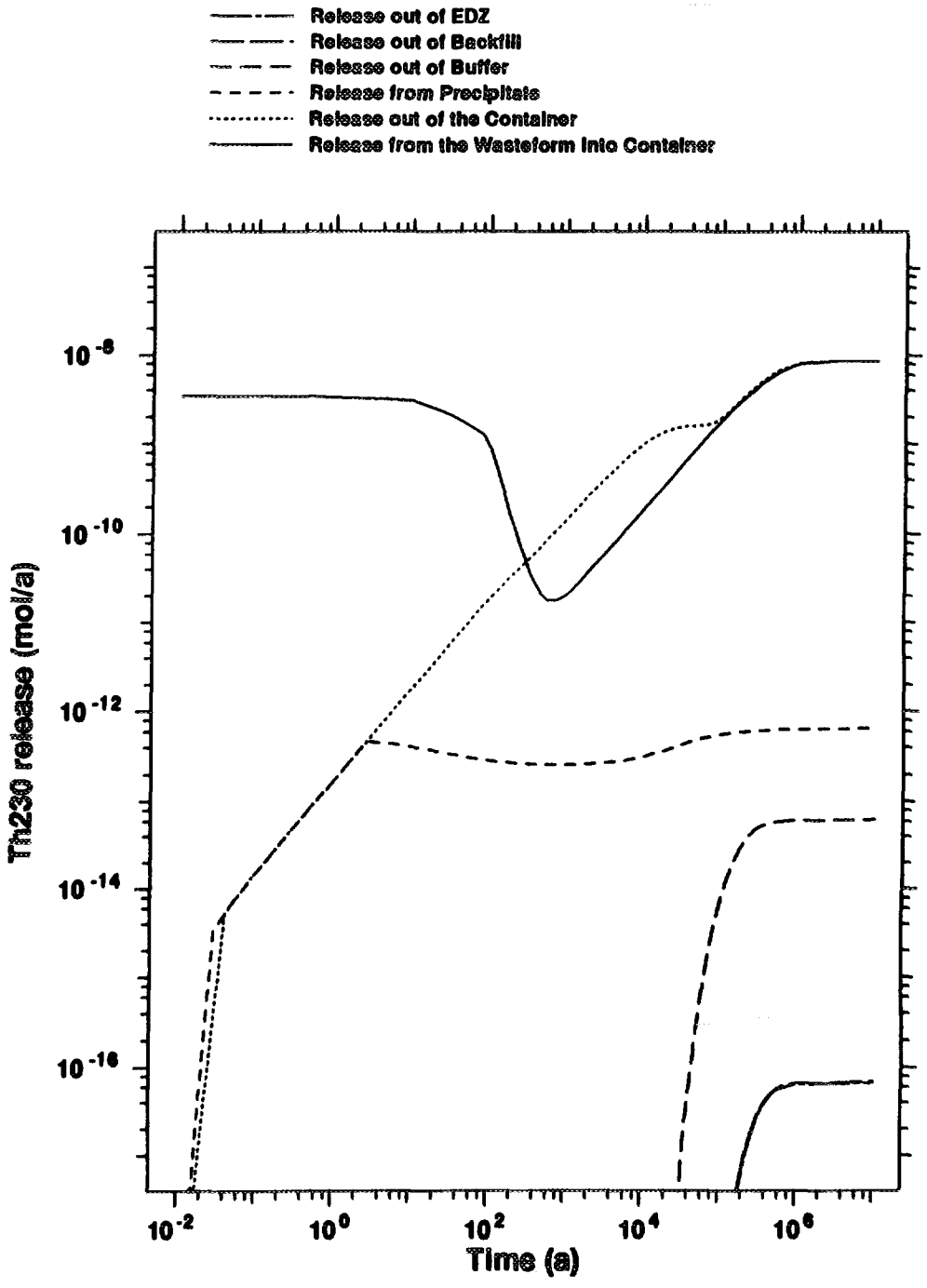

FIGURE 6.38: Release Rates of ^{230}Th from Vault Sector 11 for Simulation 27

container in the absence of solubility constraints, gradually increases in response to the input from dissolution of the fuel matrix, and after leveling off in response to the decrease in radiolytic oxidation, increases again in response to ingrowth. The initial relatively constant portion of the release rate out of the container (in the absence of solubility constraints) exhibited in the example fission products and activation products (Figs. 6.28 through 6.34) is missing for the actinides because of the absence of instant release. When solubility constraints are applied, there is a large reduction in release rate. The release rate from the precipitate fluctuates slowly with time in response to the time variation in the isotopic ratio of ^{230}Th. This fluctuation illustrates the effect of shared solubility between isotopes. There is a further reduction in release rate as ^{230}Th traverses the buffer and backfill because of sorption in these media. There is no further reduction in release rate in traversing the EDZ because of the relatively high groundwater velocity in this medium and because the capacity factor in the EDZ is smaller than in the buffer and backfill (3.0×10^{-1} in the EDZ, 2.7×10^{3} in the buffer and 5.8×10^{3} in the backfill). Other actinides exhibit similar patterns of behaviour in traversing the vault barriers.

6.5.5 Criticality

The possibility of criticality occurring in the vault is discussed in Chapter 8 of Johnson et al. (1994b). In excess of 1 kg of ^{239}Pu would have to accumulate as an undispersed solid in the container for the possibility of criticality to occur. Figure 6.39 shows the total mass of ^{239}Pu accumulated as a solid precipitate in one failed container in sector 11 of the vault for the four example simulations. The maximum amount of ^{239}Pu in the container in the four simulations (320 g) is below the amount necessary for any possibility of criticality.

7. SUMMARY AND COMPARISON WITH THE VAULT MODEL IN THE EIS CASE STUDY

A long-term safety assessment has been completed for a nuclear fuel waste disposal system based on in-room emplacement of long-lived Cu containers in a disposal vault at a depth of 500 m in the Canadian Shield. The study has been performed to illustrate the effectiveness of this particular vault design in providing containment of radionuclides under relatively permeable rock conditions, where groundwater velocities are 1000 to 10 000 times faster than in the performance assessment case study reported in the EIS (Goodwin et al. 1994).

We compare the different vault models developed for the two studies, commenting in particular on the reasons for differences in model selection and results obtained. We refer in this section to the present study as the PR4 model, and the case study in the EIS as the CC3 model.

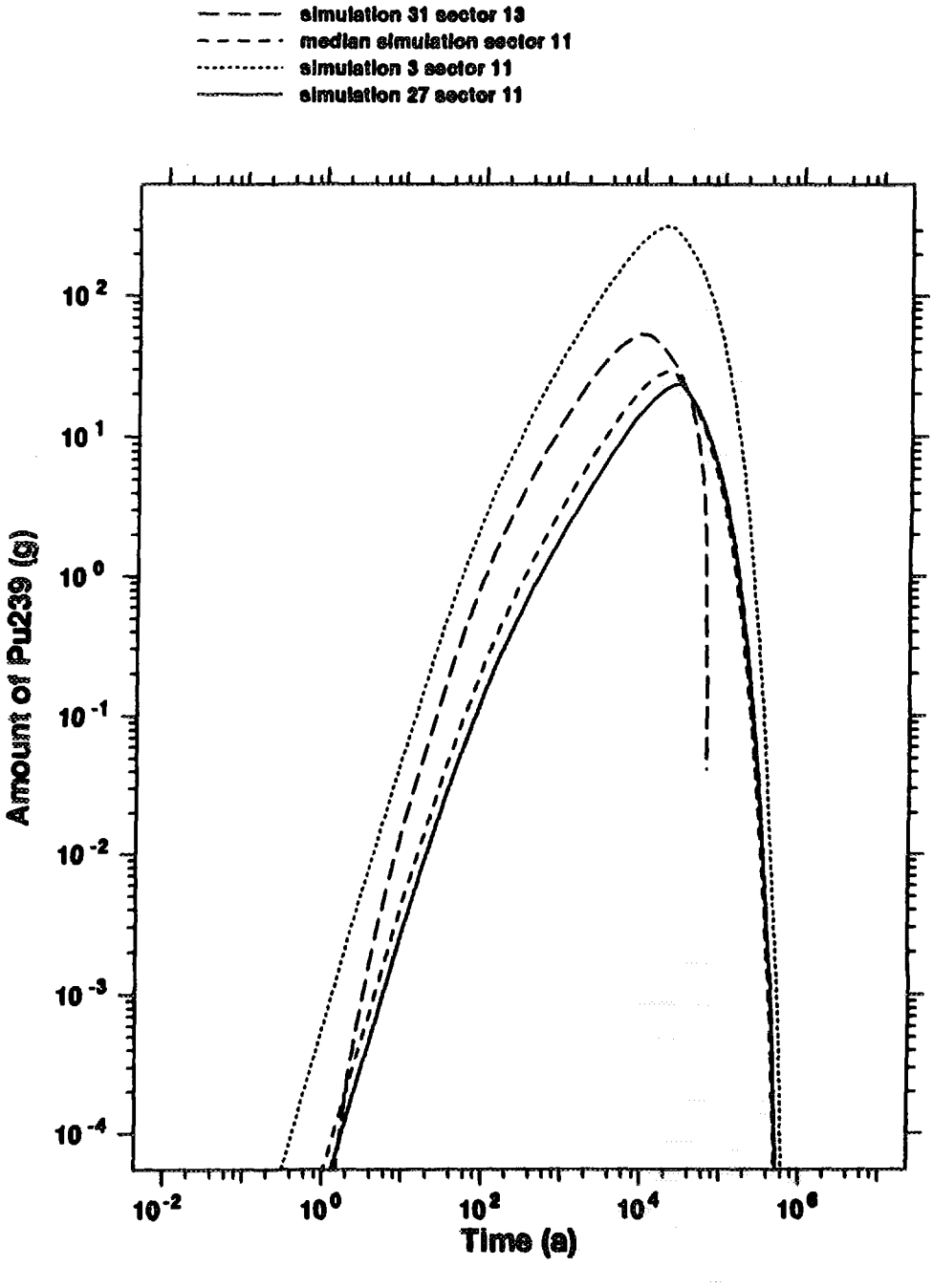

FIGURE 6.39: Amount of ^{239}Pu Precipitated Within a Defected Container

In the PR4 study, an evaluation of the performance of 25-mm wall thickness Cu containers indicates that they would experience <1 mm of corrosion by O_2 entrapped in the buffer and backfill materials, and insignificant subsequent corrosion in the anoxic deep groundwaters of the Canadian Shield.

Coupled with structural analysis studies that provide confidence that suitable container designs are available, it can be concluded that container lifetimes of $>10^6$ a are achievable. As a result, the only radionuclide release expected would be that arising from slow diffusive transport through small(0.3 to 3 mm diameter) manufacturing defects that might escape detection in the approximately 1 in 5000 containers that are assumed to fail immediately.

In the CC3 case study, the corrosion model for Grade-2 Ti containers led to virtually all containers failing between 1200 and 7000 a, with approximately 1 in 5000 containers assumed to fail immediately upon emplacement as a result of undetected manufacturing defects. In contrast to the present study, defects (whether manufacturing defects or corrosion penetrations) occurring in the Ti containers were assumed to provide no significant transport delay, i.e., radionuclide transport occurred across the entire container surface area upon failure. It is emphasized that, although Grade 2-Ti might be expected to experience crevice corrosion that could limit container lifetime, Grade-12 or 16 Ti containers could be expected to have a lifetime of $>10^5$ a (Shoesmith et al. 1995a).

In both the CC3 and the PR4 studies, groundwater is conservatively assumed to immediately saturate the low permeability clay-based buffer and backfill materials and contact the used fuel bundles in failed containers, thus initiating radionuclide release. The Zircaloy cladding is assumed to fail immediately and provide no mass transport delay to subsequent radionuclide release.

Release of radionuclides from the used fuel occurs as a result of instant-release of a fraction of the inventory of some radionuclides, and by dissolution of the used fuel matrix. In the PR4 model, based on new data, the instant release fractions were revised upward for ^{90}Sr and downward for ^{14}C, relative to the CC3 study, and ^{36}Cl, not evaluated in the CC3 study, was included in the calculations. For the matrix dissolution model in PR4, the requirement to assess only prematurely defected containers resulted in the use of a kinetic model appropriate for the conditions expected at the surface of the fuel in a container that could become saturated with groundwater while gamma and beta radiation fields are high. The long-term dissolution of the fuel in the PR4 study was modeled assuming a constant dissolution rate. This very conservative approach for the long-term rate is expected to greatly overpredict the extent of matrix dissolution, as evidenced by the geochemical stability of the Cigar Lake uranium deposit. Nonetheless, the kinetic model was retained at long times to avoid the complexity of a transition to the equilibrium model used in CC3.

The vast majority of containers in the CC3 study failed after 1000 a when the radiolytic driving force for fuel matrix dissolution was small. The total radionuclide releases from

these containers were far greater than from the few prematurely failed containers; thus, the more extensive matrix dissolution occurring in the prematurely failed containers was not incorporated in the model. However, calculations in Johnson et al.(1994b) gave estimated fuel matrix dissolution rates in prematurely failed containers that are of the same magnitude as those estimated in the PR4 study. The differences in approach between the two models, coupled with the fact that only dissolution in prematurely defected containers is modeled in the PR4 study, permits only these qualitative comparisons to be made.

The mass transport model in PR4 describes release from a point source (the failed container), diffusion through the buffer, and convection and dispersion in the backfill and EDZ, all these components of the vault being represented by concentric cylinders surrounding the source. The delay in mass transport of radionuclides through the small defect in the container shell was observed to be important in reducing the potential dose. The EDZ, with its relatively high permeability, was observed to enhance releases from the vault. This is because the high groundwater velocities in the EDZ and surrounding rock draw radionuclides out of the backfill. In the CC3 study, the borehole emplacement design was represented as a series of plane layers(buffer, backfill and rock) across which radionuclides were transported primarily by diffusion. This was shown to suitably represent the transport process provided the permeability of the surrounding rock was sufficiently low that diffusion dominated mass transport. In contrast to the PR4 study, the EDZ was shown to be unimportant because there was not expected to be a continuous high permeability path connecting the EDZ to permeable fracture zones, and because mass transport in the vault and surrounding rock was diffusion dominated.

It is not possible to make quantitative comparisons regarding the relative merits of the in-room and borehole designs in terms of radionuclide retention capability based on the two studies discussed here. This is because of the high groundwater velocities in the rock surrounding the vault in the PR4 study relative to the CC3 study. The PR4 results thus indicate more rapid release of radionuclides to the surrounding rock than in the CC3 study. Nonetheless, the in-room design provides assurance that, irrespective of the permeability of the surrounding rock, radionuclides must traverse both the buffer and backfill before being released from the vault, and thus it is judged to be a more robust design. Clearly, the combination of in-room emplacement of used fuel in long-lived containers with siting of the vault in low permeability rock will provide a very large margin of safety.

ACKNOWLEDGEMENTS

The authors acknowledge the contribution of J.C. Tait in providing the Appendix on radionuclide inventories and J. McMurry for providing the radionuclide solubility data. In addition, we thank K. Nuttall, P. Baumgartner, C.C. Davison and B.W. Goodwin for their helpful comments and critical review of the report, and M.E. McDowall for secretarial assistance.

The Canadian Nuclear Fuel Waste Management Program is jointly funded by AECL and Ontario Hydro under the auspices of the CANDU Owners Group.

REFERENCES

AECB (Atomic Energy Control Board). 1987. Regulatory policy statement. Regulatory objectives, requirements and guidelines for the disposal of radioactive wastes - long-term aspects. Atomic Energy Control Board Regulatory Document R-104.

AECL (Atomic Energy of Canada Limited). 1994a. Environmental impact statement on the concept for disposal of Canada's nuclear fuel waste. Atomic Energy of Canada Limited Report, AECL-10711, COG-93-1. Available in French and English.

AECL (Atomic Energy of Canada Limited). 1994b. Summary of the environmental impact statement on the concept for disposal of Canada's nuclear fuel waste. Atomic Energy of Canada Limited Report, AECL-10721, COG-93-11. Available in French and English.

Anderson, D.M., J.L. Fountain and C. Waddell. 1982. Chemical stability of clays employed as buffer materials in the storage of nuclear waste materials. In Abstract Volume, Annual Meeting of the Clay Minerals Society, p. 39.

ASM. 1987. Corrosion of copper and copper alloys. In Metals Handbook, Ninth edition, Volume 13, Corrosion. American Society for Metals International, Metals Park, OH, 610-640.

Atkinson, A., J.A. Hearne and C.F. Knight. 1991. Thermodynamic modelling and aqueous chemistry in the CaO-Al_2O_3-SiO_2-H_2O system. In Materials Research Society Symposia Proceedings 212 (ed. T. Abrajanao, Jr. and L.H. Johnson) (Scientific Basis for Nuclear Waste Management XIV) 395-402.

Baumgartner, P. 1995. Alternative postclosure assessment: disposal container surface and centre temperature history. Technical memoranda, GSEB-95-322, July 31; GSEB-95-328.

Baumgartner, P., D.M. Bilinsky, C. Onofrei, Y. Ates, F. Bilsky, J.L. Crosthwaite and G.W. Kuzyk. 1995. An in-room emplacement method for a used-fuel disposal facility — preliminary design considerations. AECL Technical Record, TR-665*, COG-94-533.

Baumgartner, P., D.M. Bilinsky, Y. Ates, R.S. Read, J.L. Crosthwaite and D.A. Dixon. 1996. Engineering for a disposal facility using the in-room emplacement method. Atomic Energy of Canada Limited Report, AECL-11595, COG-95-223.

Berner, U. 1995. KRISTALLIN-I: Estimates of solubility limits for safety relevant radionuclides. Paul Scherrer Institute Report, PSI 95-07.

Blackwood, D.J., A.R. Hoch, C.C. Naish, A. Rance and S.M. Sharland. 1994. Research on corrosion aspects of the Advanced Cold Process Container. Swedish Nuclear Fuel and Waste Management Co. Report, SKB 94-12.

Brandberg, F. and K. Skagius. 1991. Porosity, sorption and diffusivity data compiled for the SKB 91 study. SKB 91-16.

Bresle, A., J. Saers and B. Arrhenius. 1983. Studies in pitting corrosion on archaeological bronzes: copper. Swedish Nuclear Fuel Supply Company Report, SKBF-KBS-TR-83-05.

Brown, P.L., A. Haworth, S.M. Sharland and C.J. Tweed. 1991. HARPHRQ: a geochemical speciation program based on PHREEQE. Nirex Safety Studies Report NSS/R188.

Campbell, H.S. 1974. A review: pitting corrosion of copper and its alloys. In Localized Corrosion,(R.W. Staehle, B.F. Brown, J. Kruger and A. Agrawal, eds.), NACE International, Houston, TX, 625-638.

Chamberlain, A.H.L. and P. Angell. 1990. Influences of microorganisms on pitting of copper tube. In Microbially Influenced Corrosion and Biodeterioration, (N.J. Dowling, M.W. Mittelman and J.C. Danko, eds.), MIC Consortium, Knoxville, TN, 3/65-3/72.

Chan, T. 1989. An overview of groundwater flow and radionuclide transport modelling in the Canadian nuclear fuel waste management program. In Proc. of the Conference on Geostatistical, Sensitivity, and Uncertainty Methods for Groundwater Flow and Radionuclide Transport Modeling. Battelle Press, Columbus, OH. pp. 39-61.

Choi, J.-W. and D.W. Oscarson. 1996. Diffusive transport through Na- and Ca-bentonite. J. Cont. Hydrol. (in press).

Christensen, H. and S. Sunder. 1995. An evaluation of water layer thickness effective in the oxidation of UO_2 fuel due to radiolysis of water. J. Nucl Mater. AECL-11479.

Conca, J.L., M.J. Apted and R.C. Arthur. 1993. Direct determination of transport parameters in repository materials. In Materials Research Society Symposia Proceedings 294 (ed. C.G. Interrante and R.T. Pabalan) (Scientific Basis for Nuclear Waste Management XVI) 839-844.

Cramer, J.J. 1994. Natural analogs in support of the Canadian concept for nuclear fuel waste disposal. Atomic Energy of Canada Limited Report, AECL-10291, COG-92-258.

Cross, J.E. and F.T. Ewart. 1990. HATCHES - a thermodynamic database and management system. Nirex Safety Studies Report, NSS/R212.

Crosthwaite, J.L. 1994a. In-room emplacement study - new bottom head design for Cu-shell reference container and new particulate-porosity value. Memorandum to P. Baumgartner and F. Bilsky, Atomic Energy of Canada Limited file reference FWTB-94-422, 1994 October 7.

Crosthwaite, J.L. 1994b. The performance, assessment and ranking of container design options for the Canadian nuclear fuel waste management program. Atomic Energy of Canada Limited Technical Record, TR-500*.

Crosthwaite, J.L. 1995. Size range of detectable flaw in a copper-shell container. Memorandum to D.M. Leneveu et al., AECL file reference FWTB-95-237, 1995 August 14.

Davis, P.A., R. Zach, M.E. Stephens, B.D. Amiro, G.A. Bird, J.A.K. Reid, M.I. Sheppard, S.C. Sheppard and M. Stephenson. 1993. The disposal of Canada's nuclear fuel waste: The biosphere model, BIOTRAC, for postclosure assessment. Atomic Energy of Canada Limited Report, AECL-10720, COG-93-10.

Davison, C.C., A. Brown, R.A. Everitt, M. Gascoyne, E.T. Kozak, G.S. Lodha, C.D. Martin, N.M. Soonawala, D.R. Stevenson, G.A. Thorne and S.H. Whitaker. 1994a. The disposal of Canada's nuclear fuel waste: Site screening and site evaluation technology. Atomic Energy of Canada Limited Report AECL-10713, COG-93-3.

Davison, C.C., T. Chan, A. Brown, M. Gascoyne, D.C. Kamineni, G.S. Lodha, T.W. Melnyk, B.W. Nakka, P.A. O'Connor, D.U. Ophori, N.W. Scheier, N.M. Soonawala, F.W. Stanchell, D.R. Stevenson, G.A. Thorne, T.T. Vandergraaf, P. Vilks and S.H. Whitaker. 1994b. The disposal of Canada's nuclear fuel waste: The geosphere model for postclosure assessment. Atomic Energy of Canada Limited Report, AECL-10719, COG-93-9.

Deslouis, C., B. Tribollet, G. Mengoli and M.M. Musiani. 1988. Electrochemical behaviour of copper in neutral aerated chloride solution. I. Steady-state investigation. J. Appl. Electrochem. 18, 374-383.

Dixon, D.A. 1995. Clay/alkali interactions. Memo FWTB-95-375.

Dixon, D.A., S.C.H. Cheung, M.N. Gray and B. Davidson. 1987. The hydraulic conductivity of dense clay soils. In Proc. 40th Canadian Geotechnical Conf. Regina, SK. pp. 389-396.

Dixon, D.A., A.W.-L.Wan, J. Graham and S.L. Campbell. 1993. Assessment of self-sealing and self-healing abilities of dense, high-bentonite-content sealing materials. In Proc. 1993 Joint CSCE-ASCE National Conference on Environmental Engineering, Montreal, Quebec, pp. 737-746.

Doubt, G.L. 1984. Assessing reliability and useful life of containers for disposal of irradiated fuel waste. Atomic Energy of Canada Limited Report, AECL- 8328.

Dutton, R. 1995. A methodology to analyze the creep behaviour of nuclear fuel waste containers. Atomic Energy of Canada Limited Report, AECL-11249, COG-95-06.

Eissa, N.A., N.H. Sheta, W.M. El Meligy and H.A. Sallam. 1994. Mössbauer effect study of the effect of gamma irradiation and heat treatment on montmorillonite. Hyperfine Interactions 91, 783-787.

Eriksen, T.E. and A. Jacobsson. 1982. Diffusion of hydrogen, hydrogen sulphide and large molecular weight anions in bentonite. Swedish Nuclear Fuel Supply Co. Report, SKBF-KBS-TR-82-17.

Fischer, W., I. Hänßel and H.H. Paradies. 1988. First results of microbial induced corrosion of copper pipes. In "Microbial Corrosion-1," (C.A.C. Sequeira and A.K. Tiller, eds.) Elsevier, London, pp. 300-327.

Floyd, M.R., D.A. Leach, R.E. Moeller, R.R. Elder, R.J. Chenier and D. Obrien. 1992. In Proceedings of the Third International Conference on CANDU Fuel, Chalk River Laboratories (P.G. Boczar, ed.).

Garisto, F. 1989. The energy spectrum of a-particles emitted from used CANDU™ fuel. Ann. Nucl. Energy 16(1), 33-38.

Garroni, J.D., B. W. Leitch and J.L. Crosthwaite. 1996. A structural assessment of some alternative container designs for the disposal of CANDU used-fuel waste. Atomic Energy of Canada Limited Technical Record TR-741*, COG-96-116.

Gascoyne, M. 1996. Hydrogeochemical and geochemical data for the alternative assessment case study. Atomic Energy of Canada Limited Technical Record, TR-720*.

Gascoyne, M. and D.C. Kamineni. 1992. Groundwater chemistry and fracture mineralogy in the Whiteshell Research Area: supporting data for the geosphere and biosphere transport models. Atomic Energy of Canada Limited Technical Record, TR-516*, COG-92-24.

Gascoyne, M, S. Stroes-Gascoyne and F.P. Sargent. 1995. Geochemical influences on the design, construction and operation of nuclear waste vault. Appl. Geochem. 10, 657-671.

Gillham, R.W. and J.A. Cherry. 1982. Contaminant migration in saturated unconsolidated geologic deposits. In Recent Trends in Hydrogeology, T.N. Narasimhan (ed.). GSA Special Paper 189, Geological Society of America, Boulder, CO. pp. 31-62.

Goode, J.H. and C.M. Cox. 1970. The distribution of fission product tritium in a Zircaloy-clad UO_2 blanket rod from PWR-1. Oak Ridge National Laboratory Report, ORNL-TM-2994.

Goodwin, B.W., D.B. McConnell, T.H. Andres, W.C. Hajas, D.M. LeNeveu, T.W. Melnyk, G.R. Sherman, M.E. Stephens, J.G. Szekely, P.C. Bera, C.M. Cosgrove, K.D. Dougan, S.B. Keeling, C.I. Kitson, B.C. Kummen, S.E. Oliver, K. Witzke, L. Wojciechowski and A.G. Wikjord. 1994. The disposal of Canada's nuclear fuel waste: Postclosure assessment of a reference system. Atomic Energy of Canada Limited Report, AECL-10717, COG-93-7.

Goodwin, B.W., T.H. Andres, W.C. Hajas, D.M. LeNeveu, T.W. Melnyk, J.G. Szekely, A.G. Wikjord, D.C. Donahue, S.B. Keeling, C.I. Kitson, S.E. Oliver, K. Witzke and L. Wojciechowski. 1996a. The Disposal of Canada's Nuclear Fuel Waste: A study of postclosure safety of in-room emplacement of used CANDU fuel in copper containers in permeable plutonic rock. Volume 5: Radiological Assessment. Atomic Energy of Canada Limited Report, AECL-11494-5, COG-95-552-5.

Goodwin, B.W., W.C. Hajas and D.M. LeNeveu. 1996b. The effect of in-room emplacement on post-closure performance of a reference disposal system. Atomic Energy of Canada Limited Technical Record, TR-736*,COG-96-3.

Gray, W.J. and L.E. Thomas. 1992. Dissolution rates of as-received and partially oxidized spent fuel. In High-Level Radioactive Waste Management: Proceedings of the Third International Conference, American Nuclear Society, Inc., La Grange Park, IL, pp.1458-1464.

Gray, W.J. and L.E. Thomas. 1994. Initial results from the dissolution testing of various air-oxidized spent fuels. In Materials Research Society Symposia Proceedings 333 (ed. A. Barkatt and R.A. Van Konynenburg) (Scientific Basis for Nuclear Waste Management XVII) 391-398.

Greber, M.A., E.R. Frech and J.A.R. Hillier. 1994. The disposal of Canada's nuclear fuel waste: Public involvement and social aspects. Atomic Energy of Canada Limited Report, AECL-10712, COG-93-2.

Grondin, L., K. Johansen, W.C. Cheng, M. Fearn-Duffy, C.R. Frost, T.F. Kempe, J. Lockhart-Grace, M. Paez, Victor, H.E. Reid, S.B. Russell, C.H. Ulster, J.E. Villagran and M. Zeya. 1994. The disposal of Canada's nuclear fuel waste: Preclosure assessment of a conceptual system. Ontario Hydro Report N-03784-940010 (UFMED), COG-93-6.

Hakanen, M. and P. Hölttä. 1992. Review of sorption and diffusion parameters for TVO-92. TVO Report YJT-92-14.

Hallberg, R.O., P. Ostlund and T. Wadsten. 1988. Inferences from a corrosion study of a bronze cannon, applied to high level nuclear waste disposal. Appl. Geochem. 3, 273-280.

Harr, M.E. 1962. Groundwater and Seepage. McGraw-Hill Inc. New York.

Henderson, P.J., J.-O. Osterberg and B. Ivarsson. 1992. Low temperature creep of copper intended for nuclear waste containers. SKB Technical Report, 92-04.

Hoch, A.R. and S.M. Sharland. 1993. Assessment study of the stresses induced by corrosion in the advanced cold process canister. SKB Technical Report 94-13.

Hume, H.B. 1995. Technetium diffusion in clay-based materials under oxic and anoxic conditions. AECL Report, AECL-11419, COG-95-428.

ICRP (International Commission on Radiological Protection). 1991a. 1990 recommendations of the International Commission on Radiological Protection. Annals of the ICRP 21(1-3) (ICRP Publication 60).

ICRP (International Commission on Radiological Protection). 1991b. Annual limits on intake of radionuclides by workers based on the 1990 recommendations. Annals of the ICRP 21(4) (ICRP Publication 61).

Jefferies, N.L., C.J. Tweed, C.J. and S.J. Wisbey. 1988. The effects of changes in pH within a clay surrounding a cementitious repository. In Materials Research Society Symposia Proceedings 112 (ed. M.J. Apted) (Scientific Basis for Nuclear Waste Management XI) 43-52.

Johnson, L.H., J.C. Tait, D.W. Shoesmith, J.L. Crosthwaite and M.N. Gray. 1994a. The disposal of Canada's nuclear fuel waste: engineered barriers alternatives. Atomic Energy of Canada Limited Report, AECL-10718, COG-93-8.

Johnson, L.H., D.M. LeNeveu, D.W. Shoesmith, D.W. Oscarson, M.N. Gray, R.J. Lemire and N.C. Garisto. 1994b. The disposal of Canada's nuclear fuel waste: The vault model for postclosure assessment. Atomic Energy of Canada Limited Report, AECL-10714, COG-93-4.

Johnson, L.H., B.W. Goodwin, S.C. Sheppard, J.C. Tait, D.M. Wuschke, C.C. Davison. 1995. Radiological assessment of ^{36}Cl in the disposal of used CANDU fuel. Atomic Energy of Canada Limited Report, AECL-11213, COG-94-527.

Johnston, R.M. and H.G. Miller. 1985. Hydrothermal stability of bentonite-based buffer materials. Atomic Energy of Canada Limited Report, AECL-8376.

Jones, A.R. 1959. Radiation-induced reactions in the N_2-O_2-H_2O system. Radiation Res. 10, 655-663.

Kasprick, G.R. 1995. Unpublished data for OFE, OFHC and DLP copper tested at AECL Whiteshell Laboratories.

Kempe, T.F. 1992. Record of discussion with A. Ohuchi, Japan. Memorandum File 906-N-37450P. In Unpublished Documents Cited in the EIS and Primary References. Atomic Energy of Canada Limited Technical Record, TR-567,* COG-92-27.

King, F. 1995. A natural analogue for the long-term corrosion of copper nuclear waste containers-reanalysis of a study of a bronze cannon. Appl. Geochem. 10, 477-487.

King, F. 1996a. A model for the corrosion of copper containers in a Canadian nuclear fuel waste disposal vault. Part 1. The corrosion model. Atomic Energy of Canada Limited Report, AECL-11472, COG-95-520.

King, F. 1996b. A copper container corrosion model for the in-room emplacement of used CANDU fuel. Atomic Energy of Canada Limited Report, AECL-11552, COG-96-105.

King, F. 1996c. Microbially influenced corrosion of copper nuclear fuel waste containers in a Canadian disposal vault. Atomic Energy of Canada Limited Report, AECL-11471, COG-94-519.

King, F. 1996d. The potential for stress corrosion cracking of copper containers in a Canadian nuclear fuel waste disposal vault. Atomic Energy of Canada Limited Report, AECL-11550, COG-96-94.

King, F. and M. Kolar . 1995. Prediction of the lifetimes of copper nuclear waste containers under restrictive mass-transport and evolving redox conditions. CORROSION/95, NACE International, Houston, TX, paper no. 425.

King, F. and M. Kolar . 1996. A numerical model for the corrosion of copper nuclear fuel waste containers. In Materials Research Society Symposia Proceedings 412 (ed. W.M. Murphy and D. Knecht) (Scientific Basis for Nuclear Waste Management XIX) 555-562.

King, F. and D.M.. LeNeveu. 1992. Prediction of the lifetimes of copper nuclear fuel waste containers. In Proceedings of the ANS Topical Meeting on Nuclear Waste Packaging, FOCUS '91, American Nuclear Society, LaGrange Park, IL, 253-261.

King, F. and C.D. Litke. 1987. The corrosion of copper in synthetic groundwater at 150°C. Part 1. The results of short-term electrochemical tests. Atomic Energy of Canada Limited Technical Record, TR428*.

King, F. and C.D. Litke. 1989. The electrochemical behaviour of copper in aerated 1 $mol \cdot dm^{-3}$ NaCl at room temperature. Atomic Energy of Canada Limited Report, AECL-9571-9573.

King, F. and S. Stroes-Gascoyne. 1995. Microbially influenced corrosion of nuclear fuel waste disposal containers. In Proceedings 1995 International Conference on Microbially Influenced Corrosion, NACE International, Houston, TX, paper 35.

King, F., C.D. Litke and S.R. Ryan. 1992. A mechanistic study of the uniform corrosion of copper in compacted Na-montmorillonite/sand mixtures. Corros. Sci. 33, 1979-1995.

King, F., D.M. LeNeveu and D.J. Jobe. 1994a. Modelling the effects of evolving redox conditions on the corrosion of copper containers. In Materials Research Society Symposia Proceedings 333 (ed. A. Barkatt and R.A. Van Konynenburg) (Scientific Basis for Nuclear Waste Management XVII) 901-908.

King, F., D. LeNeveu, S. Ryan and C. Litke. 1994b. Predicting the long-term corrosion behaviour of copper nuclear fuel waste containers. In Proceedings of the International Conference on Life Prediction of Corrodible Structures, R.N. Parkins (ed.), NACE International, Houston, TX, pp. 497-512.

King, F., C.D. Litke and Y. Tang. 1995a. Effect of interfacial pH on the reduction of oxygen on copper in neutral $NaClO_4$ solution. J. Electroanal. Chem. 384, 105-113.

King, F., M.J. Quinn and C.D. Litke. 1995b. Oxygen reduction on copper in neutral NaCl solution. J. Electroanal. Chem. 385, 45-55.

King, F., C.D. Litke, M.J. Quinn and D.M. LeNeveu. 1995c. The measurement and prediction of the corrosion potential of copper in chloride solutions as a function of oxygen concentration and mass-transfer coefficient. Corros. Sci. 37, 833-851

King, F., M. Kolar and D.W. Shoesmith. 1996. Modelling the effects of porous and semi-permeable layers on corrosion processes. CORROSION/96, NACE International, Houston, TX, paper no. 380.

Kirkham, T. 1995. Development of test equipment and procedures for determination of the gas breakthrough pressure of compacted clay materials with preliminary results. M.Sc. Thesis, Dept. of Civil and Geological Engineering, University of Manitoba.

Kolar, M. and F. King. 1996a. Modelling the consumption of oxygen by container corrosion and reaction with Fe(II). In Materials Research Society Symposia Proceedings 412 (ed. W.M. Murphy and D.. Knecht) (Scientific Basis for Nuclear Waste Management XIX) 547-554.

Kolar, M. and F. King. 1996b. A model for the corrosion of copper containers in a Canadian nuclear fuel waste disposal vault. Part 2. The mathematical model., results and discussion. Atomic Energy of Canada Limited Report, AECL-11473, COG-95-521.

Kolar, M. and D.M. LeNeveu. 1995. Near-field mass transport from a point source (instantaneously failed container) located in a disposal room. Atomic Energy of Canada Limited Report, AECL11172, COG-1-94-444.

Lemire, R.J. and F. Garisto. 1989. The solubility of U, Np, Pu, Th, and Tc in a geological disposal vault for used nuclear fuel. Atomic Energy of Canada Limited Report, AECL-10009.

Lemire, R.J. and D.J. Jobe. 1996. Predicted behaviour of technetium in a geological disposal vault for used nuclear fuel - ramifications of a recent determination of the enthalpy of determination of TcO_2(cr). In Materials Research Society Symposia Proceedings 412 (ed. W.M. Murphy and D. Knecht) (Scientific Basis for Nuclear Waste Management XIX) in press.

LeNeveu, D.M. 1994. Analysis specifications for the CC3 vault model. Atomic Energy of Canada Limited Report, AECL-10970, COG-94-100.

LeNeveu, D.M. 1996. Mass transfer rates from a pinhole in a waste container for an inventory-limited and a constant concentration source. Atomic Energy of Canada Limited Report, AECL-11540, COG-96-68.

LeNeveu, D.M. and M. Kolar. 1996. Radionuclide response function to the convection-dispersion equation for a point source along the axis of nested cylindrical media. Atomic Energy of Canada Limited Report, AECL-11549, COG-96-90.

Lindblom, J., P. Henderson and F. Seitisleam. 1995. Creep testing of oxygen-free phosphorous copper and extrapolation of results. Swedish Institute for Metals Research Report, IM3197.

Litke, C.D., S.R. Ryan and F. King. 1992. A mechanistic study of the uniform corrosion of copper in compacted clay-sand soil. Atomic Energy of Canada Limited Report, AECL-10397, COG-91-304.

Lucey, V.F. 1967. Mechanism of pitting corrosion of copper in supply waters. Br. Corros. J. 2, 175-185.

Maak, P.Y.Y. 1984. Electron beam welding of thick-walled copper containers for nuclear fuel waste disposal - phase two. Atomic Energy of Canada Limited Technical Record, TR-253*.

Maak, P.Y.Y. 1987. Electron beam welding of a thick-walled oxygen-free copper pipe mock-up. Ontario Hydro Research Division Report, 86-224-K.

Maak, P.Y.Y. 1988. Electron-beam welding of thick-walled copper containers for nuclear fuel waste disposal - phase three B. Atomic Energy of Canada Limited Technical Record, TR-444*.

Moles, M.D.C. 1992. Copper inspection issues for nuclear used fuel container final closure welds. Ontario Hydro Research Division Report, M92-50-K.

Myers, J.R. and A. Cohen. 1995. Pitting corrosion in cold potable water systems. Mats. Perf. 34, 60-62.

Neretnieks, I., K. Andersson and L. Henstam. 1978. Utläackning av ^{59}Ni fran ett bergförvar. KBS Report No. 101.

Nowak, E.J. 1984. Diffusion of colloids and other waste species in brine-saturated backfill materials. In Materials Research Society Symposia Proceedings 26 (ed. G.L. McVay) (Scientific Basis for Nuclear Waste Management VII) 59-68.

Ohuchi, A. and H. Sakurai. 1988. Studies of fission products behavior in BWR fuel rods. In Proceedings of the International Topical Meeting on LWR Fuel Performance, Williamsburg, VA, 1988, pp. 180-188.

Onofrei, M. 1996. Evolution of pH in concrete/water systems. Memo FWTB-95-382.

Ophori, D.U., D.R. Stevenson, M. Gascoyne, A. Brown, C.C. Davison, T. Chan and F.W. Stanchell. 1995. Revised model of regional groundwater flow of the Whiteshell Research Area: Summary. Atomic Energy of Canada Limited Report, AECL-11286, COG-95-115.

Ophori, D.U., A. Brown, T. Chan, C.C. Davison, M. Gascoyne, N.W. Scheier, F.W. Stanchell and D.R. Stevenson. 1996. Revised model of regional groundwater flow in the Whiteshell Research Area. Atomic Energy of Canada Limited Report, AECL-11435, COG-95-443.

Oscarson, D.W. 1994. Surface diffusion: Is it an important transport mechanism in compacted clays? Clays Clay Minerals 42, 534-543.

Oscarson, D.W. and D.A. Dixon. 1989. Elemental, mineralogical, and pore-solution composition of selected Canadian clays. Atomic Energy of Canada Limited Report, AECL-9891.

Oscarson, D.W. and H.B. Hume. 1993. On the smectite-to-illite reaction. Atomic Energy of Canada Limited Report, AECL-10842, COG-93-278.

Oscarson, D.W., R.B. Heimann and R.L. Watson. 1984. Metallic iron content of candidate clays and silica sand for use in the Canadian Nuclear Fuel Waste Management Program. Atomic Energy of Canada Limited Technical Record, TR-281*.

Oscarson, D.W., D.A. Dixon, and M.N. Gray. 1990. Swelling capacity and permeability of an unprocessed and processed bentonitic clay. Eng. Geol. 28, 281-289.

Oscarson, D.W., H.B. Hume and J.-W. Choi. 1994. Diffusive transport in compacted mixtures of clay and crushed granite. Radiochim. Acta 65, 189-194.

Oscarson, D.W., N.G. Sawatsky, W.-J. Cho and J.-W. Choi. 1995. Compacted clays as barriers to radionuclide transport. In Fifth International Conference on Radioactive Waste Management and Environmental Remediation, Berlin, Germany. Sponsored by the American Society of Mechanical Engineers, pp. 751-754.

Oscarson, D.W., D.A. Dixon and H.B. Hume. 1996. Mass transport through defected bentonite plugs (submitted to Applied Clay Science).

Pusch, R. 1981. Borehole sealing with highly compacted Na-bentonite. KBS Project 15.11 + 5.111, 12-07.

Pusch, R. 1982. Chemical interaction of clay buffer materials and concrete. SKB Report SFR82-01.

Pusch, R., L. Ranhagen and K. Nilsson. 1985. Gas migration through MX-80 bentonite. National Cooperative for theStorage of Radioactive Waste Report, Nagra-NTB-85-36.

Pusch, R., L. Börgesson, and M. Erlstrom. 1987. Alteration of isolating properties of dense smectite clay in repository environment as exemplified by seven pre-quarternary clays. SKB-TR-87-10.

Pusch, R., I. Neretnieks and P. Sellin. 1991. Description of transport pathways in KBS-3 type repository. SKB Technical Report, 91-49.

Reed, D.T. and R.A. Van Konynenburg. 1991. Effect of ionizing radiation on the waste package environment. In High Level Radioactive Waste Management II, American Nuclear Society, La Grange Park, IL, pp. 1396-1403.

Roberson, H.E. and R.W. Lahann. 1981. Smectite to illite conversion rates: effects of solution chemistry. Clays Clay Miner. 29, 129-135.

Robin, M.J.L., R.W. Gillham and D.W. Oscarson. 1987. Diffusion of strontium and chloride in compacted clay-based materials. Soil Sci. Soc. Am. J. 51, 1102-1108.

Romanoff, M. 1957. Underground Corrosion. NACE International, Houston, TX.

Rowe, R.K., 1987. Pollutant transport through barriers. In Geotechnical Practice for Waste Disposal (R.D. Woods, ed.). Special Publication No. 13, ASCE, pp. 159-181.

Ryan, S.R. and F. King. 1994. The adsorption of Cu(II) on sodium bentonite in a synthetic saline groundwater. Atomic Energy of Canada Limited Report, AECL-11062, COG-I-94-125.

Sharma, V.K. and F.J. Millero. 1988. The oxidation of Cu(I) in electrolyte solutions. J. Solution Chem. 17, 581-599.

Sheppard, M.I., S. Stroes-Gascoyne, J.L. Hawkins, C.J. Hawton and M. Motycka. 1996. Methane production rates from natural organics of glacial lake clay and granitic groundwater. Atomic Energy of Canada Limited Report, AECL-11510, COG-95-578.

Shoesmith, D.W. and S. Sunder. 1991. An electrochemistry-based model for the dissolution of UO_2. Atomic Energy of Canada Limited Report, AECL-10488.

Shoesmith, D.W. and S. Sunder. 1992. The prediction of nuclear fuel (UO_2) dissolution rates under waste disposal conditions. J. Nucl. Mater., 190, 20-35. Also Atomic Energy of Canada Limited Reprint, AECL-10677.

Shoesmith, D.W., S. Sunder, L.H. Johnson and M.G. Bailey. 1985. Oxidation of CANDU UO_2 fuel by the alpha radiolysis products of water. In Materials Research Society Symposia Proceedings 50 (ed. L.O. Werme) (Scientific Basis for Nuclear Waste Management IX) 309-316.

Shoesmith, D.W., S. Sunder, M.G. Bailey and G.J. Wallace. 1989. The corrosion of nuclear fuel (UO_2) in oxygenated solutions. Corros. Sci. 29, 1115-1128. Also Atomic Energy of Canada Limited Reprint, AECL-9887

Shoesmith, D.W., F. King and B.M. Ikeda. 1995a. An assessment of the feasibility of indefinite containment of Canadian nuclear fuel wastes. Atomic Energy of Canada Limited Report, AECL-10972, COG-94-534.

Shoesmith, D.W., J.C. Tait, S. Sunder, W.J. Gray, S.A. Steward, R.E.Russo and J.D. Rudnicki. 1995b. Factors affecting the differences in reactivity and dissolution rates between UO_2 and spent nuclear fuel. Atomic Energy of Canada Limited Report, AECL-11515, COG-95-581.

Shoesmith, D.W., S. Sunder, M.G. Bailey and N.H. Miller. 1996. Corrosion of used nuclear fuel in aqueous perchlorate and carbonate solutions. J. Nucl. Mater. 227, 287-299.

Shreir, L.L. 1976. Corrosion. 2nd edition, Newnes-Butterworths, London.

Sieradzki, K., R.L. Sabatini and R.C. Newman. 1984. Stress-corrosion cracking of copper single crystals. Met. Trans. 15A, 1941-1946.

Simmons, G.R. and P. Baumgartner. 1994. The disposal of Canada's nuclear fuel waste: engineering for a disposal facility. Atomic Energy of Canada Limited Report, AECL-10715, COG-93-5.

SKB (Swedish Nuclear Fuel and Waste Management Co.). 1992. SKB91. Final disposal of spent nuclear fuel. Importance of the bedrock for safety. Swedish Nuclear Fuel and Waste Management Company Report, SKB-TR-92-20.

Spinks, J.W.T. and R.J. Woods. 1990. An Introduction to Radiation Chemistry, 3rd Ed. Wiley-Interscience, New York.

Sridhar, N. and G.A. Cragnolino. 1993. Effects of environment on localized corrosion of copper-based, high-level waste container materials. Corrosion 49, 967-976.

Stanchell, F.W., C.C. Davison, T. Melnyk, N.W. Scheier and T. Chan. 1996. The Disposal of Canada's Nuclear Fuel Waste: A study of postclosure safety of in-room emplacement of used CANDU fuel in copper containers in permeable plutonic rock. Volume 3: Geosphere Model. Atomic Energy of Canada Limited Report, AECL-11494-3, COG-95-552-3.

Stevenson, D.R., A. Brown, C.C. Davison, M. Gascoyne, R.G. McGregor, D.U. Ophori, N.W. Scheier, F.W. Stanchell, G.A. Thorne and D.K. Tomsons. 1995. A revised conceptual hydrogeologic model of a crystalline rock environment, Whiteshell Research Area, Southeastern Manitoba, Canada. Proceedings of Solutions '95, International Association of Hydrogeologists, Congress XXVI, Edmonton, Alberta, Canada.

Stevenson, D.R., A. Brown, C.C. Davison, M. Gascoyne, R.G. McGregor, D.U. Ophori, N.W. Scheier, F.W. Stanchell, G.A. Thorne and D.K. Tomsons. 1996. A revised conceptual hydrogeologic model of a crystalline rock environment, Whiteshell Research Area, southeastern Manitoba, Canada. Atomic Energy of Canada Limited Report, AECL-11331, COG-95-271.

Stroes-Gascoyne, S. Measurements of instant-release source terms for ^{137}Cs, ^{90}Sr, ^{99}Tc, ^{129}I and ^{14}C in used CANDU fuels. Submitted to J. Nucl. Materials.

Stroes-Gascoyne, S. and J.M. West. 1994. Microbial issues pertaining to the Canadian concept for the disposal of nuclear fuel waste. Atomic Energy of Canada Limited Report, AECL-10808, COG-93-54.

Stroes-Gascoyne, S., J.C. Tait, R.J. Porth, J.L. McConnell and W.J. Lincoln. 1994. Waste Management 14, 385-392.

Stroes-Gascoyne, S., L.M. Lucht, J. Borsa, T.L. Delaney, S.A. Haveman and C.J. Hamon. 1995. Radiation resistance of the natural microbial population in buffer. In Materials Research Society Symposia Proceedings 353 (ed. T. Murakami and R.C. Ewing) (Scientific Basis for Nuclear Waste Management XVIII) 345-352.

Sunder, S. 1995. Alpha, beta and gamma dose rates in water in contact with used CANDU UO_2 Fuel. Atomic Energy of Canada Limited Report, AECL-11380, COG-95-340.

Sunder, S. and D.W. Shoesmith. 1991. Chemistry of UO_2 fuel dissolution in relation to the disposal of used nuclear fuel, Atomic Energy of Canada Limited Report AECL-10395.

Sunder, S., D.W. Shoesmith, L.H. Johnson, G.J. Wallace, M.G. Bailey and A.P. Snaglewski. 1987. Oxidation of CANDU fuel by the products of alpha radiolysis of groundwater. In Materials Research Society Symposia Proceedings 84 (ed. J.K. Bates and W.B. Seefeldt) (Scientific Basis for Nuclear Waste Management X) 103-113.

Sunder, S., D.W. Shoesmith, H. Christensen and N.H. Miller. 1992a. Oxidation of UO_2 fuel by the products of gamma radiolysis of water. J. Nucl. Mater. 190, 78-86.

Sunder, S., D.W. Shoesmith, N.H. Miller and G.J. Wallace. 1992b. Determination of criteria for selecting a UO_2 fuel dissolution model for nuclear fuel waste management concept assessment. In Materials Research Society Symposia Proceedings 257 (ed. C.F. Sombret) (Scientific Basis for Nuclear Waste Management XV) 345-352.

Sunder, S., D.W. Shoesmith and N.H. Miller. 1995. Prediction of the Oxidative Dissolution Rates of Used Nuclear Fuel in a Geological Disposal Vault due to the Alpha Radiolysis of Water. In Materials Research Society Symposia Proceedings 353 (ed. T. Murakami and R.C. Ewing) (Scientific Basis for Nuclear Waste Management XVIII) 617-624.

Sunder, S., L.K. Strandlund and D.W. Shoesmith. 1996. Anodic dissolution of UO_2 in slightly alkaline sodium perchlorate solutions. Atomic Energy of Canada Limited Report, AECL-11440, COG-95-461.

Swedish Corrosion Institute. 1983. The corrosion resistance of a copper canister for spent nuclear fuel - Follow up. Report for the Swedish Nuclear Fuel Supply Company, SKBF-KBS-TR-83-24.

Tait, J.C. and J.R. Theaker. 1996. Light element radionuclides in used CANDU fuel and their potential contribution to postclosure safety assessment. Atomic Energy of Canada Limited Report. AECL-11431, COG-95-440

Tait, J.C., Gould, I. and G.B. Wilkin. 1989. Atomic Energy of Canada Limited Report. AECL-9881.

Teper, B. 1987. Test program of granular materials for the thin-walled, particulate-packed container. Ontario Hydro Research Division Report, 87-154-K

Teper, B. 1988. Test program of the prototype of the TWPP container: Part 3 - detailed stress analysis and comparison with test results. Ontario Hydro Research Division Report, 87-296-K.

Teper, B. 1992. Proposed design of copper containers for IES study. Memorandum to J.L. Crosthwaite, Ontario Hydro Technologies file reference 825.123(T).

Teper, B. 1994. Proposed redesign of top lid weld of the PASCOS container. Memorandum to L. Crosthwaite, Ontario Hydro Technologies file reference 825.123.

Teper, B. 1995. Initial stress analysis of PASCOS container. Ontario Hydro Technologies Report, A-NBP-95-121-CON.

Thompson, D.H. and A.W. Tracy. 1949. Influence of composition on the stress-corrosion cracking of some copper-base alloys. Met. Trans. 1949, 100-109.

Tuovinen, O.H. 1990. Biological fundamentals of mineral leaching processes. In Microbial Mineral Recovery. H.L. Ehrlich and C.L. Brierley, editors. McGraw-Hill Publishing Company Inc., U.S.A.

Vazquez, M.V., S.R. de Sanchez, E.J. Calvo and D.J. Schiffrin. 1994. The electrochemical reduction of oxygen on polycrystalline copper in borax buffer. J. Electroanal. Chem. 374, 189-197.

Vieno, T., A. Hautojarvi, L. Koskinen and H. Nordman. 1992. TVO-92 Safety Analysis of Spent Fuel Disposal. Nuclear Waste Commission of Finnish Power Companies Report, YJT-92-33E.

Vilks, P., Cramer, J., Bachanski, D.B., Doern, D.C. and Miller, H.G. 1993. Studies of colloids and suspended particles, Cigar Lake uranium deposit, Saskatchewan, Canada. Applied Geochemistry 8, 605-616.

Wai, R.S.C. and A.Tsai. 1995. Three-dimensional thermal and thermal-mechanical analyses for a used-fuel disposal vault with the in-room emplacement option. Ontario Hydro Report N-REP-03780-0083 R00.

Wasywich, K.M. 1992. Examination of spent CANDU fuel following 27 years of pool storage. Electric Power Research Institute Report, EPRI-TR-1006745.

Wasywich, K.M. 1993. Characteristics of used CANDU fuel relevant to the Canadian Nuclear Fuel Waste Management Program. Atomic Energy of Canada Limited Report, AECL-10463, COG-91-340.

Wikjord, A.G., P. Baumgartner, L.H. Johnson, F.W. Stanchell, R. Zach and B.W. Goodwin. 1996. The Disposal of Canada's Nuclear Fuel Waste: A study of postclosure safety of in-room emplacement of used CANDU fuel in copper containers in permeable plutonic rock. Volume 1: Summary. Atomic Energy of Canada Limited Report, AECL-11494-1, COG-95-552-1.

Zach, R., B.D. Amiro, G.A. Bird, C.R. Macdonald, M.I. Sheppard, S.C. Sheppard and J.G. Szekely. 1996. The Disposal of Canada's Nuclear Fuel Waste: A study of postclosure safety of in-room emplacement of used CANDU fuel in copper containers in permeable plutonic rock. Volume 4: Biosphere Model. Atomic Energy of Canada Limited Report, AECL-11494-4, COG-95-552-4.

---

* Atomic Energy of Canada Limited Technical Record, available through SDDO, Chalk River Laboratories, Chalk River, Ontario K0J 1J0

APPENDIX A

RADIONUCLIDE INVENTORIES

The sources for radiotoxic elements in a CANDU used-fuel bundle are activation and fission products from the UO_2 matrix, activation products of the Zircaloy fuel sheath, and activation products from impurities in both the fuel and the Zircaloy fuel sheath. The inventories of these elements, in moles per kilogram initial uranium in an unirradiated fuel bundle, were calculated for 10-year cooled Bruce reactor fuel, with an average bundle burnup of 200 $MWh \cdot kg^{-1}$ initial U (720 $GJ \cdot (kg\ U)^{-1}$) using the ORIGEN-S radionuclide generation/depletion code (Tait et al. 1989; Tait, in preparation) coupled with the WIMS-AECL lattice code (Donnelly 1986). The inventories used in the vault model are summarized in Table A-1 which also gives the distribution functions chosen to allow for variability in radionuclide inventories. The half-lives of these nuclides are also given in Table A-1. The radionuclides in Table A-1 were selected on the basis of a screening study by Goodwin et al. (1996).

The ability of the coupled ORIGEN-S/WIMS-AECL code to predict radionuclide inventories in used CANDU fuel has been validated for a number of key actinide and fission product radionuclides by direct comparison of predicted inventories with those measured by radiochemical analysis of a well characterized Bruce reactor fuel with a burnup of 221 $MWh \cdot kg^{-1}$ U (Tait et al. 1995). These data have been used to derive probability distribution functions (PDF) for the radionuclide inventories used in the vault model calculation. The errors associated with measurement of these inventories have been taken into consideration when deriving the standard deviation for the PDF's for the calculated ORIGEN-S inventories (Table A-1). Most of the measured actinide and fission product radionuclide inventories agreed reasonably will with ORIGEN-S predictions. The ORIGEN-S code was found in most cases to conservatively overpredict radionuclide inventories.

In addition to code validation, an extensive analysis was conducted of all potential impurity elements likely to be present in either the UO_2 fuel or the Zircaloy sheath, that could be activated to radionuclides with half-lives greater than 1 a (Tait and Theaker, 1996). This study estimated the maximum likely impurity concentration of all 'light elements' with atomic number less than 83 (bismuth) and recommended upper limit elemental concentrations that should be used to calculate activation product concentrations using the ORIGEN-S code. These recommended impurity concentrations were, where possible, based on maximum permissible impurity limit specifications for the manufacture of UO_2 fuel pellets or Zircaloy sheath. Where no such specifications exist for UO_2, elemental impurity concentrations were derived on the basis of chemical similarity with known impurities and arguments based on natural elemental abundances in the earth's crust. Where no specification exist for Zircaloy, elemental impurities were based on a large statistical analytical database on chemically similar Zr-2.5Nb pressure tubes whose fabrication methods and composition is similar to Zircaloy sheaths. It was

assumed that the actinide elements (those heavier than Bi) would be generated in such high concentrations in the fuel that their inventories would far outweigh any inventory generated by activation of actinide impurities. In addition, all known impurities in fuel bundle construction materials, including the Be braze used to secure the bearing pads on the Zircaloy sheath and the CANLUB (graphite) coating used on the inner surface of the outer 30 elements in a Bruce fuel bundle, were taken into consideration. The recommended elemental impurity limits were used in an ORIGEN-S/WIMS-AECL calculation to predict the inventories of activated light element impurities (Tait, unpublished results).

To allow for variability between code predictions and actual inventories, probability distribution functions (PDF) were assigned to each radionuclide inventory. Where there was good agreement between measured and predicted inventories, a normal PDF was chosen with the inventory as the mean and the analytical error as the standard deviation. Upper and lower cut-offs were chosen to be 5 standard deviations (5 sigma) higher and lower than the mean. If the lower cut-off was not meaningful as a result of its 5 sigma value being greater than the mean, the lower cut-off was chosen to be one order of magnitude lower than the mean. For radionuclides that were daughters of well characterized parents, the PDF and error bounds of the parent were used.

The concentration of the activation product ^{14}C was calculated on the basis of assumed impurity levels of 100 $\mu g \cdot g^{-1}$ N_2 (which is the primary elemental source for ^{14}C) in the fuel and is the maximum permissible impurity limit set by fuel manufacturing specifications (Tait et al. 1989). The ^{14}C concentration predicted by the ORIGEN-S code using a 100 $\mu g \cdot g^{-1}$ N impurity was 2.82 x 10^{-5} $mol \cdot kg^{-1}$ U (Tait, unpublished results). Recent measurements of total ^{14}C inventories in numerous fuels (Stroes-Gascoyne et al. 1994) have shown that the total ^{14}C inventories are on average 11.5 ± 3.9 times lower than the inventory predicted by ORIGEN-S, implying that the actual N impurity level is closer to 10 $\mu g \cdot g^{-1}$. The range of measured ^{14}C concentrations on these fuels was about 5 to 16 times lower than ORIGEN-S predictions. On this basis, the range of measured ^{14}C concentrations the upper and lower bounds ^{14}C inventory were chosen to be 5.64 x 10^{-6} $mol \cdot kg^{-1}$ U and 1.96 x 10^{-6} $mol \cdot kg^{-1}$ U respectively using a uniform PDF. The concentration of ^{14}C in Zircaloy was calculated using a N impurity concentration of 80 $\mu g \cdot g^{-1}$. A uniform PDF for ^{14}C impurity in Zircaloy has been chosen with an upper bound at the calculated ^{14}C concentration in Zircaloy and a lower bound one order of magnitude lower.

The radionuclide inventory for ^{36}Cl was based on an assumed 5 $\mu g \cdot g^{-1}$ elemental Cl impurity in the fuel and a 6 $\mu g \cdot g^{-1}$ impurity in Zr-4. The inventory for ^{36}Cl in fuel has a normal distribution while the ^{36}Cl inventory in Zircaloy has a uniform distribution with an upper bound equal to the inventory for a 6 $\mu g \cdot g^{-1}$ impurity and a lower bound one order of magnitude lower.

TABLE A-1

RADIONUCLIDE INVENTORIES FOR BRUCE FUEL WITH A BURNUP OF 200 Mwh·(kg U)$^{-1}$ AND A COOLING TIME OF 10 a

Nuclide	Source [a]	PDF[b]	Inventory (mol·(kg initial U)$^{-1}$)	Standard Deviation[c] (%)	Half-Life (a)[d]
^{14}C	FI	Uniform	5.640×10^{-6}	upper bound[e]	5730
^{14}C	ZI	Uniform	2.650×10^{-6}	upper bound[f]	5730
^{36}Cl	FI	Normal	8.980×10^{-6}	50	3.0×10^{5}
^{36}Cl	ZI	Uniform	1.330×10^{-6}	upper bound[g]	3.0×10^{5}
^{79}Se	FP	Normal	1.596×10^{-5}	10	6.5×10^{4}
^{90}Sr	FP	Normal	1.159×10^{-3}	2.5	29
^{90}Y	FP	SE[h]	3.011×10^{-7}	-	64 h
^{93}Zr	FP	Normal	1.260×10^{-3}	20	1.5×10^{6}
^{93m}Nb	FP	Normal	4.767×10^{-9}	20	13.6
^{99}Tc	FP	Normal	2.210×10^{-3}	10	2.13×10^{5}
^{107}Pd	FP	Normal	5.946×10^{-4}	10	6.5×10^{6}
^{126}Sb	FP	SE	2.163×10^{-12}	-	12.4 d
^{126}Sn	FP	Normal	4.553×10^{-5}	10	1.0×10^{5}
^{129}I	FP	Normal	3.803×10^{-4}	5	1.6×10^{7}
^{135}Cs	FP	Normal	1.780×10^{-4}	3	3.0×10^{6}
^{137}Cs	FP	Normal	1.862×10^{-3}	2	30.17
^{210}Pb	AP	Normal	5.479×10^{-16}	55	22.3
^{210}Bi	AP	Normal	3.373×10^{-19}	55	3.0×10^{6}
^{210}Po	AP	Normal	9.314×10^{-18}	55	138 d
^{222}Rn	AP	Normal	1.963×10^{-18}	55	3.8 d
^{223}Ra	AP	Normal	9.403×10^{-15}	50	11.4 d
^{225}Ra	AP	Normal	7.973×10^{-15}	50	14.8 d
^{226}Ra	AP	Normal	3.000×10^{-13}	55	1600
^{225}Ac	AP	Normal	5.386×10^{-15}	50	10.0 d
^{227}Ac	AP	Normal	6.532×10^{-12}	50	21.8
^{227}Th	AP	Normal	1.518×10^{-14}	50	18.7 d
^{229}Th	AP	Normal	1.550×10^{-9}	50	7300
^{230}Th	AP	Normal	5.865×10^{-9}	55	7.54×10^{4}
^{231}Th	AP	Normal	3.373×10^{-14}	3	25.5 h
^{234}Th	AP	Normal	6.107×10^{-11}	55	24.1 d
^{231}Pa	AP	Normal	3.503×10^{-8}	3	3.28×10^{4}
^{233}Pa	AP	Normal	4.637×10^{-12}	20	27 d

...continued

TABLE A-1 (Concluded)

RADIONUCLIDE INVENTORIES FOR BRUCE FUEL WITH A BURNUP OF 200 Mwh·(kg U)$^{-1}$ AND A COOLING TIME OF 10 a

Nuclide	Source [a]	PDF[b]	Inventory (mol·(kg initial U)$^{-1}$)	Standard Deviation[c] (%)	Half-Life (a)[d]
^{233}U	AP	Normal	3.479×10^{-5}	50	1.59×10^{5}
^{234}U	Matrix	Normal	1.863×10^{-4}	55	2.45×10^{5}
^{235}U	Matrix	Normal	8.154×10^{-3}	3	7.00×10^{8}
^{238}U	Matrix	Constant	4.136	-	4.47×10^{9}
^{237}Np	AP	Normal	1.342×10^{-4}	20	2.14×10^{6}
^{239}Np	AP	Normal	1.423×10^{-11}	20	2.35 d
^{239}Pu	AP	Normal	1.124×10^{-2}	3	2.41×10^{4}
^{241}Am	AP	Normal	3.999×10^{-4}	20	432
^{243}Am	AP	Normal	1.626×10^{-5}	20	7380
Zr	Matrix	Constant	1.289	-	-

a AP - ^{238}U activation product; FP - Fission Product; FI - Fuel impurity activation product; ZI - Zircaloy impurity activation product.

b Probability Distribution Function - SE indicates nuclide is in secular equilibrium with its parent; Constant refers to matrix concentration with no variability.

c The error (%) represents a one sigma (one standard deviation) error applied to the inventory calculated by ORIGEN-S. The normal PDF upper bound is the inventory +5▲. The error bounds were estimated from measurements of specific radionuclide inventories in used fuel (Tait et al. 1995).

d Half-lives in years except where noted. Short half-life species are daughter products from longer-lived parent.

e Upper bound 5.64×10^{-6} mol·(kg U)$^{-1}$. Lower bound 1.76e-06 mol/kg U. Upper and lower bounds derived on the basis of ^{14}C measurements (Stroes-Gascoyne et al. 1994).

f Upper bound 2.65×10^{-6} mol·(kg U)$^{-1}$ is inventory calculated using 80 μg·g^{-1} N impurity in Zr. Lower bound is one order of magnitude lower than upper bound.

g Upper bound 1.33×10^{-6} mol·(kg U)$^{-1}$ is inventory calculated using 6 μg·g^{-1} Cl impurity in Zr. Lower bound is one order of magnitude lower than upper bound.

REFERENCES

Donnelly, J.V. 1986. WIMS-CRNL: A user's manual for the Chalk River version of WIMS. Atomic Energy of Canada Limited Report, AECL-8955.

Goodwin, B.W., T.H. Andres, W.C. Hajas, D.M. LeNeveu, T.W. Melnyk, J.G. Szekely, A.G. Wikjord, D.C. Donahue, S.B. Keeling, C.I. Kitson, S.E. Oliver, K. Witzke and L. Wojciechowski. 1996a. The Disposal of Canada's Nuclear Fuel Waste: A study of postclosure safety of in-room emplacement of used CANDU fuel in copper containers in permeable plutonic rock. Volume 5: Postclosure Assessment. Atomic Energy of Canada Limited Report, AECL-11494-5, COG-95-552-5.

Stroes-Gascoyne, S., J.C. Tait, R.J. Porth, J.L. McConnell, and W.J. Lincoln. 1994. Release of ^{14}C from the gap and grain-boundary regions of used CANDU fuels to aqueous solutions. Waste Management, 14, 385-392.

Tait, J.C., I.C. Gauld, and G.B. Wilkin. 1989. Derivation of initial radionuclide inventories for the safety assessment of the disposal of used CANDU fuel. Atomic Energy of Canada Limited Report, AECL-9881.

Tait, J.C. I. Gauld and A.H. Kerr. 1995. Validation of the ORIGEN S code for predicting radionuclide inventories in used CANDU fuel. J. Nucl. Materials, 223, 109-121. (Also issued as Atomic Energy of Canada Limited Report, AECL-10891, COG-93-346 (1994)).

Tait, J.C. and J.R. Theaker. 1996. Light element radionuclides in used CANDU fuel and their potential contribution to postclosure safety assessment. Atomic Energy of Canada Limited Report. AECL-11431, COG-95-440

APPENDIX B

CONCEPTUAL MODEL FOR THE EXCAVATION-DISTURBED ZONE (EDZ)

B.1. INTRODUCTION

The overall aim of this study is to evaluate information available on the EDZ around an excavated opening in the host rock relevant to the in-room emplacement concept, and to recommend appropriate characteristics of the zone, required as input variables in the vault model.

Although the EDZ has been the subject of laboratory and field studies and modeling, only a few studies have addressed the hydraulic aspects of the EDZ. Many of the processes responsible for the formation of the EDZ are not well understood and the attributes of this zone have been described mainly in qualitative terms. However, an attempt has been made to represent the complex excavation-disturbed system by a simplified EDZ conceptual model that incorporates as many as possible of the features and factors relevant to radionuclide transport.

B.2. EDZ DEFINITION

The EDZ is defined as the near-field rock adjacent to an underground opening that has a different fracture network, and consequently different hydrological and radionuclide transport attributes, from the host rock. Various terms such as "disturbed rock zone" (Birgersson et al. 1992) or "fracture zone" (Golder Associates 1977) have been used in the literature to define this zone, which is affected by complex thermal, hydraulic, mechanical and chemical processes that take place in a repository. Changes in host rock properties that may affect the far field flow and transport depend largely on coupled Thermo-Hydro-Mechanical (T-H-M) processes. From a T-H-M equilibrium viewpoint, the near-field is non-stationary, therefore the PDFs of EDZ characteristics change with time. The concept of an equilibrium, generalized energy profile, as a function of the state of the system, is schematically illustrated in Fig. B-1. The excavation and emplacement of containers are the two main events that disturb the state of the host-rock. During the lifetime of the vault system, three sequential stages can be distinguished: the operation, heating and cooling stages. Throughout its lifetime, the vault system is in a metastable state. However, a quasi-stationary state is reached at every stage (i.e., a pseudo-steady state of T-H-M equilibrium is achieved); hence, meaningful parameters of the geometry and attributes of the disturbed zone can be developed.

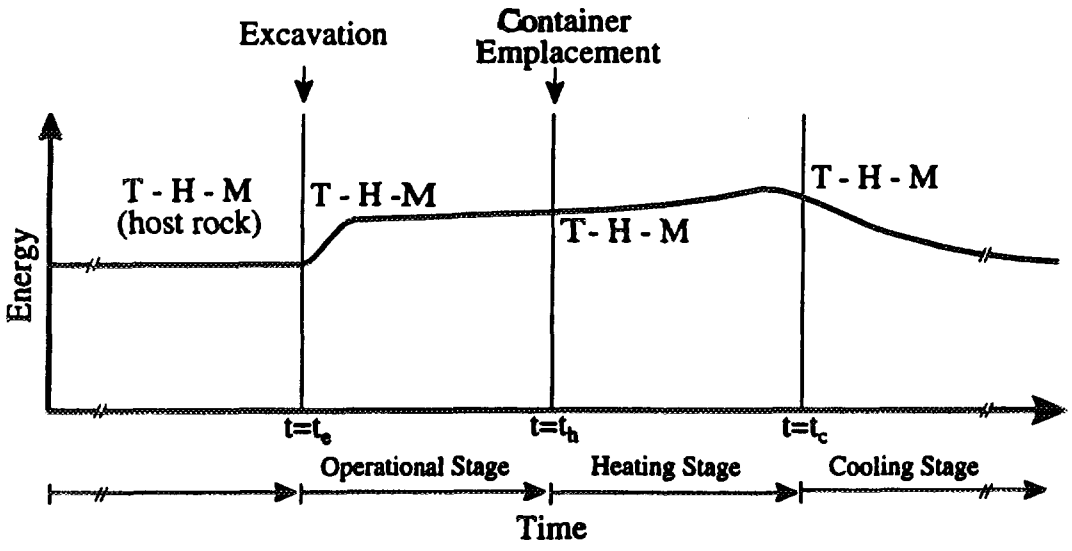

Figure B-1 Concept of T-H-M Equilibrium in the Near Field.

The effects of excavation on the attributes of the EDZ have received considerable attention, primarily in relation to rock mechanics characteristics associated with operational safety and development of engineering techniques to minimize the damage induced by blasting. The impact of thermal loading and cooling processes have been less thoroughly investigated. However, Winberg (1991b) pointed out that after cooling, the hydraulic conductivity, for example, will return to the post-excavation state value, although still with close to one order of magnitude lower than the initial excavation state. In defining the EDZ attributes in this study, emphasis was placed on alteration of the host-rock characteristics, due to the excavation by blasting (fracturing of intact rock) and stress redistribution (i.e., extending and opening/closing of some pre-existing fractures).

B.3. MASS TRANSPORT IN THE EDZ

The vault model considers the EDZ explicitly. The model encompasses a scale from a few meters to a few hundred meters (the diameter and the length of a room element of the vault and adjacent EDZ), and assumes that microscopic material properties can be characterized by macroscopic parameters. The model employs the equivalent porous medium approach to describe flow and mass transport in the discrete fracture network of the disturbed zone. A key issue is the formulation of all equivalent properties and the determination of the size of the Representative Elementary Volume (REV) over which the homogenization is valid. The REV is, in effect, a statistical index for the equivalence of properties between a fractured medium and its continuum idealization. The REV itself is not explicitly introduced. This requires a description of the EDZ using average values, i.e., by a set of deterministic values, i.e., model parameters. Since data vary between different sites as well

as within a given site and the data at a particular location within a given site are uncertain, numerical simulations of flow and transport in the EDZ with single-valued deterministic parameters are not sufficient for the performance assessment and the sensitivity analysis. The heterogeneities are described in the model as variations in effective values of the EDZ attributes, based on representative, but conservative, PDFs.

B.4. ESTIMATION OF ATTRIBUTES OF THE EDZ

The properties of the EDZ are controlled by a large set of factors that can be grouped into two categories: (1) host rock properties and (2) engineering factors. Among the most important properties of the host rock are the fracture structure and elastic isotropic characteristics of the intact rock under plane strain conditions (Barton et al. 1992), the bearing capacity of the rock mass and the distribution of tectonically induced strain, and the in situ stress field in relation to small-scale discontinuities (Pusch 1994). Among the most important engineering factors are the vault depth and position relative to highly conductive fractures, the geometry (size and shape) of the opening (Hoek and Brown 1980), the orientation of the tunnel relative to the principal in-situ stress, the excavation method that includes explosive weights and charge density (Hustrulid et al. 1992, Holmberg and Persson 1979), and sealing techniques (grouting) of the EDZ in repository (Pusch 1994).

Due to the large number of factors and processes that ultimately control the attributes of the EDZ and the inherent site-specific characteristics of the initial properties of the host rock, PDFs of EDZ attributes useful to construction of a vault ultimately have to be generated using geostatistical approaches or classical statistical techniques based on site-specific, in situ testing. The goal of the present study, that aims to be of generic interest, has been to produce reference input data for the vault model with a close correspondence to what would be expected for the EDZ of an underground opening in a fractured host rock situation. The selection of both the type of PDF and the respective parameters (location, scale and shape) was based on our understanding of typical ranges and statistics on fractured rock properties. The suggested conceptual model of the EDZ geometry and the PDF assigned to each characteristic are preliminary estimates, derived from theoretical studies (analytical evaluations), laboratory data and limited field studies. A literature review, primarily of the Stripa Project Reports and SKB Reports, was the source of information on which the derived values were based.

Permeability, porosity and dispersivity are the most important characteristics of the EDZ relevant to flow and transport of radionuclides. The permeability determines the average flux of fluid through a disturbed zone and the dispersivity determines the spreading of radionuclides. These attributes are related to each other and depend on EDZ geometric characteristics. Underlying the choice of the conceptual model of the EDZ was the observation in field studies that the presence of fractures and their relevance to radionuclide migration dictates a priori that flow can take place mainly in the direction parallel (x) and perpendicular (y) to the longitudinal axis of the opening (x, y-plane).

The porosity affects the radionuclide capacity factor. The porosity in the EDZ is always greater than that of the surrounding rock. The tortuosity would only be important in instances where mass transport is dominated by diffusion.

Three sets of EDZ attributes are of importance in the vault model: (1) extent and degree of disturbance, (2) hydraulic conductivity and permeability, and (3) dispersivity. The estimation of these attributes rests on two initial assumptions: (a) the hypothetical vault is located at a depth of 500 m and (b) the sparsely fractured rock behaves essentially elastically (Martin and Read 1996).

B.4.1 EXTENT OF AND DEGREE OF DISTURBANCE IN THE EDZ

The extent (i.e., thickness) and degree of disturbance in the EDZ in granite are controlled by two main disturbance mechanisms: (a) blasting, and (b) stress changes (including both stress relief and increases). These mechanisms act in combination, and only a few studies specifically distinguish between blast-damage and stress effects. With careful, controlled drill and blast techniques (optimal size and space between blast holes, charge weights and density) the damage zone can be minimized. Investigations of the thickness of the zone on the tunnel periphery damaged directly by blasting report depths of 0.30 m at Stripa (Andersson and Halen 1978), 0.10 to 0.15 m at the URL (Read and Martin 1996) and 0.18 to 0.28 m at Kiruna Mine (Hustrulid 1993). Within this thin skin adjacent to an opening, the fracture frequency increases significantly. Following excavation, stresses around an opening become redistributed. The concentration of compressive or tensile stresses extends the original fracture and opens or closes pre-existing fractures, with the net effect of altering the connected conductivity. Although attempts have been made, it is difficult to distinguish between the damaged zone and disturbed zone. The distinction between these two zones as well as their extent reported in the literature, from both field tests and conceptual models, varies considerably. For example, based on the data from a near-field seismic velocity study, Martin and Read (1996) defined the damage zone as the altered rockmass, due to combined effects of both blasting and stress redistribution, with an extent of 1.00 m. Bräuer and Sönnek (1995) using a variety of methods (geological, rock mechanics and geophysical) reported an EDZ of about 0.30 to 0.50 m. Based on the data generated from the Buffer Mass Test and Macro-permeability Test at Stripa in conjunction with the results from a numerical calculation, Pusch and Börgesson (1992) suggested that the major disturbance relevant to the groundwater flow occurred to a depth of 0.40 to 0.80 m in the walls and the roof and 1.00 to 2.00 m in the central part of the floor. Conceptual models based on some of the earlier field data also suggested different geometries for the EDZ. For example, the conceptual model of the geometry of the near-field around the tunnels suggested by Birgersson et al. (1992) distinguished two zones: a blast damage zone that extends 1.00 m out of tunnel and a stress-redistribution zone that extends one drift diameter out. The conceptual model suggested by Winberg (1991b) also distinguished two zones: the primary disturbed rock zone of approximately 1.00 m and a secondary zone of about 1 to 3 tunnel diameters. Hautojärvi (1991), in his model, considered two regions of equal extent each of 0.50 m.

Figure B-2 presents results from two recent field studies (Hayles et al. 1995, Bräuer and Sönnek 1995) and results from an analytical model (Kelsall et al. 1984) that provide important information regarding the extent and degree of disturbance of the EDZ and how the averaging procedure should be carried out. The p-wave velocity (pressure) near the tunnel wall recorded during the cross-hole seismic tomography survey for the Mine-By Experiment at the URL (Fig. B-2a), the frequency of open fractures based on microstructural analysis of the damage zone at the Grimsel Test Site (Fig. B-2b) and stress redistribution results from an analytical model (Fig. B-2c) suggested that the EDZ does not extend far from the opening periphery. An even more important feature of the EDZ suggested by all three sets of data is that the major disturbance takes place close to the tunnel face and that the degree of disturbance decreases rapidly in the radial direction into the rockmass. This suggests that evaluating the attributes for the equivalent porous medium would require simultaneous consideration of the extent of the EDZ and the magnitude of the attribute values.

Reported data for direct assessment of the EDZ vary. This is reasonable, taking into account the large number of factors that control the EDZ, such as blasting technique, size, shape and orientation of the opening, and field stresses. However, the field data, irrespective of origin and geological conditions, indicated several similar characteristics of an EDZ that can be summarized as follows:

a) any excavation disturbs the host rockmass by both blasting and stress redistribution, whose effects are difficult to distinguish,

b) the largest disturbances occur near the periphery of the opening and the degree of disturbance decreases (rapidly) exponentially in the radial direction from the surface of the opening,

c) the EDZ is heterogenous and anisotropic; if the rockmass is regarded as an homogenous isotropic material, then both the heterogeneity ratio and the anisotropy ratio of the EDZ can be regarded as characteristics that decrease with radial distance from the wall of the opening.

On the basis of observed field data and, to some extent, modeling results, it can be stated that a firm basis for understanding exists with regard to the geometry of the EDZ (extent and degree of disturbance). In the light of the limited statistics available, the extent of the EDZ in this study was assumed to have a normal distribution function. The parameters of the distribution, μ and σ, were derived from data suggested by Pusch and Börgesson (1992) derived from a macropermeability test conducted at Stripa designed to investigate the effect of the EDZ on the groundwater flow and transport of radionuclides. Assuming that for a probability P = 0.9998 the lower limit of the PDF has a value equal to 0.80 m, the maximum depth of the EDZ observed in the walls, and the upper limit has a value of 2.00 m, the maximum depth observed in the central part of the floor, the extent, which is a variable of the EDZ is normally distributed, with μ = 1.40 m and σ = 0.172 m, i.e., the

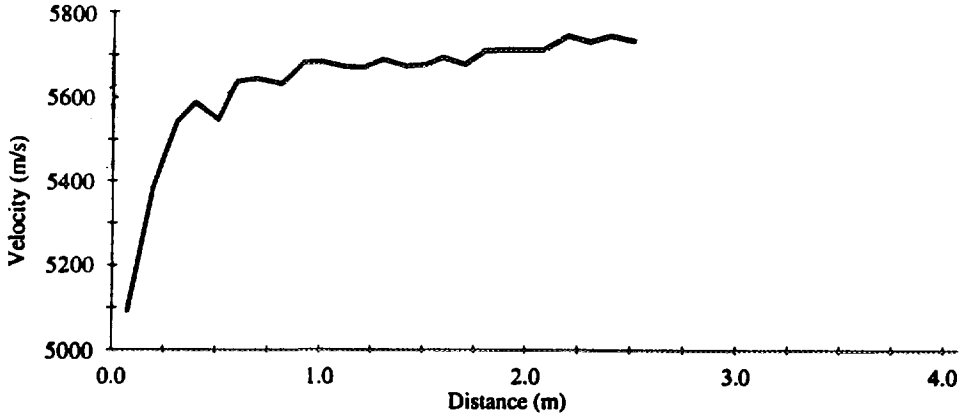

Figure B-2a. Velocity vs distance from tunnel wall (after Hayles et al. 1995).

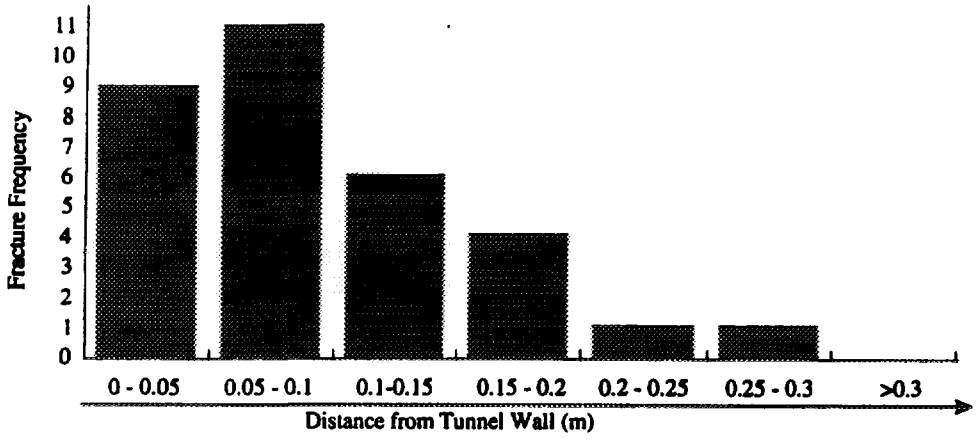

Figure B-2b. Frequency of open fractures in the EDZ (after Brauer and Sonnek 1995).

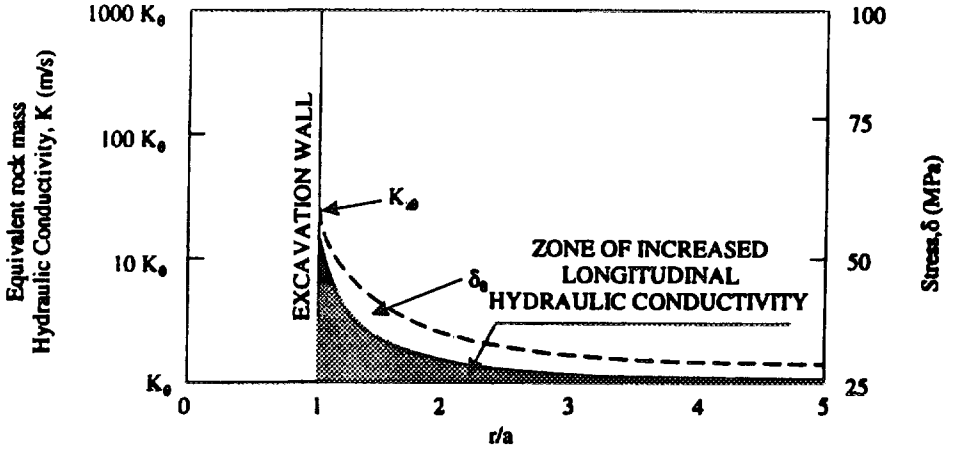

Figure B-2c. Predicted stress redistribution and axial hydraulic conductivity ($K_{z\theta}$) alteration of the disturbed zone around a circular excavation at isotropic initial stress condition, where r/a is the ratio between the extent of EDZ and the radius of the tunnel (after Kelsall et al. 1984).

Figure B-2. Extent and Degree of Disturbance of the EDZ.

extent of $EDZ_y \sim N(1.4, 0.172^2)$. For P = 0.999, the interval limits for the extent of the EDZ are 0.884 m and 1.916 m, i.e., 0.884 m $\leq EDZ_y \leq$ 1.916 m.

The suggested values for the extent of the EDZ are quite conservative. The lower limit (0.884 m) is close to the maximum depth reported by Read and Martin (1996) as well as to the deterministic single values suggested for the primary zone by Birgersson et al. (1992) and Winberg (1991b) in their conceptual models. Compared to the extent of the secondary zone considered by Birgersson et al. (1992) and Winberg (1991b), the suggested values in this study are lower. However, the degree of disturbance decreases exponentially in the radial direction from the surface of the opening; therefore, the characteristics of the secondary zone are quite similar to those of the host rockmass. The overall effect of the EDZ on groundwater flow and transport of radionuclides, using the values for the extent of the EDZ sampled from the distribution proposed, will be higher and more conservative than the values that could be obtained using the conceptual geometry proposed by either Birgersson et al. (1992) or Winberg (1991b).

B.4.2 HYDRAULIC CONDUCTIVITY AND PERMEABILITY OF THE EDZ

Common hydrological practice is to measure hydraulic conductivity K ($m \cdot s^{-1}$) or transmissivity, T = Kb ($m^2 \cdot s^{-1}$). The term permeability has been used in the past with different meanings. At times it has been used as synonymous with or as an alternative to hydraulic conductivity, and it has been used in a loosely qualitative sense to describe the readiness with which a porous medium transmits water or various fluids. In a strictly quantitative sense, the permeability [$k(m^2)$] is ideally an exclusive property of porous/fractured media and their pore/fracture geometry alone — provided the fluid and solid matrix do not interact in such a way as to change the properties of either, and the porous/fractured body is, approximately, at equilibrium. Although the dimension of k is length squared, it should be recognized that the characteristic here refers to the cross-section of the pathway, not its length. However, since the hydraulic conductivity reflects the overall effect of both material and fluid properties on the flow, the permeability can be estimated by the ratio of hydraulic conductivity to fluidity:

$$\because K = kf; \quad \therefore k = \frac{K}{f}; \; f = \frac{g}{\upsilon} = \frac{g\rho}{\mu} \qquad \text{(B-1)}$$

where f is fluidity ($m^{-1} \cdot s^{-1}$), g is gravitational acceleration ($m \cdot s^{-2}$), υ is kinematic viscosity ($m^2 \cdot s$), ρ is density ($kg \cdot m^{-3}$) and μ is dynamic viscosity ($Ns \cdot m^{-2}$).

For water at 6°C, $k = 1.05 \times 10^{-7}$ K; the permeability value is about seven orders of magnitude lower than the value of the hydraulic conductivity in m kg s units.

There are no direct measurements of the hydraulic conductivity of the EDZ from which to develop or infer a PDF. Most of the field studies describe the hydraulic conductivity in qualitative terms and estimate the order of magnitude relative to the undisturbed rockmass. Only limited data were generated from the Buffer Mass Test and Macro-permeability Test at Stripa, two of the most comprehensive studies to investigate the hydraulic conductivity of the EDZ. Pusch (1990), for example, reported a hydraulic conductivity of the undisturbed rockmass of about 10^{-11} to 10^{-10} $m \cdot s^{-1}$ and average longitudinal conductivity of the EDZ of 10^{-8} to 10^{-6} $m \cdot s^{-1}$ within 0.50 m to 1.00 m from the periphery of the tunnel. He did not explicitly correlate the extent and K values of the EDZ. However, since the degree of disturbance decreases exponentially in the radial direction from the periphery of the tunnel, it is more likely that higher K value of 10^{-6} $m \cdot s^{-1}$ was associated with shallow depth (0.50 m). This is probably why Pusch and Börgesson (1992), referring to the same experiments, reported an average axial hydraulic conductivity of 10^{-8} $m \cdot s^{-1}$ for 0.80 m thickness of the EDZ.

Bräuer and Sönnek (1995) and Read and Martin (1996), in their detailed fracture analysis, reported that the spatial orientation of fractures induced by excavation is mostly parallel to the longitudinal axis of the tunnel, highly varying in width and length. This indicates that the hydraulic conductivity is higher in the EDZ, particularly in the axial direction of the opening. However, observed results from the Macro-permeability Test at Stripa suggested that hydraulic conductivity is anisotropic; hydraulic conductivity in the radial direction was smaller than in the axial direction (Nelson and Wilson 1980). Permeability is known to be highly stress-dependent. Based on this relationship, Kelsall et al. (1984) developed an analytical model for elastic rock behaviour that suggested that the EDZ permeability in the axial direction, determined by circumferential or tangential fractures, increases about two orders of magnitude relative to the hydraulic conductivity of the undisturbed rock mass. In contrast the hydraulic conductivity of the radial fractures were reduced by about one order of magnitude compared with the rockmass (Fig. B-3). Calculated values for radial hydraulic conductivity for Stripa compared well with the values inferred from field measurements. Due to the preferential orientation of fractures parallel with the axis of the tunnel and the anisotropy in hydraulic conductivity, this zone is often referred to as "onion skin". The exact mechanism responsible for decrease in radial hydraulic conductivity is not known. Lang et al. (1992) and Pusch (1990) suggested additional causes for this phenomenon, such as blast gas introduced into fractures, drying (unsaturated rock zone) and heating effects. However, to reproduce the field data, they calibrated (fitted) their models by reducing the radial hydraulic conductivity by one to two orders of magnitude. In repository safety and performance studies, all processes need not necessarily be explicitly known. In particular, only the geometry and integral material attributes of the EDZ that are relevant to groundwater flow and transport of radionuclides are required.

The axial hydraulic characteristics of the EDZ are similar to the hydraulic characteristics of highly fractured rock zones. The functional shape and the parameters for the axial hydraulic conductivity for the present study were derived from the statistical results of the Site Characterization and Validation field test at Stripa on hydraulic conductivity of the reduced

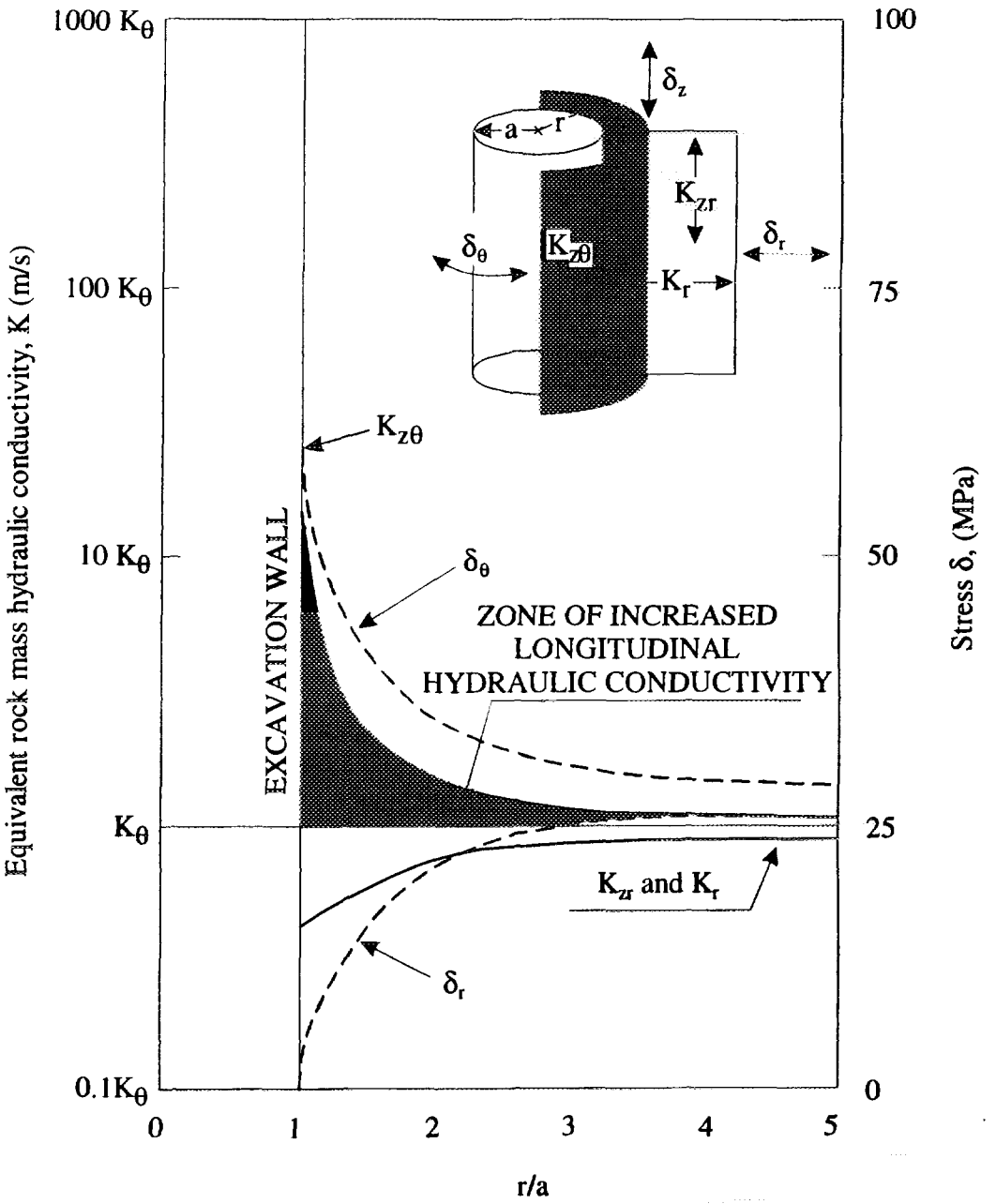

Figure B-3: Predicted Hydraulic Conductivity Alteration of the Disturbed Zone Around a Circular Excavation at Isotropical Initial Stress Condition, Where r/a is the Ratio Between the Extent of EDZ and the Radius of the Tunnel (after Kelsall et al. 1984).

K_{zr} = Hydraulic conductivity of radial fractures in the axial direction,
$K_{z\theta}$ = Hydraulic conductivity of onionskin fracture in the axial direction,
K_r = Hydraulic conductivity in the radial direction,
K_θ = Hydraulic conductivity of the undisturbed rock (isotropic).

pooled population of W1 and W2 boreholes (Winberg 1991a). Stripa granite is characterized by a great abundance of fractures (Olsson et al. 1989) and the W1 and W2 boreholes presented the highest observed hydraulic conductivity values. In addition, Winberg (1991a) revised the field data files and all clusters of ("identical") data of more than two in sequence were deleted, leaving only the higher ("top") value. The relevance of this set of data to our problem is twofold. First, the data set (n = 202 observations) is representative of real field conditions and second, the analysis performed provides detailed information on the shape and magnitude of the scale parameter (variance) of the distribution.

A logarithmic normal distribution was fitted to the data. The summary statistics on this reduced pooled data for K values were as follows: m = -9.78, $\sigma^2_{log(k)} = 2.36$, n = 202, where m = arithmetic mean of log K. The geometric mean is, $\mu_g = 1.7 \times 10^{-10}$, and variance of log(K), $\sigma^2_{log(k)} = 2.36$. It should be pointed out that μ_g does not denote the mean of the variable K, but μ_g is defined by the mean of log K. In the normally distributed population of log K values, 49.9% of the population are squeezed together in a small interval to the left of the median and another 49.9% are scattered over a comparatively larger interval to the right of the median. The mean axial hydraulic conductivity, μ_x and the interval limits for P (0.9987; $\pm 3\sigma$) expressed in $m \cdot s^{-1}$ were calculated using the following equations:

$$\mu_x = \mu_g 10^{\frac{\sigma^2}{2M}} \quad (0 < x < \infty) \tag{B-2}$$

where M=log e = 0.043425, and

$$\frac{\mu_x}{10^{3\sigma}} < K_x < \mu_x 10^{3\sigma} \tag{B-3}$$

The estimated values for μ_x and the interval limits for P (0.999) were: $\mu_x = 8.9 \times 10^{-8}$ $m \cdot s^{-1}$ and 4.1×10^{-15} $m \cdot s^{-1} < K_x < 6.7 \times 10^{-6}$ $m \cdot s^{-1}$.

Since the axial hydraulic conductivity can never be lower than the hydraulic conductivity of the undisturbed rockmass, a truncation of a known value, equal to 1.0×10^{-10} $m \cdot s^{-1}$, the estimated value for undisturbed rockmass, was assumed and the suggested interval limits for axial hydraulic conductivity of the EDZ were 1.0×10^{-10} $m \cdot s^{-1}$ to 6.7×10^{-6} $m \cdot s^{-1}$. These are conservative values. For example the mean value, $\mu_x = 8.9 \times 10^{-8}$ $m \cdot s^{-1}$, is higher than the value reported by Pusch and Börgesson (1992) as an average axial hydraulic conductivity (10^{-8} $m \cdot s^{-1}$) for a 0.80 m thickness of EDZ. Considering both the range of EDZ extent (0.884 m to 1.916 m) and the range of axial conductivity (1.0×10^{-10} $m \cdot s^{-1}$ to 6.7×10^{-6} $m \cdot s^{-1}$), the overall suggested K_x values are higher than these considered by Birgersson et al. (1992) and Hautojärvi (1991) in their models.

To account for anisotropy, the radial hydraulic conductivity, K_x, is assumed to be one order of magnitude lower than the value of axial hydraulic conductivity ($K_y = K_x/10$), the smallest anisotropy ratios recommended by Winberg (1991b) for the EDZ.

In terms of permeability, in two-dimensional space, the second-rank (symmetrical) permeability tensor is:

$$\tilde{k} = \begin{bmatrix} k_{xx} & k_{xy} \\ k_{yx} & k_{yy} \end{bmatrix}; \; k_{xy} = k_{yx} \tag{B-4}$$

For principal axes, the (diagonal) permeability tensor is:

$$\tilde{k} = \begin{bmatrix} k_{xx} & 0 \\ 0 & k_{yy} = k_{xx}/10 \end{bmatrix} \tag{B-5}$$

Using Eq. (B-1), the estimated permeability values were seven orders of magnitude lower than the hydraulic conductivity values. For the axial direction the geometric mean permeability, GM = 1.7×10^{-17} m^2 and the geometric standard deviation GSD = 34. The interval limits for permeability in the axial direction for P = 0.999 are 4.1×10^{-17} m^2 and 6.7×10^{-13} m^2, and truncated at 1.0×10^{-17}, 1.0×10^{-7} m^2 < k_x < 6.7×10^{-13} m^{-2}. The permeability in the radial direction is assumed to be one order of magnitude lower than the value of axial permeability ($k_y = k_x/10$).

B.4.3 EDZ DISPERSIVITY

The equation of mass conservation of a species α, averaged over an REV of a porous medium, also known as the equation of hydrodynamic dispersion, is generally written as:

$$\frac{\partial \rho_\alpha}{\partial t} = V - \left(\tilde{D} \nabla \rho_\alpha \right) - V \nabla \rho_\alpha \tag{B-6}$$

where ρ_α is mass density, $\tilde{D}$ is the hydrodynamic dispersion coefficient (tensor) and V is the average fluid velocity (vector).

The hydrodynamic dispersion coefficient, which includes the effect of both mechanical (convective) dispersion and molecular dispersion, can be derived with the aid of dimensional analysis (Bear 1972) and written as a sum of the coefficient of mechanical dispersion (D^*) and molecular diffusion (D^m) [$D = D^* + D^m$], D being a function of Peclet

number of molecular diffusion. Further, the mechanical dispersion coefficient is often written as a linear function of velocity V and some characteristic length scale, a_l, termed dispersion coefficient or simple dispersivity [$D^* = a_l V$]. The spreading of the mass of solute in a solution, as the flow takes place, is not isotropic even if the medium is isotropic; spreading in the direction of the main flow (longitudinal dispersivity, a_{11}) differs from that perpendicular to it (transverse dispersivity, a_{22}).

The hydraulic dispersion, mechanical dispersion and the dispersivity coefficients have been extensively analyzed by numerous investigators (Bear 1972; Freeze 1975; Gelhar and Axness 1983; Frind and Matanga 1985; Dagan 1990; Neuman 1990; Moltyaner and Wills 1991).

The medium's dispersivity is a complex four-rank tensor; for a two-dimensional isotropic system, Bear (1961) presented 16 components (4 x 4 matrix) and for a three-dimensional, anisotropic medium, Scheidegger (1961) included 81 components. A very simple approach was used in this study to describe the dispersivity of the EDZ. For uniform average velocity, two dimensions (x, y plane) and the condition that direction of the average velocity coincides with one of the axes at every instant; the dispersivity tensor takes the following form:

(a) For dispersion in the direction parallel to the tunnel axis (x direction):

$$D^*_{xx} = \begin{bmatrix} a_{xx11} & 0 \\ 0 & a_{xx22} \end{bmatrix} \qquad \text{(B-7)}$$

(b) For dispersion in the direction perpendicular to the tunnel axis (y direction):

$$D^*_{yy} = \begin{bmatrix} a_{yy11} & 0 \\ 0 & a_{yy22} \end{bmatrix} \qquad \text{(B-8)}$$

No field experiments have been carried out that have yielded quantitative results concerning dispersivity coefficients for the EDZ. In order to provide the values for these coefficients which are required as input by the vault model, it was assumed that these coefficients are completely dependent on the scale of the study, i.e., the EDZ dimensions for a room element of the vault, constant for a given realization and their values can be estimated using data from the literature. The dispersivity values reported in the literature vary widely. This is reasonable since the dispersivity coefficient, always derived from back analysis, reflects the overall outcome of actual movements of individual tracer particles through the pores/fractures and various physical and chemical phenomena that take place within a given system. Many forces and processes, most of them coupled, control each movement such as the hydraulic gradient, the geometry of pores/fractures, reactions between the liquid and solid phases (adsorption, deposition, ion exchange, etc.) and molecular diffusion.

Neuman (1990) pointed out that it is common in the groundwater literature to distinguish between four major scales: pore, laboratory, local field and regional. For the EDZ around a

room element of the vault, a local field scale, L_s, of about 100 m for the length of the room and about two orders of magnitude smaller for the radial extent would be appropriate scales for calculating the dispersivity coefficients based on some scaling rule. The distribution of dispersivity coefficient is assumed to be uniform.

The interval limits for longitudinal dispersivities, a_{xx11} were calculated using a linear model between $\log_{10}$ of the longitudinal dispersivity and $\log_{10}$ of the scale factor (Neuman 1990). The equation of the line best fitted to over 130 dispersivities from laboratory and field studies conducted on different scales given by Neuman (1990) is:

$$a_{xx11} = 0.0175 L_s^{1.46} \qquad \text{(B-9)}$$

with regression coefficient $R^2 = 0.75$ and 95% confidence intervals [0.0113, 0.0272] about the coefficient 0.0175, and [1.30, 1.61] about the exponent 1.46.

Using Eq. (B-9) and upper confidence intervals, the interval limits for a_{xx11} were estimated to be 14.556 m and 45.141 m and for a_{yy11} 0.145 m and 0.451 m, two orders of magnitude lower than the a_{xx11} values.

It is well established that transverse dispersivity (primarily induced by intensive mixing that takes place at junctions of fractures) is lower than the longitudinal dispersivity. The ratio of transverse to longitudinal dispersivity varies with the degree of anisotropy of the fractured zone in both directions, the main flow and/or gradient angle to the bedding and many other factors. The value used in this study for both the ratios, a_{xx22} / a_{xx11} and a_{yy22} / a_{yy11}, is 0.012, the average of several values (0.007, 0.04, 0.001 and 0.0014) reported for a series of field studies (Gelhar and Axness 1983). The interval values for a_{xx22} were estimated at 0.175 m and 0.5421 m, and for a_{yy22} 1.8×10^{-3} and 5.5×10^{-3} m.

B.5 CONCLUSIONS

The summary data of a conceptual model for the EDZ is presented in Table B-1.

There are no well-established criteria for defining the EDZ and its attributes and detailed information about the geometry and the attributes of the EDZ is lacking. In the absence of independent measurements on the EDZ, the suggested values are indirect derivations from literature data in conjunction with several general assumptions. These values should be regarded as preliminary estimates, but are conservative values.

TABLE B-1

THE SUMMARY DATA OF A CONCEPTUAL MODEL FOR THE EDZ[1].

CHARACTERISTIC / PDF type	Parameters of PDF		Interval limits (P=0.999)	
	μ / μ_g / A	σ / $\sigma_{log(k)}$ / B	≤ X	X≤
1) Extent (m) / Normal				
	1.400	0.172	0.884	1.92
2) Hydraulic conductivity (m s^{-1}) / Log_{10}-normal				
			Truncated at 1.0×10^{-10}	
a) Axial (K_x)	1.7×10^{-10}	34	1.0×10^{-10}	6.7×10^{-6}
b) Radial (K_y)	$K_y = K_x / 10$			
3) Permeability, k (m^2) / Log_{10}-normal				
			Truncated at 1.0×10^{-17}	
a) Axial (k_x)	1.7×10^{-17}	34	1.0×10^{-17}	6.7×10^{-13}
b) Radial (k_y)	$k_y = k_x / 10$			
4) Dispersivity (m) / Uniform				
a) Axial (x-direction)				
a1) Longitudinal (a_{xx11})	14.6	45.1	14.6	45.1
a2) Transverse (a_{xx22})	0.175	0.542	0.175	0.542
b) Radial (y-direction)				
b1) Longitudinal (a_{yy11})	1.46×10^{-1}	4.51×10^{-1}	1.46×10^{-1}	4.51×10^{-1}
b2) Transverse (a_{yy22})	1.75×10^{-3}	5.42×10^{-3}	1.75×10^{-3}	5.42×10^{-3}
5) Porosity/Log-normal				
	GM	GSD	Lower Bound	Upper Bound
	5×10^{-5}	3.16	1×10^{-5}	1
6) Tortuosity/Triangular				
		Peak	Lower Bound	Upper Bound
		3	2	8

For detail regarding symbol-notations see text.

REFERENCES

Andersson, B. and P.A. Halen. 1978. Mining methods used in the underground tunnels and test rooms at Stripa. Lawrence Berkeley Laboratory, Report 7081.

Bear, J. 1972. Dynamics of fluids in porous media. American Elsever, New York.

Bear, J. 1961. On the tensor form of dispersion. J. Geophys. Res. No. 4, 66, 1185-1197.

Barton, N., A. Makurat, K. Mounsen, G. Vik and L. Tunbridge. 1992. Rock Mechanics Characterization and Modelling of the Disturbed Zone Phenomena at Stripa. SKB Technical Report 92-12.

Birgersson, L, K. Skagius, M. Wiborgh and H. Widen. 1992. Project on Alternative Systems Study - PASS. Analysis of performance and long-term safety of repository concepts. SKB Technical Report 92-43.

Bräuer, V. and J. Sönnek 1995. Investigations of damage zones in underground hard rock laboratories. Paper presented at the 3rd International Workshop on Design and Construction of Final Repositories, "Plugging and Sealing". Troyes, France, October 18-20, 1995.

Dagan, G. 1990. Transport in heterogenous porous formations: spatial moments, ergodicity, and effective dispersion. Water Resour. Res., 26(6), 1281-1290.

Freeze, R.A. 1975. A stochastic-conceptual analysis of one-dimensional groundwater flow in nonuniform homogenous media. Water Resour. Res., 11(5), 725-741.

Frind, O.E. and B.G. Matanga. 1985. Dual formulation of flow for contaminant transport modeling. 1 Review of theory and accuracy aspects. Water Resour. Res., 21(2), 159-169.

Gelhar, W.L. and L.C. Axness. 1983. Three-dimensional stochastic analysis of macrodispersion in aquifers. Water Resour. Res., 19(1), 161-180.

Golder Associates 1977. Documentation information for peer group review report - site suitability criteria study. Report prepared by Golder Associates for Lawerence Livermore Laboratories, UoC.

Hayles, G.J., H. Serzu and S.G. Lodha. 1995. Cross-hole seismic tomoraphy surveys for the Mine-By Experiment. Atomic Energy of Canada Limited Technical Record, TR-678, COG-95-021

Hustrulid, W., R. Bennett, F. Ashland and M. Lenjani. 1992. A new Method For Predicting the Extent of Blast Damage Zone. Sprangteknisk Konferens, Nitro Nobel, Göteborg-Kiel.

Hustrulid, W. 1993. The "practical" blast damage zone in drift driving at the Kiruna Mine. LKAB Kiruna and Dept. of Mining, Colorado School of Mines, Golden, Colorado.

Hautojärvi, A. 1991. Effects of repository orientations on mass fluxes. Report YJT-91-01.

Hoek, E. and E.T. Brown. 1980. Underground Excavation in Rock. Institution for Mining and Metallurgy, Imperial College, London.

Holmberg, R. and P-A. Persson. 1979. Design of Tunnel Perimeter Blasthole Patterns to Prevent Rock Damage. Tunnelling 1979 Proceedings, Institution of Mining and Metallurgy, London 1979.

Kelsall, C. P., B.J. Case and R.C. Chabannes. 1984. Evaluation of excavation-induced changes in rock permeability. Int. J. Rock Mech. Min. Sci. & Geomech. Vol 21, 123-135.

Lang, J., A. Mauldon, K. Nelson, S. Martel, P. Fuller and K. Karasaki. 1992. Prediction of flow and drawdown for the Site Characterization and Validation Site in Stripa Mine. Stripa Project , SKB Technical Report 92-05.

Martin, C. D. and S.R. Read. 1996. AECL's Mine-by Experiment: A test tunnel in brittle rock. 2nd NARMS, 1996, Montreal.

Moltyaner, G. L. and A.C. Wills. 1991. Local and plume-scale dispersion in the Twin Lake 40- and 260-m natural gradient tracer test. Water Resour. Res., 27(8), 2007-2026.

Nelson, P. and C. Wilson. 1980. Thermomechanical and macropermeability experiments in the Stripa granite - status report. Proc. Workshop on Thermomechanical - Hydrochemical Modelling for Hardrock Waste Repository. Lawrence Berkeley Laboratory, LBL 11204.

Neuman, P. S. 1990. Universal scaling of hydraulic conductivities and dispersivities in geological media. Water Resour. Res., 26(8), 1749-1758.

Olsson , O., J. Black, J. Gale and D. Holmes. 1989. Site characterization and validation stage 2 - preliminary predictions. Stripa Project Technical Report 89-03.

Pusch, R 1990. Radionuclide transport paths in the nearfield - a KBS-3 concept study. SKB Technical Report 90-32.

Pusch, R and L. Börgesson. 1992. PASS - Project on Alternative Systems Study. Performance assessment of bentonite clay barrier in three repository concepts: VDH, KBS-3 and VLH. SKB Technical Report 92-40.

Pusch, R. 1994. Waste Disposal in Rock. In Developments in Geotechnical Engineering, 76. Elsevier Amsterdam.

Read, S.R. and C.D. Martin. 1996. Technical summary of AECL's Mine-by Experiment Phase 1: Excavation response. Atomic Energy of Canada Limited Report AECL-11311.

Scheidegger, A.E. 1961. General theory of dispersion in porous media. J. Geophys. Res. 66, 3273-3278.

Winberg, A. 1991a. Analysis of spatial correlation of hydraulic conductivity data from Stripa mine. Stripa Project. SKBTechnical Report 91-28.

Winberg, A. 1991b. The role of the disturbed rock zone in radioactive waste repository safety and performance assessment. A topics discussion and international overview. SKB Technical Report 91-25.

APPENDIX C

AMOUNT OF OXYGEN TRAPPED WITHIN THE CONTAINER

The amount of oxygen trapped in the container can be calculated from the difference between the total internal volume of the container and the volume occupied by the basket, fuel bundles and glass beads. The relevant information is given in Table C-1.

TABLE C-1

INTERNAL DIMENSIONS OF THE COPPER DISPOSAL CONTAINER (Baumgartner 1995)

Total Internal Volume of the Container	0.553 m^3
Volume of the Fuel Basket	0.040 m^3
Volume of the Fuel Bundles	0.176 m^3
Density of the Glass Beads	2491 $kg \cdot m^{-3}$
Porosity	0.35
Volume of Glass Beads	0.219 m^3
Volume of Glass Beads and the Void Space	0.337 m^3
Volume of the Void Space	0.118 m^3 (118 L.)

This void space of 118 L is full of air and at room temperature (25°C) and 1 atmosphere pressure, will contain a total amount of oxygen, Q_{ox}, given by

$$Q_{ox} = (118/22.414) \times (273.15/293.15) \times 0.20946$$
$$\sim 1.01 \text{ mol.}$$

REFERENCE

Baumgartner, P. 1995. Alternative postclosure assessment: void space within copper disposal container. Technical memorandum GSEB-95-281, 1995 July 10.

APPENDIX D

FUEL OXIDATION PRIOR TO WETTING AND ITS EFFECT ON THE SUBSEQUENT CORROSION PROCESS.

Any defective fuel bundles in the container would allow preoxidation of the fuel prior to wetting on failure and flooding of the container. For temperatures of 100°C or less, the oxidation of fuel by dry air proceeds only to the U_3O_7/U_4O_9 stage and the physical breakup of the fuel, which accompanies oxidation to U_3O_8 at higher temperatures, is not observed. According to the review and calculations of McEachern (1996), the diffusion-controlled kinetics which apply to powders also apply to the early stages of the surface oxidation of sintered pellets. McEachern has shown that this oxidation process obeys the equation

$$\tau = (K\tau)^{1/2} \qquad \text{(D-1)}$$

where τ is the oxide layer thickness and K, calculated from the activation energy for the oxidation process (95.7 $kJ \cdot mol^{-1}$) , has a value of 1.195×10^{-21} $m^2 s^{-1}$ at 100°C. At this rate a 1 μm layer of U_3O_7/U_4O_9 would take 26 a to form on the surface of the fuel.

The extent of this preoxidation process would depend on the number of defective fuel bundles and the surface area of exposed fuel. It is possible that all the available oxygen could be consumed by dry oxidation prior to wetting of the fuel. The consequences for the subsequent corrosion of the fuel would, however, be minor. Gray and Thomas (1994) have compared the dissolution (corrosion) rates of unoxidized and preoxidized LWR fuels and found only slightly higher rates for the preoxidized specimens. They concluded that this difference was most likely due to the uncertainties inherent in measuring and/or calculating the surface areas of the specimens.

REFERENCES

Gray, W.J. and L.E. Thomas. 1994. Initial results from the dissolution testing of various air-oxidized used fuels. In Materials Research Society Symposia Proceedings 333 (ed. A. Barkat and R.A. Van Konynenburg) (Scientific Basis for Nuclear Waste Management XVII) 391-398.

McEachern, R.J. 1996. A review of kinetic data on the rate of U_3O_7 formation on UO_2. J. Nucl. Mater. (Submitted)

APPENDIX E

RATE OF CONSUMPTION OF THE OXYGEN IN THE CONTAINER BY REACTION WITH THE FUEL AND/OR THE CONTAINER.

(a) Consumption by Reaction with Fuel

Johnson (1982) has conservatively estimated the fuel surface area to be ~2 $cm^2 \cdot g^{-1}$ based on the determination of the particle size distribution of fuel fragments from a Bruce bundle. While this estimate takes no account of surface roughness or fuel porosity it does include an estimate of the increased surface area due to cracks in the fuel. Each container in the vault will hold 72 fuel bundles each containing 21.3 kg of UO_2. Consequently, the total surface area of fuel exposable to water is 3.07×10^6 cm^2.

The consumption rate of O_2 by reaction with the fuel can then be calculated from the concentration of O_2 in the air-saturated water (~2×10^{-4} $mol \cdot L^{-1}$) and the corrosion rate of UO_2 in aerated solution. We have used our electrochemical model to predict a rate of ~2×10^{-8} $g \cdot d^{-1} \cdot cm^{-2}$ for the corrosion of UO_2 in aerated solution at ~25°C (Shoesmith and Sunder 1991). Since the overall reaction for the consumption of O_2 by the corrosion of fuel

$$2UO_2 + O_2 + 2H_2O \rightarrow 2UO_2^{2+} + 4OH^- \qquad \text{(E-1)}$$

shows that two molecules of UO_2 are oxidized by each molecule of O_2, this leads to a consumption rate for O_2 of ~1.315×10^{-9} $mol \cdot s^{-1}$.

(b) Consumption Rate by Reaction with Copper

The consumption rate of O_2 by the copper container can be estimated using the mixed-potential model for copper corrosion published by King et al. (1995). In this model the mechanism assumed for the anodic dissolution of copper in saline solutions is

$$Cu + Cl^- \underset{k_{-1}}{\overset{k_1}{\rightleftharpoons}} CuCl + e^- \qquad \text{(E-2)}$$

$$CuCl + Cl^- \underset{k_{-2}}{\overset{k_2}{\rightleftharpoons}} CuCl_2^- \qquad \text{(E-3)}$$

where k_1, k_{-1}, k_2, k_{-2} are rate constants for the copper reactions. The coupled cathodic reaction in this mechanism, the reduction of O_2, is

$$O_2 + 2H_2O + 4e^- \rightarrow 4OH^- \qquad \text{(E-4)}$$

The results of King et al. (1995) show that reaction (E-2) is fast and can be considered to be at equilibrium. This means that the anodic reaction is mass-transport limited as opposed to the cathodic reaction (E-4) which is kinetically limited. By combining electrochemical expressions for the anodic and cathodic current densities with mass transport equations for steady-state diffusion , the corrosion current can be expressed in terms of the O_2 concentration by the expression

$$i_{CORR}^3 = \frac{n_a F k_{ma} k_1 k_2 a_{Cl^-}^2}{k_{-1} k_{-2}} (n_c F k_c^o [O_2]_o)^2 \exp\left[\frac{F}{RT}(E_c^o - E_a^o)\right] \qquad \text{(E-5)}$$

which can be rewritten as

$$i_{CORR} = \left(\frac{n_a F K}{k_{-2}} (n_c F k_c^o [O_2]_o)^2 \exp\left[\frac{F}{RT}(E_c^o - E_a^o)\right]\right)^{1/3} \qquad \text{(E-6)}$$

where

$$K = \frac{k_{ma} k_1 k_2 a_{Cl^-}^2}{k_{-1}} \qquad \text{(E-7)}$$

which is appropriate when mass transport rates are high as will be the case inside the container. (By high we mean relative to the rates of mass transport in the compacted buffer/backfill material outside the container.) In this equation a_{Cl^-} is the activity of chloride in the groundwater, n_c is the number of electrons in the cathodic reaction, F is the Faraday constant, k_c^o is the standard rate constant for reaction (E-4), k_{ma} is the anodic mass transport coefficient (5.5×10^{-5} cm·s^{-1}) , $[O_2]_\infty$ is the O_2 concentration in the flooded void space, R is the gas constant, T is the temperature, E_a^o and E_c^o are the standard potentials for reactions (E-2) and (E-4), respectively. It is clear from this equation that i_{CORR} will decrease with time as O_2 is depleted. We can calculate an initial value of i_{CORR} (7×10^{-5} amp cm^{-2}) from Eq. (E-5) using the value of $[O_2]_\infty$ for aerated solution (2×10^{-4} mol·L^{-1}) and the values given by King et al. (1995) for the other parameters. This is equivalent to a consumption rate for O_2 of ~1.34×10^{-5} mol·s^{-1}. This rate is 1.02×10^4 faster than the rate of consumption by fuel.

(c) Time to Consume all the Oxygen

Given the large disparity in the rates of consumption of O_2, it is reasonable to assume that the great majority will be consumed by reaction with the copper container. An estimate of the time required to exhaust the available O_2 (t_{ex}) can be obtained by using a "mean"

value of i_{CORR} ($(i_{CORR})_m$) obtained from Eq. (E-5) using a value for $[O_2]_-$ equal to half the fully aerated value and the equation

$$t_{ex} = Q_{Ox}\, n_c\, F/[(i_{CORR})_m\, A_{cu}] \qquad \text{(E-6)}$$

where Q_{Ox} is the initial quantity of O_2 present in the container (1.01 mol), and A_{Cu} is the surface area of the inside of the container (3.7×10^4 cm^2). This calculation shows that all the available O_2 in the container would be consumed by reaction with the container in ~1.4 days.

REFERENCES

Johnson, L.H. 1982. The dissolution of irradiated UO_2 fuel in groundwater. Atomic Energy of Canada Limited Report, AECL-6837.

King, F., C.D. Litke, M.J. Quinn and D.M. Leneveu. 1995. The measurement and prediction of the corrosion potential of copper in chloride solutions as a function of oxygen concentration and mass-transfer coefficient. Corr. Sci. 37(5), 833

Shoesmith, D.W. and S. Sunder. 1991. An electrochemistry-based model for the dissolution of UO_2. Atomic Energy of Canada Limited Report, AECL-10488.

APPENDIX F

DOSE RATE TO WATER IN CONTACT WITH THE REFERENCE USED CANDU FUEL

We have calculated the alpha, beta and gamma dose rates to water, in contact with CANDU fuel with a burnup of 720 GJ·(kg U)$^{-1}$ (i.e., the reference used fuel in this study), Fig. 5.4, using the results and methods described in a report by Sunder (1995). This report gives the dose rates in water in contact with a *single* CANDU fuel bundle of burnup 685 GJ·(kg U)$^{-1}$, and the reference fuel in the original postclosure assessment (Johnson et al. 1994) and gives a procedure to obtain the dose rates for CANDU fuels of different burnups. The dose rates for fuel of burnup 720 GJ·(kg U)$^{-1}$ were obtained by multiplying the dose rates for the fuel of burnup 685 GJ·(kg U)$^{-1}$, by the factors obtained from Figs. 5.2, 5.4 and 5.6 respectively, in the above report. The values of these factors, used to obtain the results shown in Fig. 5.4, are 1.12, 1.08, and 1.11, for the alpha, beta and gamma dose rates, respectively. Note, the values of these factors depend not only on the burnup of the fuel but also on its age. However, the factors are weak functions of the fuel age. We have used the highest possible values of these factors to maintain conservatism in our calculations.

The most probable source of variation in the alpha dose rate is the varying range of the alpha particles in water which depends on the energy of the alpha particle. The most probable range of energies for alpha particles emitted from used CANDU fuel is from an average of 2.93 MeV to a maximum of 5.3 eV (Sunder 1995). From these energies the variation in alpha dose rates can be estimated. On the basis of this variation the alpha dose rates can be considered to be triangularly distributed with an alpha dose vary factor of 1.00 with upper and lower bounds of 1.66 and 0.77, respectively. The major source of uncertainty in calculating the beta dose rate is the variation in the ratio of the mass stopping powers of water and fuel with the energy of the beta particles. As for alpha dose rates, we can describe the variations in beta dose rate using a triangular distribution with a vary factor of 1.00 with upper and lower bounds of 1.41 and 0.75, respectively.

REFERENCES

Johnson, L.H., D.M. LeNeveu, D.W. Shoesmith, D.W. Oscarson, M.N. Gray, R.J. Lemire and N.C. Garisto. 1994. The disposal of Canada's nuclear fuel waste: the vault model for postclosure assessment. Atomic Energy of Canada Limited Report, AECL-10714, COG-93-4.

Sunder, S. 1995. Alpha, beta and gamma dose rates in water in contact with used CANDU UO_2 fuel. Atomic Energy of Canada Limited Report, AECL-11380, COG-95-340.

APPENDIX G

THE CALCULATION OF GAMMA DOSE RATE AT USED FUEL SURFACES IN THE WASTE CONTAINER

The gamma dose rate to water in a used fuel container is not only a function of the fuel burnup and cooling period but also of the amount and geometry of the fuel due to the large "half-thickness value" (i.e., the thickness of the absorber medium required to reduce the radiation intensity by one half) for gamma radiation. A water layer in contact with the used fuel receives a gamma dose rate not only from the fuel it is in contact with but also from the nearby used fuel. Therefore, the gamma dose rate inside the container would be different from that for a single bundle shown in Fig. 5.4. The alpha and beta dose rates are not a function of the amount of fuel in the container since the range of these particles is too short for the irradiation of close neighbours to occur. Here, we briefly summarize a procedure used to determine the gamma dose rates in the container from the gamma dose rates for a single fuel bundle.

While estimates of the gamma dose to water at the edge of a fuel bundle (Sunder 1995) and at the edge of a reference titanium container are known (Baumgartner 1993), the absorbed dose rate inside the reference copper container is not. The method described here calculates the absorbed dose anywhere inside the container given a known dose at some point in the container. This is done by assuming the container is filled with a uniform density of point source emitters, using the gamma attenuation equations, the Berger form of the buildup equation and assuming the volume reduction factor for a cylinder is proportional to the radius (Truby 1966). From these relationships and assumptions, the attenuation ratio, A(L), can be expressed as:

$$A(L) = N \int_0^{2\pi} \int_0^{R} \exp[-\mu\rho D(r,L,\theta)]B(D(r,L,\theta))dr d\theta \qquad \text{(G-1)}$$

Here,

$$D(r,\theta,L) = \sqrt{r^2 + L^2 - 2rL\cos(\theta)} \qquad \text{(G-2)}$$

and

$$B(D) = 1 + C\mu\rho D \exp(G\mu\rho D) \qquad \text{(G-3)}$$

μ is the gamma ray energy dependent mass attenuation coefficient; ρ is the density of the absorbing medium; L is the radial distance at which the attenuation ratio is desired; N is a normalization factor obtained from evaluating A(L) at R; *R* is the radius of the cylinder;

and C and G are gamma ray energy dependent build up coefficients, also known as Berger factors.

The average density inside the copper container considering all components, glass beads, water, used fuel and Zircaloy is 4.36 $g \cdot cm^{-3}$ (Baumgartner 1993). A mass attenuation coefficient of 0.11 $cm^2 \cdot g^{-1}$ for the gamma radiation (from ^{137}Cs, one of the main sources of the gamma radiation in the used fuel) was used based on the average density inside the container (Shleien et al. 1984). Estimated values of C (1.0) and G (0.08) were used based on Trubey (1966) and the average density.

The attenuation ratio varies with radial position in the container. Since only a single value is desired, an areal average was done of the attenuation ratio. In this manner a value of 1.97 was obtained.

According to Baumgartner (1993) and Simmons and Baumgartner (1994) the absorbed dose rate to air at the edge of a titanium container from the code ONEDANT for a burnup of 1008 $GJ \cdot (kg\ U)^{-1}$ is 53 $Gy \cdot h^{-1}$. The 6.35-mm-thick titanium container will afford very little shielding, about a factor of 0.9; thus, from this calculation the dose rate just inside the container will be about 59 $Gy \cdot h^{-1}$. A calculation by Wilkin (1985) for a burnup of 1008 $GJ \cdot (kg\ U)^{-1}$ from the 3-D Monte Carlo code MCNP gives the dose rate in air at the outer edge of a titanium container to be 22 $Gy \cdot h^{-1}$. Thus, according to the MCNP code the dose rate just inside the container would be about 24 $Gy \cdot h^{-1}$. In a latter calculation, Wilkin (1990) gives the dose rate on contact with a fuel bundle to be ~27 $Gy \cdot h^{-1}$ (Sunder 1995). This calculation was for a fuel bundle of 685 $GJ \cdot (kg\ U)^{-1}$ burnup using from the code ONEDANT. (Note, the dose rate versus time information for gamma radiation shown in Fig. 5.4 is based on this later calculation.)

All the above quoted dose rates are for air (for 10-year-old fuels). The dose rates for a water filled container would be somewhat smaller. To use the bundle dose rates we must first multiply by a factor to convert from the edge of a bundle to the edge of a container, then we must multiply by another factor to include the effect of averaging over the interior of the container. From the above information it would appear that at the edge of the container the dose rate is about twice that calculated for a single bundle (i.e., no more than about two bundles contribute to the dose rate at the edge). This information, however is for the titanium container rather than the copper. The copper container has a larger radius than the titanium and contains more fuel bundles across the diameter (Baumgartner 1993, Simmons and Baumgartner 1994). It is uncertain whether the dose rate would be larger or smaller for the copper container because the larger number of containers across the radius would be counteracted by a larger amount of shielding (~25 mm for the copper container cf. 6.3 mm for the titanium container). For now we will assume that the titanium and copper containers will have about the same dose rates at the edge.

Inside the container, our calculations suggest on average the dose rate is twice the dose at the edge for a copper container. Thus, using a factor of 2 for edge of bundle to edge of

container and a factor of 2 between edge and interior we would get a value of 4 for the final factor to go from bundle to container.

Considering nearest neighbours, the maximum dose rate amplification from bundle to container would be seven (six nearest neighbours plus one in the centre) if attenuation were ignored. Thus, a reasonable distribution for a bundle to container dose conversion factor for use in calculating UO_2 dissolution rates would be a uniform distribution between 4 and 7. This would be conservative because it ignores the effect of water versus air and it uses the ONEDANT data rather than the lower MCNP data. There is some uncertainty about the conversion from the titanium design to the copper design but using the nearest neighbour approach should give an upper bound that is unaffected by this unknown conversion factor.

REFERENCES

Baumgartner, P. 1993. Technical Specifications for a Concept Assessment Engineering Study (CAES) of a Used-Fuel Disposal Centre (UFDC). Atomic Energy of Canada Limited Technical Record, TR-410, COG-92-189.

Shleien, B., D. Pharm and M.S. Terpilak. 1984. The Health Physics Radiological Health Handbook, Nucleon Lectern Associates.

Simmons, G.R. and P. Baumgartner. 1994. The disposal of Canada's nuclear fuel waste: engineering for a disposal facility, Atomic Energy of Canada Limited Report, AECL-10715, COG-93-5.

Smith, H.J., J.C. Tait and R.E. von Massow. 1987. Radioactive decay properties of Bruce "A" CANDU™ UO_2 fuel and fuel recycle waste. Atomic Energy of Canada Limited Report, AECL-9072.

Sunder, S. 1995. Alpha, beta and gamma dose rates in water in contact with used CANDU UO_2 fuel. Atomic Energy of Canada Limited Report, AECL-11380, COG-95-340.

Trubey, D.K. 1966. A survey of empirical functions used to fit gamma-ray buildup factors. Oak Ridge National Laboratory Report, ORNL-RSIC-10.

Wilkin, B. 1985. Source strength and shielding calculations for nuclear fuel waste disposal containers. Technical memorandum, NTB-85-289.

Wilkin, B. 1990. Further CANDU bundle dose rate calculations. Technical memorandum, SAB-90-289.

APPENDIX H

CORROSION RATES USED IN THE MODEL

The procedures used to measure dissolution currents and corrosion potentials have been described elsewhere (Shoesmith et al. 1989, Sunder et al. 1996). The dissolution currents used here are those measured originally (Shoesmith and Sunder 1991) in non-complexing solutions (pH = 9.5, $[CO_3]_{total} < 10^{-3}$ mol·L^{-1}), and recent, more comprehensive measurements have yielded currents an order of magnitude or more lower (Sunder et al. 1996), Fig. H-1. These recent data show that the dissolution currents can vary substantially at the high electrode potentials at which they are measured. This scatter appears to be attributable to the varying degrees of blockage of the dissolution process by the accumulation of secondary phases (e.g. UO_3xH_2O). By extrapolating the line through our original data (1 in Fig. H-1) we ignore these complications but maintain a large measure of conservatism. Consequently, the errors in our predicted corrosion rates reflect the errors in the measured corrosion potentials only.

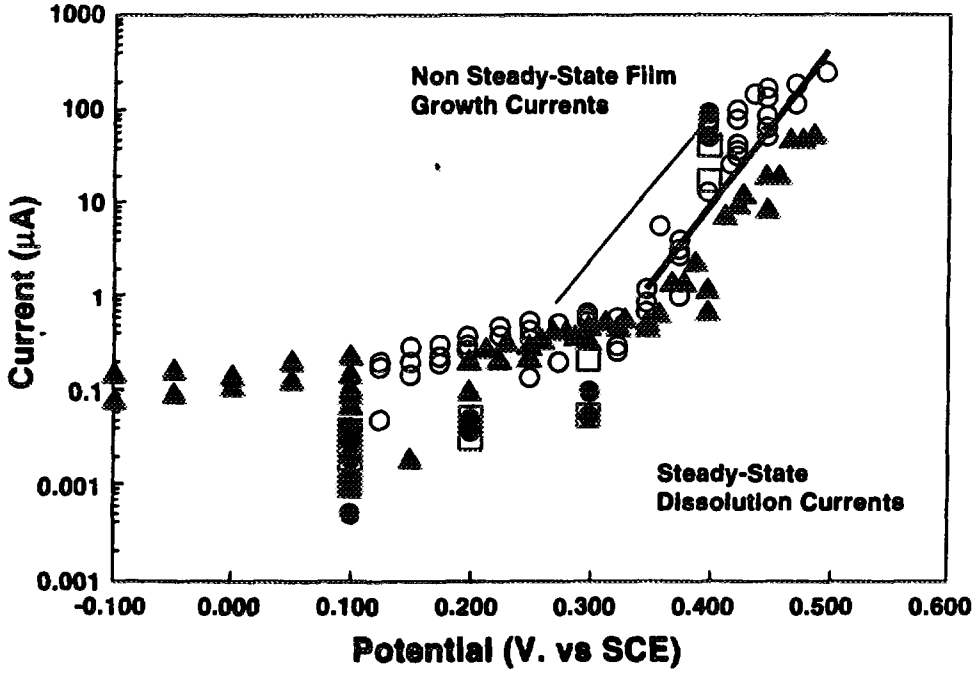

FIGURE H-1: Anodic Dissolution Currents as a Function of Applied Potential Recorded on a UO_2 Rotating Disc Electrode Rotating at 16.7 Hz in 0.1 mol·L^{-1} $NaClO_4$ (pH = 9.5) (Sunder et al. 1996)

Values of corrosion potentials measured as a function of dissolved O_2 concentration, gamma radiation dose rate and alpha source strength have been published (Shoesmith et al. 1989; Sunder et al. 1992, 1995). These values range from >150 mV in solutions exposed to the highest gamma dose rates to <-200 mV for unirradiated deaerated solutions. It is clear that an extrapolation to the more positive corrosion potentials representative of oxidizing conditions will yield more reliable values of corrosion rate than the lengthy extrapolations to the negative end of the corrosion potential range measured under much less oxidizing conditions.

In Fig. 5.5 the corrosion rates obtained in this manner are plotted logarithmically as a function of the dose rate for both gamma and alpha radiation , and the lines represent linear fits to the data. The procedure used to obtain these plots is illustrated schematically in Fig. 5.2 (Section 5.3.2.4). While this fit appears to be reasonable, it obscures a number of features of the data. Figure H-2 shows a plot of the log of the corrosion rate against the

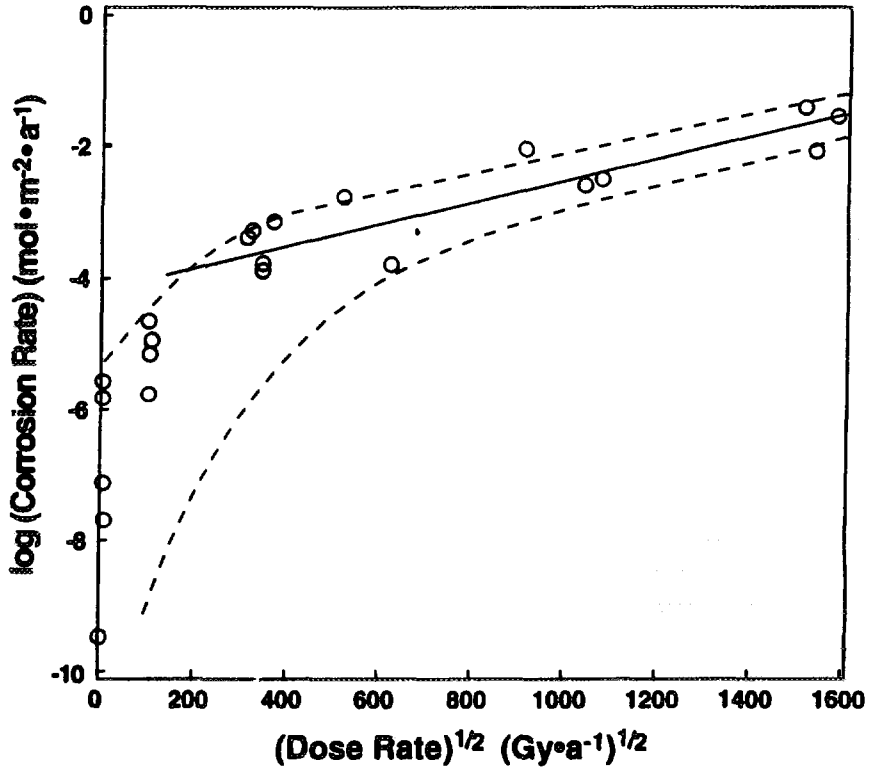

FIGURE H-2: Fuel Corrosion Rates (at 100°C) as a Function of the Square Root of the Gamma Dose Rate Predicted by the Procedure Outlined in Fig. 5.2 Using the Data from Fig. 5.5. The solid line is a linear fit to the data points for dose rates $\geq 1.6 \times 10^5$ Gy·a^{-1}. The dashed lines are envelopes for the data.

square root of dose rate for the data recorded in the presence of gamma radiation. The square root of the dose rate is approximately proportional to the concentration of radiolysis products (Christensen and Sunder 1989). The solid line drawn in Fig. H-2 shows that the corrosion rate is a linear function of dose rate for dose rates $\geq 1.6 \times 10^5$ Gy·a^{-1}. The dashed lines are simply crude envelopes for the data.

For lower dose rates, however, the dependence of corrosion rate on the concentration of radiolysis products appears to be unrealistically large, a fact that is obscured when the data are plotted logarithmically as in Fig. 5.5. Our electrochemistry and XPS results show that this deviation from first order kinetics coincides with a change in the oxidation/dissolution mechanism of UO_2 (Shoesmith and Sunder 1991). In the linear region (dose rate $\geq 1.6 \times 10^5$ Gy·a^{-1}) dissolution is occurring from an oxidized surface layer of composition $UO_{2.33}$. For dose rates $\leq 1.6 \times 10^5$ Gy·a^{-1} the surface composition is a function of potential (UO_{2+x} with x decreasing as the potential decreases) and with decreasing dose rate less positive corrosion potentials are achieved (Sunder et al. 1992). The application of our electrochemical model, therefore, predicts corrosion rates that fall rapidly as the dose rate decreases.

It is possible that this predicted decrease in corrosion rate at low dose rates is real and can be taken to represent expected fuel behaviour. However, it is also possible that extrapolation of currents measured at positive potentials (Fig. H-1) to corrosion potentials achieved in this region where the surface composition is potential-dependent is not merited; i.e., our electrochemical model no longer applies. Even if our model is still applicable, the length of the extrapolation needed to predict rates for low dose rates makes the values obtained uncertain. This uncertainty can be a few orders of magnitude as is clear from Fig. 5.5 for both gamma and alpha radiolysis. In the log fit used in Fig. 5.5, the weight of these low rates is increased with respect to the more accurate higher rates. For these reasons, the values plotted in Fig. 5.5 with closed symbols are not used in our predictions of fuel behaviour.

The consequences of not using these data points lead to conservative predictions of corrosion rates at low dose rates since it assumes that the linear relationship observed at high dose rates will still apply as they decrease. This implicitly assumes that our electrochemical model established at potentials >-100 mV (vs. SCE) applies for potentials below this value also.

REFERENCES

Christensen, H. and S. Sunder. 1989. Calculations of radiolysis in connection with UO_2 oxidation studies. Studsvik Nuclear Technical Note, NS-89/117.

Shoesmith, D.W., S. Sunder, M.G. Bailey and G.J. Wallace. 1989. The corrosion of nuclear fuel (UO_2) in oxygenated solutions. Corros. Sci. 29, 1115-1128. Also Atomic Energy of Canada Limited Reprint, AECL-9887.

Shoesmith, D.W. and S. Sunder. 1991. An electrochemistry-based model for the dissolution of UO_2. Atomic Energy of Canada Limited Report, AECL-10488.

Sunder, S., L.K. Strandlund and D.W. Shoesmith. 1996. Anodic dissolution of UO_2 in slightly alkaline sodium perchlorate solutions. Atomic Energy of Canada Limited Report, AECL-11440, COG-95-461.

Sunder, S., D.W. Shoesmith, H. Christensen and N.H. Miller. 1992. Oxidation of UO_2 fuel by the products of gamma radiolysis of water. J. Nucl. Mater. 190, 78-86.

Sunder, S., D.W. Shoesmith and N.H. Miller. 1995. Prediction of the oxidative dissolution rates of used nuclear fuel in a geological disposal vault due to the alpha radiolysis of water. Materials Research Society Symposia Proceedings 353 (ed. T. Murakami and R.C. Ewing) (Scientific Basis for Nuclear Waste Management XVIII) 617-624.

APPENDIX I

EFFECT OF TEMPERATURE ON THE DISSOLUTION RATE

The temperature at the centre of a disposal container has been calculated as a function of time of emplacement in the vault using a finite element analysis for the in-room emplacement study (Wai and Tsai 1995). This procedure, and the reliability of the results obtained, have been discussed (Baumgartner and Ates 1995, Baumgartner 1995). Figure I-1 shows a plot of the temperature-time profile predicted by this procedure. The maximum temperature is expected to be ~92°C achieved after approximately 10 a of emplacement. By 100 a the temperature will have fallen to ~65°C and by 1000 a to 55°C.

Since radiation dose rates, Fig. 5.4 are highest when fuel temperatures are highest, (Fig. 5.4, Fig. I-1), we have taken the temperature to be a conservatively constant 100°C when calculating the corrosion rates due to water radiolysis. However, by the time radiation dose rates have decayed significantly (i.e., for $t \gtrsim 200$ a) and corrosion rates fallen to below the threshold value, the temperature will have decreased to 50 to 60°C, and will remain in this range until $t \gtrsim 4000$ a (Fig. I-1). Therefore, we have assumed that dissolution at the threshold rate will persist indefinitely at a temperature of 55°C, an approximate mean value for the temperature in this range (~200 to ~4000 a).

We have chosen an activation energy of 33.5 $kJ \cdot mol^{-1}$ based on our review of activation energies (Sunder and Shoesmith 1991) and some recently reported measurements (Shoesmith et al. 1996). Our review shows that, in non-complexing solutions the measured activation energies (29 to 34 $kJ \cdot mol^{-1}$) are lower than those recorded for carbonate-containing solutions (42 to 63 $kJ \cdot mol^{-1}$). This undoubtedly reflects the inhibiting effect of oxidized surface films and deposited corrosion products, the values measured in carbonate solutions being closer to the "real" value for unimpeded corrosion. Since the groundwaters expected to flood the container will not be complexing for the uranyl ion (UO_2^{2+}) the activation energy we have chosen is the largest reported in non-complexing solutions, 33.5 $kJ \cdot mol^{-1}$.

The use of a single value of the activation energy to calculate corrosion rates at high temperatures implicitly assumes that the mechanism of (corrosion) dissolution does not change with temperature, and is controlled by a single activated step. However, experimental evidence exists to show that both the surface chemistry and the effect of radiolysis products on the corrosion processes occurring do change with temperature. Data show that the thickness of the oxidized surface layer ($UO_{2.33}$) increases with temperature (Taylor et al. 1991). This increase, possibly coupled with an increase in the extent of surface blockage by precipitated secondary phases ($UO_3 \cdot H_2O$), probably accounts for the unexpectedly small activation energies measured in non-complexing solutions and is

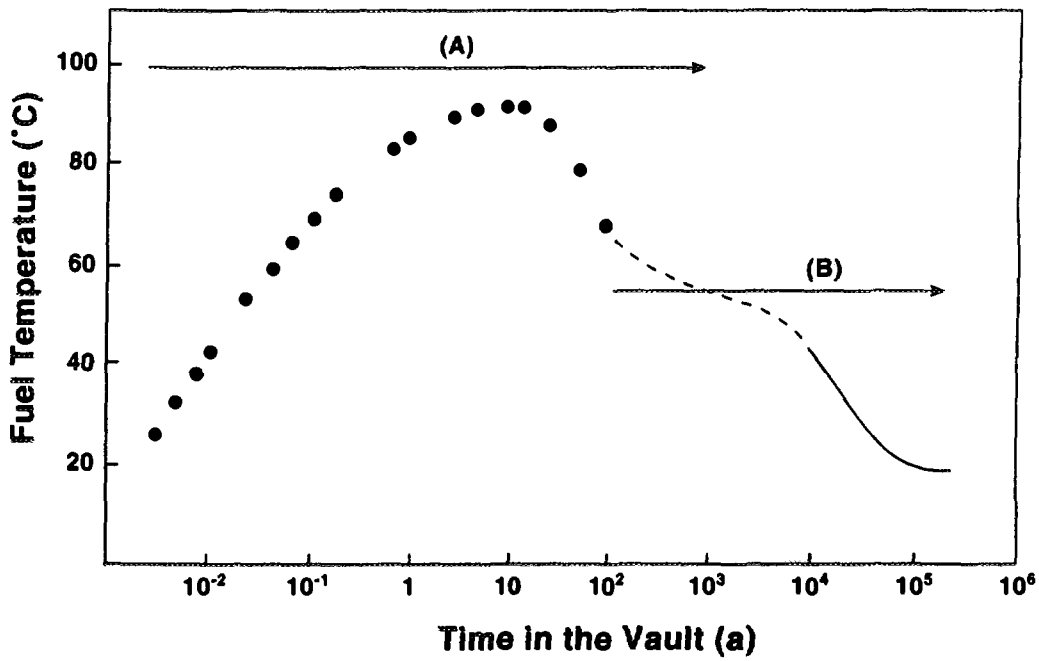

FIGURE I-1: Temperature of the Fuel as a Function of Time in the Vault from the Calculations of Wai and Tsai (1995); (o) calculated container-centre temperature; (———) far-field analysis of vault temperature; (– – – –) estimated fit (Baumgartner and Ates 1995; Baumgartner 1995). The horizontal arrows, A and B, indicate the constant temperatures assumed in calculating the corrosion rates due to water radiolysis (100°C) and the threshold rate assumed to prevail indefinitely (55°C), respectively.

implicitly included in our model as a consequence of choosing a value measured in non-complexing solution. Experiments in which UO_2 specimens are examined by XPS after exposure to irradiated high temperature water show that the degree of surface oxidation decreases as the temperature increases (Sunder et al. 1990, Sunder and Miller 1995). This suggests the kinetic influence of radiolytic reducing species increase as the temperature increases to >100°C. This would be expected to lead to a lower than anticipated rise in corrosion rate at temperatures in the vicinity of 100°C and is not included in the calculations presented in this report.

REFERENCES

Baumgartner, P. 1995. Alternative postclosure assessment: disposal container surface and centre temperature history. Technical memoranda, GSEB-95-322, GSEB-95-328

Baumgartner, P. and Y. Ates. 1995. Alternative postclosure assessment: disposal container and average disposal vault temperature history. Technical memorandum, GSEB-95-277.

Shoesmith, D.W., J.C. Tait, S. Sunder, W.J. Gray, S.A. Steward, R.E. Russo and J.D. Rudnicki. 1996. Factors affecting the differences in reactivity and dissolution rates between UO_2 and spent nuclear fuels. Atomic Energy of Canada Limited Report, AECL-11515, COG-95-581.

Sunder, S. and D.W. Shoesmith. 1991. Chemistry of UO_2 fuel dissolution in relation to the disposal of used nuclear fuel. Atomic Energy of Canada Limited Report, AECL-10395.

Sunder, S., G.D. Boyer and N.H. Miller. 1990. XPS studies of UO_2 oxidation by alpha radiolysis of water at 100°C. J. Nucl. Mater. 175, 163-169.

Sunder, S. and N.H. Miller. 1995. XPS, XRD and SEM study of UO_2 by air in gamma radiation at 150°C. Atomic Energy of Canada Limited Report, AECL-11351.

Taylor, P., D.D. Wood, D.G. Owen, W.G. Hutchings and A.M. Duclos. 1991. Microstructures and phase relationships of crystalline oxidation products formed on unused CANDU fuel exposed to aerated steam and aerated water near 200°C. Atomic Energy of Canada Limited Report, AECL-10476, COG-91-292.

Wai, R.S.C. and A. Tsai. 1995. Three dimensional thermal and thermal-mechanical analyses for a used-fuel disposal vault with the in-room emplacement option. Ontario Hydro Report No. N-REP-03780-0083 R00.

APPENDIX J

DETERMINATION OF THE FITTING PARAMETERS FOR CORROSION RATES

The corrosion rate data used in the calculations presented in this chapter are plotted in Fig. 5.6 (Section 5.4.9), and the reasons for not including the predicted rates at low gamma and alpha dose rates are discussed in Appendix I.

By discarding the values for low dose rates (Fig. 5.5), we avoid predicting a major decrease in corrosion rate for used fuel at these low doses. This is particularly important for alpha radiolysis since we are predicting rates at dose rates substantially lower than those used experimentally (Fig. 5.6A). In the absence of a firm knowledge of the distribution of errors in the experimental points, it is difficult to decide what is the most appropriate relationship to use to fit the data and subsequently to extrapolate it. Consequently, we have performed least-square fits to the power-law dependence,

$$c = b\,d^{a} \qquad \text{(J-1)}$$

where c is the dissolution rate and d is the dose rate ($\alpha(t)$, $\beta(t)$ or $\gamma(t)$) both after a logarithmic transformation of the data points ("log fit") and directly for the original points ("direct fit"). The log fit corresponds to minimizing the following sum of residuals

$$\Sigma_i \,(\log c_i - \log(bd_i^{a}))^2 \qquad \text{(J-2)}$$

which is a linear problem both in log b and in a. The sum of residuals to minimize in the direct fit is

$$\Sigma_i \,(c_i - bd_i^{a}) \qquad \text{(J-3}$$

which results in a nonlinear problem that requires a numerical solution of a single highly nonlinear equation for the unknown a.

For alpha radiolysis we have used the log fit and estimated the error in a predicted value by calculating its standard deviation (Fig. 5.6A). This log fit was deemed more appropriate than a direct fit for two reasons. Firstly, values in a residuals plot are more symmetrically distributed around zero for the log fit than for the direct fit. Secondly, the log fit effectively increases the weight of the low dose-rate points with respect to the high dose-rate points; this is appropriate since, for alpha radiolysis, we are always interpolating between the experimental points and zero dose rate (Fig. 5.6A).

For corrosion due to gamma/beta radiolysis a direct fit would be more conservative if an extrapolation to higher dose rates was required. However, as for alpha radiolysis, the predominant need is for an extrapolation to lower dose rates. For a direct fit the residuals

plot shows the typical triangular shape that warrants a logarithmic transformation (Fig. J-1), and the subsequent log fit yields a residuals plot with a more symmetrical distribution of values around zero (Fig. J-2).

This log fit yields a value for the slope of 1.39 ± 0.12 and would yield very conservative predictions of corrosion rates if extrapolated to higher dose rates. However, its extrapolation to lower dose rates will be particularly dependent on the accuracy of our experimental data points at lower dose rates. When deciding which data points were appropriate to fit, we discarded a number of points for low dose rates because they were corrosion rates predicted from low corrosion potentials in the region where the fuel surface composition is changing with potential (Appendix H). In this region our model may not apply, or, if it does, will yield corrosion rates which decrease rapidly with dose rate (Fig. H-2). This is consistent with our understanding of the UO_2 oxidation/dissolution process. However, if the corrosion rate does decrease rapidly with dose rate for d $<10^5$ Gy·a.$^{-1}$ then the four points at d ~10^4 Gy·a^{-1} (Fig. 5.6) are in error and grossly overpredict the rate for this dose rate. Their inclusion in our fit will, however, exert a significant influence on the slope since the log fit gives extra weight to these points, and a value for the slope of $\sim 1.3 \pm 0.2$ is obtained.

If these data points are not included in our fit then a lower slope would be obtained and the extrapolation of this fit would predict higher corrosion rates at the lower dose rates than the extrapolation of the log fit when these data points are included. To avoid underestimating predicted corrosion rates at lower dose rates without excluding these points we have forced a fit through our data with a unit slope (Fig. 5.4). Also shown in this figure is the unforced fit to illustrate the conservatism inherent in the forced fit procedure.

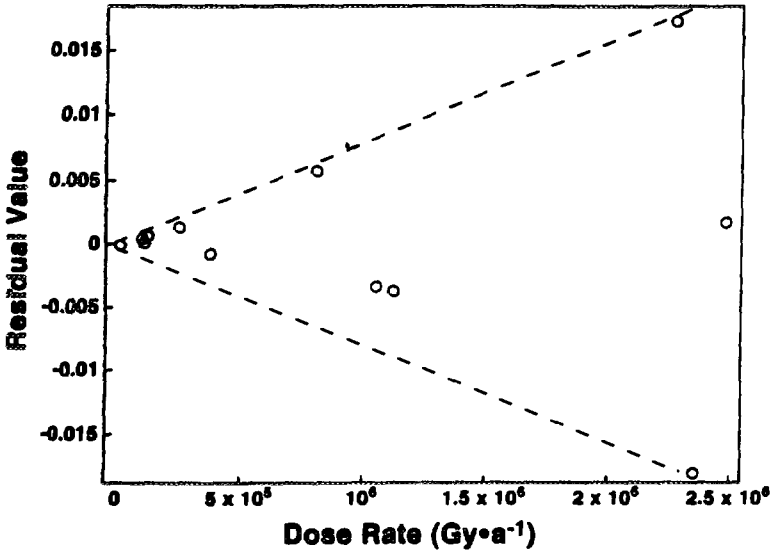

FIGURE J-1: Residuals Plot for the Least-Square Fit of the Corrosion Rates Due to Gamma Radiolysis as a Function of Gamma Dose Rate (direct fit, data from Fig.5.6B)

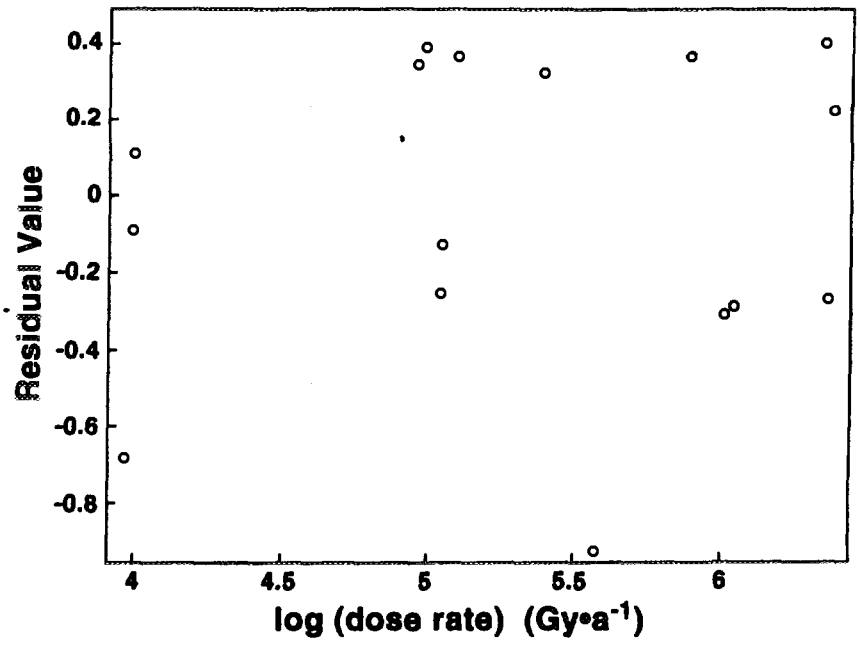

FIGURE J-2: Residuals Plot for the Least-Square Fit of the Corrosion Rates Due to Gamma Radiolysis as a Function of Gamma Dose Rate after a Logarithmic Transformation of the Data Points (data from Fig. 5.6B)

Cat. No. / N° de cat.: CC2-11494/2E
ISBN 0-660-16501-5
ISSN 0067-0367

To identify individual documents in the series, we have assigned an AECL- number to each. Please refer to the AECL- number when requesting additional copies of this document from

Scientific Document Distribution Office (SDDO)
AECL
Chalk River, Ontario
Canada K0J 1J0

Fax: (613) 584-1745 Tel.: (613) 584-3311
ext. 4623

Price: E

Pour identifier les rapports individuels faisant partie de cette série, nous avons affecté un numéro AECL- à chacun d'eux. Veuillez indiquer le numéro AECL- lorsque vous demandez d'autres exemplaires de ce rapport au

Service de Distribution des documents officiels (SDDO)
EACL
Chalk River (Ontario)
Canada K0J 1J0

Fax: (613) 584-1745 Tél.: (613) 584-3311
poste 4623

Prix: E